8-2023

Understanding the Hydromechanical Effects of Extreme Events To Improve the Performance of Infrastructure Foundations

Siddharth Marathe
sjmarat@g.clemson.edu

UNDERSTANDING THE HYDROMECHANICAL EFFECTS OF EXTREME EVENTS TO IMPROVE THE PERFORMANCE OF INFRASTRUCTURE FOUNDATIONS

A Dissertation
Presented to
the Graduate School of
Clemson University

In Partial Fulfillment
of the Requirements for the Degree
Doctor of Philosophy
Civil Engineering

---

by
Siddharth Jitendra Marathe
August 2023

Accepted by:
Dr. Nadarajah Ravichandran, Committee Chair
Dr. Ronald D. Andrus
Dr. Abdul A. Khan
Dr. Lawrence C. Murdoch

ABSTRACT

Extreme hydroclimatic events like heavy rainfall, flooding, and prolonged drought can potentially cause the failure of infrastructure foundations, leading to socio-economic losses. Extreme drought events are often ended by heavy rainfall events in U.S. states like California, New Mexico, Nevada, and Utah, resulting in massive flood events which have damaged house foundations. Foundations in expansive soils are prone to damage caused by the shrink-swell potential of such soils when subjected to wetting and drying. Thus, it is important to understand and quantify the effects of extreme hydroclimatic events on the behavior of deep foundations supporting large infrastructures to prevent potential damage to infrastructure and loss of life. These extreme events are predicted to be increasingly common in the future. The bearing capacity of deep foundations depends on the strength and deformation characteristics of the surrounding soil, which vary with changes in the matric suction and/or degree of saturation during the occurrence of an extreme hydroclimatic event. The non-linear relationship between the matric suction/pore pressure and fundamental soil properties underlies these problems, but methods for including these non-linearities in pile design are currently unavailable. Significant progress has been made in developing methods for simulating non-linear hydromechanical effects in soil mechanics, but insights from these simulations have been slow to be incorporated into methods for designing piles. One reason for this is the lack of data describing the performance of deep foundations under conditions representing the range of extreme hydroclimatic events anticipated for the future. Another shortcoming is the lack of data

describing the strain, and stress change in soil, caused by initially creating the pile and then later as pore pressures change.

The objective of this dissertation is to understand the deformation and bearing capacity behavior of drilled shafts subjected to extreme hydroclimatic events, including heavy rainfall, prolonged drought, and earthquake. The sub-objectives included (1) developing a procedure for experimental testing and calibration and numerical analysis for drilled shafts subjected to heavy rainfall, flooding, and drought; (2) understanding the impact of heavy rainfall and earthquake occurring in sequence on the deformation and bearing capacity of drilled shafts; and (3) simplifying the procedure for prediction of the structural response of drilled shafts caused by the liquefaction-induced lateral spreading. This study attempts to contribute to the advancement of the knowledge on this topic which will help in updating the existing design methodology of drilled shafts in the future to achieve a robust and economical design that will have broad impacts on the U.S. economy and quality of life. The broad approach of the investigation for sub-objective (1) is to use both numerical simulations and intermediate-scale laboratory experiments for drilled shafts under different extreme hydrological loads; for sub-objective (2) is to use numerical simulations for drilled shafts under extreme hydrological and earthquake loading; and for sub-objective (3) is to use numerical simulations of the drilled shafts under liquefaction-induced lateral spreading caused by extreme earthquake loading.

The deformation and bearing capacity behavior of drilled shafts in unsaturated soil conditions subjected to heavy rainfall followed by prolonged drought was evaluated using the fully-coupled Geotechnical-Hydrological finite element code PLAXIS 2D. Among the

many constitutive models available in the literature, a modified Mohr-Coulomb constitutive model, which updates the yield criterion and modulus with changes in the matric suction and/or degree of saturation, was used as the model parameters are easy to implement and are known to be robust for a variety of scenarios. A full-scale drilled shaft subjected to time-varying hydrological load in the sand and silty sand was evaluated separately. The analysis was then repeated for a proportionate small-scale drilled shaft in the sand and silty sand. The results show that during rainfall, the drilled shaft settled caused by a decrease in the porewater pressure in the sand leading to a decrease in the axial bearing capacity, and displaced upwards during drought, caused by an increase in the porewater pressure in the sand leading to increase in the axial bearing capacity. This behavior was the opposite in the case of silty sand. Then, for a realistic approach, an experimental setup was constructed and calibrated to investigate the effects of three different rainfall intensities on the deformation and bearing capacity behavior of the small-scale drilled shaft and to validate the small-scale finite element model. The materials and methods adopted for the construction of the experimental setup are discussed in detail. The results obtained from the experimental investigation were used to validate the Finite Element Model (FEM) in PLAXIS 2D. It was observed that the wetting front moves at the same rate in FEM as compared to the experiment and also reaches the drilled shaft bottom at the same time. The axial force variation at various time intervals for the FEM matches with the experiment qualitatively in various aspects.

The impact of natural hazards on deep foundations can be critical and highly unpredictable when extreme hydrological and seismic events occur simultaneously or in

sequence. Thus, to understand the structural response of deep foundations subjected to hydrological loads followed by an earthquake load, a multi-hazard analysis was carried out in PLAXIS 2D. The individual effect of the earthquake load and the combined effect of the hydrological and earthquake loads on the foundation structural demands for the full-scale drilled shaft in the sand were analyzed. When the drilled shaft was subjected to the dynamic load from heavy rainfall followed by dynamic load from the earthquake, the vertical settlement for the drilled shaft was significantly high (7.74 mm) compared to the case where the drilled shaft was subjected to dynamic load from the earthquake (0.01 mm). Hence, the combined effect of heavy rainfall and earthquake can cause more damage to the deep foundations.

Liquefaction-induced lateral spreading can cause damage to a bridge foundation and superstructure if not accounted for in the design stage. The available analytical methods to account for such effects in the design are complex and difficult to follow, as described in the design manuals. Hence, a case study was adopted to predict the structural response of drilled shaft at the end bent of a proposed bridge subjected to liquefaction-induced lateral spreading caused by extreme earthquake events. The structural response of the bridge foundation before, during, and after liquefaction-induced lateral spreading was predicted using the analytical and finite element methods, and the results were compared, which showed that the during-liquefaction scenario was the worst. The accuracy of the analytical methods could not be assessed, and their accuracy needs to be validated by comparison studies between the results of analytical methods with more documented case histories of liquefaction-induced lateral spreading and centrifuge experiments.

DEDICATION

To my beloved parents, Smita Marathe, Jitendra Marathe, and my wife, Kshitija Ghorpade, for their endless love and support throughout my Ph.D. I would like to highlight two truly exceptional people, my best friends, Ameya Patki and Aniraj Jadhav, for making the past 4.5 years much more enjoyable and keeping me sane throughout the whole process.

ACKNOWLEDGMENT

First and foremost, I am extremely grateful to my supervisor, Dr. Nadarajah Ravichandran, for his invaluable advice, continuous support, constant encouragement, patience, and belief in me during my Ph.D. study. It was a great privilege and honor to work and study under his guidance. I am extremely grateful for what he has offered me. I would also like to thank and recognize the other members of my doctoral committee, Dr. Ronald D. Andrus, Dr. Lawrence C. Murdoch, and Dr. Abdul A. Khan, for providing me with additional guidance, valuable ideas, and critique. I want to extend my sincere gratitude to the Shrikhande family for supporting my study through the prestigious Aniket Shrikhande Memorial Assistantship and Fellowship. Further, I would like to extend many thanks to my family for their support, patience, unconditional love, sacrifice, and motivation. I would like to thank my lab mate, Nathan Kidd, and lab technicians, Rodney Morgan and Rodney Merck, for their help and always being there for discussions about anything that I was unsure about. Also, I am very thankful to my friends (Shweta Shrestha, Tharshikka Vickneswaran, Vishnu Saketh Jella, Camilius Amevorku, Zakia Tasnim, Ram Prasad, Shapal Phuyal, and Bikal Shakya) at Clemson University for their support, encouragement, motivation, and friendship.

TABLE OF CONTENTS

ABSTRACT i

DEDICATION v

ACKNOWLEDGMENT vi

TABLE OF CONTENTS vii

LIST OF FIGURES x

LIST OF TABLES xv

CHAPTER 1. INTRODUCTION 1

1.1. OVERVIEW AND MOTIVATION 1

1.2. OBJECTIVE AND APPROACH 3

1.3. DISSERTATION ORGANIZATION 4

1.4. CONTRIBUTION OF THIS DISSERTATION 6

REFERENCES 7

CHAPTER 2. NUMERICAL ANALYSIS OF DEEP FOUNDATIONS SUBJECTED TO EXTREME HYDROCLIMATIC EVENTS 9

2.1. ABSTRACT 9

2.2. INTRODUCTION 10

2.3. Conceptual model 13

2.4. MATERIAL PROPERTIES 14

2.4.1. Soil properties 14

2.4.2. Groundwater flow parameters 17

2.4.3. Drilled shaft properties 20

2.5. ANALYTICAL DESIGN 20

2.6. Determination of mechanical and hydrological loads 21

2.7. NUMERICAL MODELING 22

2.8. Results and discussion 24

2.8.1 Baseline study 24

2.8.2. Full-scale drilled shaft subjected to constant mechanical load and varying hydrological load 27

2.8.3. Small-scale drilled shaft subjected to constant mechanical load and varying hydrological load 32

2.9. DeterminatioN of soil-pile interface properties 34

2.10. CONCLUSION....37

REFERENCES 38

CHAPTER 3. CONSTRUCTION AND CALIBRATION OF EXPERIMENTAL SETUP 43

3.1. ABSTRACT....43

3.2. INTRODUCTION 43

3.3. EXPERIMENTAL INVESTIGATION....46

3.3.1. Construction of small-scale precast drilled shaft....46

3.3.2. Construction of soil box....48

3.3.3. Instrumentation and calibration of sensors 50

3.3.4. Instrumentation and calibration of mechanical loading setup 72

3.3.5. Design of configuration layout and construction of mechanical loading setup....74

3.3.6. Instrumentation and calibration of hydrological loading setup 76

3.3.7. Experimental setup procedure....83

3.3. CONCLUSION....85

REFERENCES 86

CHAPTER 4. EXPERIMENTAL TESTING AND FINITE ELEMENT MODEL VALIDATION....88

4.1. ABSTRACT....88

4.2. INTRODUCTION 89

4.3. SMALL-SCALE EXPERIMENTAL MODEL TESTING 90

4.3.1. Static pile load testing under mechanical load....91

4.3.2. Hydrodynamic pile load testing under hydroclimatic load....96

4.4. COUPLED FINITE ELEMENT MODEL AND ITS VALIDATION....117

4.4.1. Results and discussion 122
4.5. CONCLUSION 142
REFERENCES 144
Chapter 5. MULTI-HAZARD ANALYSIS OF DEEP FOUNDATION 147
5.1. ABSTRACT 147
5.2. INTRODUCTION 148
5.3. MATERIAL PROPERTIES AND LOADING CONDITIONS 150
5.3.1. Soil properties 150
5.3.2. Drilled shaft properties 152
5.3.3. Mechanical load 152
5.3.4. Earthquake load 154
5.3.5. Hydrological load 154
5.4. PUSHOVER ANALYSIS 155
5.4.1. Drilled shaft subjected to pseudo-static load from the earthquake 157
5.4.2. Drilled shaft subjected to combined axial and pseudo-static load from the earthquake 158
5.5. MULTI-HAZARD ANALYSIS 160
5.5.1. Drilled shaft subjected to dynamic load from the earthquake 162
5.5.2. Drilled shaft subjected to dynamic load from heavy rainfall 163
5.5.3. Drilled shaft subjected to dynamic load from heavy rainfall and earthquake 165
5.6. CONCLUSION 167
REFERENCES 168
CHAPTER 6. COMPARISON OF STRUCTURAL RESPONSE OF BRIDGE DRILLED SHAFT PREDICTED FROM DIFFERENT METHODS SUBJECTED TO LIQUEFACTION-INDUCED LATERAL SPREADING 170
6.1. ABSTRACT 170
6.2. INTRODUCTION 171
6.3. CASE STUDY 174
6.3.1. Site location 174

6.3.2. Soil properties 175

6.3.3. Initial drilled shaft geometry and properties 177

6.4. METHOD 1: STRUCTURAL RESPONSE OF DRILLED SHAFT USING SIMPLIFIED ANALYTICAL METHOD 177

6.4.1. Simplified Analytical Method for Determination of the Design Displacement Demand 178

6.4.2. Minimum Penetration Analysis 189

6.4.3. Analysis and Discussion 190

6.5. METHOD 2: STRUCTURAL RESPONSE OF DRILLED SHAFT USING RIGOROUS ANALYTICAL METHOD 191

6.5.1. Rigorous Analytical Method for Determination of the Design Displacement Demand 192

6.5.2. Analysis and Discussion 196

6.6. METHOD 3: STRUCTURAL RESPONSE OF DRILLED SHAFT USING COUPLED FINITE ELEMENT METHOD 198

6.6.1 Finite Element Model 198

6.6.2. Analysis and Discussion 199

6.9. CONCLUSION 205

REFERENCES 206

CHAPTER 7 SUMMARY AND CONCLUSIONs 210

LIST OF FIGURES

Figure 2.1. Conceptual model 13
Figure 2.2. SWCC for Test Sand and H-SM 19
Figure 2.3. Hydrological load-time history for (a) full-scale and (b) small-scale drilled shafts 22
Figure 2.4. Simulation domain for the 2D axisymmetric model for the small-scale model 23
Figure 2.5. Temporal variation of (a) vertical displacement and DOS, and (b) vertical displacement and PWP in Test Sand at different depths 26
Figure 2.6. Temporal variation of (a) vertical displacement and DOS and (b) vertical displacement and PWP in H-SM at different depths 27
Figure 2.7. Degree of saturation contours at various time intervals for the full-scale drilled shaft in silty sand subjected to hydrological loads 28

Figure 2.8. Temporal variation of vertical displacement of (a) soil 1 m away from the full-scale drilled shaft, and (b) full-scale drilled shaft in Test Sand 29
Figure 2.9. Temporal variation of vertical displacement of (a) soil 1 m away from the full-scale drilled shaft and (b) full-scale drilled shaft in H-SM 30
Figure 2.10. Temporal variation of (a) total skin resistance and (b) end bearing resistance in Test Sand for full-scale drilled shaft 31
Figure 2.11. Temporal variation of (a) total skin resistance and (b) end bearing resistance in H-SM for full-scale drilled shaft 31
Figure 2.12. Temporal variation of vertical displacement in H-SM for small-scale drilled shaft 33
Figure 2.13. Temporal variation of (a) total skin resistance and (b) end bearing resistance in H-SM for small-scale drilled shaft 33
Figure 3.1. Small-scale precast drilled shaft (a) holder frame design, (b) constructed holder frame, and (c) final precast drilled shaft 48
Figure 3.2. (a) Soil box drawing, (b) Constructed soil box, and (c) precast drilled shaft installed on the base layer 49
Figure 3.3 (a) EC-5 soil moisture sensor and (b) Em5b data logger 51
Figure 3.4 Design of EC-5 moisture sensor configuration layout 52
Figure 3.5 RT-1 temperature sensor 53
Figure 3.6 Design of RT-1 temperature sensor configuration layout 53
Figure 3.7 Depiction of reflected and transmitted spectrum of FBG for a broadband light source. 55
Figure 3.8 SM125-500 interrogator for FBG sensor 56
Figure 3.9 (a). Deformed shape of simulation domain (Scale- 5 times) in PLAXIS 2D .. 58
Figure 3.9 (b). Deformed shape of simulation domain with vertical displacement contours (Scale- 5 times) in ABAQUS 3D 58
Figure 3.10. Vertical (a) displacement and (b) strain profiles at drilled shaft center 59
Figure 3.11. Vertical (a) displacement and (b) strain profiles at the soil-pile interface ... 60
Figure 3.12. Vertical (a) displacement and (b) strain profiles in soil at 70 mm away from the drilled shaft center 61
Figure 3.13. Vertical (a) displacement and (b) strain profiles in the soil at 500 mm away from the drilled shaft center 62
Figure 3.14. Radial strain variation at various depths from ground level in the soil away from drilled shaft 62
Figure 3.15 Design of vertical and radial FBG fiber configuration layout 63
Figure 3.16. Procedure for installing FBG fiber on the bias-ply ribbon 66
Figure 3.17 (a). Ribbon without glued sand in Direct Shear Test setup 67
Figure 3.17 (b). Ribbon with glued sand in Direct Shear Test setup 67
Figure 3.18. Stress-strain variation for (a) 24 kPa and (b) 96 kPa vertical pressure 68
Figure 3.19. Procedure for installing FBG fiber in rebar (a) 1.5x 1.5mm slit on rebar, (b) laying and clamping of fiber on rebar, and (c) conical urethane caste on the splice for protection 70
Figure 3.20. Procedure for installing FBG fiber on concrete surface 72
Figure 3.21. (a) LDI-619-050-A010S and (b) LD620-50 LVDT models 73

Figure 3.22. LC402-25K load cell model 74
Figure 3.23. (a) Design and (b) procedure for mechanical loading setup construction.... 76
Figure 3.24. (a) Placement of water cups and (b) test run for the POC test 78
Figure 3.25. Configuration 1 layout and spray variation using four square spray nozzles at 2.56 ft height from ground level 79
Figure 3.26. Configuration 2 layout and spray variation using four square spray nozzles and one cone spray nozzle at 2.56 ft height from ground level 80
Figure 3.27 (a) Configuration 3 layout and spray variation using four square spray nozzles and one cone spray nozzle at 4 ft. height from ground level 81
Figure 3.27 (b) Smoothened spray variation for Configuration 3 layout 82
Figure 3.25. Drought setup comprising two heaters 83
Figure 3.26. Summary flowchart for experimental setup construction 84
Figure 4.1. Sensor configuration 91
Figure 4.2. Pile load testing setup 94
Figure 4.3. Measured load-settlement curves 95
Figure 4.4. (a) Temporal variation of strain and (b) axial force distribution in the drilled shaft during static pile load testing 96
Figure 4.5. Rainfall application 97
Figure 4.6. Temporal variation of the degree of saturation (a) 0.10 m, (b) 0.20 m, (c) 0.30 m, (d) 0.61 m, (e) 0.91 m, (f) 1.22 m (g) 1.52 m depths from ground level for low-intensity rainfall in the experiment 101
Figure 4.7. Temporal variation of the degree of saturation (a) 0.10 m, (b) 0.20 m, (c) 0.30 m, (d) 0.61 m, (e) 0.91 m, (f) 1.22 m (g) 1.52 m depths from ground level for medium-intensity rainfall in the experiment 103
Figure 4.8. Temporal variation of the degree of saturation (a) 0.10 m, (b) 0.20 m, (c) 0.30 m, (d) 0.61 m, (e) 0.91 m, (f) 1.22 m (g) 1.52 m depths from ground level for high-intensity rainfall in the experiment 105
Figure 4.9. Spatial variation of the degree of saturation (a) before, (b) during, and (c) after low-intensity rainfall in the experiment 106
Figure 4.10. Spatial variation of the degree of saturation (a) before, (b) during, and (c) 24 hours after medium-intensity rainfall in the experiment..... 107
Figure 4.11. Spatial variation of the degree of saturation (a) before, (b) during, and (c) 24 hours after high-intensity rainfall in the experiment..... 107
Figure 4.12. Temporal variation of mechanical load for low-intensity, medium-intensity, and high-intensity rainfall in the experiment 109
Figure 4.13. Temporal variation of vertical displacement for (a) low-intensity, (b) medium-intensity, and (c) high-intensity rainfall in the experiment..... 112
Figure 4.14. Temporal variation of vertical strain in the drilled shaft at various depths for (a) low-intensity, (b) medium-intensity, and (c) high-intensity rainfall in the experiment..... 114
Figure 4.15. Spatial variation of axial force at various time intervals for (a) low-intensity rainfall, (b) medium-intensity rainfall, and (c) high-intensity rainfall in the experiment 115
Figure 4.16. SWCC for the Test Sand used for the finite element model 119

Figure 4.17. Finite element mesh of small-scale drilled shaft in Test Sand 122
Figure 4.18. Experimental and FEM comparison of temporal variation of the degree of saturation at (a) 0.10 m, (b) 0.20 m, (c) 0.30 m, (d) 0.61 m, (e) 0.91 m, (f) 1.22 m (g) 1.52 m depths from ground level for low-intensity rainfall..... 124
Figure 4.19. Experimental and FEM comparison of temporal variation of the degree of saturation at (a) 0.10 m, (b) 0.20 m, (c) 0.30 m, (d) 0.61 m, (e) 0.91 m, (f) 1.22 m (g) 1.52 m depths from ground level for medium-intensity rainfall..... 126
Figure 4.20. Experimental and FEM comparison of temporal variation of the degree of saturation at (a) 0.10 m, (b) 0.20 m, (c) 0.30 m, (d) 0.61 m, (e) 0.91 m, (f) 1.22 m (g) 1.52 m depths from ground level for high-intensity rainfall..... 128
Figure 4.21. Experimental and FEM comparison of spatial variation of the degree of saturation (a) before, (b) during, and (c) 24 hours after low-intensity rainfall..... 130
Figure 4.22. Experimental and FEM comparison of spatial variation of the degree of saturation (a) before, (b) during, and (c) 24 hours after medium-intensity rainfall 130
Figure 4.23. Experimental and FEM comparison of spatial variation of the degree of saturation (a) before, (b) during, and (c) 24 hours after high-intensity rainfall..... 131
Figure 4.24. (a) FEM, and (b) Experimental and FEM comparison of temporal variation of vertical displacement for low-intensity rainfall 133
Figure 4.25. (a) FEM, and (b) Experimental and FEM comparison of temporal variation of vertical displacement for medium-intensity rainfall 134
Figure 4.26. (a) FEM, and (b) Experimental and FEM comparison of temporal variation of vertical displacement for high-intensity rainfall 135
Figure 4.27. Spatial variation of axial force at various time intervals for (a) low-intensity, (b) medium-intensity, and (c) high-intensity rainfall in FEM 137
Figure 4.28. Experiment and FEM comparison of spatial variation of axial force at various time intervals for low-intensity rainfall 138
Figure 4.29. Experiment and FEM comparison of spatial variation of axial force at various time intervals for medium-intensity rainfall 140
Figure 4.30. Experiment and FEM comparison of spatial variation of axial force at various time intervals for high-intensity rainfall 141
Figure 5.1. Plan and elevation view of the building 153
Figure 5.2. 1994 Northridge earthquake time history (a) acceleration and (b) displacement 154
Figure 5.3. (a) Horizontal displacement, (b) shear force, and (c) bending moment variation in drilled shaft subected to pseudo-static lateral load from the earthquake..... 157
Figure 5.4. (a) Vertical displacement, (b) horizontal displacement, (c) Axial force, (d) skin resistance, (e) shear force, and (f) bending moment variation in drilled shaft subjected to combined axial and pseudo-static load from the earthquake..... 159
Figure 5.5. Simulation domain in PLAXIS 2D..... 161
Figure 5.6. (a) Vertical displacement, (b) horizontal displacement, (c) Axial force, (d) skin resistance, (e) shear force, and (f) bending moment variation in drilled shaft subjected to dynamic load from the earthquake..... 163

Figure 5.7. (a) Vertical displacement, (b) horizontal displacement, (c) Axial force, (d) skin resistance variation in drilled shaft subjected to dynamic load from heavy rainfall 164
Figure 5.8. (a) Vertical displacement, (b) horizontal displacement, (c) Axial force, (d) skin resistance, (e) shear force, and (f) bending moment variation in drilled shaft subected to dynamic load from heavy rainfall and earthquake..... 166
Figure 6.1. (a) Proposed location of the new bridge, (b) old bridge, (c) new bridge under construction, and (d) soil profile and the new bridge elevation..... 175
Figure 6.2. Seismic slope stability analysis for AL scenario and free field conditions using the simplified analytical method..... 181
Figure 6.3. Seismic slope stability analysis for DL scenario and free field conditions using the simplified analytical method..... 182
Figure 6.4. Seismic slope stability analysis for AL scenario with restraining element (FS=1) using the simplified analytical method 183
Figure 6.5. Seismic slope stability analysis for DL scenario with restraining element (FS=1) using the simplified analytical method 184
Figure 6.6. Displacement response of sliding mass (Curve 3) for (a) AL and (b) DL scenarios using the simplified analytical method 185
Figure 6.8. (a) Foundation resisting force vs. soil displacement (Curve 1) and (b) Running average of the foundation resisting force vs. soil displacement (Curve 2) for the DL scenario using the simplified analytical method..... 188
Figure 6.9. Interaction curves for (a) AL and (b) DL scenarios using the simplified analytical method..... 188
Figure 6.10. (a) Imposed soil displacement profiles for AL and DL scenarios; Foundation lateral displacement profiles resulting from minimum penetration analysis for (b) AL and (c) DL scenarios using the simplified analytical method..... 189
Figure 6.11. (a) Lateral deflection, (b) shear force, and (c) bending moment profiles for AL and DL scenarios using the simplified analytical method 191
Figure 6.12. San Fernando (1971) earthquake (a) acceleration and (b) displacement time history 193
Figure 6.13. Interaction curves for (a) Northridge (1994), (b) San Fernando (1971), and (c) Mammoth Lakes (1980) earthquakes for AL scenario and (d) Northridge (1994), (e) San Fernando (1971), and (f) Mammoth Lakes (1980) earthquakes for DL scenario using the rigorous analytical method..... 195
Figure 6.14. (a) Lateral pile head deflection, (b) shear force, and (c) bending moment profiles for AL and DL scenarios using the rigorous analytical method..... 197
Figure 6.15. Simulation domain for the dynamic phase in RS2 199
Figure 6.16. (a) Lateral pile deflection, (b) shear force, and (c) bending moment profiles for BL, DL, and AL scenarios using the finite element method..... 201
Figure 6.17. Comparison of methods showing lateral pile deflection profiles for (a) Northridge (1994), (b) San Fernando (1971), and (c) Mammoth Lakes (1980) earthquakes, shear force profiles for (d) Northridge (1994), (e) San Fernando (1971), and (f) Mammoth Lakes (1980) earthquakes, and bending moment profiles for (g)

Northridge (1994), (h) San Fernando (1971), and (i) Mammoth Lakes (1980) earthquakes for the AL and DL scenarios..... 203

LIST OF TABLES

Table 2.1. Properties of Test Sand and H-SM 16
Table 2.2. Groundwater flow parameters for H-SM and Test sand. 19
Table 2.3. Estimation of C_i for the full-scale drilled shaft in Test Sand..... 35
Table 2.4. Estimation of Ci for the full-scale drilled shaft in H-SM 36
Table 3.1. Summary of friction angles determined from direct shear tests 69
Table 4.1. Loading rate for static pile load test..... 93
Table 4.2. Design parameters for rainfall simulation 98
Table 4.3. Properties and flow parameters of the Test Sand 118
Table 5.1. Input soil properties in RSPile..... 151
Table 5.2. Input soil properties in PLAXIS 2D 151
Table 5.3. Input drilled shaft properties..... 152
Table 6.1. Input soil properties for SLIDE2, RSPile, and RS2 176
Table 6.2. Selected time histories from the database..... 192
Table 6.3. Comparison of maximum structural responses for the DL and AL scenarios203
Table 6.4. Comparison of predicted and field-measured lateral spread displacements from case studies..... 204

CHAPTER 1. INTRODUCTION

1.1. OVERVIEW AND MOTIVATION

Global warming has caused the atmospheric temperature to rise, potentially leading to heavy rainfall and flood events. Moreover, high temperatures may cause some regions to experience more frequent droughts. (NOAA 2022). On average, over the past 50 years, a disaster related to weather, climate, or water hazard has occurred every day, killed 115 people and causing US$ 202 million in losses daily (WMO 2021). Forecasts indicate that such extreme hydroclimatic events will become more frequent in the future (IPCC 2013). Currently, the adverse effects of extreme hydroclimatic events on the geotechnical systems, including deep foundations in unsaturated soil conditions, are poorly understood (Vickneswaran and Ravichandran, 2023). For a better understanding of such effects, prediction by using the finite element method and its validation by conducting an experimental investigation would help in updating the existing design methodology of deep foundations to achieve a robust and economical design that will have broad impacts on the U.S. economy and quality of life.

For the finite element method, many constitutive models are available in the literature for unsaturated soils for the finite element modeling of the deep foundations in unsaturated soils subjected to such extreme hydroclimatic events. Among these models, the Barcelona basic model (BBM) proposed by Alonso et al. (1990) is one of the fundamental models. Other constitutive models for unsaturated soils include an elastoplastic constitutive model that fully couples hydraulic hysteresis with the mechanical

behavior of the unsaturated soil presented by Wheeler et al. (2003). Robert (2017) proposed a modified Mohr-Coulomb model within a generalized effective stress framework considering material softening and suction hardening effects to capture the mechanical behavior of unsaturated soils. Ng et al. (2020) proposed a simple framework for the state-dependent hydromechanical behavior of unsaturated soils. Their framework uses mean net stress, deviator stress, and suction as the constitutive stress variables. There are nine variables with clear physical meanings in their proposed framework. A new hydraulic coupling bounding surface model for unsaturated soils, considering the effects of microscopic pore structure and bonding effect, was proposed by Han et al. (2020). There are many other similar sophisticated constitutive models that are available in the literature, but most of the models are difficult to understand by practicing engineers and numerically unstable or computationally expensive when used for analyzing coupled problems. Also, the model parameters are difficult to determine from the data in standard subsurface exploration reports. In this dissertation, a Modified Mohr-Coulomb (MMC) constitutive model (Vickneswaran and Ravichandran 2022) is used, which modified the simple and widely used linear elastic-perfectly plastic MC model for unsaturated soil. The MMC model updates the yield criterion and modulus with the change in matric suction and/or degree of saturation. The MMC model parameters are easy to implement and are known to be robust for a variety of scenarios. The MMC model can be implemented as a user-defined model in the widely used industry Geotechnical-Hydrological finite element code, PLAXIS 2D.

Moreover, the adverse effects of natural hazards on deep foundations can be critical and highly unpredictable when extreme hydrological and seismic events occur simultaneously or in sequence. Most major environmental disasters result from compound climate extremes (Zscheischler et al. 2018). Hence, multi-hazard analysis is required to understand and predict the combined effect of hydrological and earthquake events on the behavior of deep foundations. In the case of bridge foundations, the seismic events can cause liquefaction-induced lateral spreading in loose soil deposits, which imposes an additional lateral load on the foundation, which can exceed the lateral capacity of the foundation and cause damage to the foundation and the bridge if not accounted in the design stage.

The motivation of this study is to improve the existing design methodology of deep foundations supporting large infrastructures by understanding and quantifying the hydrological and seismic effects of extreme events, including heavy rainfall, flooding, prolonged drought, and earthquake, on the behavior of deep foundations, which will help to achieve a resilient design of deep foundations and reduce socio-economic losses.

1.2. OBJECTIVE AND APPROACH

To objective of this study is to advance the understanding of the effects of extreme hydroclimatic events and earthquakes on the deformation and bearing capacity behavior of deep foundations. The approach is to use a combination of laboratory experiments and numerical simulations to meet the project objectives. Laboratory experiments will be conducted by measuring the deformation of piles placed in tanks filled with sand and

subjected to constant axial loading and varying moistures and temperatures selected to represent different hydroclimatic events. For example, the tanks will be filled with water to raise the pore pressure and represent a flood, or to use a pressure nozzle setup over the ground surface to represent heavy rainfall, and then they will be drained, and their surfaces will be dried with heat lamps to create conditions resembling drought. Instruments in the experimental tanks will measure the deformation of the piles and enveloping sand, as well as the degree of saturation and temperature. A finite element code that solves equations of fully-coupled poroelasticity and plasticity and is widely used in geotechnical engineering will be calibrated using data from the experiments, and constitutive and flow models will be refined as needed to improve the calibration. The calibrated model will then be used to evaluate the performance of deep foundations at full scale under conditions of wide variations of pore pressure expected during extreme climatic events. Accelerations resembling seismicity will be included in the simulations to evaluate the effects of an earthquake occurring after an extreme hydroclimatic event.

1.3. DISSERTATION ORGANIZATION

The dissertation consists of six chapters. In Chapter 1, the introduction is presented, which consists of the objectives, motivation, and organization of the entire dissertation. In Chapter 2, numerical methods were used to predict the deformation and bearing capacity behavior of a full-scale and a small-scale drilled shaft subjected to extreme hydroclimatic events, including heavy rainfall and prolonged drought. A new modified Mohr-Coulomb constitutive model, which updates the yield criterion and modulus with changes in the

matric suction and/or degree of saturation, was used in the fully-coupled Geotechnical-Hydrological finite element code PLAXIS 2D.

In Chapter 3, the construction and calibration of an experimental setup to investigate the effects of extreme hydrological loads on the deformation and bearing capacity behavior of the small-scale precast drilled shaft are carried out. The materials and methods adopted for the construction of the experimental setup are discussed. The design and construction of the precast drilled shaft and soil box are discussed. The instrumentation and calibration of sensors and loading setups, consisting of the working, specifications, data acquisition, and configuration layout, are discussed in detail. In Chapter 4, the results of the experimental investigation and validation of the fully-coupled Geotechnical-Hydrological finite element model for a small-scale drilled shaft in sand subjected to constant mechanical load and varying hydrological loads are discussed.

In Chapter 5, multi-hazard analysis was carried out in the coupled Geotechnical-Hydrological finite element code PLAXIS 2D for a full-scale drilled shaft. The foundation structural responses were predicted for the full-scale drilled shaft caused by the individual effect of earthquake load and the combined effect of hydrological and earthquake loads, including heavy rainfall followed by the seismic load. In Chapter 6, a case study was adopted to predict the structural response of a deep foundation at the end bent of a bridge subjected to liquefaction-induced lateral spreading caused by an extreme seismic event. The structural responses on the bridge foundation before, during, and after liquefaction-induced lateral spreading were predicted using the analytical methods and finite element method, and the results are compared for relative accuracy. In Chapter 6, the overall

summary of the conclusions and the recommendations for future research studies are provided.

1.4. CONTRIBUTION OF THIS DISSERTATION

The major contributions of this dissertation are:

1. Designing and constructing model scale experimental setup for understanding the behavior of deep foundations under extreme hydroclimatic events.
2. Understanding the behavior of deep foundations under extreme hydroclimatic events using experimental and numerical methods.
    2.1. The axial bearing capacity of deep foundations changed with the deformation of the surrounding soil when subjected to extreme hydroclimatic events and depended on the intensity of the events and the flow and deformation properties of the soil.
    2.2. Lower-intensity rainfall caused a decrease in the axial bearing capacity of deep foundations due to the volumetric contraction of the surrounding soil. In comparison, higher-intensity rainfall caused an increase in the axial bearing capacity at shallow depths due to the volumetric expansion of the surrounding soil and an increase in axial bearing capacity at deeper depths due to the volumetric contraction of the surrounding soil.
3. Understanding the behavior of deep foundations under combined rainfall and earthquake scenarios using numerical methods.

3.1. The combined effect of heavy rainfall and earthquake caused significantly high settlement of the drilled shaft as compared to the vertical settlement caused by the individual effect of heavy rainfall and earthquake.

4. Developing/Interpreting the analytical procedure for prediction of the structural response of deep foundations caused by the liquefaction-induced lateral spreading by comparison with the finite element method.

4.1. The finite element method provided more realistic results.

REFERENCES

Alonso, E.E., Gens, A. and Josa, A. (1990) 'A constitutive model for partially saturated soils,' Géotechnique, 40(3), pp. 405–430. doi:10.1680/geot.1990.40.3.405.

Han, B., Cail, G., Xie, L., Li, J., and Zhao, C. (2020). Bounding surface constitutive model for unsaturated soils considering microscopic pore structure and bonding effect. E3S Web of Conferences 195, 02007. https://doi.org/10.1051/e3sconf/202019502007.

IPCC.(2013). Climate Change 2013: The Physical Science Basis. Cambridge University Press.

Ng, C.W.W., Zhou, C. & Chiu, C.F (2020). Constitutive modeling of state-dependent behaviour of unsaturated soils: an overview. Acta Geotech. 15, 2705–2725 (2020). https://doi.org/10.1007/s11440-020-01014-7

NOAA (2022). U.S. Billion-Dollar Weather & Climate Disasters 1980-2022. https://www.ncei.noaa.gov/access/billions/events.pdf

Robert, D. (2017). A Modified Mohr-Coulomb Model to Simulate the Behavior of Pipelines in Unsaturated Soils. Computers And Geotechnics, 91, 146-160. doi: 10.1016/j.compgeo.2017.07.004

Wheeler, S.J., Sharma, R.S. and Buisson, M.S. (2003) 'Coupling of hydraulic hysteresis and stress–strain behaviour in unsaturated soils,' Géotechnique, 53(1), pp. 41–54. doi:10.1680/geot.2003.53.1.41.

WMO (2021). https://public.wmo.int/en/media/press-release/weather-related-disasters-increase-over-past-50-years-causing-more-damage-fewer

Vickneswaran, T. and Ravichandran, N. (2023) 'Performance of Geotechnical Systems Under Extreme Hydroclimatic Events Using a New User-defined Soil Model in PLAXIS". Journal of GeoEngineering. Mar 2023, Vol. 18 Issue 1, p21-31. 11p.

Zscheischler, J., Westra, S., van den Hurk, B. J. J. M., Seneviratne, S. I., Ward, P. J., Pitman, A., AghaKouchak, A., Bresch, D. N., Leonard, M., Wahl, T., & Zhang, X. (2018). Future climate risk from compound events. Nature Climate Change, 8(6), 469–477. https://doi.org/10.1038/s41558-018-0156-3

CHAPTER 2. NUMERICAL ANALYSIS OF DEEP FOUNDATIONS SUBJECTED TO EXTREME HYDROCLIMATIC EVENTS

2.1. ABSTRACT

In this study, the effect of extreme hydroclimatic events, including heavy rainfall and prolonged drought, on the behavior of drilled shafts was predicted using a numerical method. For numerical analysis, a new modified Mohr-Coulomb constitutive model, which updates the yield criterion and modulus with changes in the matric suction and/or degree of saturation, was used in the fully-coupled Geotechnical- Hydrological finite element code PLAXIS 2D. First, a full-scale model with a 0.6 m diameter and 12 m long drilled shaft was modeled separately in the sand and silty sand, then subjected to a constant mechanical load and varying extreme hydrological loads. Then, the analysis was repeated for a small-scale model with a 76 mm diameter and 1.52 m long drilled shaft and compared with the results of the full-scale model. The results show that during rainfall, the drilled shaft settled caused by a decrease in the porewater pressure in the sand leading to a decrease in the axial bearing capacity, and displaced upwards during drought, caused by an increase in the porewater pressure in the sand leading to increase in the axial bearing capacity. This behavior was the opposite in the case of silty sand. The total percentage change in the total ultimate bearing capacity for the full-scale drilled shaft was significantly lower (0.75%) as compared to the small-scale drilled shaft (55.29%) in silty sand.

2.2. INTRODUCTION

Deep foundations are used to support large, critical infrastructure and typically consist of multiple shafts, or piles, driven or cast several meters deep into the soil. These foundations must carry the load of all the structural elements within an acceptable factor of safety. The conventional design methods are based on hydrostatic soil conditions, and also the common perception in practice is to ignore the effects of unsaturated soil to consider the worst-case scenario. However, this perception can lead to inaccurate conclusions (Siemens 2018). The axial capacity of the deep foundation is controlled by its skin and end-bearing resistances, which depend on the strength and deformation characteristics of the surrounding soil. These soil characteristics vary with changes in matric suction and/or degree of saturation (DOS) of the soils. Matric suction is one of the stress state variables that control the strength and deformation behavior of unsaturated soil (Fredlund et al. 1978). It can change significantly in response to changes in saturation caused by extreme hydroclimatic events (Fredlund et al. 2012), decreasing during heavy rainfall and flooding and increasing during drought. The increase in matric suction increases the stiffness and strength of soils and potentially increases the coefficient of friction on the sides of the pile. However, a significant increase in matric suction can cause the surrounding soil to shrink and lose contact with the pile. Thus, prolonged drought can cause loss of normal stress at the soil-pile interface and result in significant loss of skin resistance. Hence, considering fully saturated soil conditions may not be the worst case for design. There is a need to consider the effects of extreme hydroclimatic events, as forecasts indicate that these events will become more frequent in the future (IPCC 2013). As per the

National Oceanic and Atmospheric Administration (NOAA), some parts of central and western USA are predicted to have a 50-100% chance of below-normal precipitation until next year. Also, the western and some parts of the eastern USA are predicted to have a 50-100% chance of above-normal temperatures until next year. Moreover, the current drought outlook shows the existence of persistent drought in the Western USA (National Drought Mitigation Center, United States Department of Agriculture, and National Oceanic and Atmospheric Administration).

More understanding and quantification of the impacts of extreme hydroclimatic events on deep foundations are needed where unsaturated soil mechanics principles are considered for updating the existing design procedures. The objective of this study is to understand the deformation and bearing capacity behavior of drilled shafts subjected to extreme hydroclimatic events, including heavy rainfall and prolonged drought, using the finite element method. Many constitutive models are available in the literature for unsaturated soils. Among these models, the Barcelona basic model (BBM) proposed by Alonso et al. (1987) is one of the fundamental models. Other constitutive models for unsaturated soils include an elastoplastic constitutive model that fully couples hydraulic hysteresis with the mechanical behavior of the unsaturated soil presented by Wheeler et al. (2003). Ng et al. (2020) proposed a simple framework for the state-dependent hydromechanical behavior of unsaturated soils. Their framework uses mean net stress, deviator stress, and suction as the constitutive stress variables. There are nine variables with clear physical meanings in their proposed framework. There are many other similar sophisticated constitutive models that are available in the literature, but most of the models

are difficult to understand by practicing engineers and numerically unstable or computationally expensive when used for analyzing coupled problems. Also, the model parameters are difficult to determine from the data in standard subsurface exploration reports. Ravichandran and Vickneswaran (2021) used a numerical method to show that flooding-induced settlements caused the failure of shallow foundations in unsaturated soils. Mahmoudabadi and Ravichandran (2021) developed a new procedure based on unsaturated soil mechanics principles to couple the site-specific hydrological loads, such as precipitation, evapotranspiration, and water table depth with conventional geotechnical design to quantify the impact of the site-specific extreme hydrological cycle on the performance of a shallow foundation.

In this study, a Modified Mohr-Coulomb (MMC) constitutive model (Vickneswaran and Ravichandran 2022) was used, which modified the simple and widely used linear elastic-perfectly plastic MC model for unsaturated soil. The constitutive model parameters are easy to calculate, and this model can be used as a user-defined model in the widely used industry Geotechnical-Hydrological finite element code, PLAXIS 2D. The MMC model updates the yield criterion and modulus with the change in matric suction and/or degree of saturation. The MMC constitutive model was used to understand the effect of extreme hydroclimatic events on the strength and deformation behavior of the surrounding soil and predict the deformation and bearing capacity behavior of drilled shafts. A full-scale model with a 0.6 m diameter and 12 m long drilled shaft subjected to time-varying hydrological load in the sand and silty sand was evaluated separately. The analysis was then repeated for a proportionate small-scale model with a 76.2 mm diameter

and 1.83 m long drilled shaft in the sand and silty sand to facilitate validation with an experimental study.

2.3. CONCEPTUAL MODEL

A conceptual model was put together in order to have a clear understanding of the effect of various parameters which control the flow and deformation behavior of soil when subjected to extreme hydroclimatic events, including rainfall and drought. Figure 2.1 enlists different controlling variables and how they can affect the deformation and flow in soil when subjected to rainfall and drought. Ravichandran et al. (2021) and Mehndiratta and Sawant (2019) evaluated the effect of wetting due to rainfall on the response of shallow foundations in unsaturated soils and concluded that the movement of the wetting front induces additional settlement of the foundation.

Flow and deformation controlling variables	Effect of controlling variables on flow and deformation in soil during rainfall	Effect of controlling variables on flow and deformation in soil during drought
• Hydraulic conductivity (k) • Void ratio (e) • Soil Water Characteristic Curve • Strength and deformation properties • Intensity of rainfall and drought • Mechanical load on the foundation	• Higher/lower 'k' allows faster/slower movement of the wetting front. • Higher/lower 'e' allows higher/lower flow. • Higher/lower volumetric strains in soil with low/high Young's modulus. • Higher/lower volumetric strains in soil with high/low Poisson's ratio. • Lower/higher effect on deformation for high/low shear strength parameters. • Higher rainfall intensity can induce positive volumetric strains in soil (expansion). • Higher/lower effect on soil deformation for higher/lower mechanical load on foundation.	• Higher/lower 'k' allows faster/slower movement of the drying front. • Higher/lower 'e' allows higher/lower flow. • Higher/lower volumetric strains in soil with low/high Young's modulus. • Higher/lower volumetric strains in soil with high/low Poisson's ratio. • Lower/higher effect on deformation for high/low shear strength parameters. • Higher drought intensity can induce negative volumetric strains in soil (contraction). • Higher/lower effect on soil deformation for higher/lower mechanical load on foundation.

Figure 2.1. Conceptual model

Mehndiratta and Sawant (2019) also concluded that the soil and foundation settlement are higher when the wetting front moves down when the foundation is subjected

to a higher mechanical load. Bushra and Laith (2014) conducted an experiment on model piles in very high expansive soil subjected to wetting and drying. They observed the upward and downward movement of the piles caused by the upward and downward movement of the surrounding soil when the soil swells and shrinks due to wetting and drying. The conceptual model was the basis of understanding the results obtained from further analyses in this study.

2.4. MATERIAL PROPERTIES

This section enlists the soil properties, groundwater parameters, and drilled shaft properties used in this study.

2.4.1. Soil properties

The site-specific soil properties of the Houston silty sand (H-SM), TX (Aviles Engineering Corporation 2010) were used for numerical modeling. The Test Sand properties were obtained by conducting laboratory tests, including sieve analysis (ASTM C136-01), hydrometer analysis (ASTM D7928-17), standard proctor test (ASTM D698), direct shear test (ASTM D3080-04), and constant head permeability test (ASTM D2434), and used for numerical modeling and experimental validation. The two types of soils were selected to facilitate a comparison of the hydroclimatic effect on the behavior of the drilled shaft. The Test Sand was later used for conducting small-scale experiments, which will provide data for validation of the small-scale numerical model. Table 2.1 lists the soil properties.

The soil deformation properties change with the flow of water (degree of saturation); hence it is crucial to couple the flow with the soil deformation. The fully-coupled flow-deformation code PLAXIS 2D was used, where the deformation and flow models are developed separately and then coupled to consider the effects of pore pressures (suction) on the deformation behavior and deformation on the pore pressure development and dissipation behavior. The deformation model is derived by considering the body force, boundary traction, Bishop's effective stress equation for the unsaturated soil, and the stress-strain relationship. Bishop's effective stress equation (Bishop 1955, 1959) is given by Equation (2.1).

$$\sigma' = \sigma - u_a + \chi(u_a - u_w) \tag{2.1}$$

where σ' is the effective stress in the unsaturated soil, σ is the total stress, u_a is the pore-air pressure, and pore-water pressure, χ is a parameter related to the degree of soil saturation of the soil and an implied fraction of water mineral contact area.

The MMC constitutive model was used, which updates the yield criterion and Young's modulus with a change in matric suction and/or degree of saturation (Vickneswaran and Ravichandran 2022). For updating the MC yield criterion with suction, the change in cohesion due to matric suction was considered by keeping the friction angle constant. The relationship of modified cohesion ($c_{modified}$) and matric suction $(\psi = u_a - u_w)$ (Vickneswaran and Ravichandran 2022), as given by Equation 2.2, was incorporated in PLAXIS 2D.

$$c_{\text{modified}} = c' + g_n \left(\frac{\theta_r}{n} \right) \log \left(\frac{\psi + P_{atm}}{P_{atm}} \right) \tag{2.2}$$

where c' is the effective cohesion relative to zero suction, P_{atm} is the atmospheric pressure, n is the porosity, g_n is the van Genuchten SWCC model fitting parameter, and θ_r is the residual water content.

For updating Young's modulus with suction, the relationship between unsaturated modulus and matric suction (Oh et al. 2009) was incorporated in PLAXIS 2D as given by Equation (2.3)

$$E_{s(unsat)} = E_{s(sat)} \left[1 + \alpha_e (u_a - u_w) S^{\beta_e} \right] \tag{2.3}$$

where $E_{s(sat)}$ is the modulus of elasticity under the saturated condition at a strain level of 1%, ($u_a - u_w$) is the matric suction, α and β_e are fitting parameters, and is the degree of saturation. The recommended fitting parameter equals 1 and 2 for coarse- and fine-grained soils, respectively. Also, the fitting parameter α depending upon the plasticity index (I_P) can be computed using the following empirical equation (Equation 2.4), developed by Oh et al. (2009).

$$1/\alpha = 0.5 + 0.063(I_P) + 0.036(I_P)^2 \qquad (0 \le I_P(\%) \le 16) \tag{2.4}$$

Table 2.1. Properties of Test Sand and H-SM

General properties	**Test Sand**	**H-SM**
Specific gravity	2.68~	2.68~
Void ratio	0.88	0.48

Dry unit weight (kN/m^3)	13.95	17.75[*]
Moisture content (%)	17.67(OMC)	26.00(NMC)
Saturated unit weight (kN/m^3)	18.57	20.94
Saturated Young's modulus (MN/m2)	35.65	14.50[*$]
Poisson's ratio	0.30	0.30
Effective angle of friction (°)	39.22	35.61[*^]
Effective cohesion (kPa)	-	5.00
Plasticity index (I_P)	-	3.00
MMC model parameters		
α_e	2.00	0.987
β_e	1.00	1.00
S	25.76	37.88

[#]Budhu (2000); [~] Lee & Seed (1967); [*]Aviles Engineering Corporation (2010); [$]Kulhawy & Mayne (1990); [^]Wolff (1989); NMC: Natural Moisture Content; OMC: Optimum Moisture Content. Note - All the values were either calculated or assumed unless otherwise stated.

2.4.2. Groundwater flow parameters

To define the saturation-suction behavior of soil, there are many Soil Water Characteristic Curves (SWCCs) and corresponding relative hydraulic conductivity functions available in the literature. In this study, the Mualem-van Genuchten model (Mualem 1976; van Genuchten 1980) and the van Genuchten model (van Genuchten 1980) were used for defining the relative hydraulic conductivity functions and the SWCC, which

are available in PLAXIS 2D. The van Genuchten function relating the saturation to the matric suction is shown in Equation 2.5.

$$\frac{S(\psi)-S_{res}}{(S_{sat}-S_{res})}=\left\{1+(g_a\,|\,\psi\,|^{g_n}\right\}^{g_c} \qquad 2.5$$

where $S(\psi)$ is the degree of saturation, S_{res} is the residual degree of saturation, S_{sat} is the degree of saturation at a fully saturated state, ψ is the matric suction, g_a is a fitting parameter related to the air entry value of the soil, g_n is a fitting parameter related to the rate of water extraction from the soil once air entry value has been exceeded, and g_c is another fitting parameter related to g_n as, $g_c=(1-g_n)/g_n$.

The unsaturated hydraulic conductivity (k_{unsat}) is calculated as a product of saturated hydraulic conductivity (k_{sat}) and relative hydraulic conductivity (k_r), as shown in Equation 2.6. Mualem-van Genuchten (Mualem 1976; van Genuchten 1980) proposed the model, as shown in Equation 2.7, for the relative hydraulic conductivity based on the corresponding SWCC.

$$k_{unsat}=k_r k_{sat} \qquad (2.6)$$

$$k_r(S)=(S_e)^{g_l}\left[1-\left(1-S_e^{\frac{g_n}{g_n-1}}\right)^{\frac{g_n-1}{g_n}}\right]^2 \qquad (2.7)$$

where S_e is the effective degree of saturation $\left(\text{i.e.,}\, S_e=\frac{S-S_{res}}{S_{sat}-S_{res}}\right)$

The van Genuchten groundwater flow parameters for H-SM and Test Sand were obtained from Bentley (2021) (Carsel and Parrish 1988) and enlisted in Table 2.2. The SWCCs for Test Sand and H-SM are shown in Figure 2.2. The saturated hydraulic conductivity for Test Sand was obtained from the constant head permeability laboratory test.

Table 2.2. Groundwater flow parameters for H-SM and Test sand.

Groundwater flow parameters	**Test Sand**	**H-SM**
Residual water content, (θ_r)	0.045	0.065
Saturated water content, (θ_s)	0.43	0.41
Model fitting parameter, g_a (m^{-1})	14.5	7.5
Model fitting parameter, g_n	2.68	1.89
Saturated hydraulic conductivity, k_{sat} (m/day)	21.78	1.06

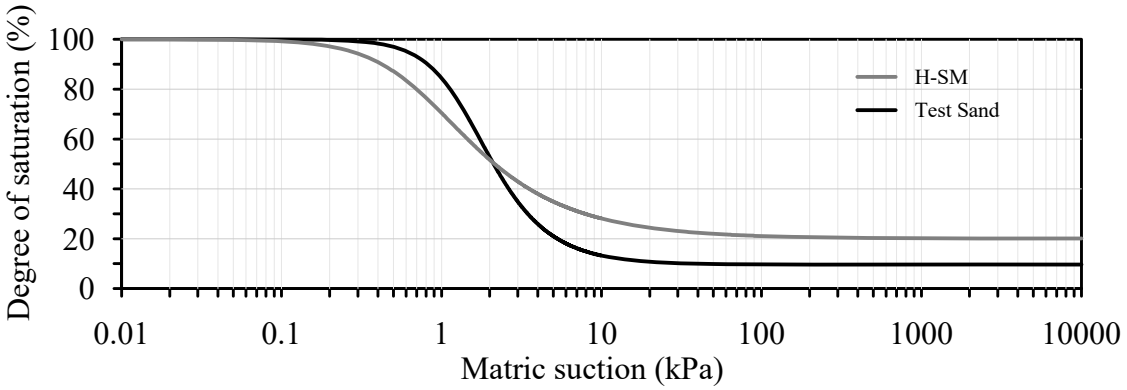

Figure 2.2. SWCC for Test Sand and H-SM

2.4.3. Drilled shaft properties

A full-scale drilled shaft (0.6 m diameter, 12 m long) and a small-scale drilled shaft (76.2 mm diameter, 1.52 m long) were used. A concrete mix design of 1:2:2.5 was used (ACI 543R 2012) to obtain the 28-day compressive strength of 35 MPa, Young's modulus of 27.80 GPa, and Poisson's ratio of 0.15.

2.5. ANALYTICAL DESIGN

Initially, the total ultimate bearing capacities of full-scale and small-scale drilled shafts were calculated as a sum of total skin resistance using the Beta method (Kulhawy et al. 1983; Kulhawy 1991) and end bearing resistance (Coyle and Castello 1981). The settlement corresponding to the total ultimate load was calculated using the Fellenius (1999) method. Then, axially loaded pile analysis was conducted in RSPILE software (O'Neill and Reese 1988), where the previously calculated total ultimate load was applied as the axial load, and the corresponding settlement was obtained. It was observed that the settlement of the drilled shaft obtained from axially loaded pile analysis using RSPILE software (O'Neill and Reese 1988) was lower compared to the settlement obtained from Fellenius (1999) method. Hence, for a conservative approach, the Beta method, Coyle and Castello's (1981) method, and Fellenius (1999) method were selected for the analytical design.

The total ultimate capacities of the full-scale drilled shaft in the sand and silty sand were calculated as 1784 kN and 2117 kN, respectively (Kulhawy et al. 1983; Kulhawy 1991; Coyle and Castello 1981). The total settlements of full-scale drilled shafts in sand

and silty sand were calculated as 60.20 and 60.90 mm, respectively (Fellenius 1999). The total ultimate capacities of the small-scale drilled shaft in sand and silty sand were calculated as 3.65 kN and 4.96 kN, respectively (Kulhawy et al. 1983; Kulhawy 1991; Coyle and Castello 1981; Fellenius 1999). The total settlement small-scale drilled shaft in sand and silty sand were calculated as 7.62 mm and 7.70 mm (Fellenius 1999). The end bearing resistance and total skin resistance for the full-scale and small-scale drilled shafts in the sand were 87.4% and 12.6%, respectively, of the total ultimate capacity. The end bearing resistance and total skin resistance for the full-scale and small-scale drilled shafts in silty sand were 88.34% and 11.65%, respectively, of the total ultimate capacity.

2.6. DETERMINATION OF MECHANICAL AND HYDROLOGICAL LOADS

Constant mechanical loads equal to the total ultimate capacities of the full-scale and small-scale drilled shafts were used for the numerical analysis. Figure 2.3 depicts the hydrological load-time histories used for the full-scale and small-scale numerical models. First, the rainfall intensities resulting from the heavy rainfall events, which occurred from 26th August 2017 to 29th August 2017 in Houston, TX, were obtained (NCDC). The maximum heavy rainfall intensity of 306 mm/day, which was recorded on 26th August 2017, was selected. Then, the rate of potential evapotranspiration (PET) was calculated (Hamon 1963) based on the mean temperature of 81°F which was recorded on 26th August 2017 (NCDC), and subtracted from the selected heavy rainfall intensity, which resulted in heavy rainfall intensity of 265 mm/day which was used as the infiltration rate in finite element modeling. The drought intensity of 99 mm/day was calculated (Hamon 1963) based on the maximum temperature of 106°F, which was recorded on 27th August 2011 in

Houston, TX (NCDC). For the numerical analyses, a hydrological load comprising 12.5 days and 10.5 days of 265 mm/day intensity heavy rainfall was applied to ensure the wetting front reaches the bottom of the full-scale and small-scale drilled shafts, respectively, followed by the application of prolonged drought of 99 mm/day intensity for a total duration of 5 years.

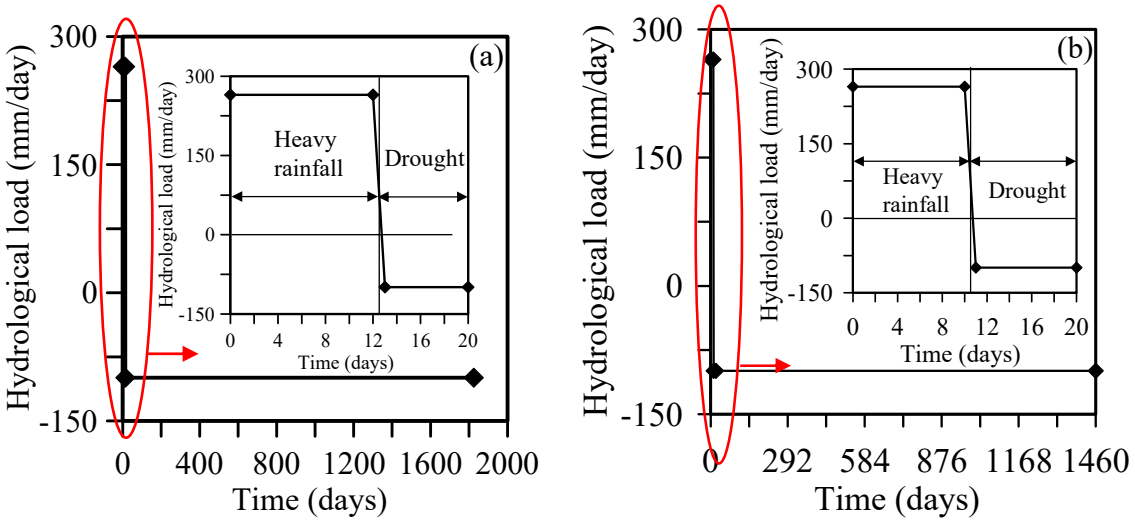

Figure 2.3. Hydrological load-time history for (a) full-scale and (b) small-scale drilled shafts

2.7. NUMERICAL MODELING

Finite element analyses were carried out in PLAXIS 2D using the 2D axisymmetric formulation for modeling the full-scale and small-scale drilled shaft in the Test Sand and H-SM. A new modified Mohr-Coulomb model capable of updating the yield criterion and modulus with changes in matric suction and/or degree of saturation (Vickneswaran and Ravichandran 2022) was used to model the soil. Figure 2.4 shows the simulation domain

for the small-scale drilled shaft in silty sand. For the full-scale drilled shaft, the domain size was 20 m in length and 30 m in height.

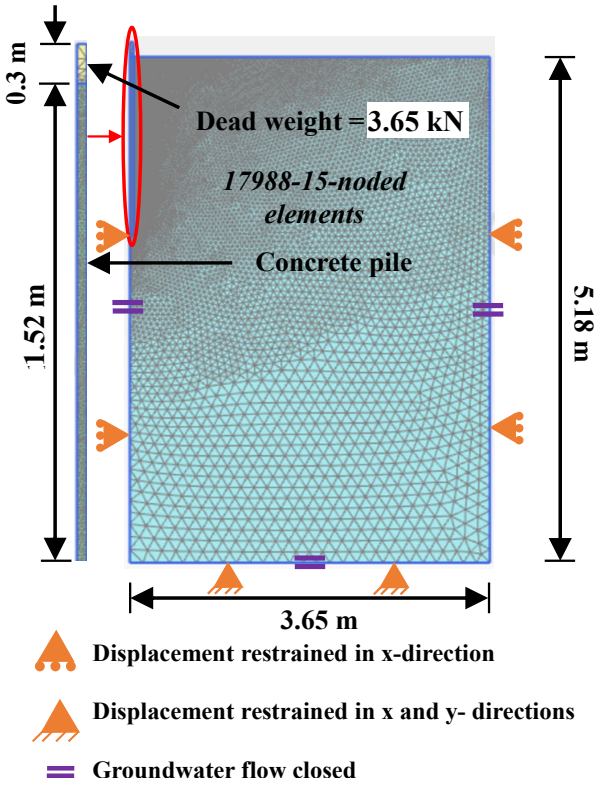

Figure 2.4. Simulation domain for the 2D axisymmetric model for the small-scale model

The drilled shaft and the deadweight equal to the total ultimate capacity of the drilled shaft representing the mechanical load were modeled using a non-porous linear elastic material. The hydrological load-time histories were applied for full-scale and small-scale models separately. The 265 mm/day was applied as an inflow boundary condition for simulating heavy rainfall, and 99 mm/day was applied as an outflow boundary condition to simulate drought at the top boundary of the simulation domain. The finite element mesh was refined around the drilled shaft and ground surface to capture the stress and

deformation variation accurately. A size and mesh sensitivity study was performed to select the size and mesh of the simulation domain, which does not affect the computed results. For the vertical boundaries of the domain, the displacement was restrained in the x-direction, and for the bottom horizontal boundary of the domain, displacement was restrained in both x and y- directions. The groundwater flow was closed for both the vertical boundaries and the bottom horizontal boundaries of the domain. A baseline study was analyzed for the full-scale model where the effect of the hydrological load on the poroelastic deformation of the Test Sand and H-SM were separately evaluated, followed by an analysis of the full-scale soil-foundation system where modification of the poroelastic deformation by the drilled shaft was evaluated. Finally, the small-scale soil-foundation system was evaluated in H-SM to compare with the full-scale model.

2.8. RESULTS AND DISCUSSION

The following section shows the analysis results for the baseline study and the soil-foundation study when subjected to constant mechanical and varying hydrological loads.

2.8.1 Baseline study

A baseline study was conducted to evaluate the effects of hydrological load on the poroelastic deformation of Test Sand and H-SM at different depths and middle of the simulation domain. The full-scale domain size was used with the hydrological load-time history shown in Figure 2.3 (a). The effect of the degree of saturation and porewater pressure on the vertical displacements of the partially saturated soils was evaluated. Figures 2.5 and 2.6 show the vertical displacement of the Test Sand and H-SM, respectively, and

the corresponding degree of saturation (DOS) and porewater pressure (PWP) at different depths. The porewater pressure in PLAXIS 2D considers unsaturated soil conditions and is calculated as given by Equation (2.8) obtained from Bentley (2021).

$$PWP = S_e(P_{steady} + P_{excess}) \tag{2.8}$$

where P_{steady} is the steady state porewater pressure and P_{excess} is the excess porewater pressure.

A negative value of PWP signifies suction, whereas a positive value of PWP signifies pressure. Also, at 100% degree of saturation, the PWP was zero. Overall, it was observed that vertical settlement of the soil was caused by a decrease in the PWP, and upward vertical soil displacement was caused by an increase in the PWP. In the case of Test Sand, at all depths, settlement occurs during rainfall caused by a decrease in PWP and upward displacement during drought caused by an increase in PWP. In the case of H-SM, upward displacement up to a depth of 10 m occurs during rainfall caused by an increase in PWP, and settlement occurs during drought caused by a decrease in PWP. Below 10 m depth, the deformation behavior is similar to the Test Sand. Bushra and Laith (2014) conducted an experiment on model piles in very high expansive soil subjected to wetting and drying. They observed the upward and downward movement of the piles caused by the upward and downward movement of the surrounding soil when the soil swells and shrinks due to wetting and drying.

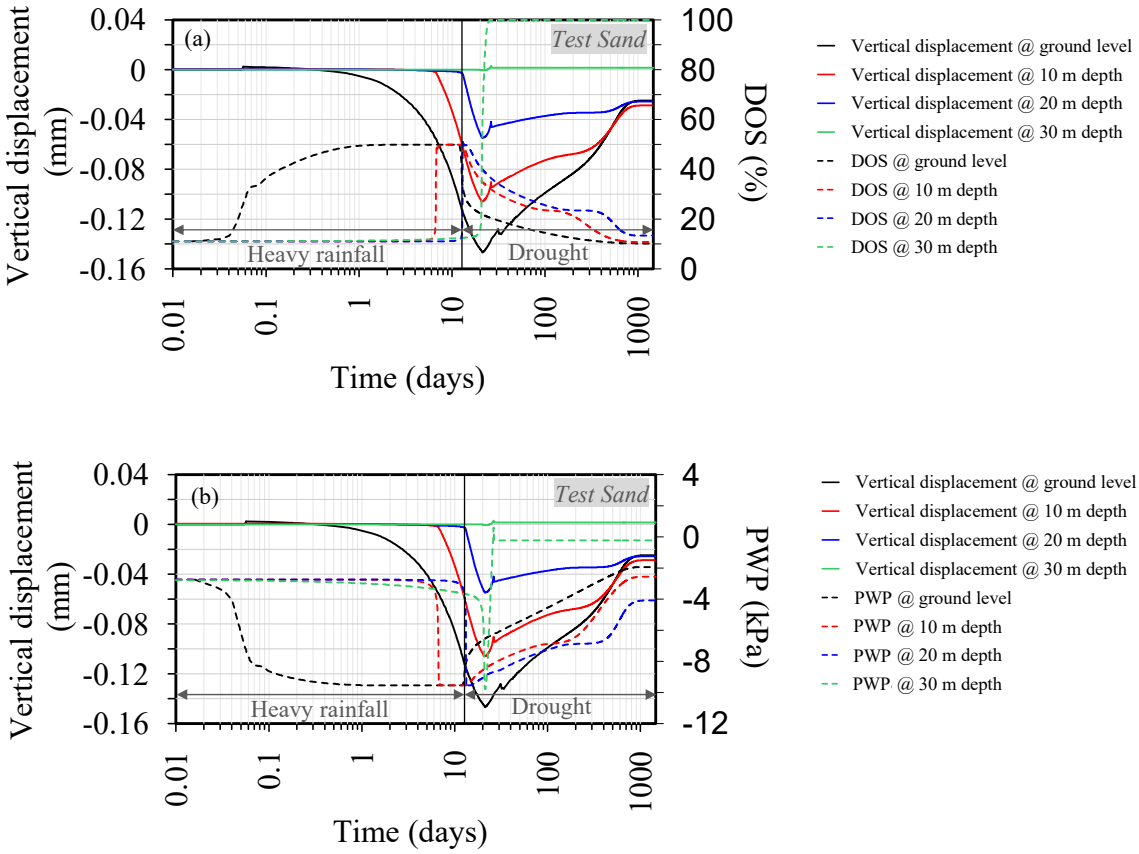

Figure 2.5. Temporal variation of (a) vertical displacement and DOS, and (b) vertical displacement and PWP in Test Sand at different depths

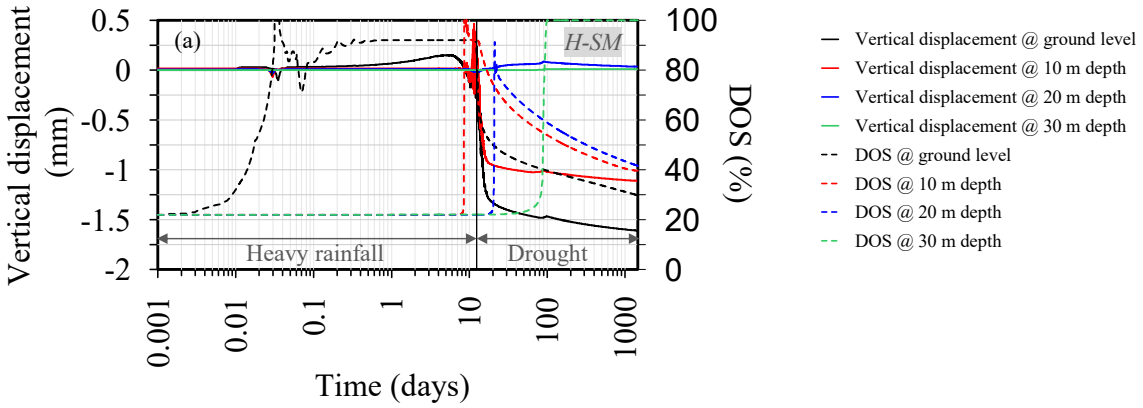

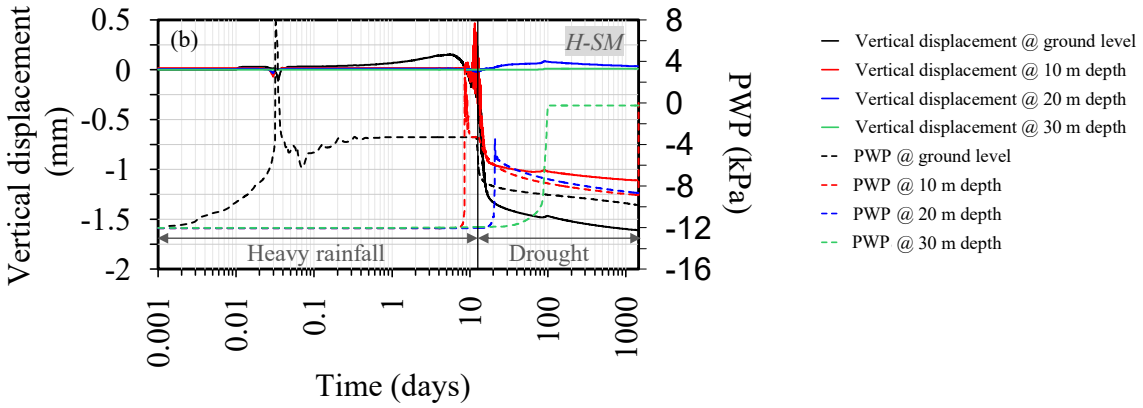

Figure 2.6. Temporal variation of (a) vertical displacement and DOS and (b) vertical displacement and PWP in H-SM at different depths

2.8.2. Full-scale drilled shaft subjected to constant mechanical load and varying hydrological load

Two simulation domains with full-scale drilled shafts in Test Sand and H-SM were developed and subjected to the mechanical load calculated from the analytical design and the hydrological load from Figure 2.3 (a). Figure 2.7 shows the degree of saturation contours at various time intervals of the hydrological load for the full-scale model in H-SM. The wetting front reached halfway of the drilled shaft length in 10.5 days and below the shaft bottom in 20 days of rainfall with a maximum DOS of 82%. After one year of drought, the DOS dropped to about 35% and further decreased to about 20% DOS after four years. The DOS within the wetting front for the Test Sand was 56.3% as compared to H-SM with 82%.

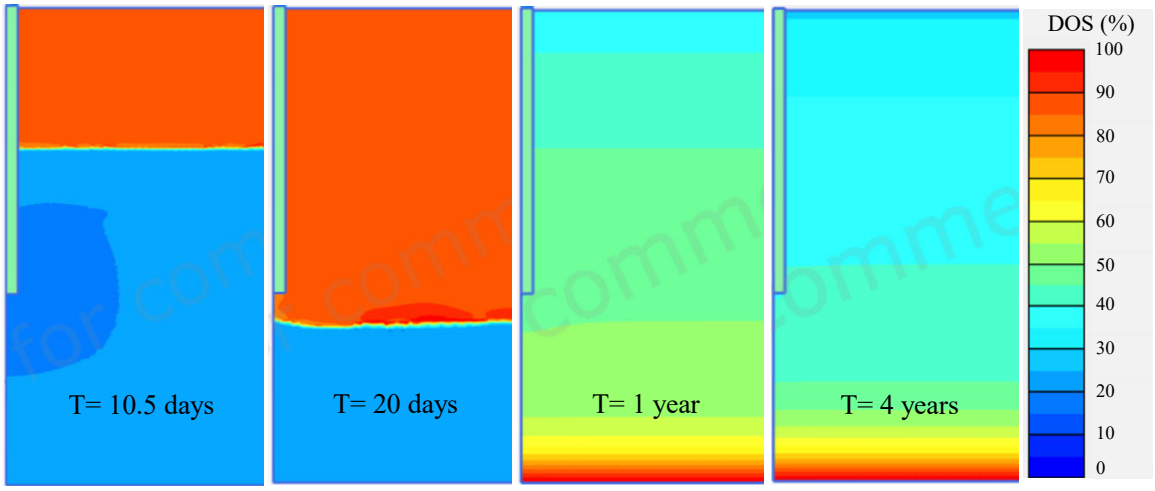

Figure 2.7. Degree of saturation contours at various time intervals for the full-scale drilled shaft in silty sand subjected to hydrological loads

The following figures show the results for the full-scale drilled shaft in the Test Sand and H-SM subjected to constant mechanical load and varying hydrological load, including heavy rainfall having an inflow intensity of 265 mm/day followed by prolonged drought having an outflow intensity of 99 mm/day. In the Test Sand (Figure 2.8), vertical settlement of the soil and drilled shaft with a negligible value of around 0.1 mm was observed during heavy rainfall. This settlement was in the elastic range and negligible. The Test Sand being loose, settlement of the soil causes the drilled shaft to settle during rainfall which was attributed to the hydrodynamic load induced by the heavy rainfall on the ground and the decrease in PWP as seen in Figure 2.5 (b). Upward vertical displacement of soil and drilled shaft during drought was observed, which may be attributed to the rebound of elastic settlement as the DOS decreases and hydrodynamic loading on the ground is reduced and also due to an increase in PWP as seen in Figure 2.5 (b).

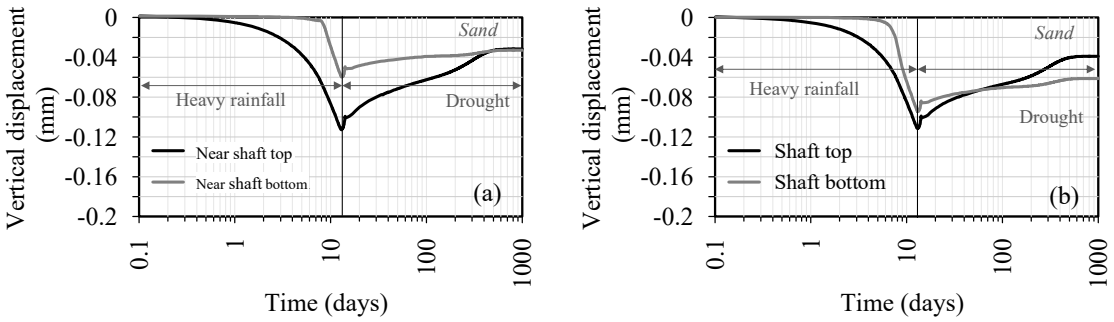

Figure 2.8. Temporal variation of vertical displacement of (a) soil 1 m away from the full-scale drilled shaft, and (b) full-scale drilled shaft in Test Sand

In the H-SM (Figure 2.9), the soil displaces vertically upward until the end of rainfall and then settles until the end of drought. The maximum upward vertical displacement of 1.9 mm was observed at ground level at the end of rainfall. The soil causes the drilled shaft to displace vertically upward at the end of rainfall. The drilled shaft displaces vertically upward slightly at the start of rainfall, settles slightly by 0.02 mm during heavy rainfall, and displaces vertically upward significantly by 0.42 mm at the end of rainfall, followed by a high settlement of 1.4 mm by the end of the drought. The H-SM being relatively dense compared to Test Sand, the upward vertical displacement of soil and drilled shaft due to rainfall was attributed to an increase in the soil volume as DOS increases to 82% as rainwater enters the soil matrix and also increase in PWP as seen in Figure 2.6 (b). Then during drought, settlement of the drilled shaft was attributed to a decrease in soil volume as the DOS dropped to a residual value from 82% and also a decrease in PWP, as seen in Figure 2.6 (b).

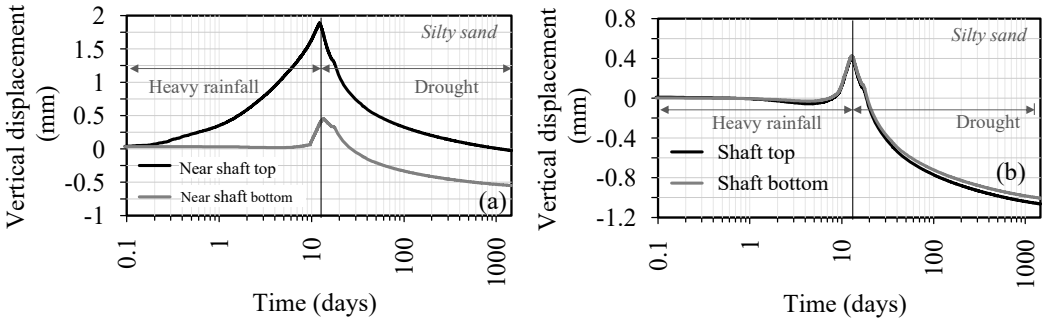

Figure 2.9. Temporal variation of vertical displacement of (a) soil 1 m away from the full-scale drilled shaft and (b) full-scale drilled shaft in H-SM

Figure 2.10 shows the temporal variation of the skin friction and end bearing resistance of a full-scale drilled shaft in the sand and silty sand. In the case of foundation in sandy soil, the contribution of skin resistance and end bearing to the total bearing capacity was 83.34% and 16.65%, respectively. The skin resistance decreased by 32.55 kN up to the end of rainfall and then increased by 12 kN up to the end of the drought. Similarly, the end-bearing resistance increased up to the end of rainfall and then decreased up to the end of drought by the same magnitude as skin resistance. The DOS reached a maximum value of 56.3% at 12.95 days when the wetting front reached the shaft bottom. Hence, the skin resistance decreases when the drilled shaft settles due to rainfall, and the load is transferred to the bottom of the shaft. After the end of rainfall during drought, the load was transferred back to the skin of the drilled shaft as the shaft displaced vertically upwards. The total percentage change in the total ultimate bearing capacity was 1.76% in the sand.

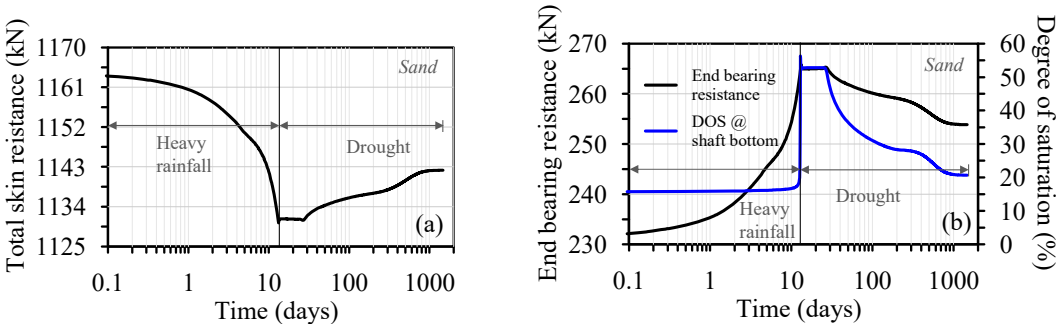

Figure 2.10. Temporal variation of (a) total skin resistance and (b) end bearing resistance in Test Sand for full-scale drilled shaft

Figure 2.11 shows the temporal variation in the case of silty sand, where the contribution of skin resistance and end bearing to the total bearing capacity was 75.28% and 24.71%, respectively. The skin resistance increased by 20.68 kN up to the end of rainfall and then decreased by 12.74 kN up to the end of the drought. The DOS reached a maximum value of 81.95% at 19 days when the wetting front reached the shaft bottom. Similarly, the end-bearing resistance decreased up to the end of rainfall and then increased up to the end of drought by the same magnitude as skin resistance.

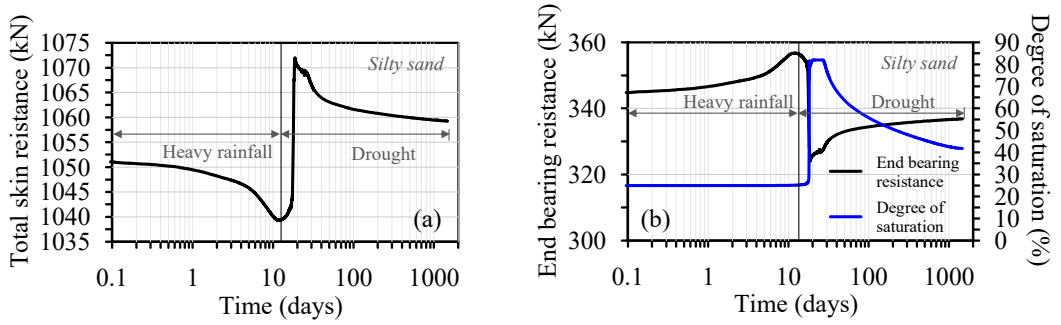

Figure 2.11. Temporal variation of (a) total skin resistance and (b) end bearing resistance in H-SM for full-scale drilled shaft

Hence, the end bearing resistance decreased when the drilled shaft was displaced upward due to rainfall, and the load was transferred to the skin of the shaft. After the end

of rainfall, the load was transferred back to the bottom of the drilled shaft as the shaft settled vertically during the drought phase. The total percentage change in the total ultimate bearing capacity was 0.75% in silty sand.

2.8.3. Small-scale drilled shaft subjected to constant mechanical load and varying hydrological load

The following figures show the results for the small-scale drilled shaft in the Test H-SM subjected to constant mechanical load and varying hydrological load, including heavy rainfall having an inflow intensity of 265 mm/day followed by prolonged drought having an outflow intensity of 99 mm/day. Figure 2.12 shows the temporal variation of the vertical displacement of small-scale drilled shafts in silty sand due to constant mechanical and varying hydrological loads. It can be seen that all the values were negligible. Vertical settlement of the shaft was observed until the 6th day of rainfall, where the end bearing resistance increased by 0.11 kN, and the maximum settlement was 0.02 mm at the shaft top. Then, upward shaft displacement was observed until the end of rainfall. The DOS reached a maximum value of 74% at 9.9 days when the wetting front reached the shaft bottom. The shaft bottom was displaced upward by 0.006 mm with a decrease in end bearing resistance by 0.04 kN at the end of rainfall. The shaft displaced upwards until 337 days when the maximum settlement at the shaft bottom was 0.03 mm, after which the shaft settled by 0.03 mm at the end of the drought.

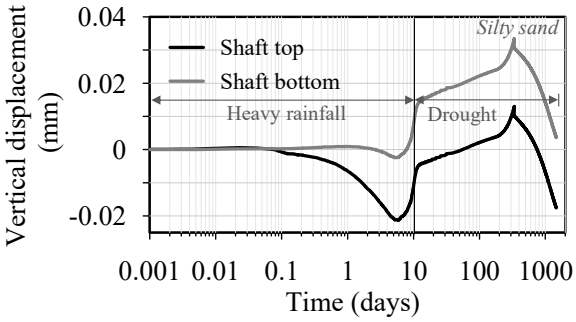

Figure 2.12. Temporal variation of vertical displacement in H-SM for small-scale drilled shaft

It can be seen from Figure 2.13 that the contribution of skin resistance and end bearing to the total bearing capacity was 95.33% and 4.67%, respectively. Unlike the full-scale drilled shaft in silty sand, the end bearing resistance increased up to the end of rainfall and then further increased up to the end of the drought with a total increase of 0.12 kN for the small-scale drilled shaft in silty sand. The total percentage change in the total ultimate bearing capacity for the small-scale drilled shaft was 55.29% in silty sand.

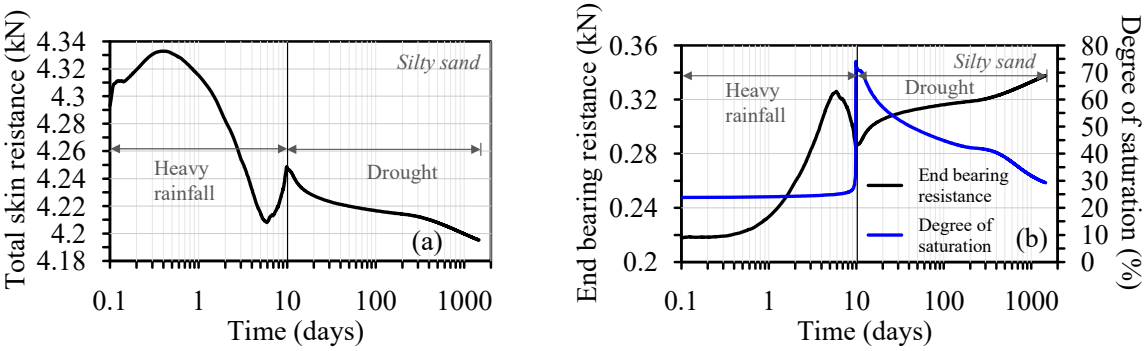

Figure 2.13. Temporal variation of (a) total skin resistance and (b) end bearing resistance in H-SM for small-scale drilled shaft

Hence, the total percentage change in the total ultimate bearing capacity of the small-scale drilled shaft (55.29%) was significantly high as compared to the full-scale

drilled shaft in silty sand (0.75%). This shows that the total ultimate bearing capacity of the small-scale drilled shaft was more influenced by the varying hydrological load as compared to the full-scale drilled shaft.

2.9. DETERMINATION OF SOIL-PILE INTERFACE PROPERTIES

A soil-pile interface element can be modeled in PLAXIS 2D. The interface properties were determined for use in subsequent studies. The interface properties comprise stiffness properties, including elastic normal stiffness (K_N) and elastic shear stiffness (K_S), and strength properties, including interface cohesion (C_{int}) and interface friction angle (ϕ_{int}). The interface stiffness properties were calculated using Equations (2.8) and (2.9) (Rocscience, 2022).

$$K_S = C_i E_{soil} \tag{2.8}$$

where C_i is the interface stiffness reduction factor, and E_{soil} is the saturated Young's modulus of soil.

$$K_N = 10 K_S \tag{2.9}$$

The interface strength properties were calculated using Equations (2.10) and (2.11) (Bentley, 2021; Rocscience, 2021).

$$C_{int} = R_{int} C_{soil} \tag{2.10}$$

where C_{int} is the interface cohesion, R_{int} = 2/3 is the interface strength reduction factor (smooth soil to concrete surface contact assumed), and C_{soil} is the effective cohesion of soil.

$$\phi_{int} = \tan^{-1}(\tan(\phi_{soil})R_{int}) \quad (2.11)$$

where ϕ_{int} is the interface friction angle, ϕ_{soil} is the effective friction angle of soil.

A calibration study was conducted for the determination of interface stiffness reduction factor (C_i) in PLAXIS 2D. The numerical modeling procedure, as described in Section 2.6, was adopted for this study. The groundwater conditions were set to global conditions, and the groundwater level was defined at the ground level. The interface elements were added along the length and the bottom of the drilled shaft, and the interface properties were assigned where the C_i was varied as 0.67, 0.75, and 0.95 to match the end bearing and skin resistance values obtained from the simulations with the values obtained from analytical methods. The axial force variation was obtained from the output using the "Structural forces" in the "volumes" tool option in the output window and multiplied by 2 to calculate the axial forces from which the end bearing capacity and total skin resistance values were calculated. The analysis was repeated for drilled shaft for silty sand. Tables 2.3 and 2.4 enlist the end bearing capacity, skin resistance, and vertical displacement values for different values of C_i for the full-scale drilled shaft in Test Sand and H-SM, respectively.

Table 2.3. Estimation of C_i for the full-scale drilled shaft in Test Sand

Parameter	Analytical	PLAXIS 2D				
C_i	-	0.67	0.75	0.85	0.95	NI[#]
Ultimate bearing capacity (kN)	1784	1784	1784	1784	1784	1784
End bearing resistance (%)	87.50	85.11	85.00	85.15	85.29	22.79

Total skin resistance (%)	12.50	14.88	15.00	14.85	14.70	77.20
Vertical shaft settlement (mm)	60.20	406.40	410.00	404.00	399.2	33.72

Note: #No interface element was used.

Table 2.4. Estimation of Ci for the full-scale drilled shaft in H-SM

Parameter	Analytical	PLAXIS 2D				
C_i	-	0.67	0.75	0.85	0.95	NI#
Ultimate bearing capacity (kN)	2117	2117	2117	2117	2117	2117
End bearing resistance (%)	88.35	44.77	83.72	83.68	83.56	21.44
Total skin resistance (%)	11.65	55.23	16.28	16.31	16.43	78.56
Vertical shaft settlement (mm)	60.90	851.30	850.60	843.9	840	68.88

Note: #No interface element was used.

It was observed that varying the interface stiffness reduction factor had a slight effect on the end bearing capacity, total skin resistance, and settlement values for the Test Sand. When the interface element was used for Test Sand, the difference in the end bearing capacity/total skin resistance values between the analytical method and PLAXIS 2D was approximately 2%. For H-SM, the difference in the end bearing capacity/total skin resistance values was approximately 4.5% for all Ci values except for 0.67, which had a difference of 43.58%. This shows that the stiffness of the interface for the full-scale drilled shaft in H-SM was greatly reduced for C_i of 0.67, which corresponds to the elastic shear modulus of 9715 kPa and as compared to the elastic modulus of H-SM is 14500 kPa.

Hence, the C_i value of 0.95 was selected to be most appropriate and was used for the finite element analysis in Chapter 4.

2.10. CONCLUSION

The effect of extreme hydroclimatic events on the behavior of drilled shafts in unsaturated soils was predicted using the fully-coupled Geotechnical-Hydrological finite element code, PLAXIS 2D. Following were the key observations.

1. Overall, the effects on the deformation and bearing capacity were very small. The Test Sand being loose, settlement of the soil caused the full-scale drilled shaft to settle during rainfall was attributed to the hydrodynamic load induced by the heavy rainfall on the ground and decrease in PWP. Upward vertical displacement of the soil and full-scale drilled shaft during drought in the Test Sand was observed, which was attributed to the rebound of elastic settlement as the DOS decreased and hydrodynamic loading on the ground was reduced, and also PWP increases.
2. The H-SM being relatively dense compared to Test Sand, upward vertical displacement of soil and drilled shaft occurred due to rainfall which was attributed to an increase in the soil volume as DOS increases to 82% as rainwater enters the soil matrix and PWP increases. Then during drought, settlement of the drilled shaft was attributed to a decrease in soil volume as the DOS dropped to a residual value from 82% and a decrease in PWP.

3. For the full-scale drilled shaft in the Test Sand, settlement of drilled shaft was observed during rainfall, which caused a decrease in skin resistance/increase in end bearing resistance. During drought, upward vertical displacement of the drilled shaft was observed, which caused an increase in skin resistance/decrease in end-bearing resistance.
4. For the full-scale drilled shaft in H-SM, upward vertical displacement of the drilled shaft was observed during rainfall, which caused an increase in skin resistance/decrease in end-bearing resistance. During drought, settlement of drilled shaft was observed, which caused a decrease in skin resistance/increase in end bearing resistance.
5. The total percentage change in the total ultimate bearing capacity for the full-scale drilled shaft was significantly lower (0.75%) as compared to the small-scale drilled shaft (55.29%) in silty sand.
6. It should be noted that the loss of skin resistance caused by loss of normal stress at the soil-pile interface due to shrinkage of soil during drought is not captured in numerical modeling, and hence, an experimental investigation is crucial for observing realistic behavior. Thus, the results show the importance of consideration of the change in soil characteristics due to extreme hydroclimatic events for pile design.

REFERENCES

ACI Committee 543. (2012). Design, Manufacture, and Installation of Concrete Piles.

ASTM C136-01. Standard Test Method for Sieve Analysis of Fine and Coarse Aggregates.

ASTM D7928-17. Standard Test Method for Particle-Size Distribution (Gradation) of Fine-Grained Soils Using the Sedimentation (Hydrometer) Analysis.

ASTM D698. Standard Test Methods for Laboratory Compaction Characteristics of Soil Using Standard Effort.

ASTM D3080-04. Standard Test Method for Direct Shear Test of Soils Under Consolidated Drained Conditions.

ASTM D2434-19. Standard Test Method for Permeability of Granular Soils (Constant Head)

Aviles Engineering Corporation. (2010). Geotechnical Investigation, City of Houston, Surface Water Transmission Program, Houston, Texas (p. 65). Houston, Texas: Aviles Engineering Corporation.

Bentley. (2021). PLAXIS 2D- Reference Manual.

Bishop, A.W. (1955,1959). "The Principle of Effective Stress," Lecture delivered in Oslo, Norway in 1955, printed in Teknisk Ukeblad, Vol. 106, No. 39, pp. 859- 863.

Budhu, M. (2000). Soil Mechanics and Foundations. Wiley, New York.

Bushra Suhale Al-Busoda, & Laith Kadim Al-Anbarry. (2014). Wetting-Drying Cycles Effect on Piles Embedded in a Very High Expansive Soil. International Journal of Architectural, Civil and Construction Sciences, 7.0(1). https://doi.org/10.5281/zenodo.1336512

Carsel, R.F., Parrish, R.S. (1988). Developing joint probability distributions of soil water retention characteristics. Water Resources Research, 24(5), 755–769.

Coyle, H. M. and Castello, R. R. (1981). "New Design Correlations for Piles in Sand," Journal of the Geotechnical Engineering Division, American Society of Civil Engineers, Vol. 107, No. GT7, pp. 965–986.

Fellenius B. H. (1999). Bearing capacity - A delusion? Proceedings of the Deep Foundation Institute 1999 Annual Meeting, Dearborn, Michigan, October 14 -16, 1999.

Fredlund, D.G., Morgenstern, N.R., Widger, R.A. (1978). "The shear strength of unsaturated soils." Can. Geotech. J, 15 (3), 313–321.

Fredlund, D. G., Rahardjo, H., and Fredlund, M. D. (2012). Unsaturated Soil Mechanics in Engineering Practice, Wiley, Chichester, U.K.

IPCC.(2013). Climate Change 2013: The Physical Science Basis. Cambridge University Press.

Hamon, W.R., 1963. Computation of Direct Runoff Amounts From Storm Rainfall. Int. Assoc. Sci. Hydrol. Pub. 63:52-62.

Kulhawy, F.H., and Mayne, P.W. (1990). Manual on Estimating Soil Properties for Foundation Design. Report EL-6800, Electric Power Research Institute, Palo Alta, CA.

Kulhawy, F. H., Trautmann, C.H., Beech, J.F., O'Rourke, T.D., McGuire, W., Wood, W.A. and Capano, C. (1983) Transmission Line Structure Foundations for Uplift-Compression Loading. Report No. EL-2870, Electric Power Research Institute, Palo Alto.

Kulhawy, F.H. (1991) Drilled shaft foundations. Chapter 14 in Foundation Engineering Handbook, 2nd ed., Hsai-Yang Fang, Van Nostrand Reinhold, New York.

Lee, K., & Seed, H. (1967). Drained Strength Characteristics of Sands. Journal Of The Soil Mechanics And Foundations Division, 93(6), 117-141.

Mahmoudabadi, V. and Ravichandran, N. (2021). Impact of Site-Specific Extreme Hydrological Cycle on Footing Performance. Geo-Extreme 2021.

Mehndiratta, S. and Sawant, V.A. (2019) 'Wetting-drying effect on the response of footing resting on partially saturated soils,' International Journal of Geotechnical Engineering, 16(2), pp. 187–199. doi:10.1080/19386362.2019.1656920.

Oh, W. T., Vanapalli, S. K., and Puppala, A. J. (2009). "Semi-Empirical Model for the Prediction of Modulus of Elasticity for Unsaturated Soils." Canadian Geotechnical Journal, 46(8), 903-914.

Ravichandran, N., Vickneswaran, T., Marathe, S., and Jella, V. (2021). "Numerical Analysis of Settlement Response of Shallow Footing Subjected to Heavy Rainfall and Flood Events." International Journal of Geosciences, 12(02), pp.138-158.

Ravichandran, N., Vickneswaran, T., Marathe, S. and Jella, V.S. (2021). "Numerical Analysis of Settlement Response of Shallow Footing Subjected to Heavy Rainfall and Flood Events." International Journal of Geosciences, 12, 138-158.

Reese, L.C. and O'Neill, M.W. (1988) "Drilled Shafts: Construction Procedures and Design Methods." Prepared for U.S. Department of Transportation, Federal Highway Administration, in cooperation with the Association of Foundation Drilling.

Rocscience.com. 2022. *Documentation | Define Joint Properties*. [online] Available at: <https://www.rocscience.com/help/rs2/documentation/rs2-model/joints/define-joint-properties> [Accessed 18 July 2022].

Siemens, G. (2018). Thirty-Ninth Canadian Geotechnical Colloquium: Unsaturated soil mechanics — bridging the gap between research and practice. Canadian Geotechnical Journal, 55(7), pp.909-927.

van Genuchten, M.Th. (1980). "A closed-form equation for predicting the hydraulic conductivity of unsaturated soils," Soil Science Society of American Journal, 44(5), 892-898.

Vickneswaran, T., and Ravichandran, N. (2023). "Performance of Geotechnical Systems Under Extreme Hydroclimatic Events Using a New User-defined Soil Model in Plaxis." Journal of GeoEngineering, Vol. 18 Issue 1, p21-31. 11p

Wolff, T. F. (1989). "Pile Capacity Prediction Using Parameter Functions." Predicted and Observed Axial Behavior of Piles, Results of a Pile Prediction Symposium, sponsored by the Geotechnical Engineering Division, ASCE, Evanston, IL (June) 1989, ASCE Geotechnical Special Publication 23, 96–106.

CHAPTER 3. CONSTRUCTION AND CALIBRATION OF EXPERIMENTAL SETUP

3.1. ABSTRACT

As a realistic approach, an experimental study to investigate the effects of extreme hydroclimatic events on the deformation and bearing capacity behavior of a 76.2 mm diameter and 1.83 m long small-scale precast drilled shaft and the deformation behavior of the surrounding soil is carried out. The materials and methods adopted for the construction of the experimental setup are discussed. A 1.5 m x 1.5 m x 2.25 m wooden soil box was constructed to accommodate the small-scale soil-pile-loading system. The design and construction of the precast drilled shaft and soil box are discussed. Several types of sensors were used in this study, including moisture sensors, temperature sensors, and Fiber Bragg Grating sensors to monitor the moisture content, temperature, and strain variation in the precast drilled shaft, surrounding soil, and soil-pile interface. A mechanical loading setup was constructed for the application of mechanical load on the precast drilled shaft. A hydrological loading setup capable of simulating heavy rainfall, flooding, and drought was also constructed. The instrumentation and calibration of sensors and loading setups, consisting of the working, specifications, data acquisition, and configuration layout, are discussed in detail. A summary of the construction of the experimental setup is illustrated.

3.2. INTRODUCTION

The conventional methods for deep foundation design are based on hydrostatic soil conditions. However, there is a need to consider the effects of extreme hydroclimatic

events, as forecasts indicate that these events will become more frequent in the future (IPCC 2013). The hydrological cycle strongly depends on the temperature, and global warming has caused the atmospheric temperature to rise, which means that the atmosphere can hold larger amounts of water which can potentially lead to heavy rainfall events. Moreover, high temperatures may cause some regions to experience more frequent droughts. This causes greater evaporation which leads to less absorbent soils, which in turn means less water is absorbed by vegetation and thus leads to flooding during heavy rainfall events (NOAA 2022). Hence, increasing global temperatures can disrupt the hydrological cycle, causing extreme events like drought, flooding, and heavy rainfall, which may lead to loss of life and property damage. A disaster related to weather, climate, or water hazard occurred every day on average over the past 50 years, killing 115 people and causing US$ 202 million in losses daily (WMO 2021). Severe drought conditions continue to impact the Western and Southern Plains states. Extreme drought events are often ended by heavy rainfall events in U.S. states like California, New Mexico, Nevada, and Utah, resulting in massive flood events. Such extreme events have led to damage to house foundations, seen in the form of cracks to the foundation (Scripps media 2022). Foundations in expansive soils are prone to damage caused by the shrink-swell potential of such soils when subjected to wetting and drying. Thus, it is important to understand and quantify the effects of extreme hydroclimatic events like heavy rainfall, flooding, and prolonged drought on the behavior of deep foundations supporting large infrastructures to prevent potential damage to infrastructure. The common perception in practice is to ignore the effects of unsaturated soil to consider the worst-case scenario. However, the axial capacity of the deep foundation

is controlled by its skin and end-bearing resistances, which depend on the strength and deformation characteristics of the surrounding soil. These soil characteristics vary with changes in matric suction and/or Degree Of Saturation (DOS) of the soils.

An experimental investigation is required for a better understanding of the effects of extreme hydroclimatic events and the contribution of matric suction on the behavior of deep foundations. An experimental setup consisting of a 1.5 m x 1.5 m x 2.25 m wooden soil box was constructed to accommodate the small-scale soil-pile-loading system. The setup is currently under construction at the Rich lab, Clemson University, SC, USA, to investigate the effects of heavy rainfall, flooding, and prolonged drought on the deformation and bearing capacity behavior of the 76.2 mm diameter and 1.83 m long small-scale drilled shaft and the deformation behavior of the surrounding soil. The moisture sensors were used to monitor the moisture content variation in the soil, and the temperature sensors were used to monitor the temperature variation in the soil. The Fiber Bragg Grating (FBG) sensors were used to monitor the vertical and radial strain variation in the soil, the vertical strain variation in the precast drilled shaft, and the vertical and radial variation in the soil-pile interface. The measured vertical strain in the precast drilled shaft will be used to determine the axial force variation, which will provide insight into changes in skin resistance and end bearing resistance of the precast drilled shaft due to hydrological load. The vertical and radial strain measurements in the soil-pile interface will provide insight into changes in skin resistance and slip and gap formation at the interface due to hydrological load. A mechanical loading setup was constructed for the application of mechanical load. The hydrological loading setup capable of simulating heavy rainfall,

flooding, and drought was also constructed. The instrumentation and calibration of sensors and loading setups, consisting of the working, specifications, data acquisition, and configuration layout, are discussed in detail. A summary of the construction of the experimental setup is provided at the end. The finite element results for the small-scale model were validated in Chapter 4.

3.3. EXPERIMENTAL INVESTIGATION

An experimental setup consisting of the small-scale soil-pile-loading system is currently under construction at the Rich lab, Clemson University, SC, USA. The following sections describe the construction of the small-scale drilled shaft and soil box and the instrumentation and calibration of various sensors and loading setups used for this study.

3.3.1. Construction of small-scale precast drilled shaft

A 76.2 mm diameter and 1.83 m long precast drilled shaft having a single US#3 rebar at the center was constructed using a wooden holder frame. The following construction procedure was adopted for the small-scale precast drilled shaft: (1) A 76.2 mm (3") inner diameter and 2.0 m long PVC Schedule 40 pipe was cut longitudinally to produce two halves and was used as the mold; (2) A wooden holder frame was designed and constructed as shown in Figures 3.1 (a) and (b) to hold the mold in place during concrete pouring. A 10 mm deep cavity was drilled at the center of the base of the holder frame, and a wooden cap with a cavity, as shown in Figure 3.1 (b), was used to facilitate keeping the US#3 rebar in place during concrete pouring. Two 76.2 mm inner diameter flexible rubber couplings were fastened at the top and bottom of the mold to avoid any

water leakage when concrete is poured into the mold; (3) A concrete mix design of 1:2:2.5 was prepared (ACI 543R 2012) with a 28-day compressive strength of 35 MPa; (4) The mold and the rebar were fixed to the holder frame, and the assembly was tilted at 45 degrees with the ground level to avoid any segregation of concrete during pouring. The prepared concrete was poured in three lifts, and each lift was tamped with a steel tamping rod for the expulsion of any possible entrapped air; (5) The wooden cap was fixed at the top of the US#3 rebar, and the precast drilled shaft was allowed to harden for 24 hours, after which the drilled shaft was allowed to cure for 28 days in a curing tank. Figure 3.1 (c) shows the final precast drilled shaft after taking it out from the mold.

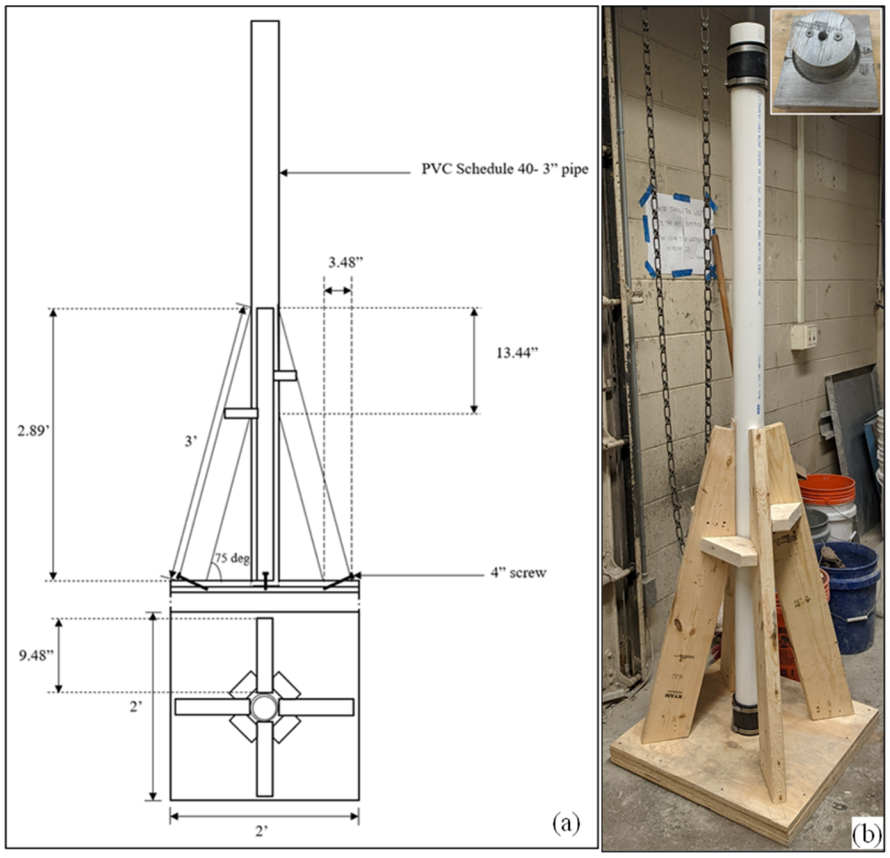

Figure 3.1. Small-scale precast drilled shaft (a) holder frame design, (b) constructed holder frame, and (c) final precast drilled shaft

3.3.2. Construction of soil box

A 1.5 m x 1.5 m x 2.25 m wooden box was constructed to accommodate the small-scale soil pile-loading system. The following construction procedure was adopted: (1) First, the bottom of the soil box was constructed, which consisted of a PVC pipe drainage system supported by two 2x4s. A 0.13 m thick layer of fine sand was filled to protect the drainage system (Figure 3.2 (a)). The drainage system consisted of four drainage holes as shown in Figure 3.2 (b); (2) The plywood sidings reinforced by 2 x 4s and 4 x 4s were used to construct the soil box; (3) A waterproof exterior stain for wood was applied on the interior of the soil box. A roofing membrane was also attached and sealed using waterproofing sealant on the inside of the soil box; (4) A 0.12 m of gravel layer using #57 aggregate and covered with a geomembrane to prevent the sand from entering the drainage system; (5) The Test Sand was filled and compacted in uniformly distributed 2-inch lifts to achieve maximum compaction. This was done by saturating the Test Sand before each lift and manually compacting it with a wooden handheld compactor (Figure 3.2 (c)); (6) The Test Sand was compacted up to 0.25 m from the top of the gravel layer to form a base layer, and the precast drilled shaft was installed and hooked at the center of the box; (7) Then, sensors were installed in the Test Sand at the designed configurations with simultaneous

compaction of Test Sand up to the top of the precast drilled shaft leaving 0.3 m between the top of the compacted Test Sand and the top edge of the soil box to allow for flooding.

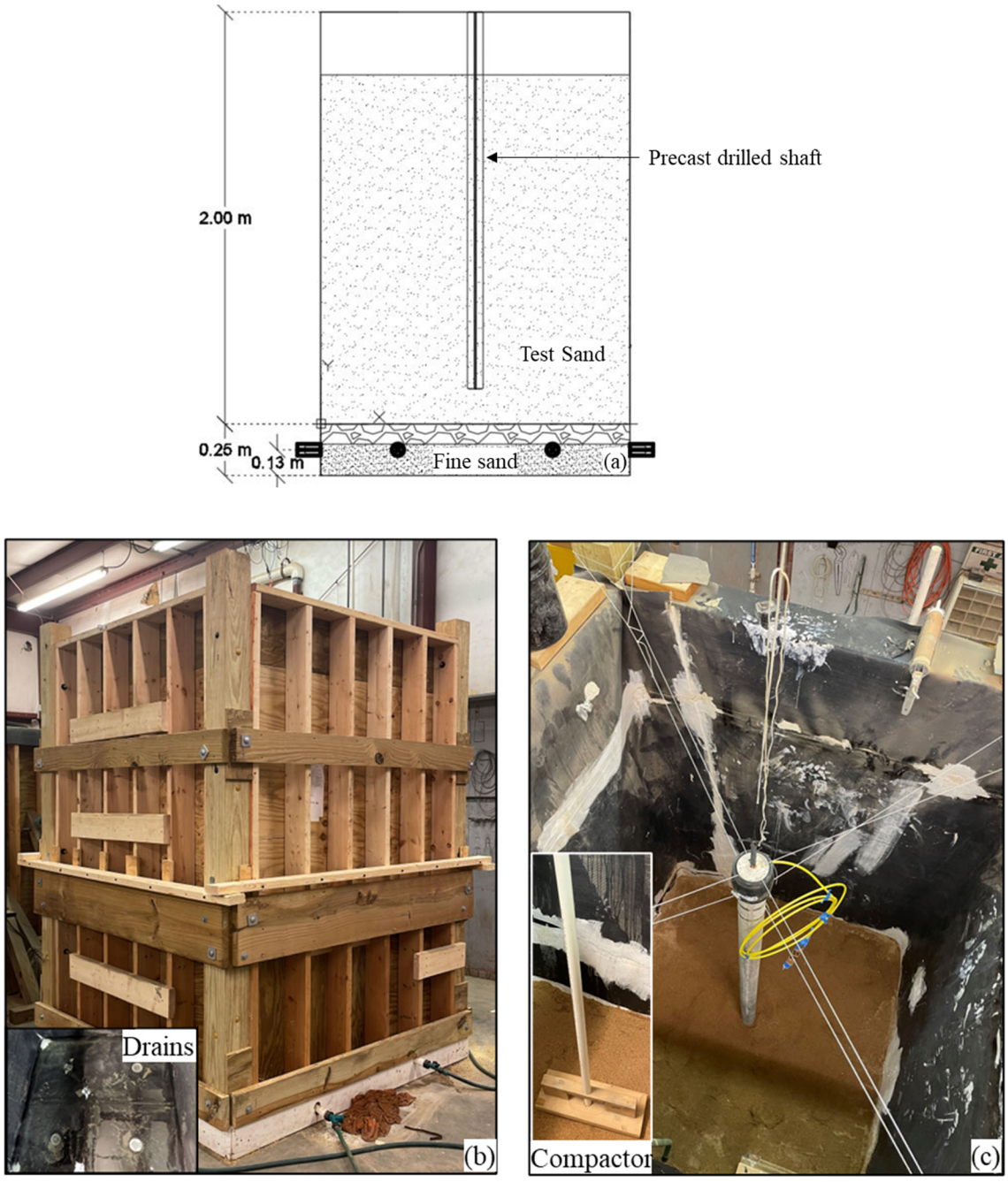

Figure 3.2. (a) Soil box drawing, (b) Constructed soil box, and (c) precast drilled shaft installed on the base layer

3.3.3. Instrumentation and calibration of sensors

Various types of sensors, including moisture sensors, temperature sensors, and Fiber Bragg Grating (FBG) sensors, were used to monitor the moisture content, temperature, and strains, respectively, in the soil and precast drilled shaft. The following sections describe the working, specifications, data acquisition, and design layout for all the sensors used in this study.

3.3.3.1. Measurement of soil moisture content by Meter Group's EC-5 sensors and Data Acquisition (DAQ) system

3.3.3.1.1. Specifications, working and data acquisition

The EC-5 moisture sensors measure the soil volumetric moisture content with a resolution of 0.0007 m^3/m^3, an accuracy of ±0.031 m^3/m^3, and a range of -0.401 to 2.574 m^3/m^3 (Decagon Devices, 2001-2010). The EC-5 moisture sensor dimensions are 8.9 cm X 1.8 cm X 0.7 cm. Figure 3.3 depicts the EC-5 sensor. The Em5b data logger with five input channels was used for the data acquisition from the EC-5 moisture sensor, as shown in Figure 3.3 (b). The ECH_20 utility software for setting up and downloading data (Decagon Devices, 2001-2010). The downloaded data is available as an excel file (.csv) which was used to perform necessary calculations.

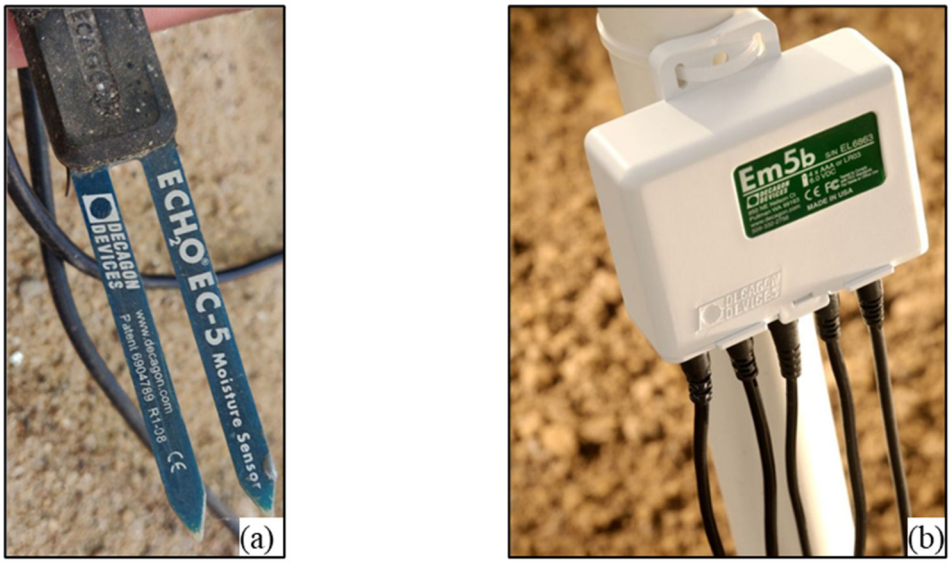

Figure 3.3 (a) EC-5 soil moisture sensor and (b) Em5b data logger

.3.3.1.2. Design of sensor configuration

The EC-5 moisture sensors were densely and equally spaced up the depth of 0.35m from the top of the Test Sand (ground level) and sparsely spaced below 0.35 m depth up to the bottom of the precast drilled shaft. Figure 3.4 shows the EC-5 moisture sensor configuration layout.

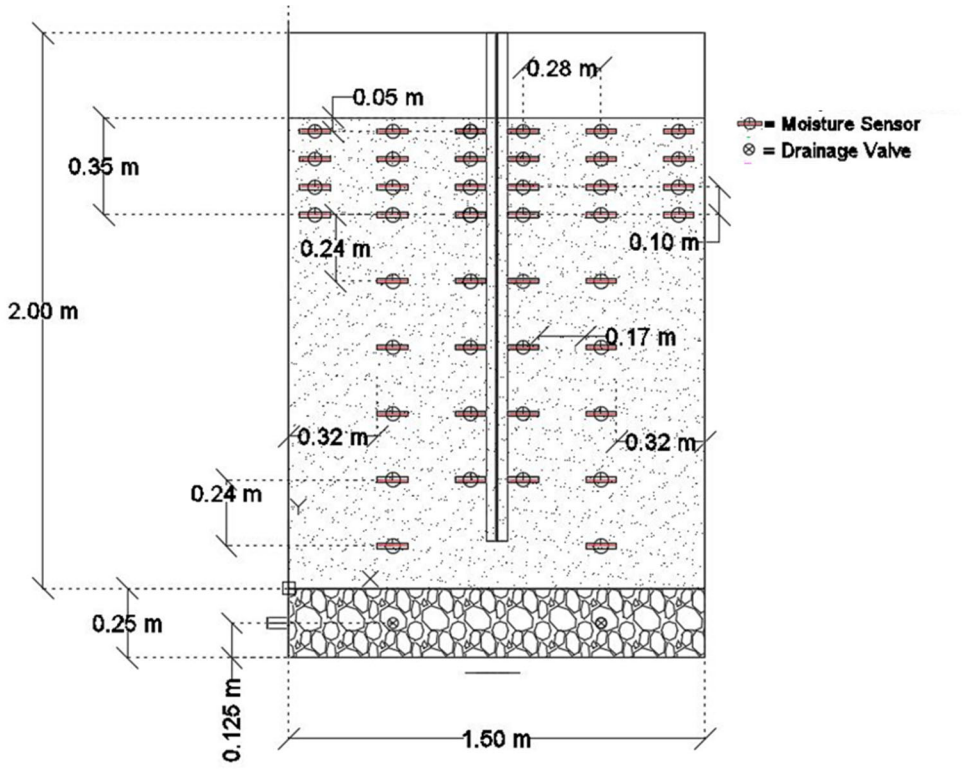

Figure 3.4 Design of EC-5 moisture sensor configuration layout

3.3.3.2. Measurement of soil temperature by Meter Group's RT-1 soil temperature sensors and Data Acquisition (DAQ) system

3.3.3.2.1. Specifications, working and data acquisition

The RT-1 temperature sensors measure the soil temperature with a resolution of 0.1°C, accuracy of ±0.5°C, and temperature range of -40 to 80°C (Meter Group 2022). The RT-1 temperature sensor dimensions are 2 cm x 0.075 cm. Figure 3.5 depicts the RT-1 temperature sensor. The Em5b data logger with five input channels was used for the data acquisition from the EC-5 moisture sensor. The ECH$_2$0 utility software for setting up and

downloading data (Decagon Devices, 2001-2010). The downloaded data is available as an excel file (.csv) which was used to perform necessary calculations.

Figure 3.5 RT-1 temperature sensor

3.3.3.2.2. Design of sensor configuration

Figure 3.6 shows the RT-1 temperature sensor configuration layout of the moisture sensors.

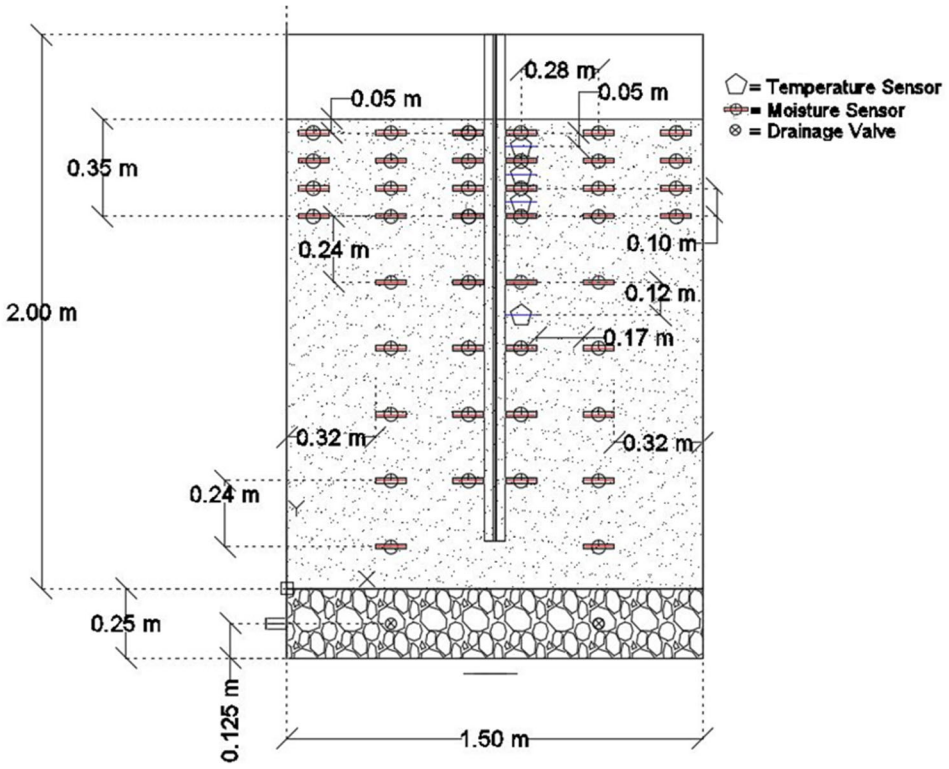

Figure 3.6 Design of RT-1 temperature sensor configuration layout

The RT-1 temperature sensors were densely and equally spaced up the depth of 0.35m from the top of the Test Sand (ground level) and sparsely spaced below 0.35 m depth up to the bottom of the precast drilled shaft.

3.3.3.3. Measurement of strain by Femto Gratings' Fiber Bragg Grating (FBG) sensor fibers

3.3.3.3.1. Specifications, working and data acquisition

Fiber Bragg Grating sensors are composed of a fiber optic strand with a Distributed Bragg Reflector (DBR), a type of multi-layer material that can reflect wavelengths of a spectrum. The placement and design of each DBR are calibrated such that they will reflect a certain wavelength back in a certain time (Fempto Fibertec 2022). The Bragg condition is given by the coupled mode theory given by Equation (3.1),

$$\lambda_B = 2\Lambda\eta_{eff} \tag{3.1}$$

where λ_B is the Bragg wavelength, Λ is the grating period that forms the distance between two adjacent grating planes, and η_{eff} is the effective core refractive index.

Figure 3.7 shows the working of an FBG. The first graph is the complete input spectrum, the second graph is the continuation of the spectrum after passing through one DBR, and the final graph is the Bragg wavelength that is reflected (Ferraro et al. 2002). The external parameters like temperature and change in physical properties of the material cause the change in the grating period and/or effective refractive index of the DBR, which

causes a shift in the wavelength of the reflected spectrum either to the left or right of the central wavelength or Bragg wavelength.

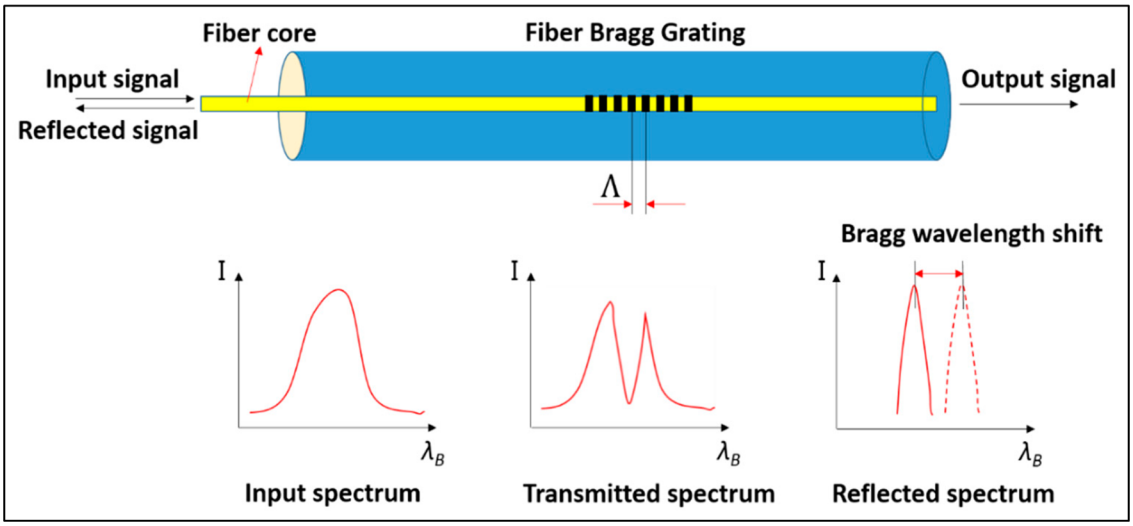

Figure 3.7 Depiction of reflected and transmitted spectrum of FBG for a broadband light source.

The shift of Bragg wavelength, $\Delta\lambda_B$ due to the applied strain and temperature can be evaluated by differentiating Equation (3.1) and simplifying in the common form given by Equation (3.2) (Campanella et al. 2018; Hill & Meltz 1997; Kreuzer 1970),

$$\frac{\Delta\lambda_B}{\lambda_0} = (1-p)*(\varepsilon_m + \alpha_{sp}*\Delta T) + \alpha_\delta * \Delta T \tag{3.2}$$

where $p = 0.22$ (Germanium doped core) is the photo-elastic coefficient (Kreuzer), $(1-p) = k$ is called the gage factor, which is defined as the relative shift of Bragg wavelength per longitudinal strain, λ_0 is the base wavelength at the start of the test, ΔT is

the temperature change in deg. K, α_{sp} is the expansion coefficient per K of the specimen (11 to 13E-6/K for steel, 22 to 23E-6/K for aluminum), α_{δ} is the change in refraction index (5 to 8E-6/K), ε_m is the mechanically caused strain, $\varepsilon_T = \alpha_{sp} * \Delta T$ is the temperature caused strain, and $\alpha_{\delta} * \Delta T$ describes the change in glass refraction index caused only by temperature.

The FBG fiber used for this study comprised a standard single mode (Germanium doped for higher refraction index) fiber with a 9-micron inner core and outer part of the pure glass (micro cladding) of 125 microns. The glass fiber is coated with a 250-micron acrylate coating. The wavelength accuracy of the sensors is 0.2 nm, and grating spacing is 6 nm at a central wavelength of 1550 nm (Fempto Fibertec 2022). The FBG fiber is wired into the SM125-500 interrogator. The SM125-500 specializes in reading wavelength data. To utilize the SM125-500 interrogator, a computer with MOE ENLIGHT, Micron Optics' data interpretation software was used. The wavelength accuracy for this interrogator is 1 pm, and the strain accuracy is one microstrain (Micronoptics 2022).

Figure 3.8 SM125-500 interrogator for FBG sensor

3.3.3.3.2. Design of sensor configuration

The FBG sensor fiber configurations were designed based on the displacement and strain variation in the small-scale drilled shaft, soil-pile interface, and surrounding soil obtained from finite element codes PLAXIS 2D and ABAQUS 3D. In PLAXIS 2D, a 2D finite element model with axisymmetric formulation using 15-noded triangular elements was created. In ABAQUS 3D, a 3D finite element model with a 2 m diameter and 3 m height using 4-noded quadrilateral elements was created. For both PLAXIS 2D and ABAQUS 3D models, the 76.2 mm diameter and 1.52 m long drilled shaft and the deadweight equal to the total ultimate capacity of the drilled shaft representing the mechanical load were modeled using a non-porous linear elastic material. The Test Sand was modeled as a linear elastic material. The finite element mesh was refined around the drilled shaft and ground surface to capture the stress and deformation variation accurately. A size and mesh sensitivity study was performed to select the size and mesh of the simulation domain, which does not affect the computed results. For the vertical boundaries of the domain, the displacement was restrained in the x-direction, and for the bottom horizontal boundary of the domain, displacement was restrained in both x- and y-directions. The groundwater flow was closed for both the vertical boundaries and the bottom horizontal boundaries of the domain. Figures 3.9 (a) and (b) show the deformed shape of the simulation domain for PLAXIS 2D and ABAQUS 3D. The sign convention for tensile strain is negative, and for compressive strain is positive.

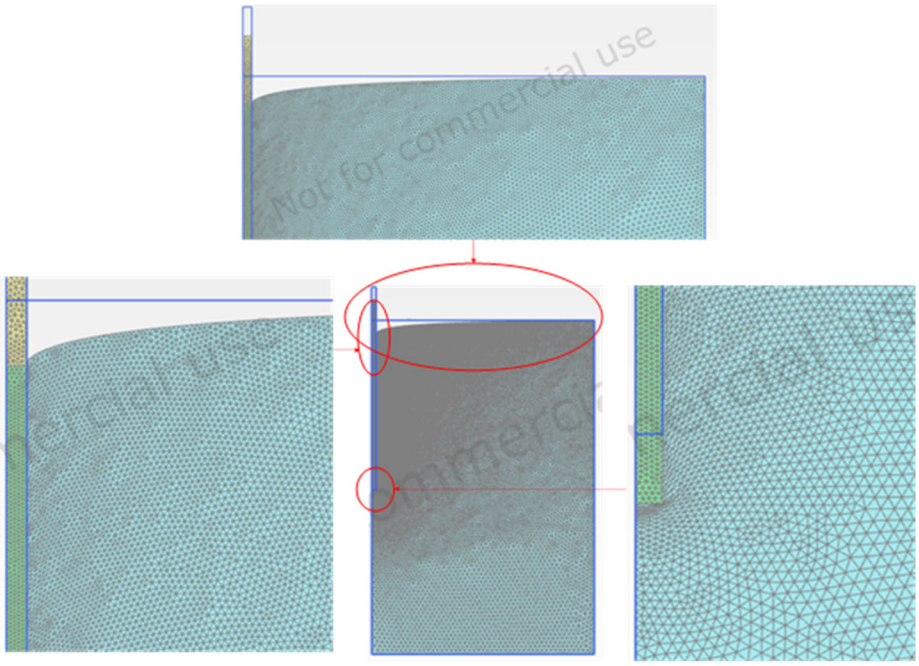

Figure 3.9 (a). Deformed shape of simulation domain (Scale- 5 times) in PLAXIS 2D

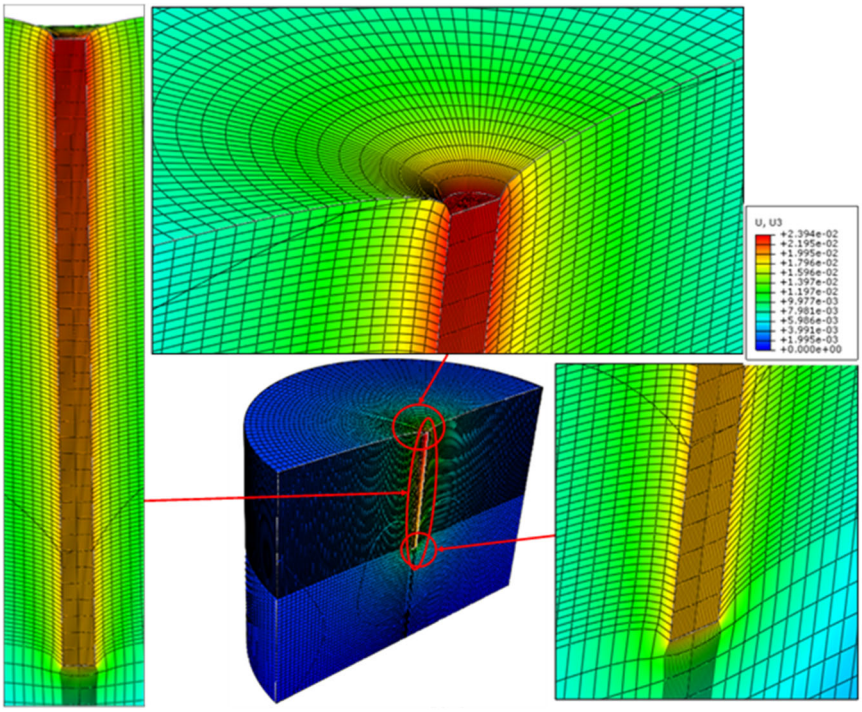

Figure 3.9 (b). Deformed shape of simulation domain with vertical displacement contours (Scale- 5 times) in ABAQUS 3D

Figures 3.10 (a) and (b) show the vertical displacement and strain profiles, respectively, at the center of the drilled shaft obtained from PLAXIS 2D and ABAQUS 3D. The vertical displacement at the top and bottom of the shaft was 24.16 mm and 19.68 mm, respectively, in PLAXIS 2D. The vertical displacement at the top and bottom of the shaft was 24 mm and 19.46 mm, respectively, in ABAQUS 3D. Compressive vertical strains were observed in the shaft. The value of vertical strain decreased from 5284 με at the top to 250.8 με at the shaft bottom in PLAXIS 2D. The value of vertical strain decreased from 4777 με at the top of the shaft to 438 με at the bottom of the shaft in ABAQUS 3D.

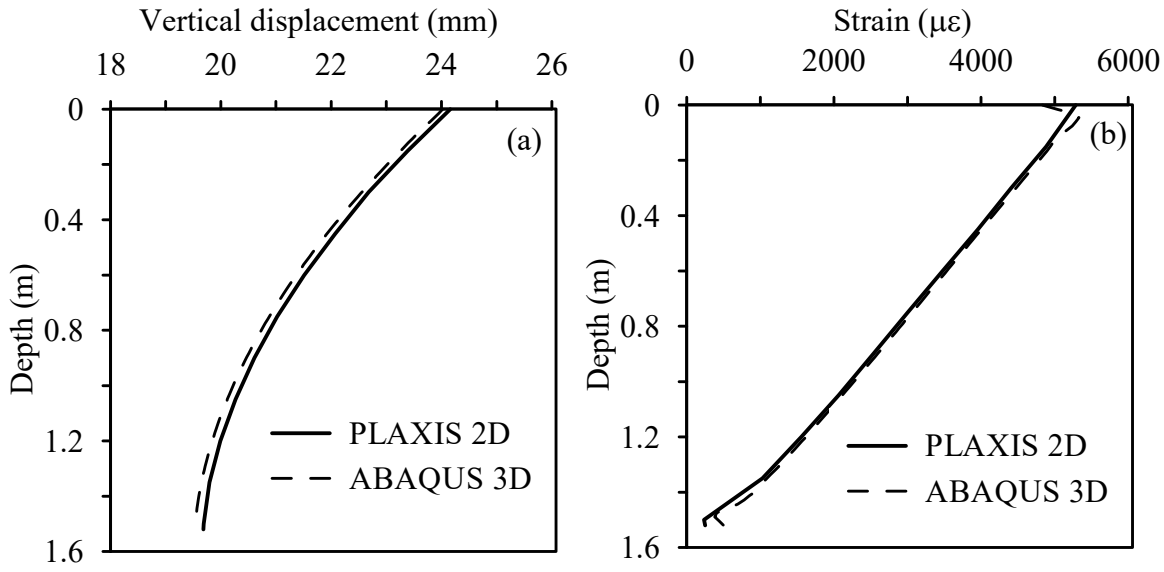

Figure 3.10. Vertical (a) displacement and (b) strain profiles at drilled shaft center

Figures 3.11 (a) and (b) show the vertical displacement and strain profiles, respectively, at the soil-pile interface obtained from PLAXIS 2D and ABAQUS 3D. The vertical displacement at the top and bottom of the shaft was 23.61 mm and 18.31 mm, respectively, in PLAXIS 2D. The vertical displacement at the top and bottom of the shaft

was 23.54 mm and 18.68 mm, respectively, in ABAQUS 3D. Compressive strains were observed at the interface. At a depth of 20 mm from ground level, 5143 με was observed in PLAXIS 2D. At 20 mm above the drilled shaft bottom, a strain equal to 1602 με was seen in PLAXIS 2D. In ABAQUS 3D, 5125 με was observed 20 mm below ground level, and 3683 με was observed at 20 mm above the bottom of the drilled shaft.

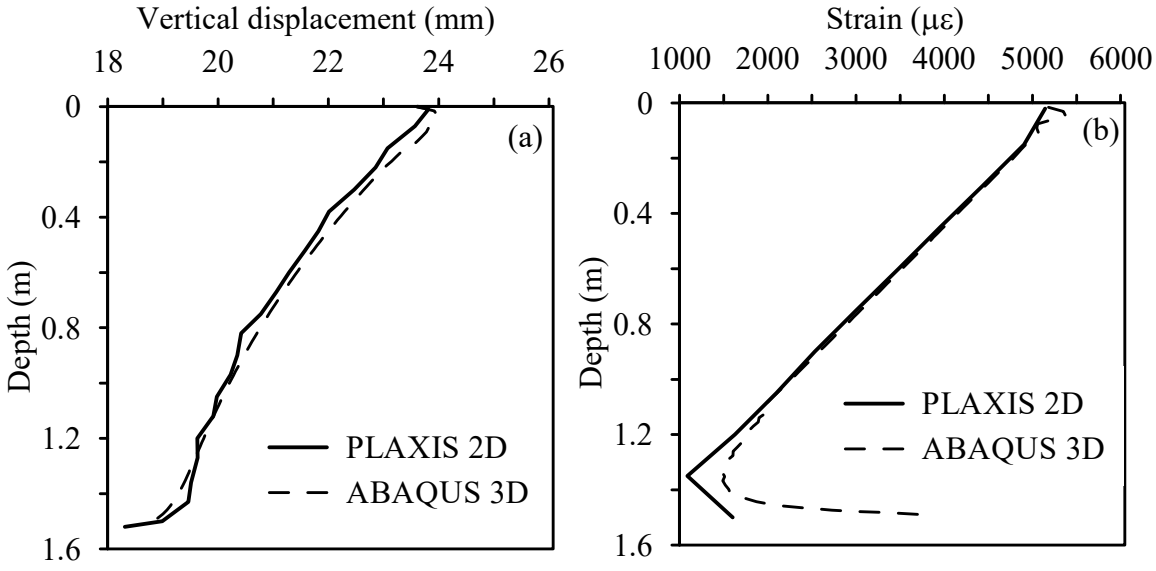

Figure 3.11. Vertical (a) displacement and (b) strain profiles at the soil-pile interface

Figures 3.12 (a) and (b) show the vertical displacement and strain profiles, respectively, in the soil at 70 mm from the wall of drilled shaft obtained from PLAXIS 2D and ABAQUS 3D. The vertical displacement at the top and bottom of the shaft was 19.37 mm and 13.5 mm, respectively, in PLAXIS 2D. The vertical displacement at the top and bottom of the shaft was 19.54 mm and 13.53 mm, respectively, in ABAQUS 3D. Tensile vertical strains are observed at ground level, while compressive vertical strains are observed at the level of the shaft bottom. The tensile strain at the top was 25275 με, and

the compressive strain at the bottom was 35961 με in PLAXIS 2D. The tensile strain at the top was 18273 με, and the compressive strain at the bottom was 27492 με in ABAQUS 3D.

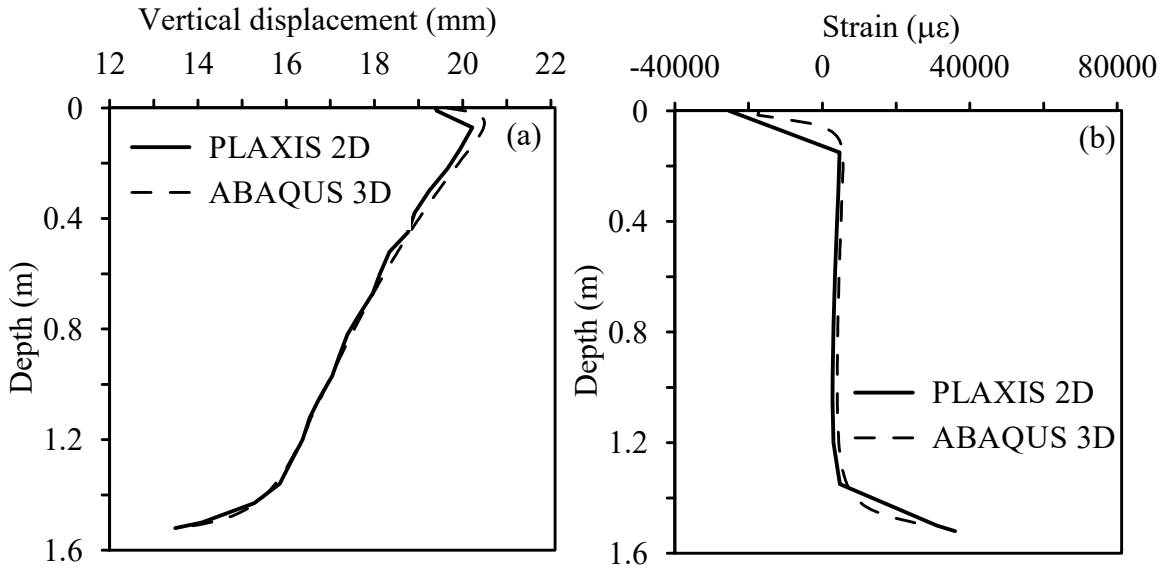

Figure 3.12. Vertical (a) displacement and (b) strain profiles in soil at 70 mm away from the drilled shaft center

Figures 3.13 (a) and (b) shows the vertical displacement and strain profiles, respectively, in the soil at 500 mm from the center of the shaft. The vertical displacement at the top and bottom of the shaft was 6.95 mm and 4.38 mm, respectively, in PLAXIS 2D. The vertical displacement at the top and bottom of the shaft was 6.81 mm and 4.27 mm, respectively, in ABAQUS 3D. The vertical tensile strain at the top was 1537 με, and the vertical compressive strain at the bottommost point was 3729 με in PLAXIS 2D. The vertical tensile strain at the top was 1404 με, and the vertical compressive strain at the bottommost point was 3565 με in ABAQUS 3D.

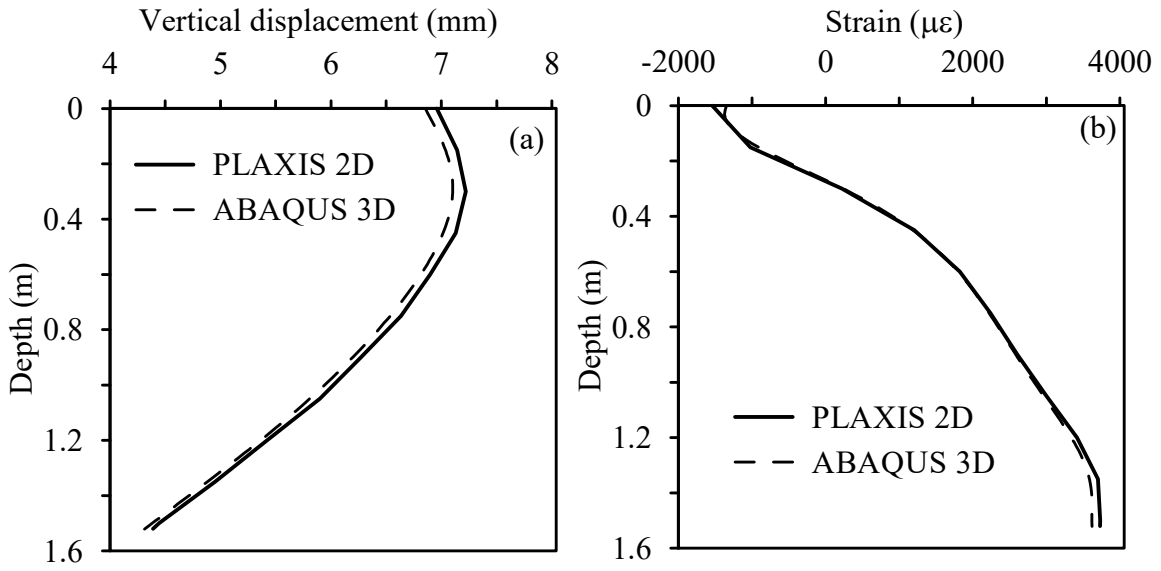

Figure 3.13. Vertical (a) displacement and (b) strain profiles in the soil at 500 mm away from the drilled shaft center

Figure 3.14 shows the radial strain variation at various depths from ground level in the soil away from the drilled shaft wall.

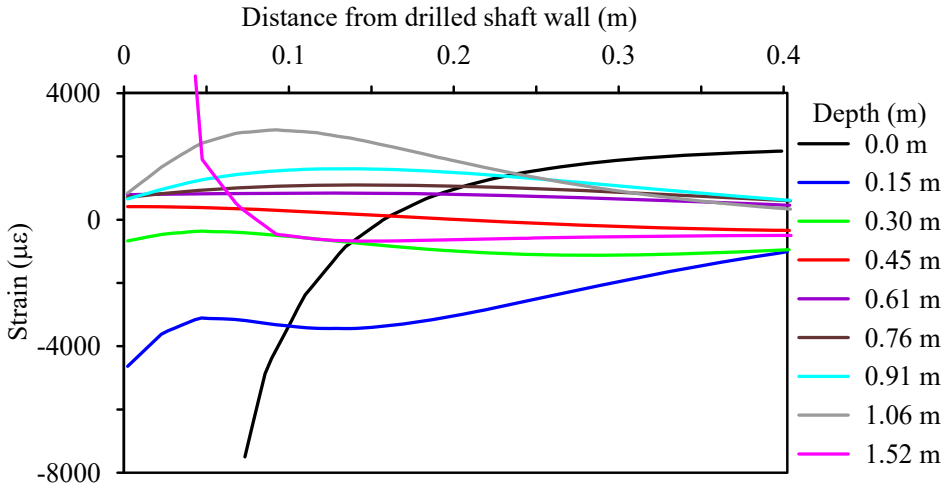

Figure 3.14. Radial strain variation at various depths from ground level in the soil away from drilled shaft

It can be seen that negative radial strains occur at depths below 0.45 m, and positive radial strains occur above 0.45 m. Also, the majority of the variation in radial strain is observed approximately 0.1 m away from drilled shaft wall, after which the values converge toward zero. The radial strains at 0 m and 1.52 m, being exceptionally high, were ignored for this study.

Figure 3.15 shows the vertical and radial configuration layout for the FBG fibers on US#3 rebar in the precast drilled shaft (Fiber#1), at the soil-pile interface (Fiber #2), and in Test Sand (Fiber#3 and Fiber#4). Fiber#1 has 150 mm for FBG sensors to capture the vertical strain in the drilled shaft.

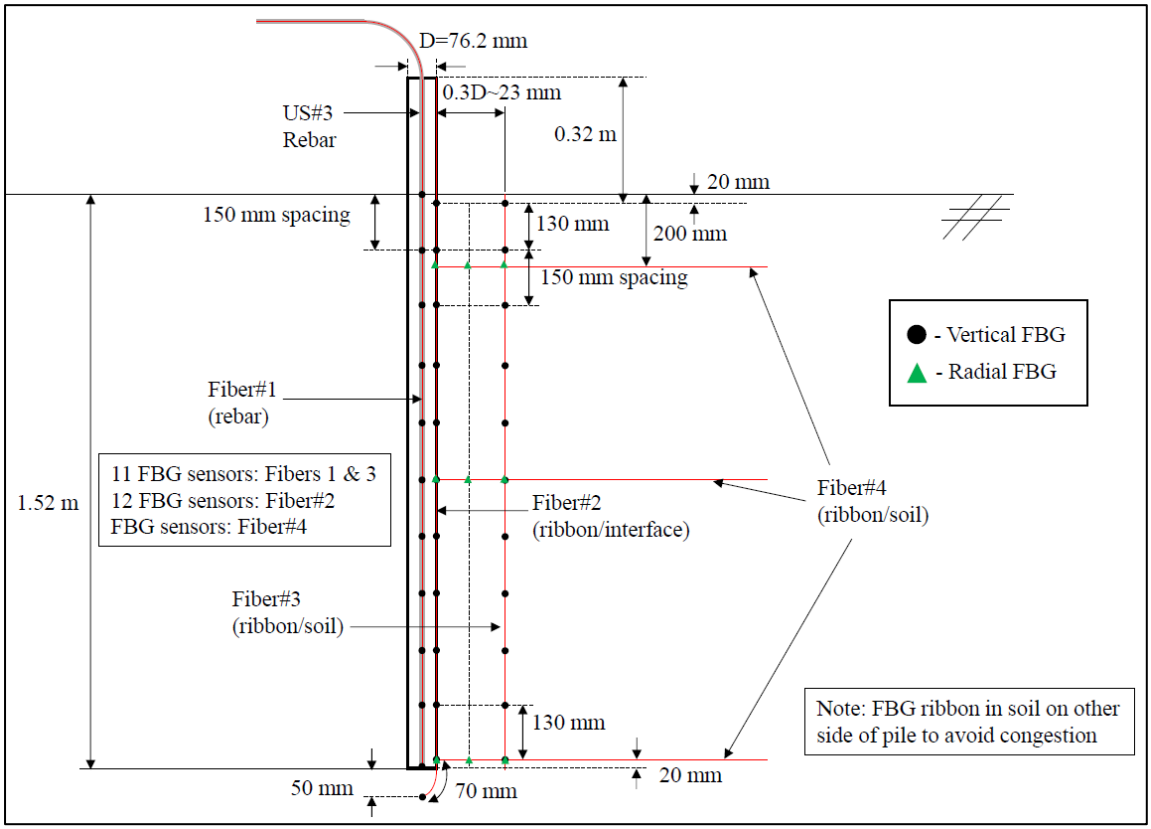

Figure 3.15 Design of vertical and radial FBG fiber configuration layout

Fiber#2 has 150 mm spacing for FBG sensors, with topmost and bottommost FBG sensors at 20 mm offset from ground level and bottom of the precast drilled shaft, respectively, to capture the vertical strains at the soil-pile interface. The vertical strain variation will be used to determine the vertical force variation, which will provide insight into the skin resistance variation and slip formation in the soil-pile interface. The 20 mm offset from the bottom of the precast drilled shaft was designed because the bottom corner of the drilled shaft induces very high compressive strains (Figure 3.11 (b)), which might damage the FBG sensor. The 20 mm offset from ground level to avoid potential damages to the FBG sensor caused by disturbance from activities on the ground. Also, an additional FBG sensor is designed to capture strains in the soil at the bottom of the drilled shaft. Fiber#3 was designed to capture the maximum strains in the influence zone around the drilled shaft. Fiber#3 has 150 mm of FBG sensor spacing and is designed at approximately 0.3D (D is the diameter of the drilled shaft), which lies at approximately half the radial distance of the influence zone around the drilled shaft where maximum strains are expected to occur. This decision was based on the observation made in Figure 3.12 (c), which shows that the maximum strains occur within the range of 70 mm from the drilled shaft center or 32 mm from drilled shaft wall. Similar to Fiber#2, 20 mm offsets from ground level and the bottom of the precast drilled shaft were designed for Fiber#3. Fiber#4 was designed to capture the high radial strains in the soil near the top and bottom of the drilled shaft (Figure 3.14) in the influence zone (0.3D) and the radial strain at the soil-pile interface, which will be used to determine radial forces at the soil-pile interface. The radial force variation at the

interface will provide insight into the skin resistance variation and gap formation in the soil-pile interface.

3.3.3.3.3. Construction and calibration of FBG fiber (Fiber#3 and Fiber#4) to determine vertical and radial displacements in soil and radial force variation in soil-pile interface

A fiber with a single FBG sensor was constructed as a trial for Fiber#3 and Fiber#4, as shown in (Figure 3.16). To install the FBG fiber in the soil, protection was necessary, and the following procedure was adopted: (1) A ribbon of bias-ply fabric, made in a way that will prevent significant lateral stretching, was used to hold our FBG fiber in place. The bias-ply was rolled out into a wooden plank with a cavity, which was supported by a wooden stand, and FBG fiber was laid on the bias-ply fabric; (2) A urethane rubber mold compound was used to protect the FBG fiber on the bias-ply fabric. The urethane was prepared by mixing two compounds (A & B) in a ratio of 2:1; (3) A silicone stick was used to mix the urethane compounds to avoid moisture entering the compound. The prepared urethane compound has a setting time of 20 minutes; (4) A vacuum pump and air entrainment meter were used to remove the air bubbles from the urethane; (5) Then, a thin layer of urethane was laid on the corner of the cavity on the bias-ply ribbon to protect the FBG fiber; (6) After a curing time of 24 hours, another layer of urethane was applied to fill the entire cavity, and sand was poured; (7) The FBG was tested for any possible damages that may have occurred during construction by connecting a laser to the FBG fiber connector. Then, the urethane was allowed for complete curing for 48 hours; (8) The result was a strong strand of flexible fabric that would protect the FBG from damage; (9) D-rings were attached to both ends of the ribbon for pilot testing purposes.

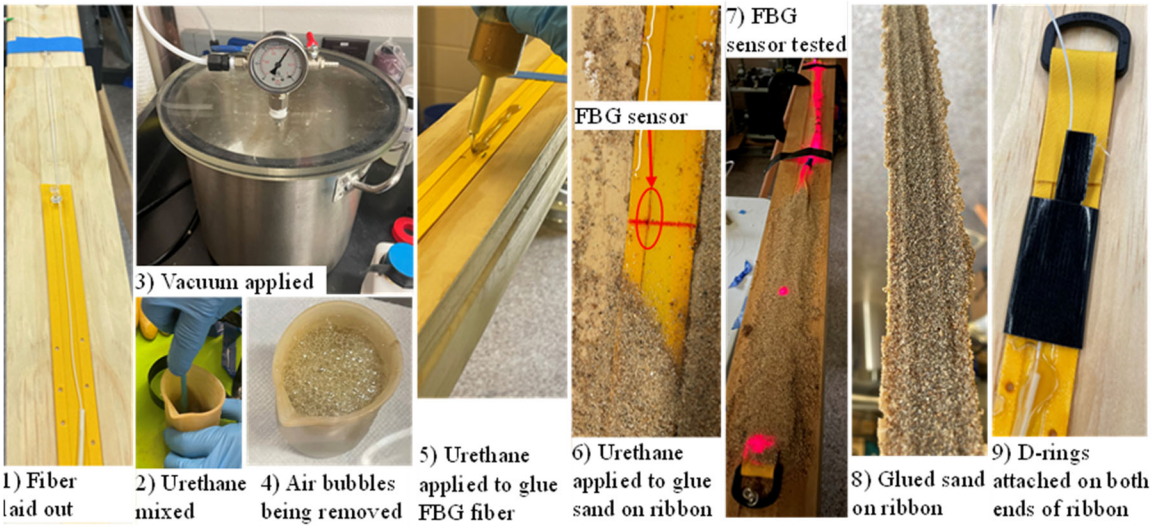

Figure 3.16. Procedure for installing FBG fiber on the bias-ply ribbon

It is crucial to have the interface friction angle between the Fiber#3 and the Test Sand equal to the friction angle of the Test Sand to simulate actual conditions. To calibrate Fiber#3 for this condition, direct shear tests were conducted on the Test Sand, ribbon without glued Test Sand (Figure 3.17 (a)), and ribbon with glued Test Sand (Figure 3.17 (b)). The direct shear tests were conducted for 24 kPa and 96 kPa vertical pressures considering approximate overburden pressures that would occur at the drilled shaft bottom. The following procedure was adopted for the sample preparation for direct shear tests: (1) Wooden cylinders of diameter 63.5 mm (2.5") and thickness 12.7 mm (0.5") were cut; (2) The bias-ply ribbons glued with sand and without sand were cut to the required dimensions and glued to the top of the wooden cylinders using epoxy; (3) The thickness of the cylinder was reduced by using sandpaper to make sure the that the top of the ribbon (Figure 3.17 (a)) and top of the sand on the ribbon (Figure 3.17 (b)) was flush with the top edge of the bottom half of shear box; (4) The top half of the shear box was assembled, and sand was

filled up to (25.4 mm (1”); (5) A porous stone was placed on the top, and then the top pedestal for vertical loading was placed.

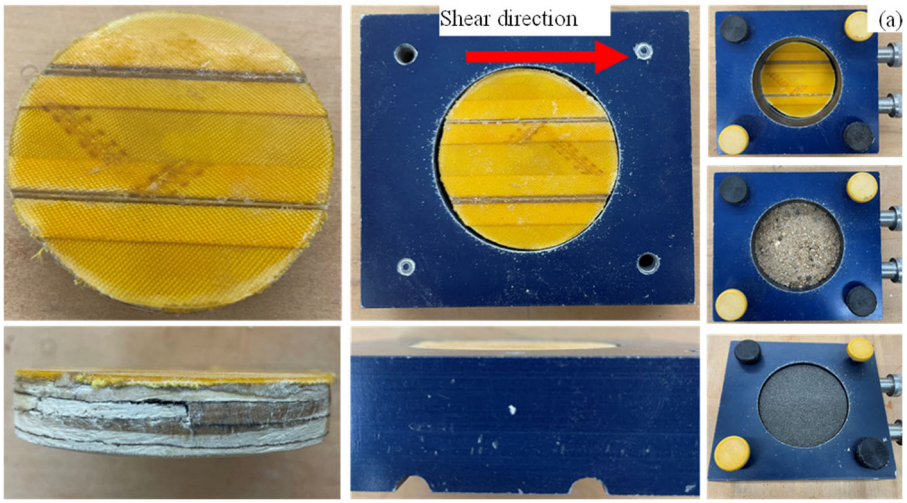

Figure 3.17 (a). Ribbon without glued sand in Direct Shear Test setup

Figure 3.17 (b). Ribbon with glued sand in Direct Shear Test setup

Figures 3.18 (a) and (b) show the stress-strain plots for 24 kPa and 96 kPa constant vertical pressures. It can be seen from Figure 3.19 (a) that the maximum value of peak shear stress for 24 kPa vertical pressure is for sand (2.9 MPa), followed by a ribbon with sand (3.0 MPa) and then a ribbon without sand (2.5 MPa). From Figure 3.18 (b), it can be seen that for the 96 kPa vertical loading, the maximum peak shear stress equal to 11.59 MPa was observed for sand, followed by the ribbon with sand with a slightly lower value of 11.56 MPa. On the other hand, the peak shear stress value for ribbon without sand was considerably lower equal to 9.09 MPa.

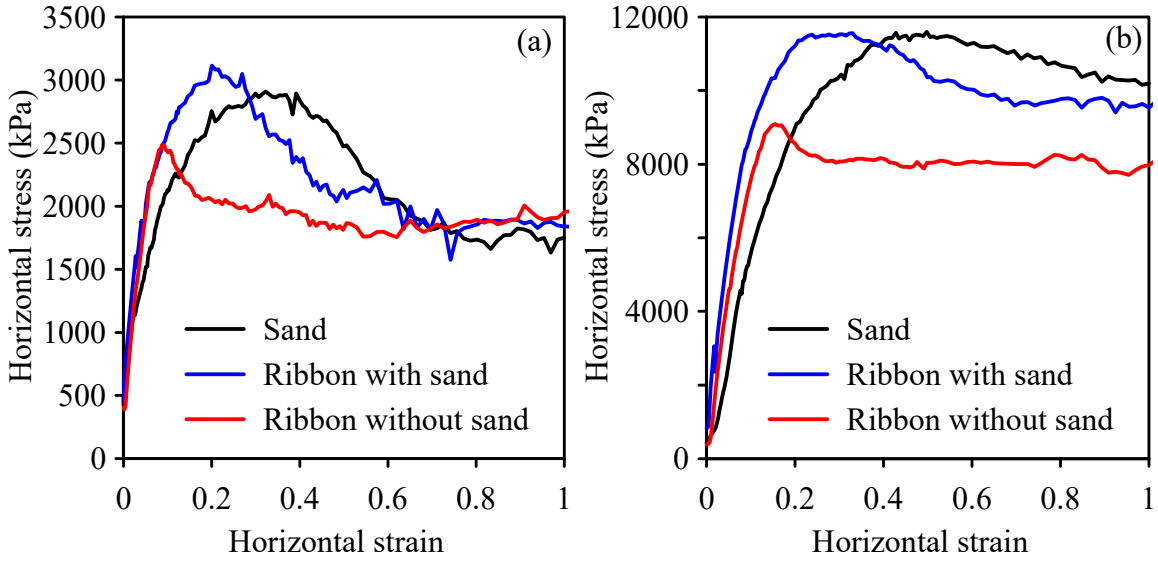

Figure 3.18. Stress-strain variation for (a) 24 kPa and (b) 96 kPa vertical pressure

Table 3.1 shows the friction angle value for sand and interface friction angles for ribbon with sand and ribbon without sand. It can be seen that the ribbon without sand has the lowest value (32 degrees), and the ribbon with sand value (38 degrees) is slightly lower than the friction angle of sand (39 degrees).

Table 3.1. Summary of friction angles determined from direct shear tests

Direct Shear Test	Friction angle (degree)
Sand	39
Ribbon with sand	38
Ribbon without sand	32

The interface friction angle between Sand and Ribbon sand was very close to the friction angle of sand. On the other hand, the interface friction angle for Sand and the Ribbon without sand was considerably lower than the friction angle of sand. Hence, using ribbon glued with sand proved to be effective.

3.3.3.3.4. Construction of FBG fiber (Fiber#1) to determine axial force variation in the drilled shaft

Fiber#1 is designed to be installed on the US#3 rebar to measure the vertical strain variation, which will be used to calculate axial force variation in the precast drilled shaft. The axial force variation will provide the skin resistance and end-bearing capacity of the precast drilled shaft. A fiber with a single FBG sensor was constructed as a trial for Fiber#1. To install a single FBG fiber in rebar, the following procedure was adopted: (1) A Dremel tool was used to cut a 1.51x 1.51 mm slit for the FBG fiber and 2.0 x 2.0 mm for the splice between the fiber and the wire connecting the interrogator (Figure 3.19 (a)); (2) In this slit, a layer of JB Weld epoxy was inserted to prepare an even bed of epoxy to install the FBG

fiber, filling the slit approximately half the depth of cut; (3) A popsicle stick was then used to smooth out the epoxy, to make sure the corners and crevasses were filled, and the top surface was leveled. The FBG fiber, along with the splice, was then laid on this epoxy bed; (4) Using tweezers, the FBG was repositioned, making sure that no part of it was outside the slit. The splice was also positioned such that it was about 5 mm offset from the cut for the FBG fiber to create a gap for epoxy; (5) Then, a new layer of the epoxy was placed on top, sealing the FBG inside the rebar; (6) The splice was clamped to the rebar with a silicone tape in between to ensure a strong bond (Figure 3.19 (b)); (7) To prevent the fiber optic cable from breaking due to sharp movements, a conical urethane resin membrane was cast around the end of the rebar near the splice (Figure 3.19 (c)).

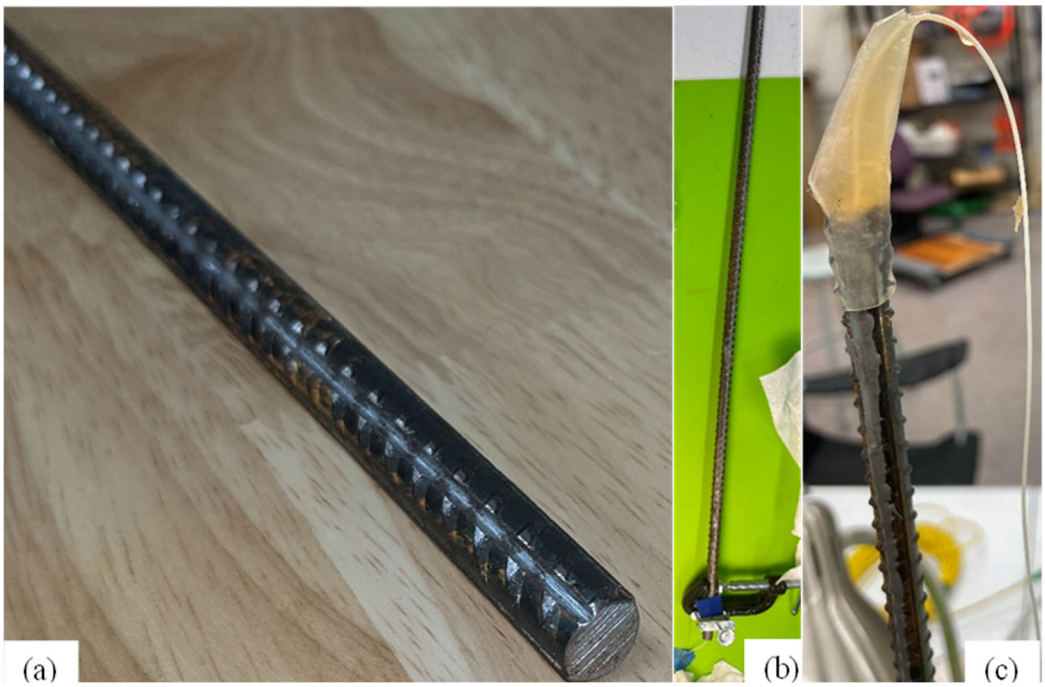

Figure 3.19. Procedure for installing FBG fiber in rebar (a) 1.5x 1.5mm slit on rebar, (b) laying and clamping of fiber on rebar, and (c) conical urethane caste on the splice for protection

3.3.3.5.5. Construction of FBG fiber (Fiber#2) to determine vertical force variation in the soil-pile interface

Fiber#2 is designed to be installed longitudinally on the concrete surface of the precast drilled shaft to capture the vertical strains at the soil-pile interface. The vertical strain variation will be used to determine the vertical force variation, which will provide insight into the skin resistance variation and slip formation in the soil-pile interface. A fiber with three FBG sensors was constructed as a trial for Fiber#2, as shown in Figure 3.20. To install the FBG fiber on the concrete surface comprising three FBG sensors, the following procedure was adopted: (1) A Dremel tool was used to cut a 1.51x 1.51 mm slit on the concrete surface longitudinally to accommodate the FBG fiber. A nylon tube (NewAge Industries 2022) was used to support the FBG fiber at the top of the pile, which connects to the fiber splice and then connects to the interrogator; (2) The FBG fiber was pushed through the nylon tube and fiber splice; (3) A small silicone cylinder with a slit accommodated the FBG fiber inside the fiber splice; (4) The nylon tube along with another silicone tube to provide additional stiffness to the FBG fiber were clamped at the top of the pile with O-rings; (5) The JB construction adhesive was used to glue the end of the nylon tube to the concrete surface. The FBG fiber was laid in the slit present on the concrete surface, and the JB weld epoxy was used to embed the fiber in the slit with the help of a silicone tip tool and a sculpting tool. This epoxy has a 2-hour working time; (6) The precast drilled shaft was ready to install in the soil box after 24-hour curing.

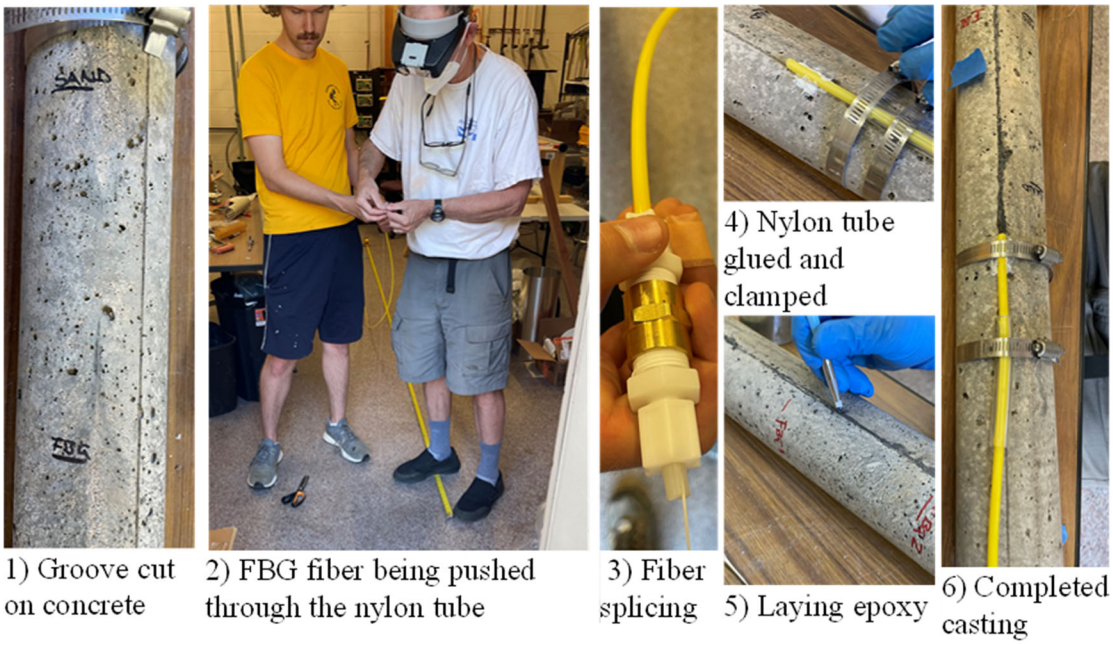

Figure 3.20. Procedure for installing FBG fiber on concrete surface

3.3.4. Instrumentation and calibration of mechanical loading setup

The main components of the mechanical loading setup consisted of the Linear Variable Differential Transformer (LVDT), load cell, reaction beam, and hydraulic jack. The following sections describe the working, specifications, and data acquisition of the sensors and design configuration layout and construction of the mechanical loading setup used in this study.

3.3.4.1. Measurement of the drilled shaft and ground displacement by Omega LVDT and Data Acquisition (DAQ) system

The temporal vertical displacement of the precast drilled shaft and ground will be measured by the LVDT and DAQ system. The LVDT models LDI-619-050-A010S and LD620-50 and the DAQ model OM-DAQXL (Omega 2022) will be used. The resolution

of the LVDTs is 12.5 µm with a range of 0 to 50 mm for the LDI-619-050-A010S and -50 to 50 mm for the LD620-50 (Range- -50 to 50 mm). The LDI-619-050-A010S will be mounted on the mechanical load setup to measure the vertical displacement of the precast drilled shaft. The LD620-50 will be used to measure ground displacements. The OM-DAQXL has a capacity of 8 input channels with a maximum sampling and logging rate of 125 samples /second and available external excitation of 10 VDC (an additional 24VDC can be provided). The logged data is available in excel format (.csv) and can be used for calculations. The LVDTs were pre-calibrated (Omega 2022). Figures 3.21 (a) and (b) show the LDI-619-050-A010S and LD620-50 models, respectively.

Figure 3.21. (a) LDI-619-050-A010S and (b) LD620-50 LVDT models

3.3.4.2. Measurement of load on the drilled shaft by Omega load cell and Data Acquisition (DAQ) system

The temporal load variation on the drilled shaft will be monitored by the load cell model LC402-25K and DAQ model OM-DAQXL (Omega 2022). The LC402-25K has a capacity of 111.21 kN (25000 lbs), resolution of (0.11 kN) 25 lbs, excitation voltage of 10 VDC, sensitivity of 29.972 mVDC, and resistance of 59 k ohm. The logged data is available in excel format (.csv) and can be used for calculations. The load cell was pre-calibrated (Omega 2022). Figure 3.22 shows the LC402-25K model.

Figure 3.22. LC402-25K load cell model

3.3.5. Design of configuration layout and construction of mechanical loading setup

Linear Variable Differential Transformer (LVDT) was used to monitor the ground displacement and precast drilled shaft displacement, and the load cell was used to measure the applied mechanical load. The loading will be applied by using a hydraulic jack and reaction beam system, as shown in Figure 3.23 (a) and (b). A constant mechanical load of 4.5 kN will be applied over the entire time duration of each experiment.

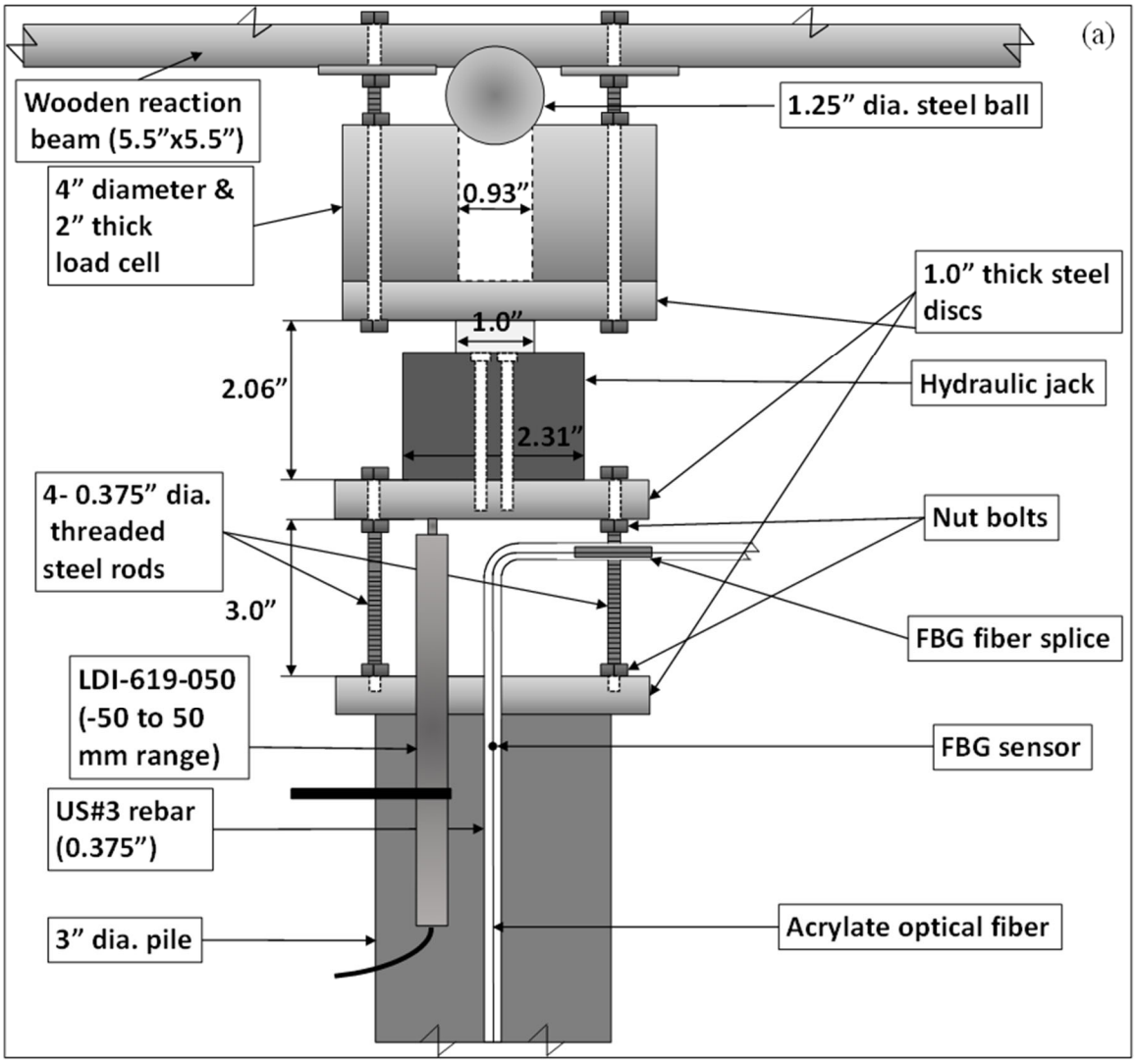
(a)
Wooden reaction beam (5.5”x5.5”)
1.25” dia. steel ball
4” diameter & 2” thick load cell
0.93”
1.0” thick steel discs
1.0”
2.06”
Hydraulic jack
2.31”
4- 0.375” dia. threaded steel rods
Nut bolts
3.0”
FBG fiber splice
LDI-619-050 (-50 to 50 mm range)
FBG sensor
US#3 rebar (0.375”)
3” dia. pile
Acrylate optical fiber

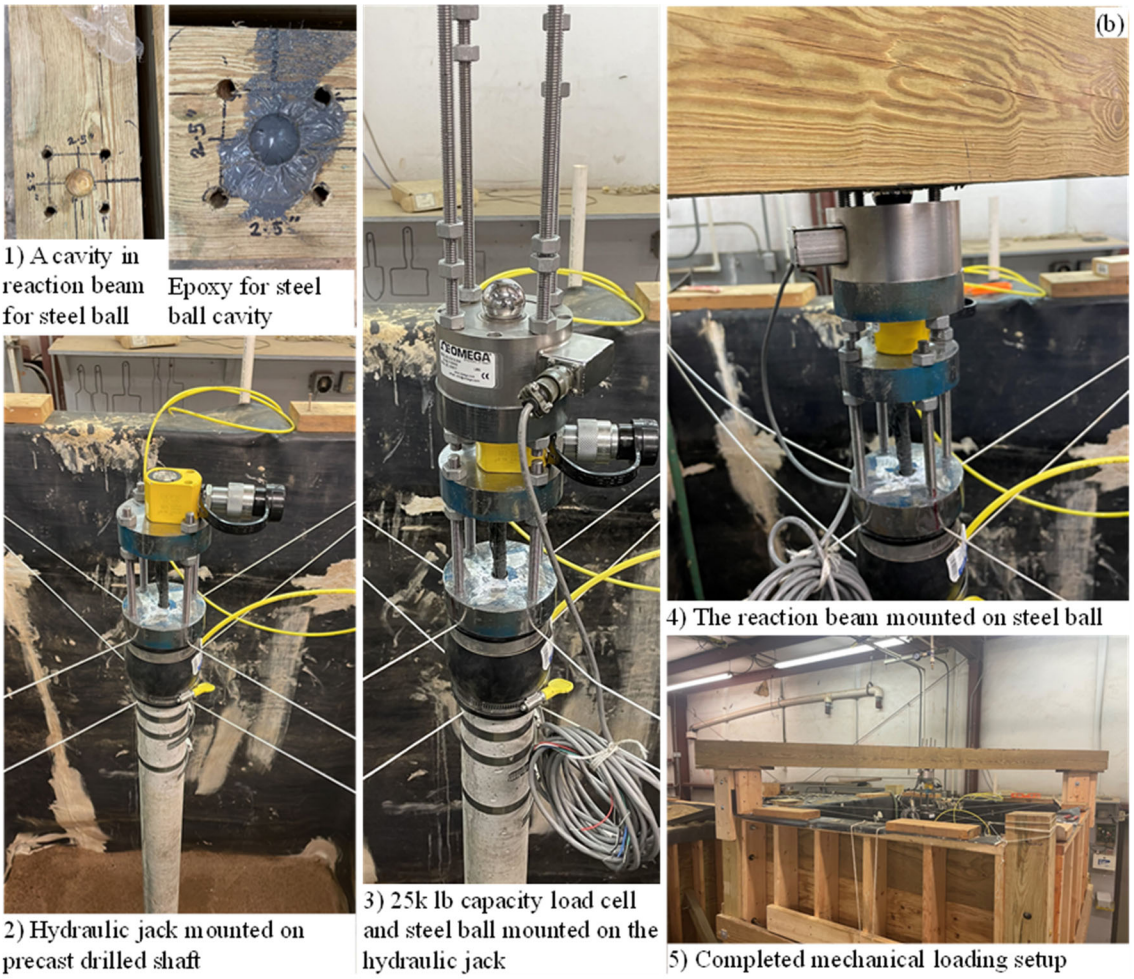

Figure 3.23. (a) Design and (b) procedure for mechanical loading setup construction

3.3.6. Instrumentation and calibration of hydrological loading setup

The hydrological loading setup consisted of a spray nozzle system to simulate heavy rainfall and flooding and a pair of heaters to simulate drought conditions. The following sections describe the specifications and construction for the hydrological setup used in this study.

3.3.5.2. Heavy rainfall/ flooding setup

The heavy rainfall/ flooding will be simulated by using a spray nozzle system that will provide a uniform, vertical, constant intensity, and square area of coverage rainfall. The chosen nozzle type are four Spraying Systems Co. brass 3.6SQ nozzles and one cone nozzle (5Cone) (Spraying Systems Co. 2022). A wooden frame with four 1/8G-3.6SQ nozzles in a square pattern and one 5cone nozzle at the center were constructed for coverage of the entire ground surface. The wooden frame provided stability with height adjustability. The rainfall intensity was adjusted by a pressure gauge (100 psi capacity). A Proof of Concept (POC) study was conducted to design and optimize the rainfall setup configuration for the simulation of heavy rainfall and flood. The horizontal and diagonal spray variation of the square nozzle (3.6SQ) and the cone nozzle (5Cone) (Spraying Systems Co. 2023) and the most optimum configuration of nozzles which will provide the maximum coverage area, was determined. The height of the nozzles from ground level was determined based on the spray area and spray angle (Spraying Systems Co., 2023). Two tests were conducted to determine the configurations. The following procedure was adopted for the POC study for the two tests: (1) The nozzle was connected to a T-joint which was connected to a 100 psi pressure gauge, and a 2-inch OD CPVC pipe which was connected to the water hose. This setup was mounted on a metal post at the height corresponding to the selected nozzle. The square nozzle was adjusted such that the groove on the nozzle aligns as a cross in the square test area; (3) Water cups were arranged to collect water as shown in Figure 3.24 (a); (4) The POC test was conducted for a duration of 2 minutes, the pressure of 137.89 kPa (20 psi) and height of 78 cm as shown in Figure 1 (b); (5) The water collected in the cups was

measured; (6) The POC test was conducted for both nozzles by replacing the nozzle on the setup.

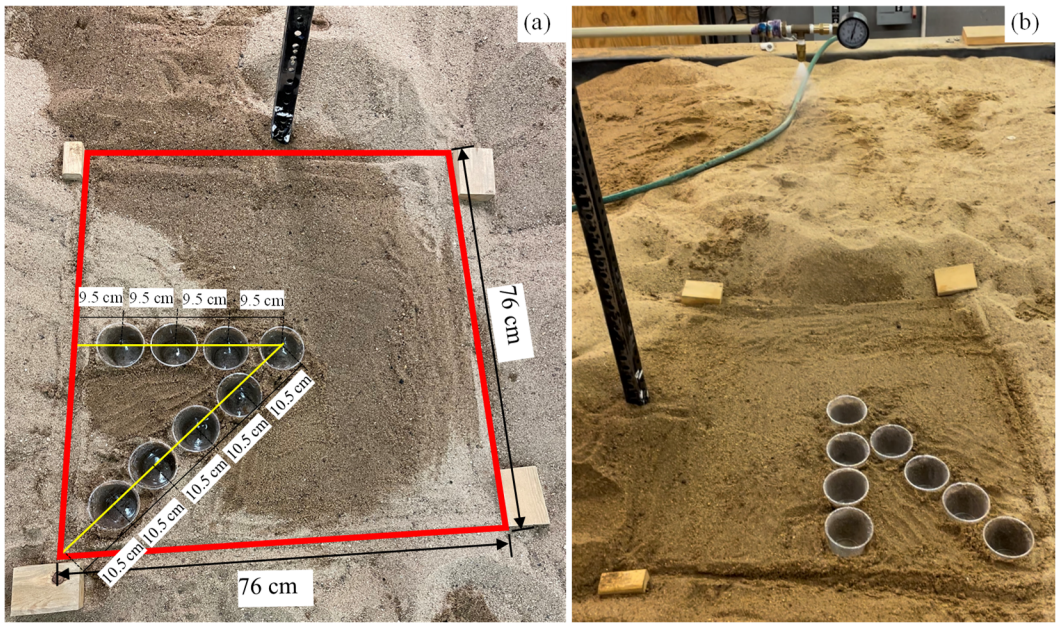

Figure 3.24. (a) Placement of water cups and (b) test run for the POC test

The height of the 3.6SQ and 5Cone nozzles were set to 78 cm (2.56 ft) for Test 1. Figure 3.25 shows the horizontal and diagonal spray variation for Configuration 1. For this configuration, four 3.6SQ nozzles were placed at the center of the soil box in a square pattern. The effective square spray area for each nozzle was determined to be 45.6 cm x 45.6 cm (1.5ft x 1.5ft). The total effective area was determined to be 9.0 sq. ft. out of the total available area of 25 sq. ft (36%).

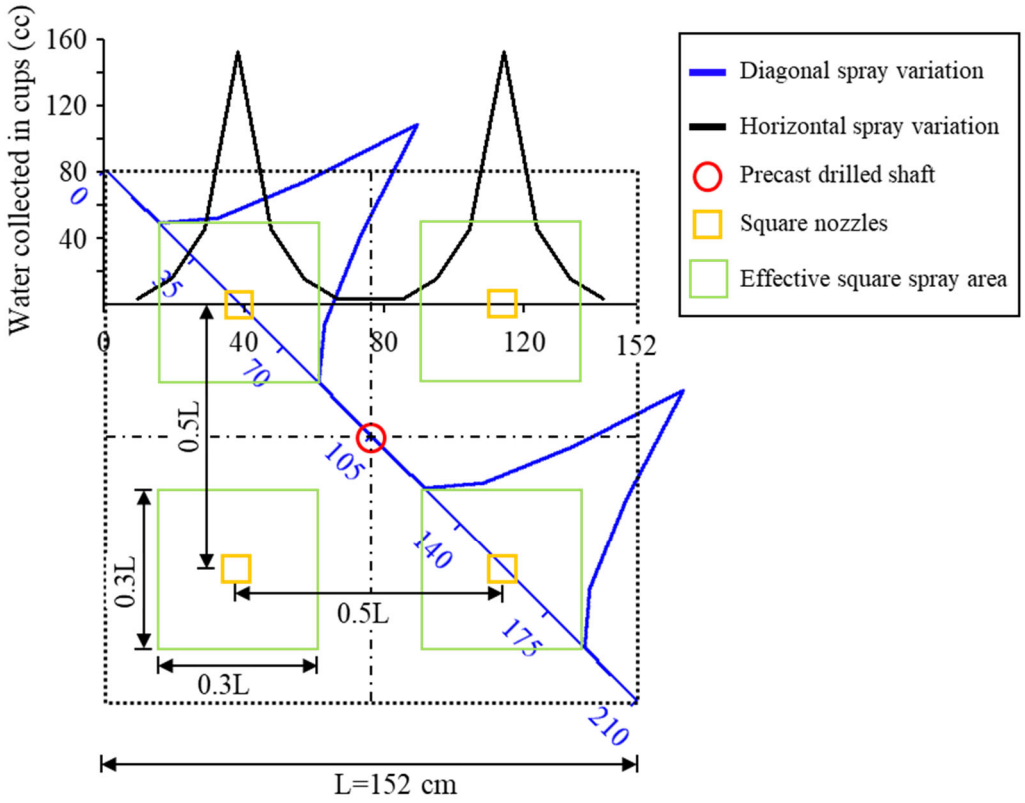

Figure 3.25. Configuration 1 layout and spray variation using four square spray nozzles at 2.56 ft height from ground level

Figure 3.26 shows the horizontal and diagonal spray variation for Configuration 2. For this configuration, four 3.6SQ nozzles were placed at the center of the soil box in a square pattern, and one 5Cone nozzle was placed at the center of the soil box. The effective cone spray area for the 5Cone nozzle was determined to be 76 cm x 76 cm (2.5ft x 2.5ft). The total effective area was determined to be 13.91 sq. ft. out of the total available area of 25 sq. ft (55.64%). Hence, this configuration proved to be more effective than Configuration 1.

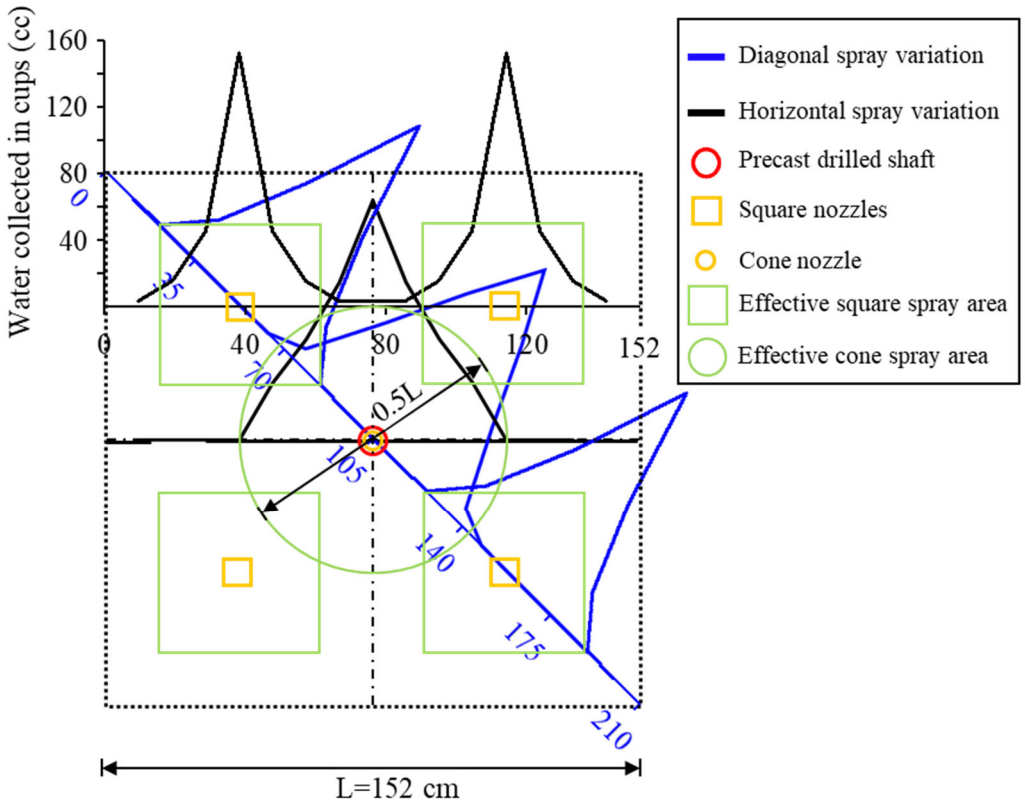

Figure 3.26. Configuration 2 layout and spray variation using four square spray nozzles and one cone spray nozzle at 2.56 ft height from ground level

The height of the 3.6SQ and 5Cone nozzles was set to 122 cm (4.0 ft) for Test 2. Figure 3.27 (a) shows the horizontal and diagonal spray variation for Configuration 3. For this configuration, four 3.6SQ nozzles were placed at the center of the soil box in a square pattern at 76.2 cm (2.5 ft) spacing, and one 5Cone nozzle was placed at the center of the soil box. The maximum water was collected at the center for both types of nozzles- 84.4 cc for the 3.6SQ nozzle and 78.4 cc for the 5Cone nozzle. The effective square spray area was determined as 61 cm x 61 cm (2 ft x 2 ft), and the effective circular spray area was

determined as 91.2 cm (3.5 ft) in diameter. The total effective area was determined to be 19.5 sq. ft. out of the total available area of 25 sq. ft (78%). Figure 3.27 (b) shows the smoothened spray variation for Configuration 3. The horizontal variation by the 5Cone nozzle will compensate for the low water depth observed at the middle of the horizontal variation by 3.6SQ.

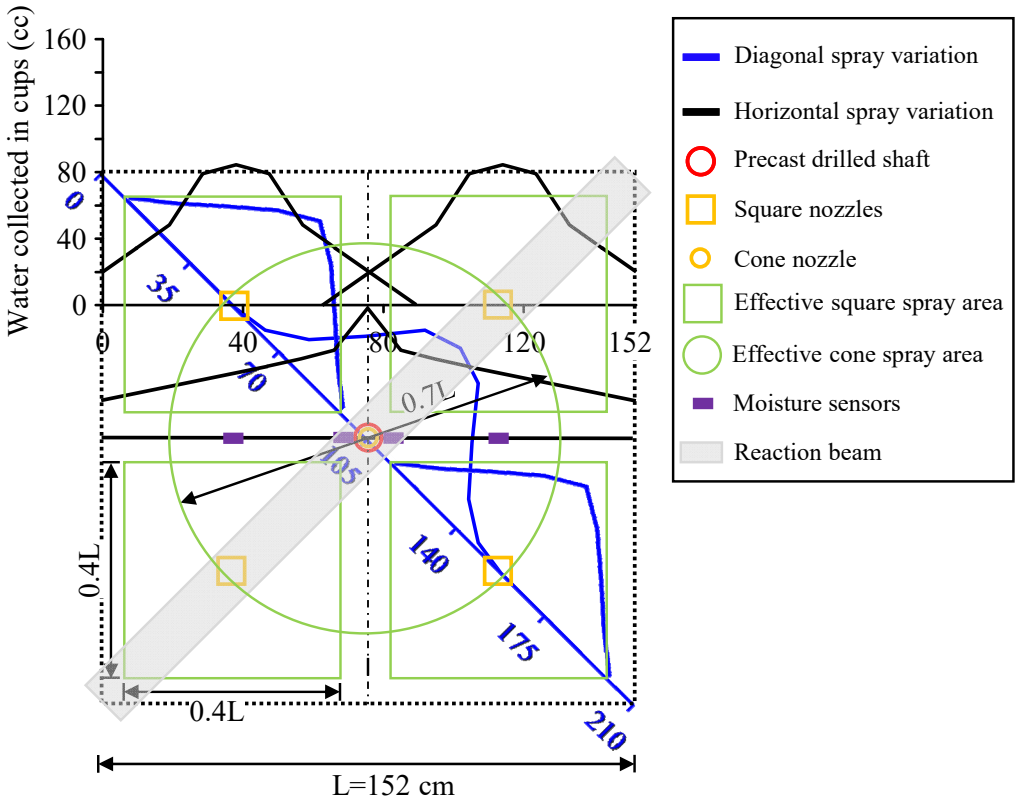

Figure 3.27 (a) Configuration 3 layout and spray variation using four square spray nozzles and one cone spray nozzle at 4 ft. height from ground level

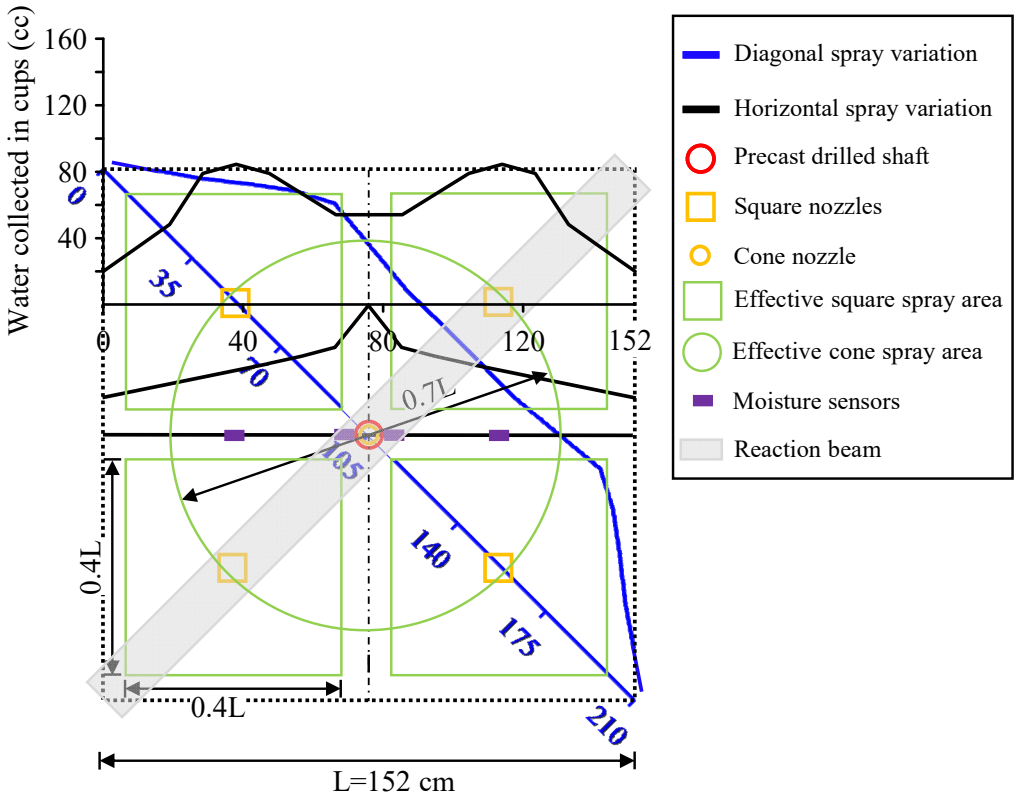

Figure 3.27 (b) Smoothened spray variation for Configuration 3 layout

Configuration 3 was the most optimum, providing a coverage area of 78% which is acceptable (Luk et al. 1993; Aksoy et al. 2012). For Configuration 3, the water collected at the center for both nozzles was maximum- 84.4 cc for the 3.6SQ nozzle and 78.4 cc for the 5Cone nozzle. For Configuration 3, the horizontal variation by the 5Cone nozzle was compensated for the low water depth observed in the middle of the horizontal variation by the 3.6SQ nozzles. The uniformity of the rainfall was maximum for Configuration 3 and finalized.

3.3.5.3. Drought setup

The drought setup will allow for evaporation to occur near the ground and consists of two heaters (Figure 3.25) that will provide an output of 1500 BTU/ft2/day with a temperature of 106 deg. C at the ground surface. This temperature was selected based on the maximum temperature recorded on 27th August 2011 in Houston, TX (NCDC), which was also used in the numerical study.

Figure 3.25. Drought setup comprising two heaters

3.3.7. Experimental setup procedure

The setup consists of a 1.5 m x 1.5 m x 2.24 m wooden soil box where a 76 mm diameter and 1.83 m long precast reinforced concrete shaft will be installed and subjected to mechanical and hydrological loads. The mechanical loading will be applied by a

hydraulic jack and reaction beam setup. The mechanical load will be measured by using a load cell. A single LVDT will be placed in the mechanical loading setup, and two separate LVDTs will be away from the drilled shaft on the ground surface to measure drilled shaft and ground displacement.

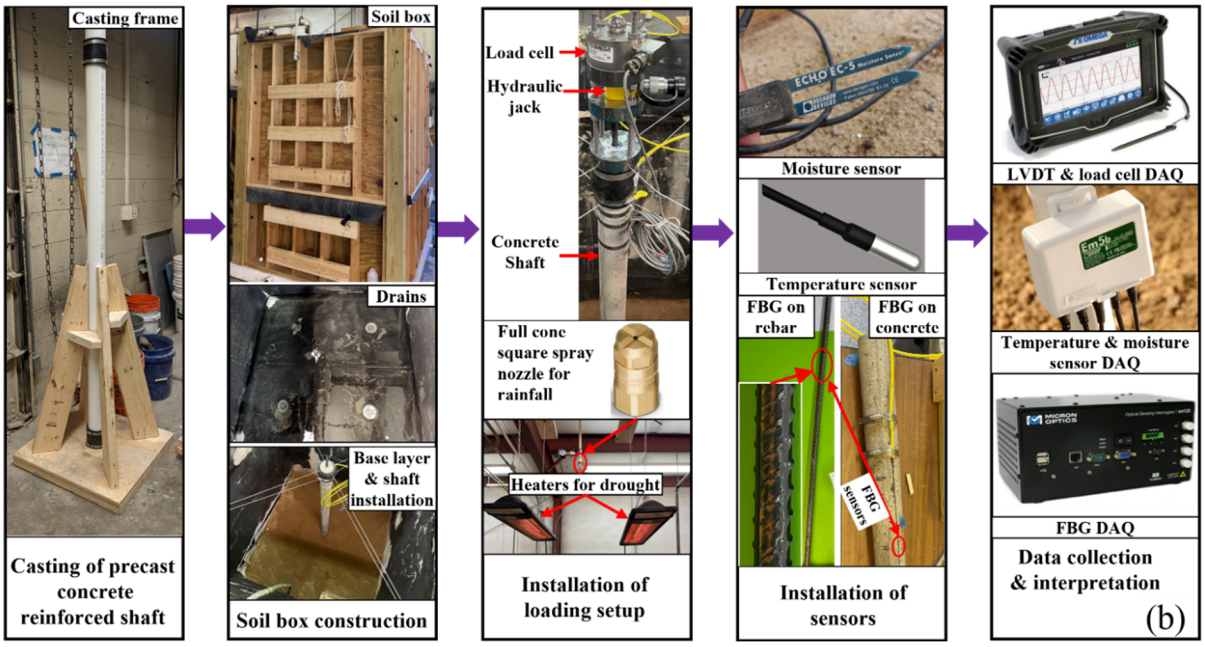

Figure 3.26. Summary flowchart for experimental setup construction

For simulating rainfall and drought, four spray nozzles capable of simulating moderate to heavy rainfall (0.12 m/hour to 0.97/hour) and two heaters, each capable of providing an output of 1500 BTU/ft2/day, respectively, will be used. The temperature and moisture sensors will be buried in the soil near the drilled shaft and ground surface to capture the temporal and spatial variation of moisture content and temperature caused due to heavy rainfall and drought, respectively. The Fiber Bragg Grating (FBG) sensors installed in the soil, on the rebar, and on the surface of the drilled shaft will measure the

strain from which the temporal and spatial variation of displacement in the soil at various depths, the axial force distribution in the drilled shaft, and the force transfer between the soil-pile interface will be calculated. Figure 3.26 illustrates the summary flowchart for the experimental setup.

3.3. CONCLUSION

The construction and calibration of the components of the experimental setup to investigate the effects of extreme hydroclimatic events on the deformation and bearing capacity behavior of the small-scale precast drilled shaft are discussed. Following were the major discussions:

1. The configurations of the Fiber Bragg Grating (FBG) sensors to be used in the pile, at the soil-pile interface, and in the soil were determined based on linear elastic analysis in finite element codes, PLAXIS 2D and ABAQUS 3D.
2. A bias-ply FBG ribbon is proposed to be used to measure the vertical and radial strains in the soil. It was shown that the friction angle of the sand was close to the interface friction angle between the bias-ply FBG ribbon and sand by conducting direct shear tests, which would help to better capture the strains in the soil.
3. The most optimum heavy rainfall frame configuration was determined based on Proof Of Concept (POC) tests which resulted in four 3.6SQ

nozzles at the corners of the rainfall frame and a single 5Cone nozzle at the center of the frame, which would provide a coverage area of 78%.

REFERENCES

ACI Committee 543. (2012). Design, Manufacture, and Installation of Concrete Piles.

Aksoy, H. *et al.* (2012) "A rainfall simulator for laboratory-scale assessment of rainfall-runoff-sediment transport processes over a two-dimensional flume," *CATENA*, 98, pp. 63–72. Available at: https://doi.org/10.1016/j.catena.2012.06.009.

Campanella, C., Cuccovillo, A., Campanella, C., Yurt, A. and Passaro, V. (2018). Fibre Bragg Grating Based Strain Sensors: Review of Technology and Applications. *Sensors*, 18(9), p.3115.

Decagon Devices. (2001-2010). EC-20, EC-10, EC-5: User's Manual. Pullman, WA: Author.

Fempto Fibertec (2022). FEMTO FIBER TEC - FEMTO FIBER TEC. (n.d.). Retrieved May 12, 2022, from https://www.femtofibertec.de/en/home#home

Ferraro, P. and De Natale, G. (2002). On the possible use of optical fiber Bragg gratings as strain sensors for geodynamical monitoring. Optics and Lasers in Engineering, 37(2-3), pp.115-130.

Hill, K. and Meltz, G. (1997). Fiber Bragg grating technology fundamentals and overview. *Journal of Lightwave Technology*, 15(8), pp.1263-1276.

IPCC.(2013). Climate Change 2013: The Physical Science Basis. Cambridge University Press.

Kreuzer, M. (1970) Strain measurement with fiber Bragg grating sensors: Semantic scholar. Available at: https://www.semanticscholar.org/paper/Strain-Measurement-with-Fiber-Bragg-Grating-Sensors-Kreuzer/1b00007973bbc79670d6919b5d2688085266d048.

Luk, S.H., Abrahams, A.D., Parsons, A.J., 1993. Sediment sources and sediment transport by rill flow and interrill flow on a semi-arid piedmont slope, Southern Arizona. Catena 20 (1/2), 93–111.

Meter Group (2022). https://www.metergroup.com/en/meter-environment/products/rt-1-soil-temperature-sensor

Micronoptics (2022). http://micronoptics.ru/uploads/library/documents/Datasheets/Micron%20Optics%20sm125.pdf

NewAge Industries. (2022). https://www.newageindustries.com/products/tubing-hose/nylon/nylotube-nylon-tubing/

NOAA (2022). U.S. Billion-Dollar Weather & Climate Disasters 1980-2022. https://www.ncei.noaa.gov/access/billions/events.pdf

Omega (2022). https://www.omega.com/en-us/

Scripps media (2022). https://www.denver7.com/news/national/extreme-drought-causing-home-foundation-issues-in-western-u-s

Spraying Systems Co. (2022). https://www.spray.com/

WMO (2021). https://public.wmo.int/en/media/press-release/weather-related-disasters-increase-over-past-50-years-causing-more-damage-fewer

CHAPTER 4. EXPERIMENTAL TESTING AND FINITE ELEMENT MODEL VALIDATION

4.1. ABSTRACT

Experimental testing of a small-scale drilled shaft with a 76 mm diameter and 1.52 m length was carried out. Multiple mechanical pile load tests were conducted to determine the ultimate bearing capacity of the drilled shaft under study. The drilled shaft was then subjected to a constant mechanical load equal to the estimated ultimate bearing capacity and varying hydrological loads consisting of low-, medium-, and high-intensity rainfall followed by gravity drainage. Then, the variation in axial force in the drilled shaft caused by the hydrological events was measured. A fully-coupled Geotechnical-Hydrological Finite Element Model (FEM) was developed to simulate the small-scale experiment using PLAXIS 2D. The stress-strain behavior of the partially saturated soil was represented by a Modified Mohr-Coulomb (MMC) constitutive model, which updates the yield criterion and modulus with changes in the matric suction and/or degree of saturation in PLAXIS 2D. The FEM results were computed and validated using the experimental results using qualitative comparisons. The wetting front moved at the same rate in FEM as compared to the experiment and also reached the drilled shaft bottom at the same time. The low-intensity rainfall caused the settlement of the drilled shaft, which caused a decrease in the total bearing capacity of the drilled shaft due to the mobilization of the skin resistance to the bottom of the drilled shaft. The axial force variation at various time intervals for the FEM matched with the experiment qualitatively in various aspects.

4.2. INTRODUCTION

In this study, experimental testing of the small-scale with a 76 mm diameter and 1.52 m long drilled shaft in Test Sand in the experimental setup discussed in Chapter 3 was conducted. Initially, multiple mechanical pile load tests were conducted using the mechanical loading setup, as discussed in Chapter 3, to determine the ultimate bearing capacity of the drilled shaft in the Test Sand (Davisson 1972; NYDOT 2015). Then, the design parameters, including the spray angle, spray height, and spray pressure, were determined for three different rainfall intensities (Spraying Systems Co. 2023). Finally, the mechanical loading setup was used to maintain a constant mechanical load equal to the determined ultimate bearing capacity on the drilled shaft, and the three different rainfall intensities were applied to evaluate the effect on the axial capacity of the drilled shaft. The results included temporal and spatial variation of Degree of Saturation (DOS), temporal variation of vertical displacement of the drilled shaft and ground, and the axial force profiles.

This study also attempts to validate the small-scale fully-coupled finite element model developed in PLAXIS 2D. In the finite element model, the tress-strain behavior of the partially saturated soil was represented by a Modified Mohr-Coulomb (MMC) constitutive model, which updates the yield criterion and modulus with changes in the matric suction and/or degree of saturation. The degree of saturation and matric suction relationship was represented by the van Genuchten (1980) Soil Water Characteristics Curve (SWCC). The temporal variation of vertical displacements of the drilled shaft and

ground and the axial force profiles obtained from the finite element model were then compared with the experiment results.

4.3. SMALL-SCALE EXPERIMENTAL MODEL TESTING

Experimental tests were conducted on the small-scale with a 76 mm diameter and 1.52 m long drilled shaft in Test Sand. Figure 4.1 shows the configuration layout of the moisture sensors, Fiber Bragg Grating (FBG) sensors, LVDTs, and load cell. Two LD620-50 LVDTs were mounted at 0.25 m and 0.5 m from the center of the drilled shaft to monitor the vertical ground displacement and a single LDI-619-050-A010S LVDT was mounted on the loading frame to monitor the vertical displacement of the drilled shaft. Fiber#2, as discussed in Chapter 3, was installed on the concrete surface of the drilled shaft at 0.15 m, 0.30 m, and 0.45 m from ground level. The EC-5 moisture sensors were buried at 0.10 m from ground level up to 0.3 m depth and then at 0.30 m intervals up to the bottom of the drilled shaft. The moisture sensors at the soil-pile interface were grouped at I1 and I2, and the moisture sensors at 0.38 m from the center of the drilled shaft were grouped as S1 and S2 for ease of plotting and evaluation. Proctor density tests were conducted as per ASTM D698 to achieve a relative compaction of 96% for the small-scale experiment.

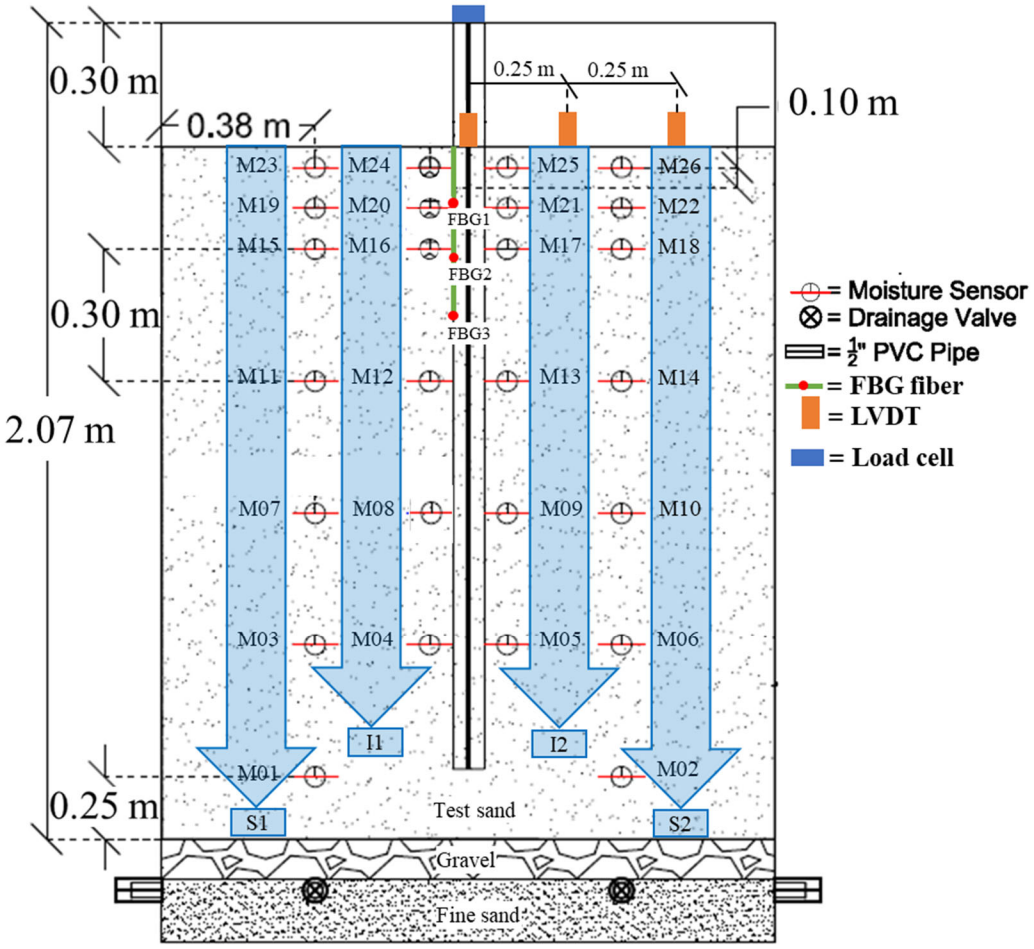

Figure 4.1. Sensor configuration

4.3.1. Static pile load testing under mechanical load

The static pile load testing was conducted on a 76.2 mm diameter and 1.83 m long precast drilled shaft in the Test Sand. The following procedure was adopted for performing the static pile load testing.

1. *Settings:* It was ensured that the data loggers were recording data for FBG sensors, moisture sensors, temperature sensors, LVDTs, and load cell (manual recording as backup). The loading setup was centered on the pile, the hydraulic jack piston in the

retracted position was flush with the base plate of the load cell, and the LVDTs were vertically aligned.

2. *Load and loading rate:* The loading rate was applied, as shown in Table 1 (NYDOT 2015). The load was applied slowly to avoid losing detection of the peak of the power spectrum for the FBG sensor from the data logger.

a) The design load was obtained from the analytical design and applied at the pile head. The total ultimate capacity equal to 3.65 kN and the total settlement corresponding to 7.62 mm were obtained from the analytical design (Kulhawy et al. 1983; Kulhawy 1991; Coyle and Castello 1981; Fellenius 1999). The design load was 1.46 kN, corresponding to the safety factor of 2.5.

b) The loading was continued beyond the ultimate load calculated from analytical methods up to 900% of the design load (increased by 50% of the design load) to achieve bearing capacity failure.

c) After the bearing capacity failure, the pile was unloaded and reloaded using the same loading schedule. The unloading-reloading was repeated until the load-settlement curve was vertical. Table 4.1 shows the loading rate for the pile load test. Figure 4.2. shows the mechanical pile load testing setup.

Table 4.1. Loading rate for static pile load test

Percentage of design load (%)	Load (kN)	Duration (minutes)
0	0.00	5
20	0.29	5
40	0.58	5
60	0.88	5
80	1.17	5
100	1.46	5
110	1.61	5
120	1.75	5
130	1.90	5
140	2.04	5
150	2.19	5
160	2.34	5
170	2.48	5
180	2.63	5
190	2.77	5
200	2.92	5
250	3.65	10
300	4.38	10
350	5.11	10
400	5.84	10

450	6.57	10
500	7.30	10
550	8.03	10
600	8.76	10
650	9.49	10
700	10.22	10
750	10.95	10
800	11.68	10
850	12.41	10
900	13.14	10
Unloading	0	-

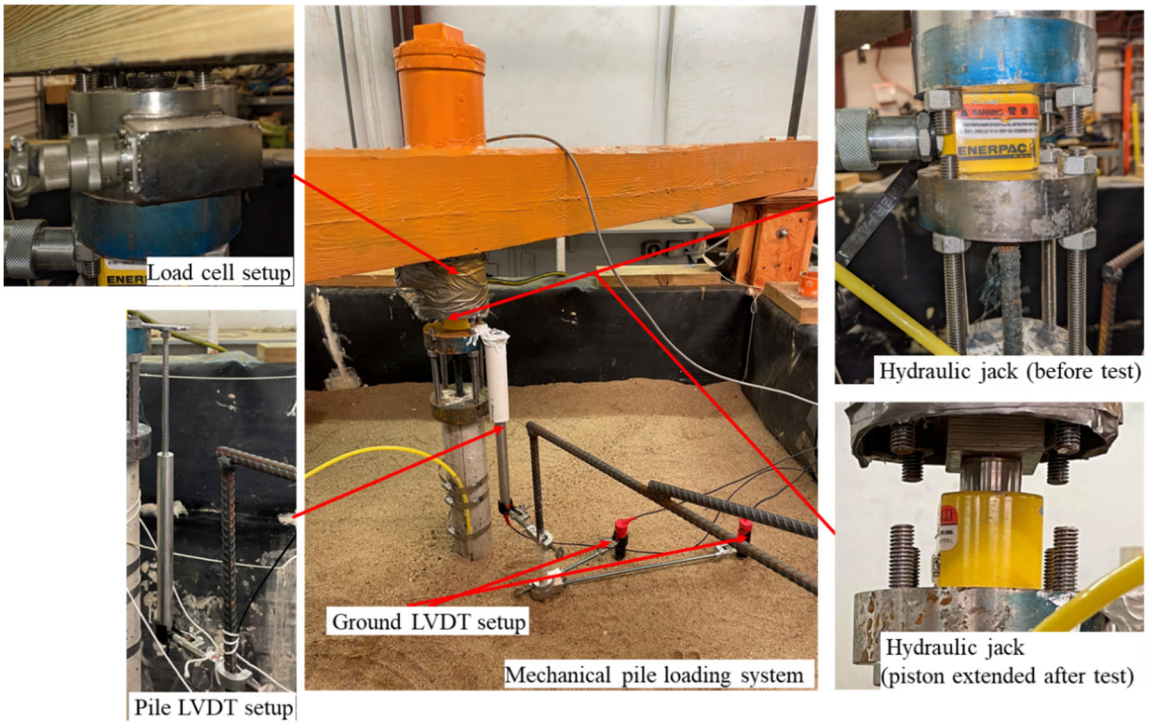

Figure 4.2. Pile load testing setup

4.3.1.1. Results and discussion

Figure 4.3 shows the measured load settlement curve. From the pile load test, the ultimate capacity was calculated using Davisson's method equal to 10.74 kN, which was about three times that of the ultimate capacity calculated using analytical methods equal to 3.65 kN. Figure 4.4 (a) shows the temporal variation of strain during the pile load testing. The axial force profile, as shown in Figure 4.4 (b), was calculated up to 0.45 m depth from ground level from the vertical strain values at the end of the first loading as the subsequent variations in strain for reloading were similar. The axial force values below 0.45 m depth were linearly extrapolated using the data points at 0.30 m and 0.45m depths shown by dashed lines in Figure 4.4 (b). The axial force variation shows that all the load was taken by the skin resistance as the force at the bottom of the pile was 0 kN.

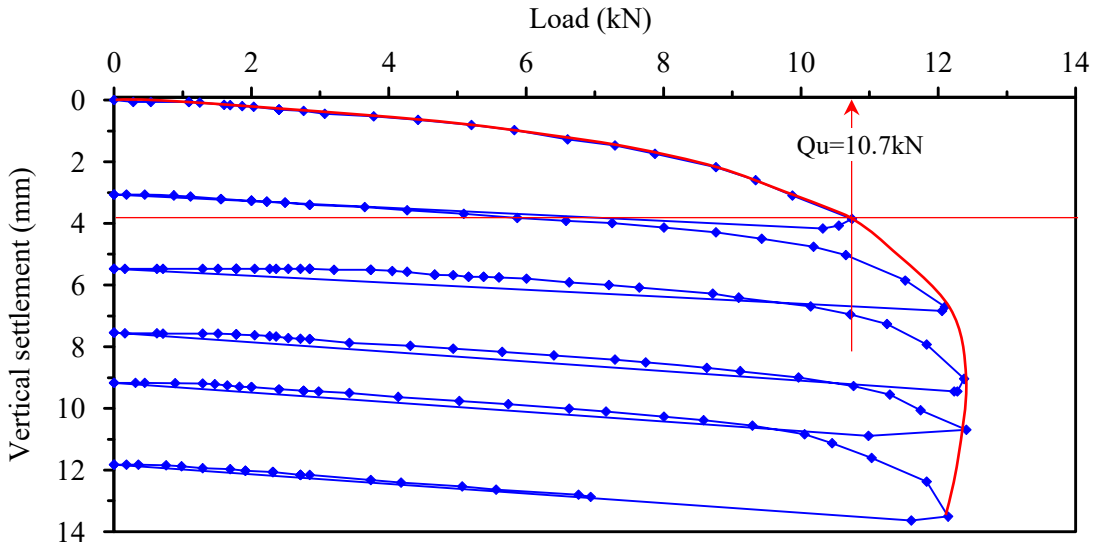

Figure 4.3. Measured load-settlement curves

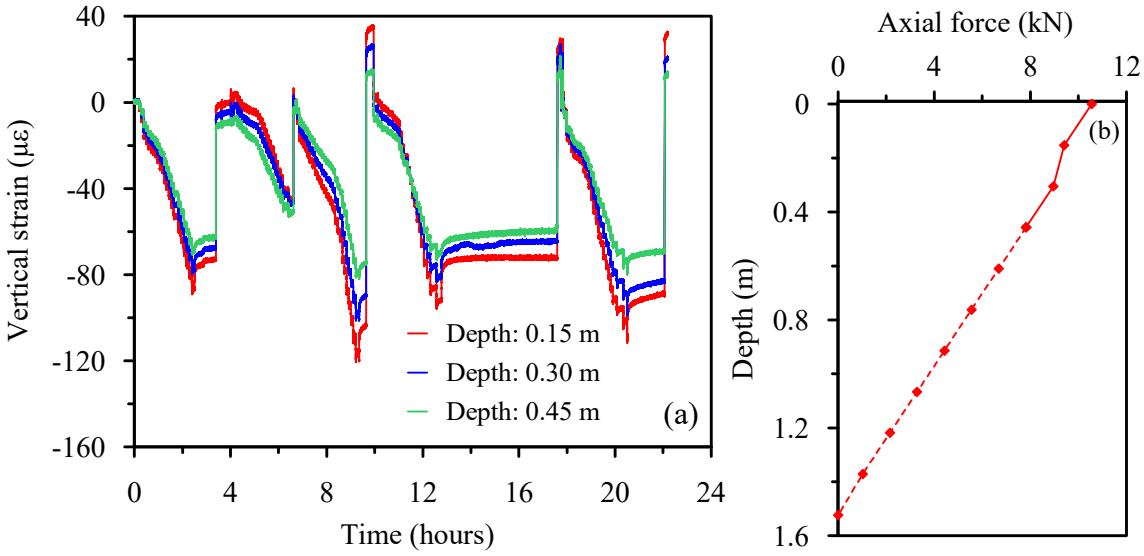

Figure 4.4. (a) Temporal variation of strain and (b) axial force distribution in the drilled shaft during static pile load testing

4.3.2. Hydrodynamic pile load testing under hydroclimatic load

The drilled shaft 76 mm diameter and 1.52 long drilled shaft in Test Sand was subjected to a constant mechanical load equal to the estimated ultimate bearing capacity of 10.7 kN and varying hydroclimatic loads, low-, medium, and high-intensity rainfall. Configuration 3, resulting from Proof OF Concept (POC) tests from Chapter 3, was used. Table 4.2 shows the design parameters for simulating low, medium, and high-intensity rainfall. The spray angle, flow rate capacity, and pressure were obtained from Spraying Systems Co. (2023). The spray height was calculated using basic trigonometry to achieve the desired theoretical spray area. The actual spray area and effective coverage were calculated based on POC tests. The rainfall intensities were measured as the volume of water collected from the nozzles and added together. The rainfall was applied, as shown in Figure 4.5.

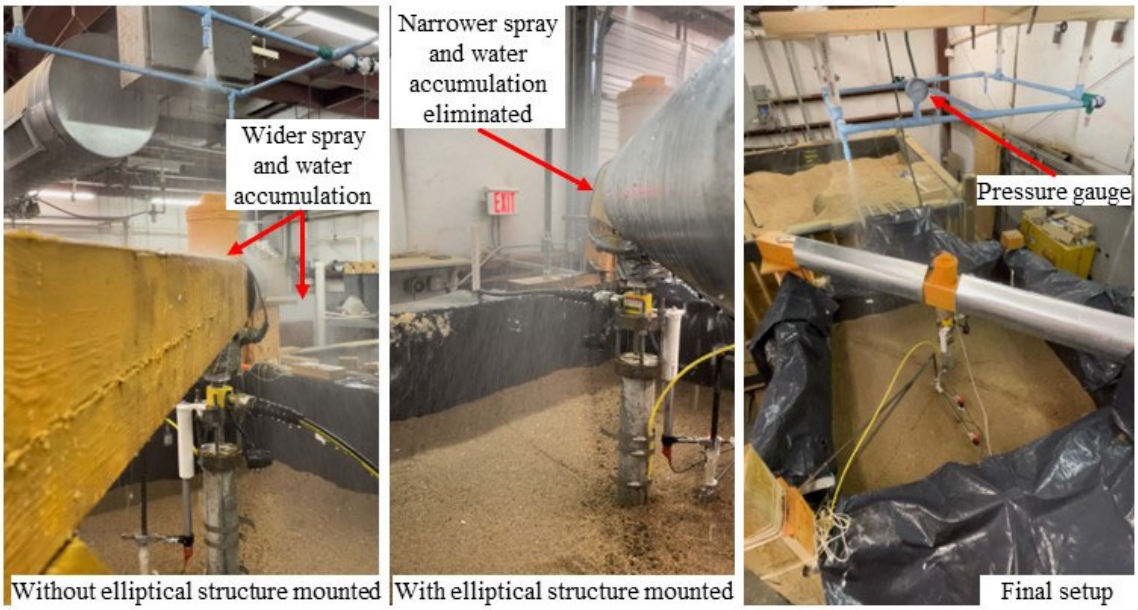

Figure 4.5. Rainfall application

Table 4.2. Design parameters for rainfall simulation

Rainfall type	Model	Spray angle, degrees	Flow rate capacity, l/min	Pressure,	Spray height, m (ft)	Theoretical spray area	Actual spray area	Effective coverage (%)	Intensity, m/day
Low	3.6SQ nozzle*	42.77*	1.26*	68.95 (10)*	1.52 (5)	1.19 x 1.19 sq. m	0.61 x 61 sq. m	83.65	4.45
	5Cone nozzle*	55*	1.89*	68.95 (10)*	1.52 (5)	1.58 m	0.94 m		
Medium	3.6SQ nozzle*	52*	1.89*	137.89 (20)	1.22 (4)	1.19 x 1.19 sq. m	0.61 x 61 sq. m	78	5.98
	5Cone nozzle*	65*	2.661*	137.89 (20)*	1.22 (4)	1.52 m	0.91 m		
High	3.6SQ nozzle*	50.33*	2.57*	275.79 (40)*	1.52 (5)	1.43 x 1.43 sq. m	0.73 x 0.73 sq. m	100	7.70
	5Cone nozzle*	63*	3.59*	275.79 (40)*	1.52 (5)	1.86 m	1.11 m		

* Spraying Systems Co. (2023)

4.3.2.1 Results and discussion

This section discusses the results obtained for the hydroclimatic pile load tests, including drilled shaft subjected to low, medium, and high-intensity rainfall and their comparison. Figures 4.6 (a-g) show the temporal and spatial variation of DOS for low-intensity rainfall. The moisture sensors with odd numbering (Example: M21) are located at the soil-pile interface and even numbering at 0.38 m away from the center of the drilled shaft. It can be observed that before rainfall, the DOS was around 4% to 20%; during rainfall, the DOS reaches around 32% to 58%, and at the end of gravity drainage at 24 hours, the DOS drops in the range of 7% to 24%. The wetting front reaches the pile bottom in approximately 1.5 hours of rainfall, as seen in Figure 3.6 (g).

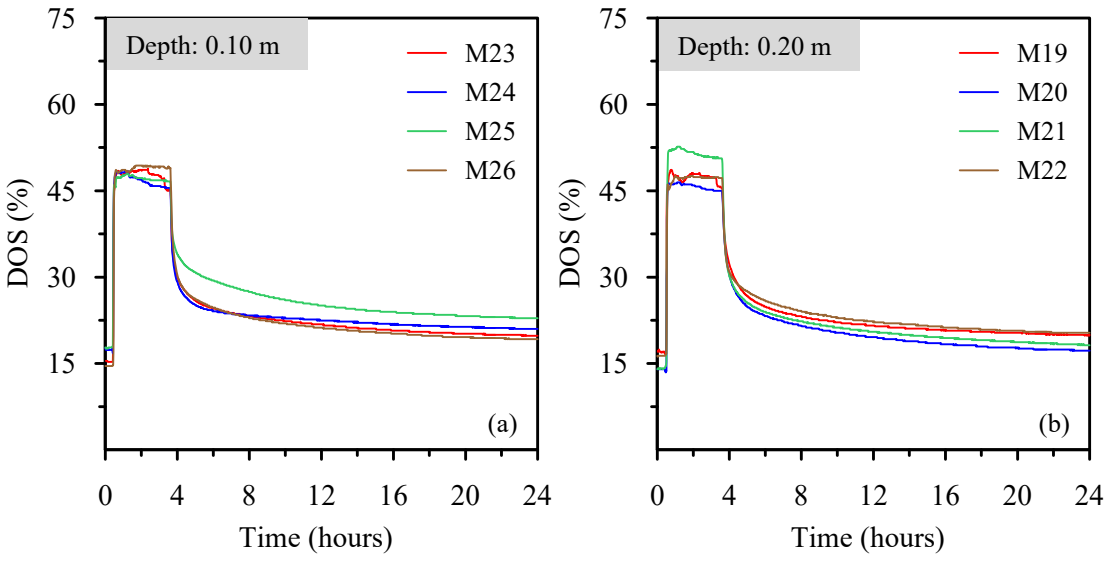

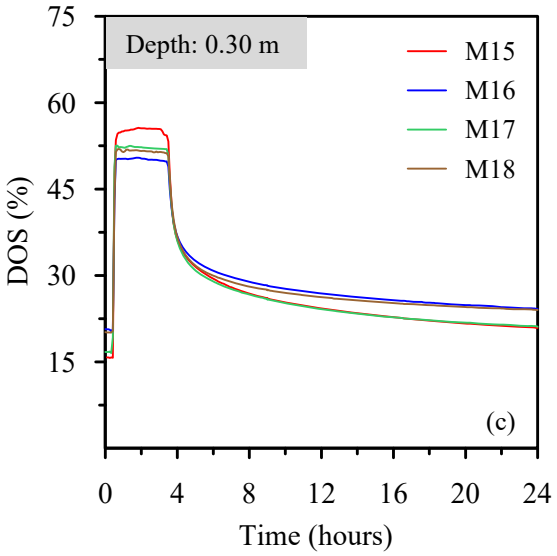
Depth: 0.30 m
M15
M16
M17
M18
DOS (%)
Time (hours)
(c)

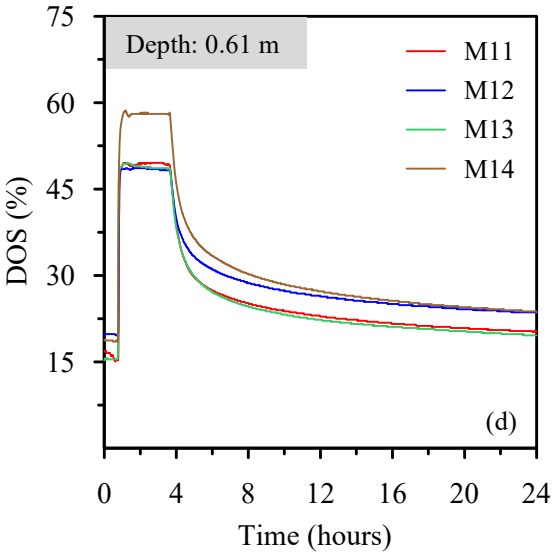
Depth: 0.61 m
M11
M12
M13
M14
DOS (%)
Time (hours)
(d)

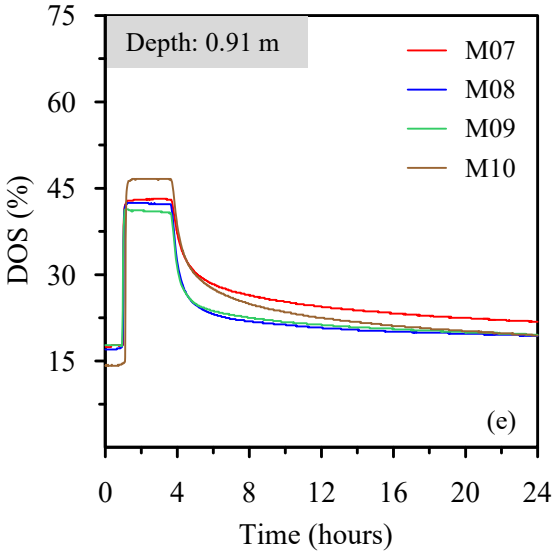
Depth: 0.91 m
M07
M08
M09
M10
DOS (%)
Time (hours)
(e)

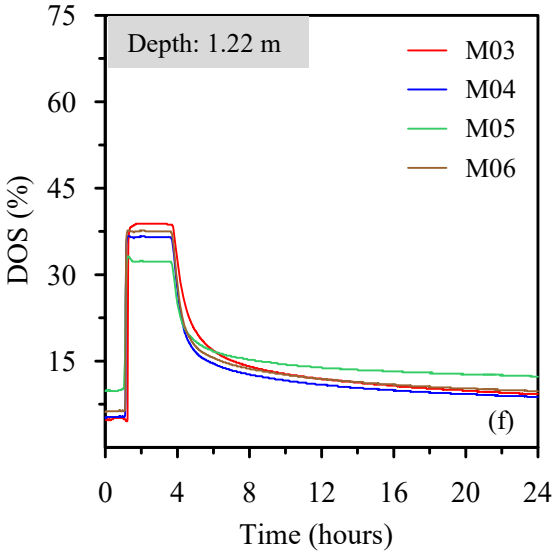
Depth: 1.22 m
M03
M04
M05
M06
DOS (%)
Time (hours)
(f)

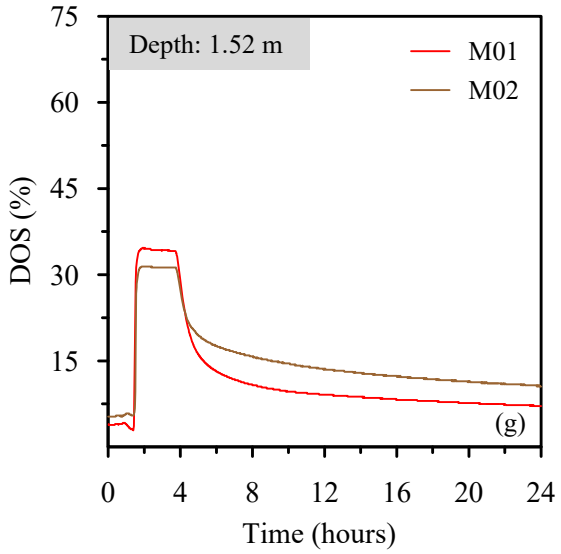

Figure 4.6. Temporal variation of the degree of saturation (a) 0.10 m, (b) 0.20 m, (c) 0.30 m, (d) 0.61 m, (e) 0.91 m, (f) 1.22 m (g) 1.52 m depths from ground level for low-intensity rainfall in the experiment

Figures 4.7 (a-g) show the temporal and spatial variation of DOS for medium-intensity rainfall. It can be observed that before rainfall, the DOS was observed to be around 5% to 21%; during rainfall, the DOS reaches 35% to 61%, and at the end of gravity drainage at 24 hours, the DOS drops in the range of about 7.5% to 24.5%. The wetting front reaches the pile bottom in approximately 1.4 hours of rainfall, as seen in Figure 4.7 (g). Hence, during rainfall, the DOS was about 3% higher for medium-intensity rainfall compared to low-intensity rainfall.

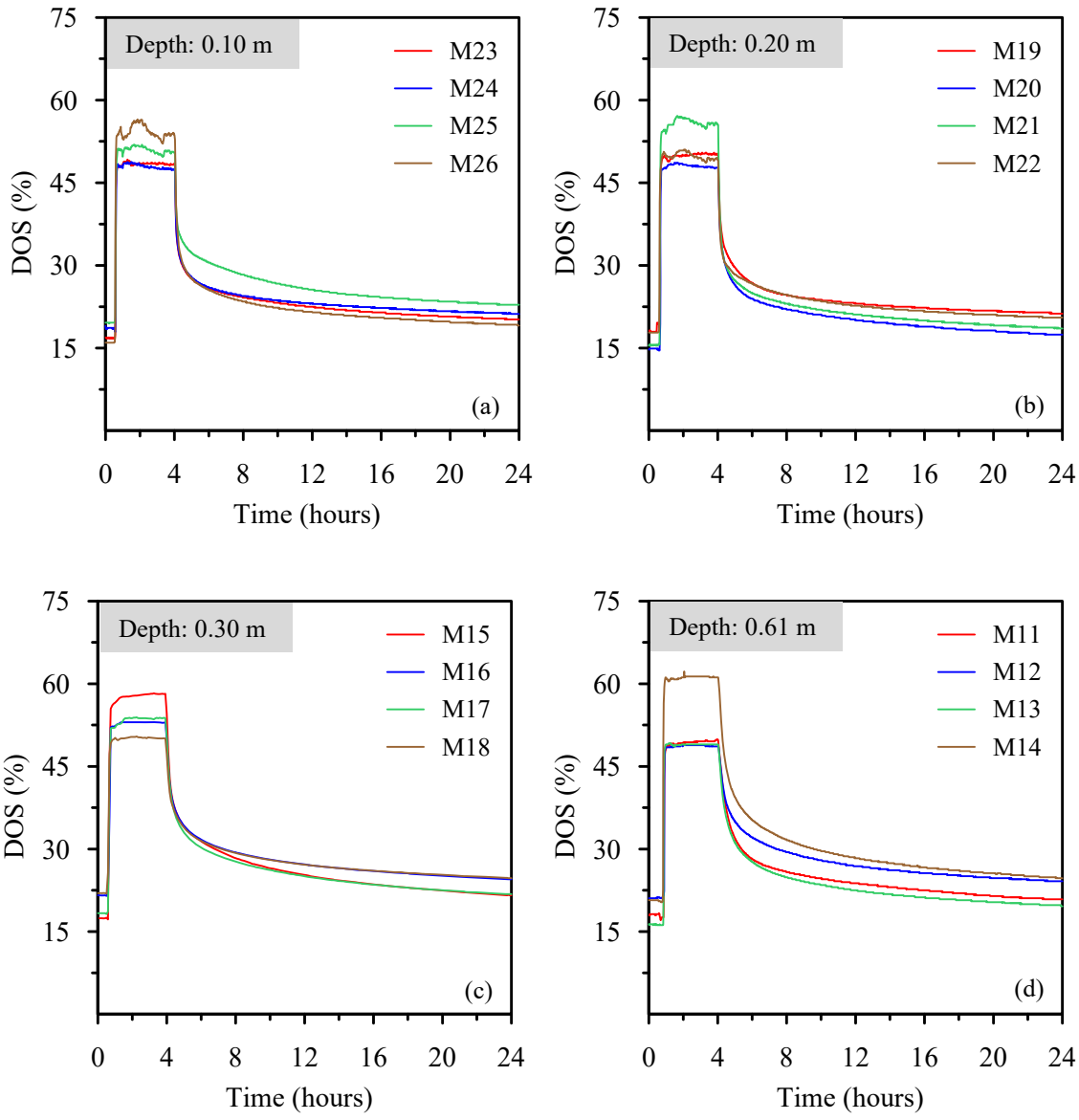
Depth: 0.10 m
M23
M24
M25
M26
(a)
Depth: 0.20 m
M19
M20
M21
M22
(b)
Depth: 0.30 m
M15
M16
M17
M18
(c)
Depth: 0.61 m
M11
M12
M13
M14
(d)
DOS (%)
Time (hours)
75
60
45
30
15
0
4
8
12
16
20
24

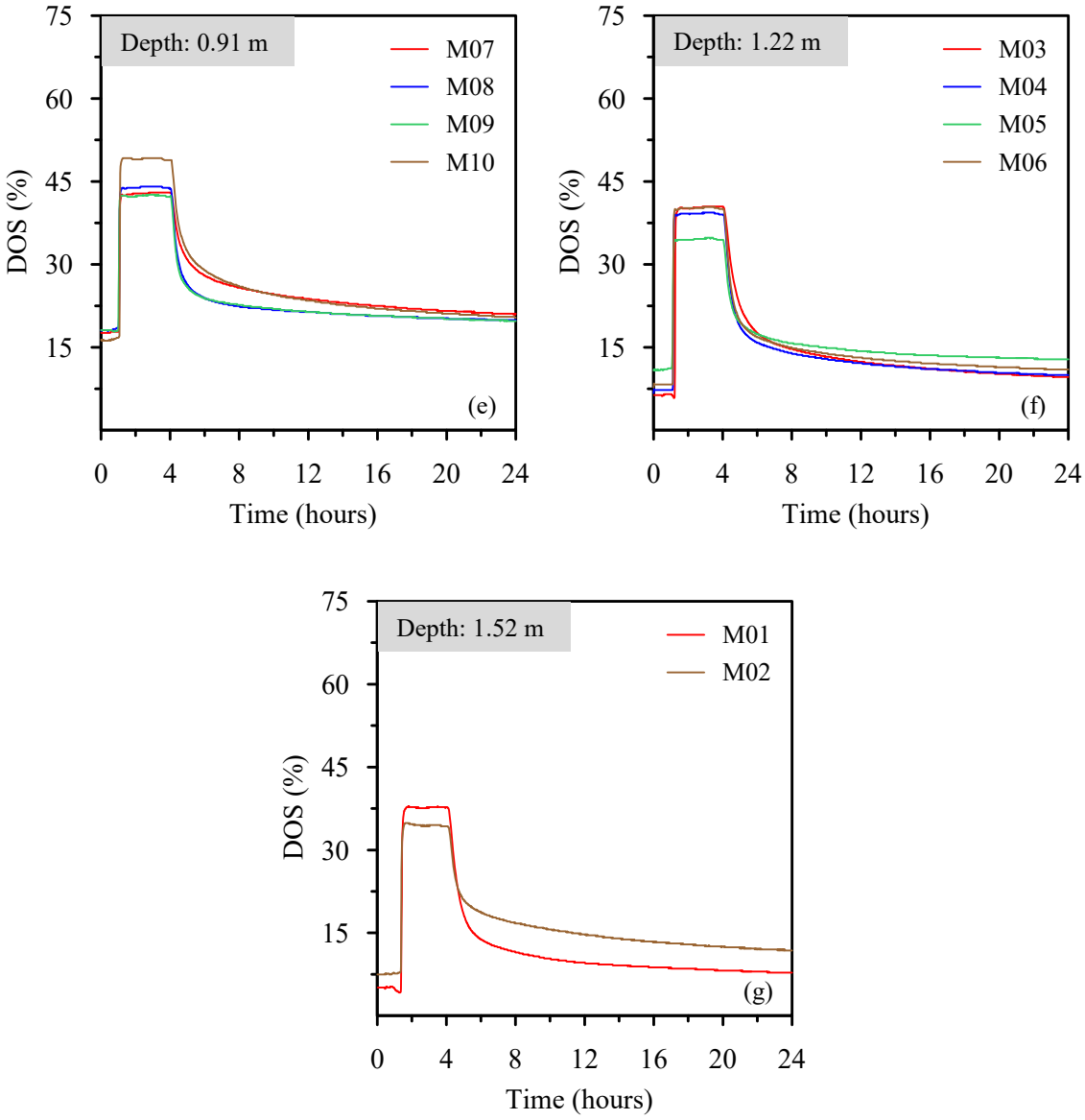

Figure 4.7. Temporal variation of the degree of saturation (a) 0.10 m, (b) 0.20 m, (c) 0.30 m, (d) 0.61 m, (e) 0.91 m, (f) 1.22 m (g) 1.52 m depths from ground level for medium-intensity rainfall in the experiment

Figures 4.8 (a-g) show the temporal and spatial variation of DOS for high-intensity rainfall at different depths. It can be observed that before rainfall, the DOS was observed to be around 5% to 21%; during rainfall, the DOS reaches 38% to 63%, and at the end of gravity drainage at 24 hours, the DOS drops in the range of about 7.5% to 24.5%. The

wetting front reaches the pile bottom in approximately 1.2 hours of rainfall, as seen in Figure 4.8 (g). Hence, during rainfall, the DOS was about 3% higher for the higher-intensity rainfall compared to the medium-intensity rainfall and 6% higher than the low-intensity rainfall.

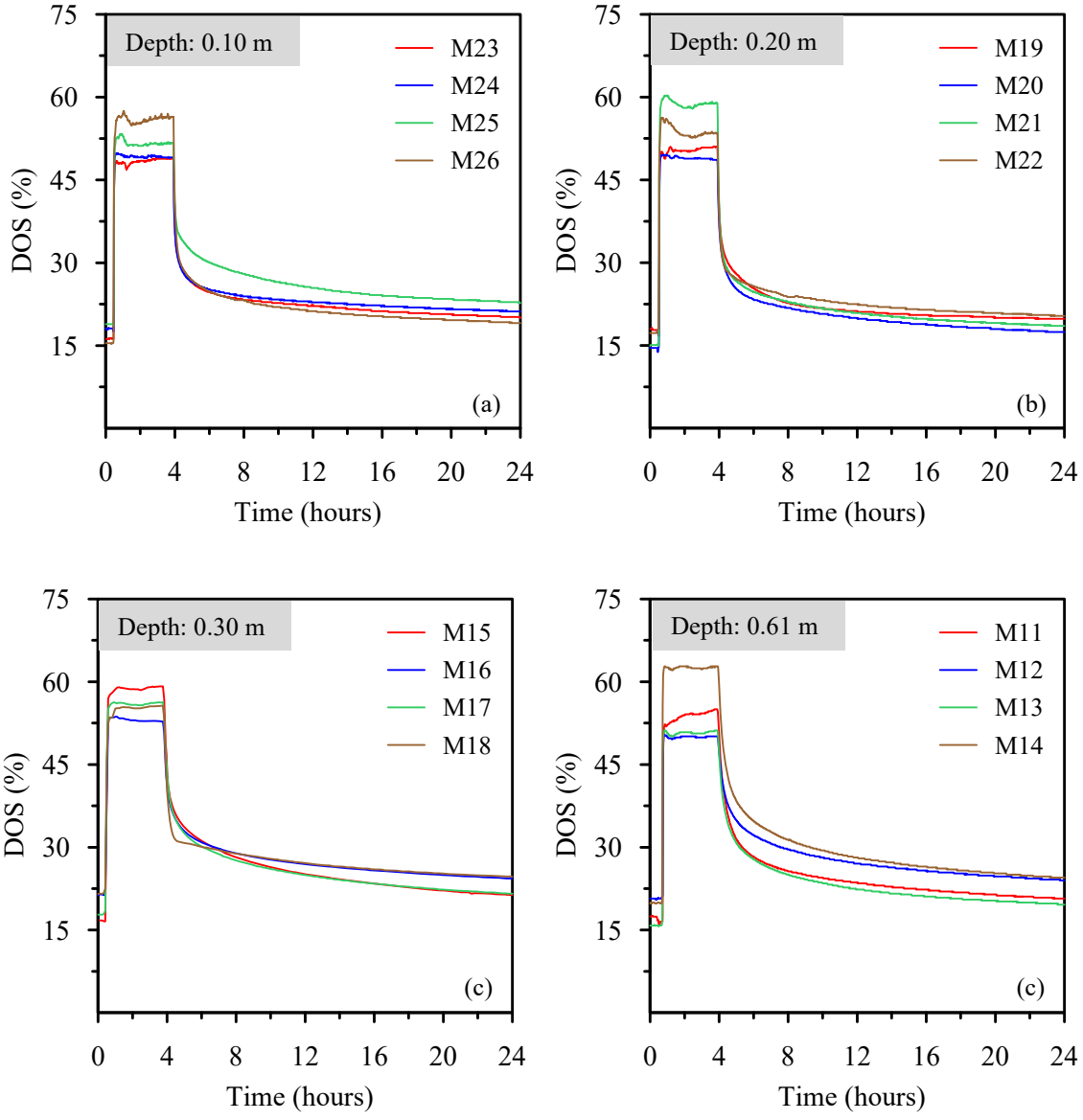

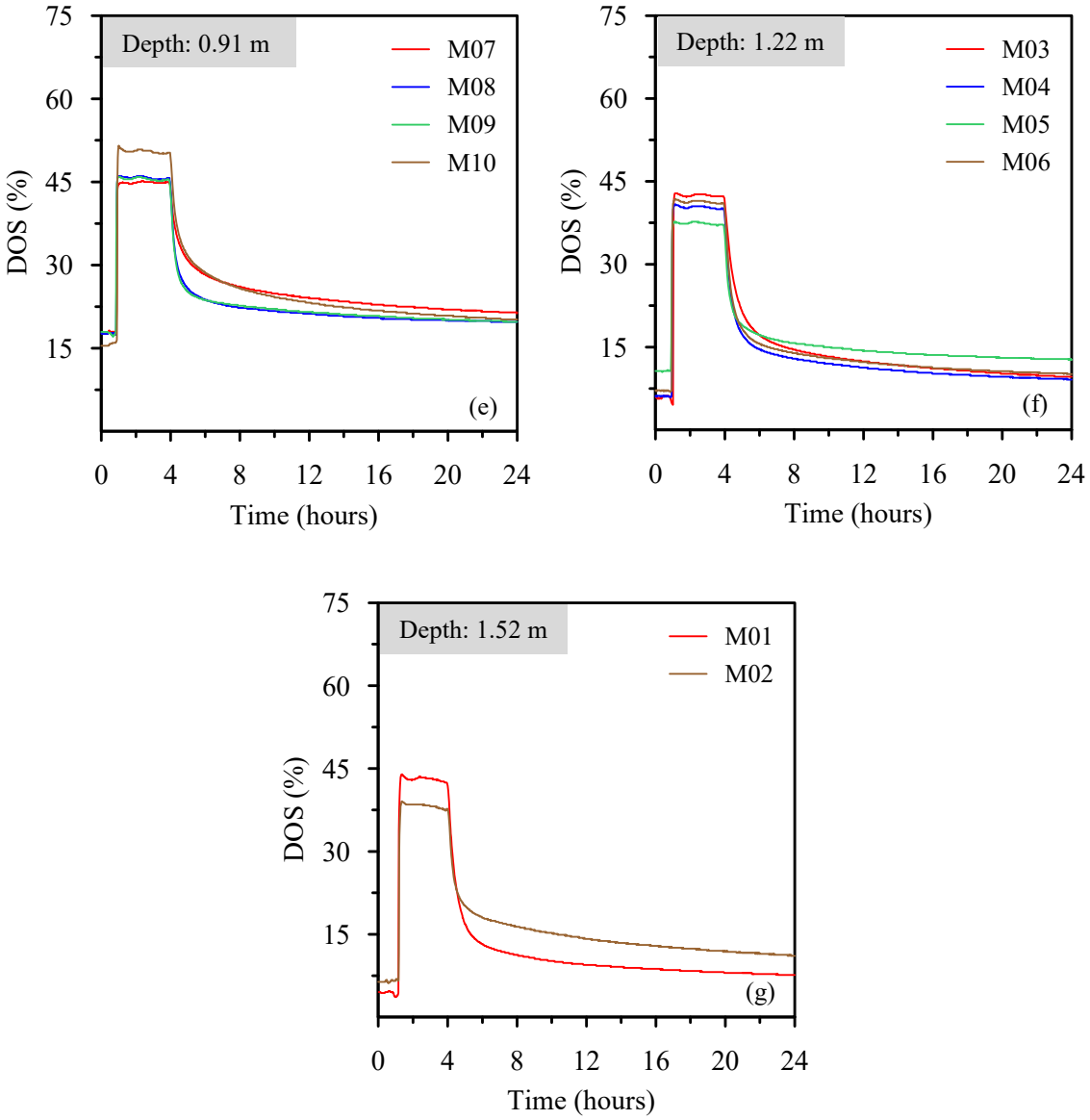

Figure 4.8. Temporal variation of the degree of saturation (a) 0.10 m, (b) 0.20 m, (c) 0.30 m, (d) 0.61 m, (e) 0.91 m, (f) 1.22 m (g) 1.52 m depths from ground level for high-intensity rainfall in the experiment

Figures 4.9-4.11 show the spatial variation of the DOS for the low-, medium-, and high-intensity rainfall. To obtain the DOS profiles during rainfall for the low-, medium-, and high-intensity rainfall, maximum values of DOS from the corresponding DOS temporal variations were used. It can be observed that the DOS profiles are uniform up to

the depth of 0.6 m from ground level and then reduces up to the bottom of the pile, i.e., at 1.52 m from ground level. This decrease in DOS is attributed to the initial mechanical pile load tests conducted, which may have disturbed the soil around the EC-5 moisture sensors. Mechanical loading of the pile could have caused the compacted soil to dilate, causing disturbance to the moisture sensors. The above-mentioned observation is for the three rainfall cases, i.e., low-, medium-, and high-intensity rainfall.

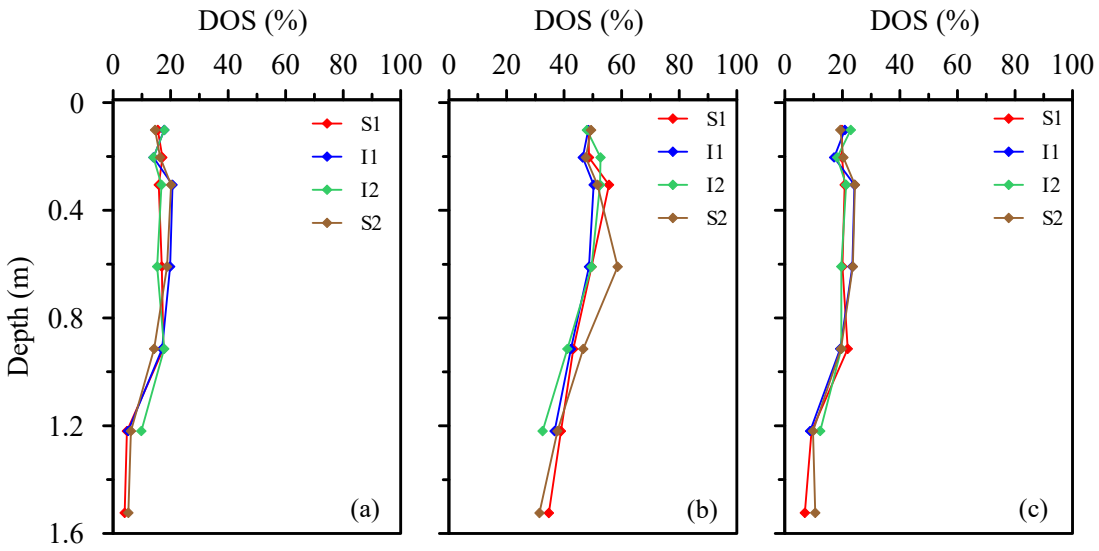

Figure 4.9. Spatial variation of the degree of saturation (a) before, (b) during, and (c) after low-intensity rainfall in the experiment

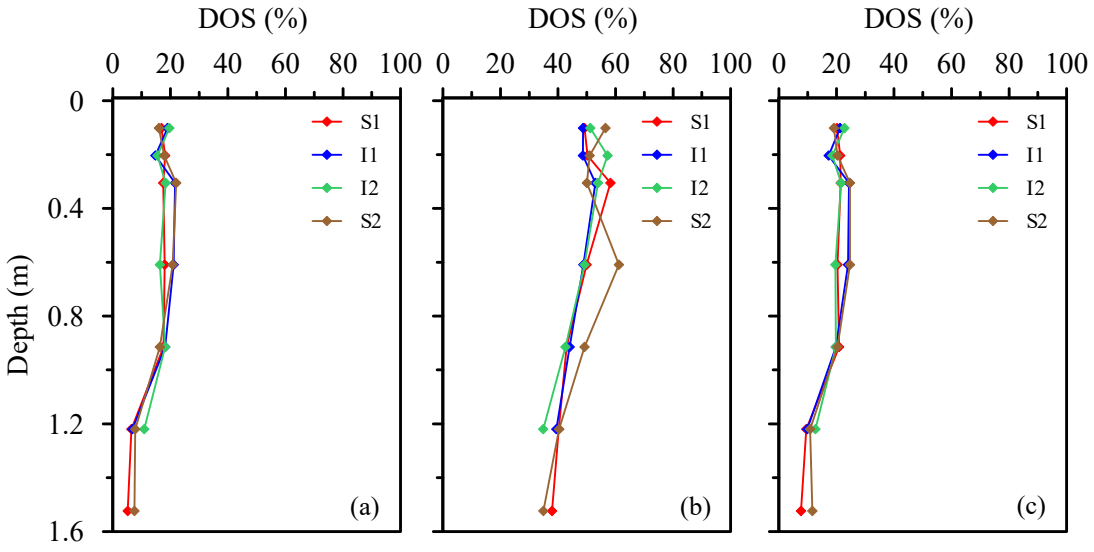

Figure 4.10. Spatial variation of the degree of saturation (a) before, (b) during, and (c) 24 hours after medium-intensity rainfall in the experiment

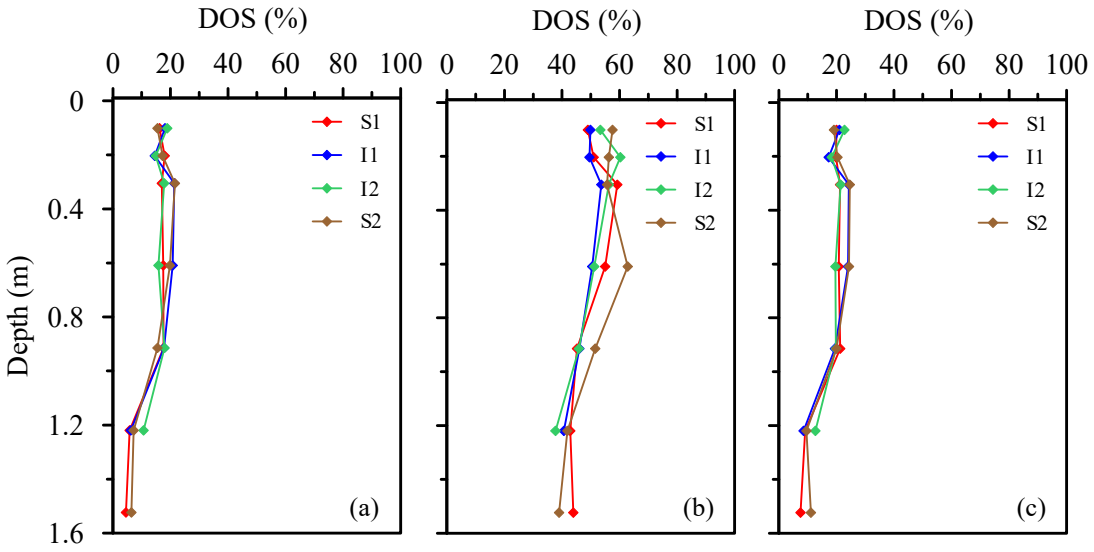

Figure 4.11. Spatial variation of the degree of saturation (a) before, (b) during, and (c) 24 hours after high-intensity rainfall in the experiment

There were several inconsistencies observed in the readings from the EC-5 moisture sensors at depths of 0.91 m, 1.22 m, and 1.52 m. Some sensors provided negative and

unreasonably high volumetric water content (VWC) readings which led to incorrect Degree Of Saturation (DOS) calculations. This can be attributed to the following reasons:

1. Possible disturbance to the sensors during the pile load testing.
2. Placing sensors too close to the pile.
3. Poor calibration.

These issues cause the moisture sensors to be subjected to air which has a dielectric constant of 0. Also, one of the sensors at 1.22 m depth gave unreasonably high volumetric water content values, which means that the moisture sensor was subjected to mostly water as water has a high dielectric constant of 80. The VWC is measured indirectly by the moisture sensors by calibrating the sensors for a non-linear relationship between the VWC and the dielectric constant (k). An error of 1-2% means that the generic VWC-k equation used by the manufacturers does not match with our soil, i.e., calibration is needed. However, the high magnitude of negative and positive VWC occurs because of disturbance to the sensors and placing sensors too close to the pile. Hence due to the above-stated reasons, the moisture sensors provided an unreasonably high, negative, and unrealistic degree of saturation values which were calculated from VWC. The calibration can be done for specific soils by using the homogenized soil method. The Topp et al. 1980 equation can be used for this purpose. For this study, negative values of DOS were entered as zero or linearly extrapolated. At depths below 0.6 m, a decrease in DOS was observed for all the cases in Figures 3.9-3.11. This decrease is attributed to the disturbance of the moisture sensors caused by the initial multiple mechanical pile load tests. These pile load tests may

have caused dilation of the compacted soil, thereby disturbing the soil around the moisture sensors. For ensuring steady-state flow, the inflow and outflow for the medium-intensity rainfall were measured to be the same, which was approximately 10 liters/minute.

Figure 4.12 shows the temporal variation of mechanical load for low, medium, and high-intensity rainfall. It can be seen that mechanical load drops by about 0.3 kN during rainfall for low and medium intensity rainfall and by 0.6 kN for high-intensity rainfall and then stays the same during gravity drainage for low intensity, slightly increases for medium-intensity rainfall, and decreases further for high-intensity rainfall. A significant fluctuation of the mechanical load is observed during gravity drainage for the three cases. Most of the decay in mechanical load is attributed to creep in the soil and less to rainfall.

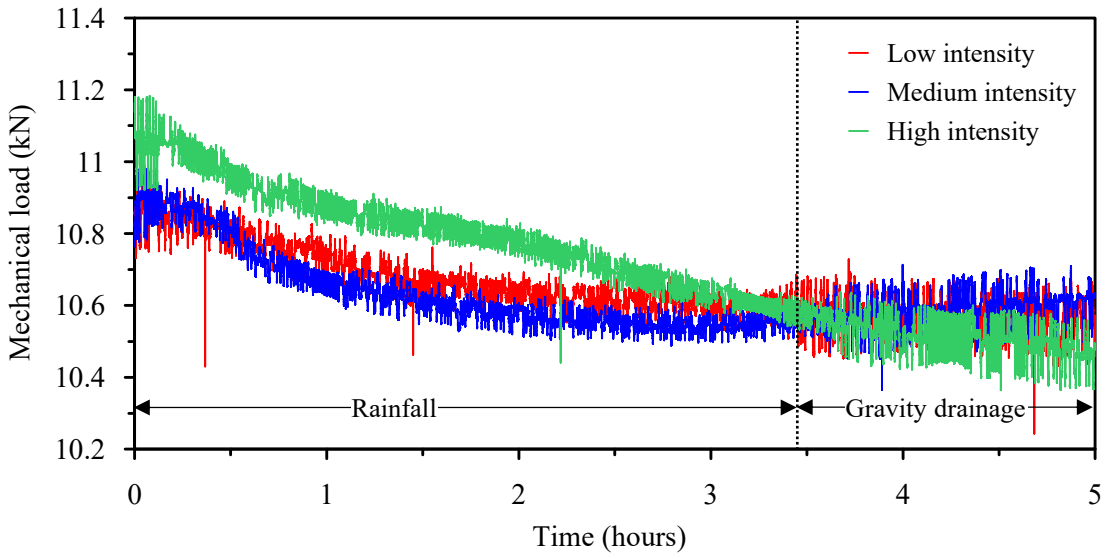

Figure 4.12. Temporal variation of mechanical load for low-intensity, medium-intensity, and high-intensity rainfall in the experiment

Figure 4.13 shows the temporal variation of vertical displacement of pile and ground for the low-, medium-, and high-intensity rainfall. For the low-intensity rainfall,

the upward vertical displacement of the top of the drilled shaft and ground surface at 0.25 m away from the pile center by 0.7 mm is observed, which continues until approximately 1 hour of rainfall. Then a small settlement of 0.3 mm of the pile is observed, followed by more pile settlement during gravity drainage. The ground at 0.5 m away from the pile center settles by 0.9 mm after 0.15 hours of rainfall, and then gradual upward vertical displacement up to 1.5 mm is observed until the end of rainfall.

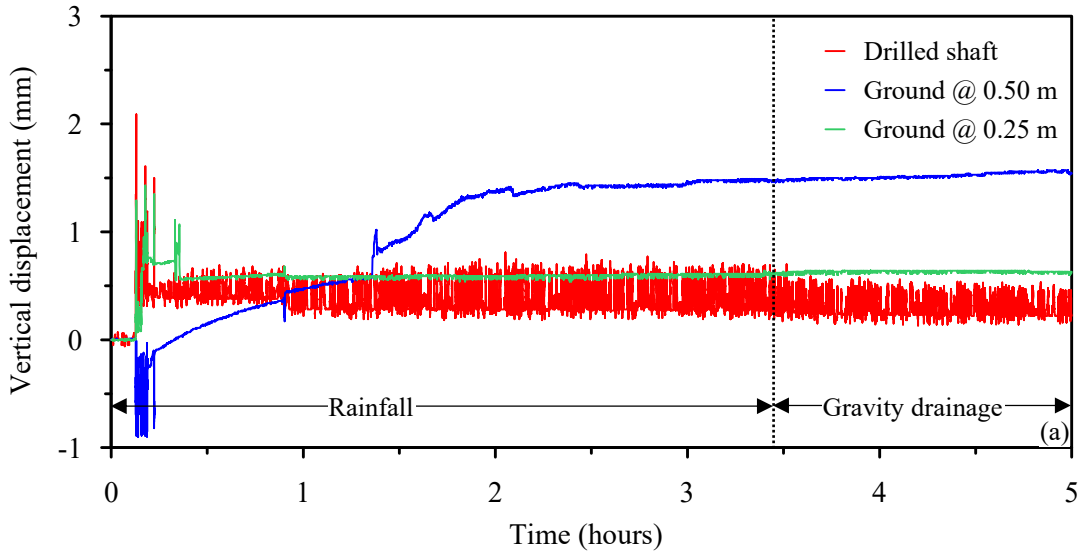

For medium-intensity rainfall, similar behavior of pile and ground surface is observed as the low-intensity rainfall. During rainfall, the upward vertical displacement of the top of the drilled shaft by 0.4 mm, the upward vertical displacement of the ground surface 0.25 m away from drilled shaft center by 0.9 mm, and the upward vertical displacement of the ground surface at 0.5 m away from drilled shaft center by 1.3 mm are observed. By the end of gravity drainage, the drilled shaft settles by 0.2 mm, the ground surface near drilled shaft displaces vertically upward more by 0.1 mm and then settles by

0.08 mm, and the ground surface away from drilled shaft displaces vertically upward more by 0.4 mm, reaching a total upward vertical displacement of 1.7 mm.

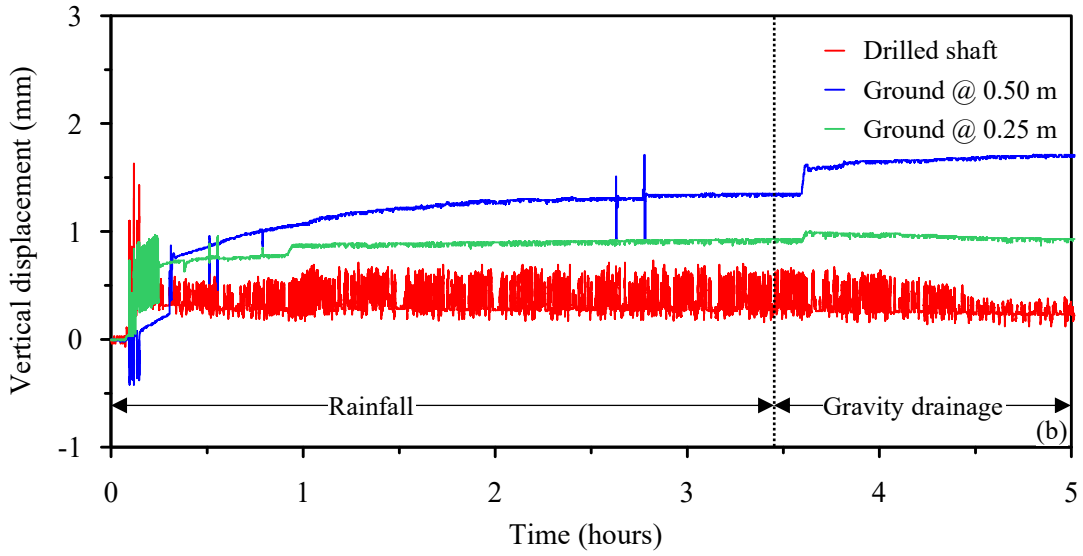

For the high-intensity rainfall, similar behavior of drilled shaft and ground surface is observed as in the low and medium-intensity rainfall cases. During rainfall, the upward vertical displacement of the top of the drilled shaft by 0.65 mm, the upward vertical displacement of the ground surface 0.25 m away from the drilled shaft center by 1.3 mm, and the upward vertical displacement of the ground surface at 0.5 m away from the drilled shaft center by 0.9 mm is observed. By the end of gravity drainage, the drilled shaft settles by 0.1 mm, the ground surface near the drilled shaft settles by 0.6 mm, and the ground surface away from the drilled shaft settles by 0.1 mm.

Hence, at the end of 24 hours, the top of the drilled shaft displaces vertically upward by 0.4 mm for low and medium-intensity rainfall and by 0.55 mm for high-intensity rainfall, the ground surface at 0.25 m away from drilled shaft center displaces vertically

upward by 0.4 mm for low-intensity rainfall, 0.9 mm for medium intensity rainfall, and 0.7 mm for high-intensity rainfall, and the ground surface 0.35 m away from drilled shaft center displaces vertically upward by 1.5 mm for low-intensity rainfall, 1.7 mm for medium intensity rainfall, and 0.8 for high-intensity rainfall. Overall, the permanent top of the drilled shaft and ground surface upward vertical displacement is observed for the three cases. The combined effect of pile settlement due to the creep and upward vertical displacement due to rainfall should be considered in future studies.

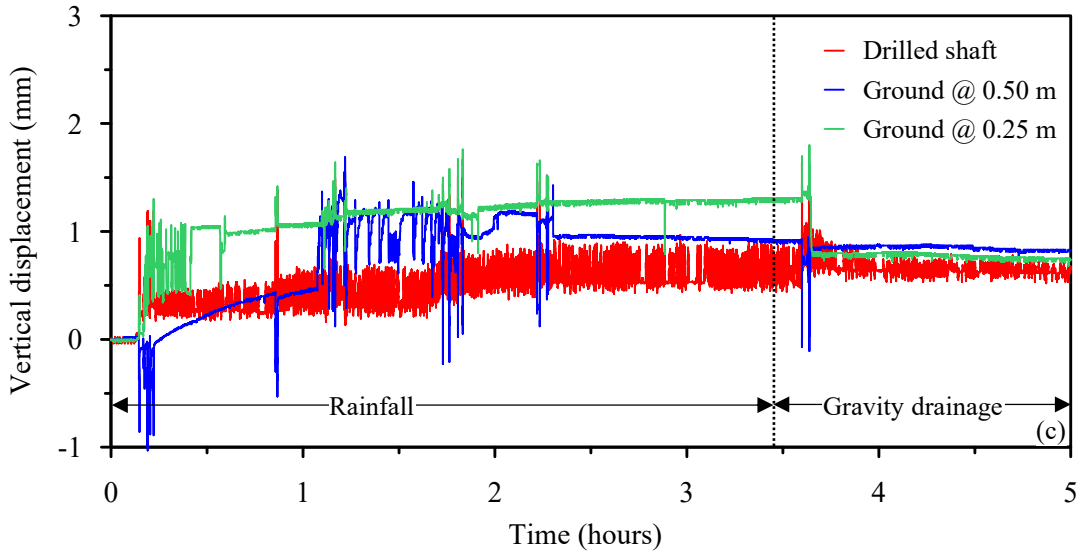

Figure 4.13. Temporal variation of vertical displacement for (a) low-intensity, (b) medium-intensity, and (c) high-intensity rainfall in the experiment

Figure 4.14 shows the temporal variation of vertical strain in the pile. Compressive strains are induced in the drilled shaft due to the upward vertical displacement of the top of the drilled shaft caused by the upward vertical displacement of the surrounding soil. On the other hand, tensile strains are induced in the drilled shaft due to the settlement of the drilled shaft caused by the settlement of surrounding soil. For the low-intensity rainfall,

initially, slight compressive strains of about 2με are induced in the drilled shaft within approximately 0.8 hours of rainfall, and tensile strains of about 7 to 9 με are immediately induced until the end of rainfall. Hence, slight upward vertical displacement of the top of the drilled shaft is observed until 0.8 hours of rainfall, followed by settlement until the end of rainfall. For medium-intensity rainfall, compressive strains are induced until the end of rainfall, followed by an increase in tensile strains during gravity drainage. For high-intensity rainfall, behavior similar to medium-intensity rainfall is observed. Hence, upward vertical displacement of the top of the drilled shaft is observed until the end of rainfall, and settlement of the top of the drilled shaft is observed during gravity drainage for medium- and high-intensity rainfall.

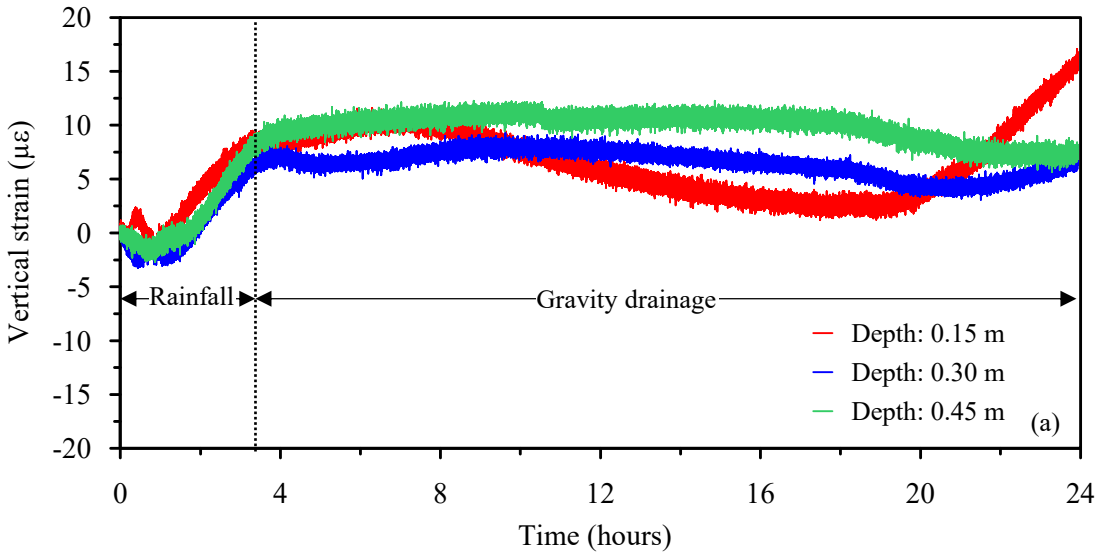

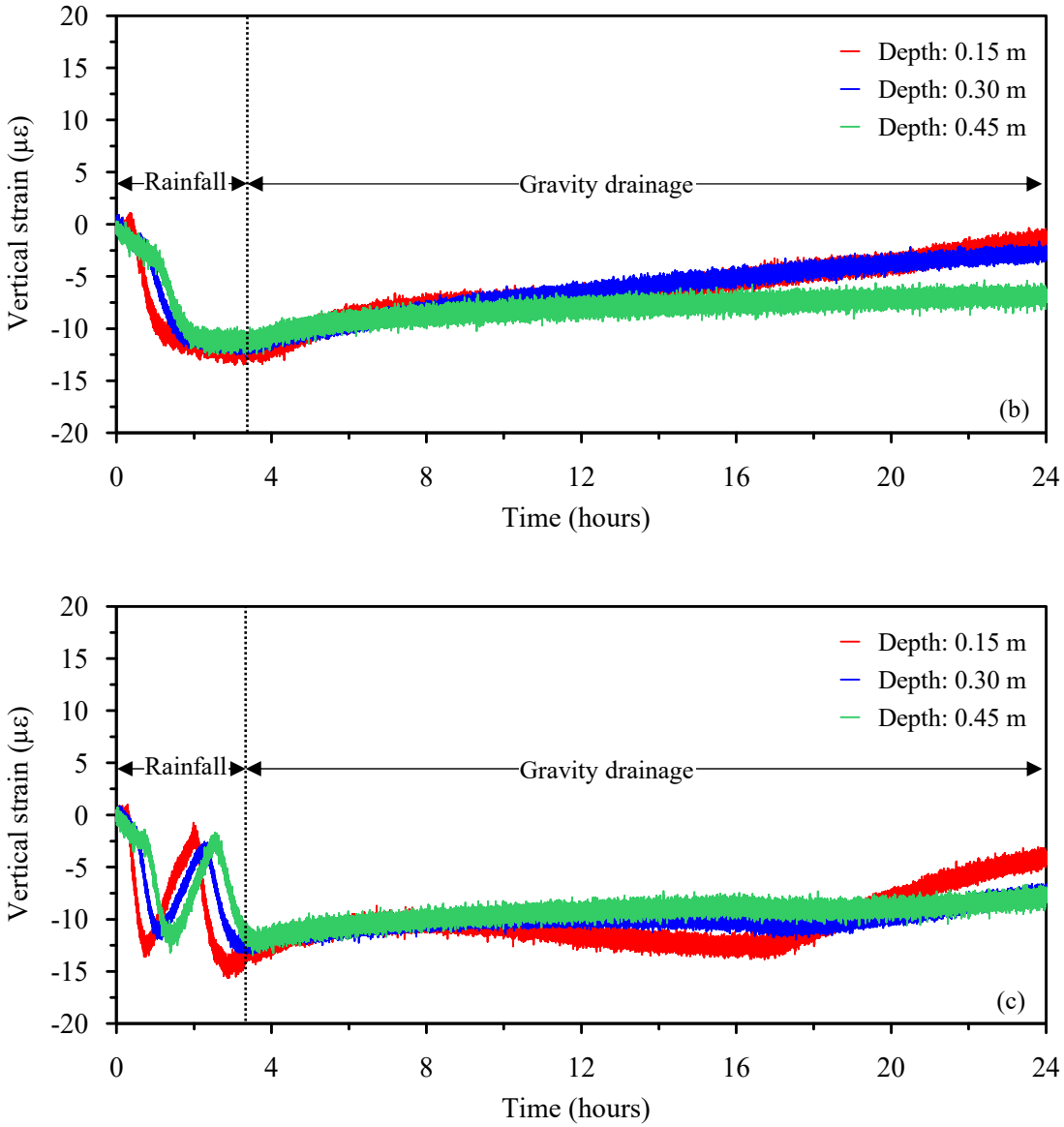

Figure 4.14. Temporal variation of vertical strain in the drilled shaft at various depths for (a) low-intensity, (b) medium-intensity, and (c) high-intensity rainfall in the experiment

Figure 4.15 shows the spatial variation of axial force before, during, end of rainfall and 24 hours after rainfall (end of gravity drainage) for low-, medium-, and high-intensity rainfall. The axial force values up to 0.45 m depth were calculated from the vertical strain values from FBG sensors for before, during, and after rainfall cases. The axial force values

below 0.45 m depth were linearly extrapolated using the data points at 0.30 m and 0.45m depths, shown by dashed lines in Figure 4.15. For low-intensity rainfall, after 1.35 hours of rainfall, the axial force slightly decreases up to 0.45 m depth and increases below this depth. At the end of rainfall, the axial force increases up to 0.45 m depth and then increases more up to the bottom of the drilled shaft. At 24 hours, there is a significant increase in axial force at 0.15 m depth. An overall increase in the axial force is seen at 24 hours. Hence up to 0.45 m depth, the axial force decreases slightly during rainfall and then increases until the end of gravity drainage. This is caused by initial compressive strains during rainfall, as seen in Figure 4.14 (a), followed by an increase in the tensile strains until the end of gravity drainage. This behavior is also confirmed in Figure 4.13 (a), where slight initial upward vertical displacement followed by settlement of the top of the drilled shaft during gravity drainage is seen.

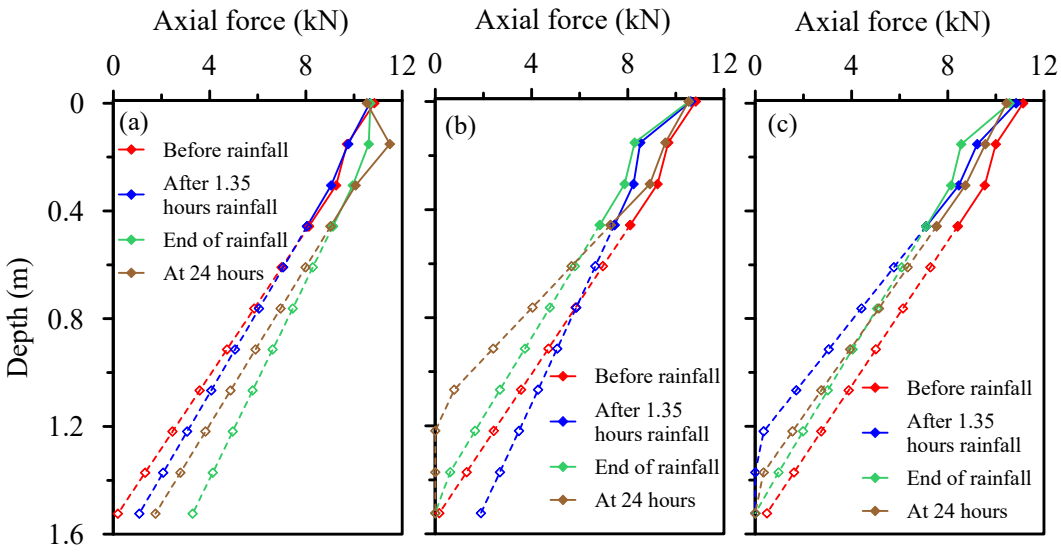

Figure 4.15. Spatial variation of axial force at various time intervals for (a) low-intensity rainfall, (b) medium-intensity rainfall, and (c) high-intensity rainfall in the experiment

For medium-intensity rainfall, after 1.35 hours of rainfall, the axial force decreases significantly up to 0.75 m depth and then increases below this depth. At the end of rainfall, the axial force decreases more than during rainfall up to the bottom of the drilled shaft. At 24 hours, an increase in the axial force up to 0.45 m depth and then a significant decrease in axial force up to the bottom of the drilled shaft is seen. Hence up to 0.45 m depth, the axial force decreases during rainfall and continues to decrease until the end of rainfall, followed by an increase until the end of gravity drainage. This is caused by the increase in compressive strains until the end of rainfall, followed by an increase in tensile strains until the end of gravity drainage, as seen in Figure 4.14 (b). This behavior is also confirmed in Figure 4.13 (b), where upward vertical displacement of the top of the drilled shaft is observed until the end of rainfall, followed by settlement of the drilled shaft during gravity drainage is seen.

For high-intensity rainfall, after 1.35 hours of rainfall, the axial force decreases significantly and reaches zero at 1.2 m depth. At the end of rainfall, the axial force decreases more than during rainfall up to 0.45 m depth and then increases more than during rainfall up to the bottom of the drilled shaft. At 24 hours, an increase in the axial force up to 0.45 m depth and then a slight decrease in axial force up to the bottom of the drilled shaft is seen. Hence up to 0.45 m depth, the axial force decreases during rainfall and continues to decrease until the end of rainfall, followed by an increase until the end of gravity drainage. This is caused by an increase in compressive strains until the end of rainfall, followed by an increase in tensile strains until the end of gravity drainage, as seen in Figure 4.14 (c). This behavior is also confirmed in Figure 4.13 (c), where upward vertical

displacement of the top of the drilled shaft is observed until the end of rainfall, followed by settlement of the drilled shaft during gravity drainage is seen. To summarize, upward vertical displacement of the top of the drilled shaft is observed, which increases with the intensity of rainfall, thereby causing a decrease in the axial force, and settlement of the top of the drilled shaft is observed during gravity drainage, which causes an increase in the axial force.

4.4. COUPLED FINITE ELEMENT MODEL AND ITS VALIDATION

The drilled shaft and the deadweight equal to the total ultimate capacity of the drilled shaft representing the mechanical load were modeled using a non-porous linear elastic material. The soil deformation properties change with the flow of water (degree of saturation); hence it is crucial to couple the flow with the soil deformation. A modified Mohr-Coulomb (MMC) model capable of updating the yield criterion and modulus with changes in matric suction and/or degree of saturation (Vickneswaran and Ravichandran 2022) was used to represent the stress-strain behavior of the partially saturated soil in PLAXIS 2D. The flow of water, in general, in the three-phase media is represented by the well-known Richards equation (Dogan and Motz 2005), which is also used in PLAXIS 2D. To define the saturation-suction behavior of soil, there are many Soil Water Characteristic Curves (SWCCs) and corresponding relative hydraulic conductivity functions available in the literature. In this study, the Mualem-van Genuchten model (Mualem 1976; van Genuchten 1980) and the van Genuchten model (van Genuchten 1980) were used for defining the relative hydraulic conductivity functions and the SWCC, which are available

in PLAXIS 2D. The unsaturated hydraulic conductivity (k_{unsat}) is calculated as a product of saturated hydraulic conductivity (k_{sat}) and relative hydraulic conductivity (k_r). The soil properties and groundwater parameters for the Test Sand from Chapter 4 were revised for the relative compaction of 96% and moisture content of 8%. The residual water content was calculated using a residual saturation of 0.17 which was calculated as a median value from the before-rainfall case of the small-scale experiment. A parametric study was conducted by varying the van Genuchten model fitting parameters, ga, and gn (Carsel and Parrish 1988), to achieve similar temporal and spatial variations of the DOS as obtained in the small-scale experiment. Table 4.3 enlists the updated Test Sand properties. Figure 4.16 shows the resulting SWCC for the Test Sand from the parametric study, which was used for the finite element simulations.

Table 4.3. Properties and flow parameters of the Test Sand

General properties	Test Sand
Specific gravity	2.68
Void ratio	0.82
Dry unit weight (kN/m^3)	14.44
Moisture content (%)	8.00
Saturated unit weight (kN/m^3)	18.86
Saturated Young's modulus, E_{soil} (MN/m2)	35.65
Poisson's ratio	0.30
Effective angle of friction, ϕ_{soil} (°)	39.22

Plasticity index (I_P)	-
MMC model parameters	**Test Sand**
α	2.00
β_e	1.00
S (%)	100
Groundwater flow parameters	**Test Sand**
Residual water content, (θ_r)	0.077
Saturated water content, (θ_s)	0.43
Model fitting parameter, g_a (m^{-1})	43.00
Model fitting parameter, g_n	8.11
Saturated hydraulic conductivity (m/day)	21.78

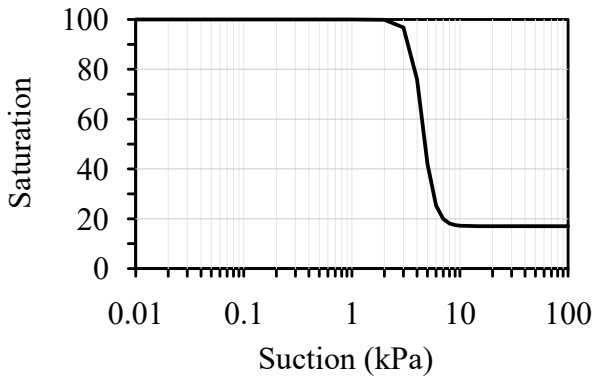

Figure 4.16. SWCC for the Test Sand used for the finite element model

Interface elements were used for accurate modeling of the soil-structure interaction. The interface properties comprise stiffness properties, including elastic normal stiffness (K_N) and elastic shear stiffness (K_S), and strength properties, including interface cohesion (C_{int}) and interface friction angle (ϕ_{int}). The stiffness properties were calculated using Equations (2.1) and (2.2) (Rocscience, 2022).

$$K_S = C_i E_{soil} \tag{2.1}$$

where C_i is the interface stiffness reduction factor, and E_{soil} is the saturated Young's modulus of soil.

$$K_N = 10 K_S \tag{2.2}$$

The strength properties were calculated using Equations (2.3) and (2.4) (Bentley, 2021; Rocscience, 2021).

$$C_{int} = R_{int} C_{soil} \tag{2.3}$$

where C_{int} is the interface cohesion, R_{int} = 2/3 is the interface strength reduction factor (smooth soil to concrete surface contact assumed), and C_{soil} is the effective cohesion of soil which was assumed to be 5 kPa for the Test Sand for numerical stability.

$$\phi_{int} = \tan^{-1}(\tan(\phi_{soil}) R_{int}) \tag{2.4}$$

where ϕ_{int} is the interface friction angle, ϕ_{soil} is the effective friction angle of soil.

Based on the parametric study conducted in Chapter 2, the C_i value of 0.95 was selected.

The hydrological load-time histories were applied at the top boundary of the simulation domain as an inflow boundary condition, with the same intensity as that applied in the small-scale experiment, which included the application of the low-intensity, medium-intensity, and high-intensity rainfall followed by gravity drainage. The finite element mesh was refined around the drilled shaft and ground surface to capture the stress and deformation variation accurately. A mesh sensitivity study was performed to select the size and mesh of the simulation domain, which does not affect the computed results. For the vertical boundaries of the domain, the displacement was restrained in the x- direction, and for the bottom horizontal boundary of the domain, displacement was restrained in both x and y- directions. The groundwater flow was closed for both the vertical boundaries and the bottom horizontal boundaries of the domain. Figure 4.17 shows the finite element mesh and dimensions of the simulation domain.

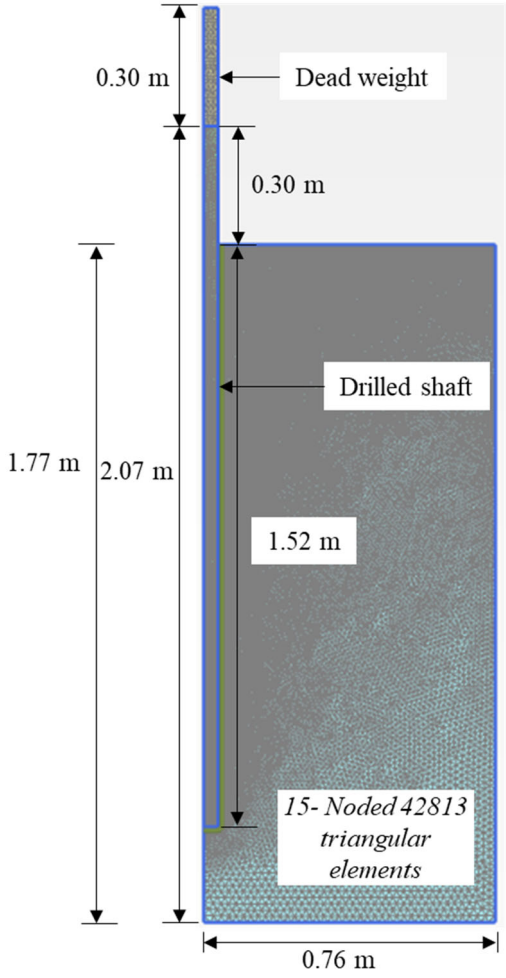

Figure 4.17. Finite element mesh of small-scale drilled shaft in Test Sand

4.4.1. Results and discussion

The finite element results were compared with the small-scale experimental results for the low-, medium-, and high-intensity rainfall to validate the Finite Element Model. Figure 4.18 shows the comparison of temporal variation of DOS at various depths for the low-intensity rainfall application for the small-scale experiment and FEM. The moisture sensors with odd numbering (Example: M21) are located at the soil-pile interface and even

numbering at 0.38 m away from the center of the drilled shaft. The maximum DOS for FEM for low-intensity rainfall was 67%.

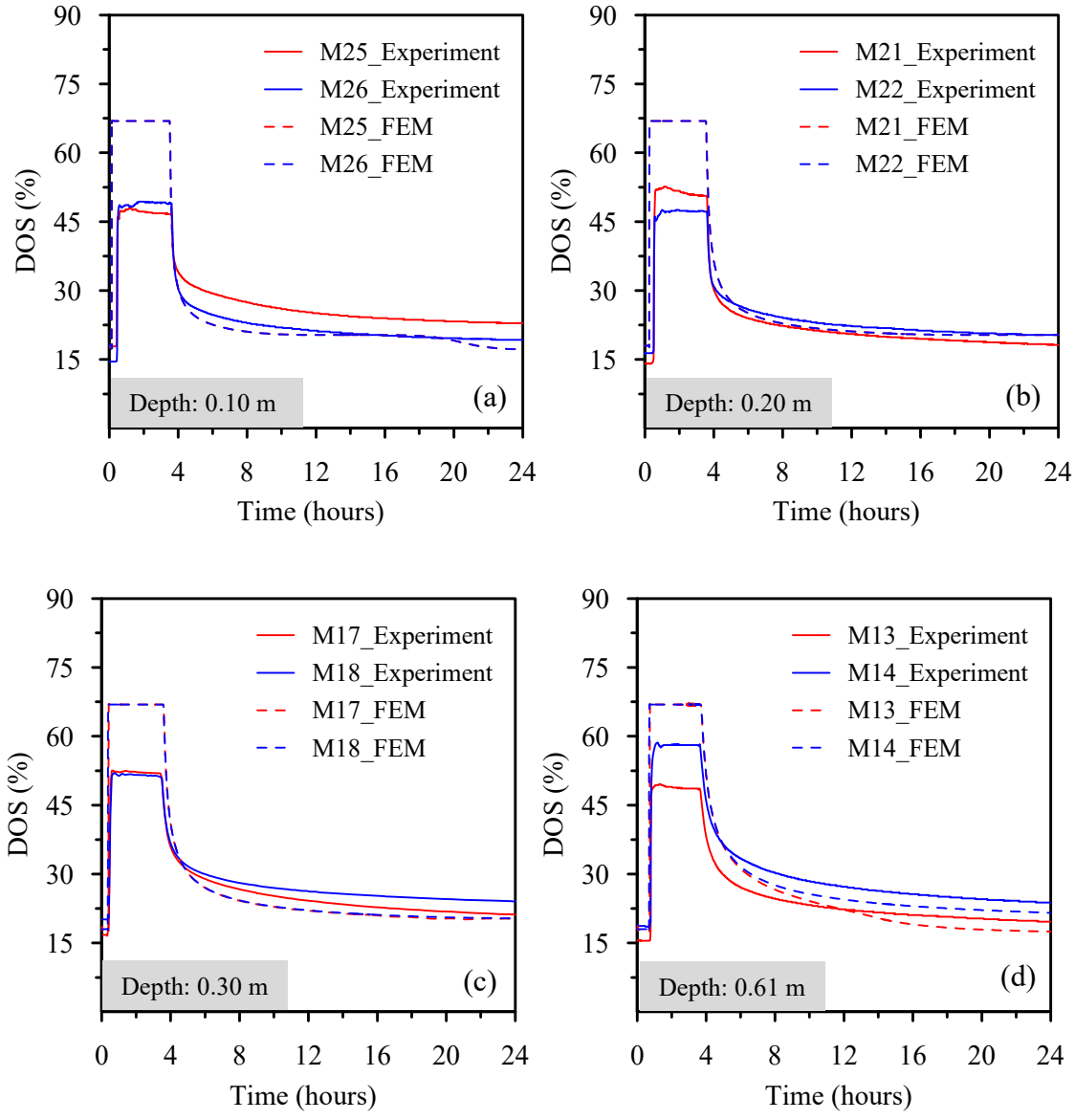

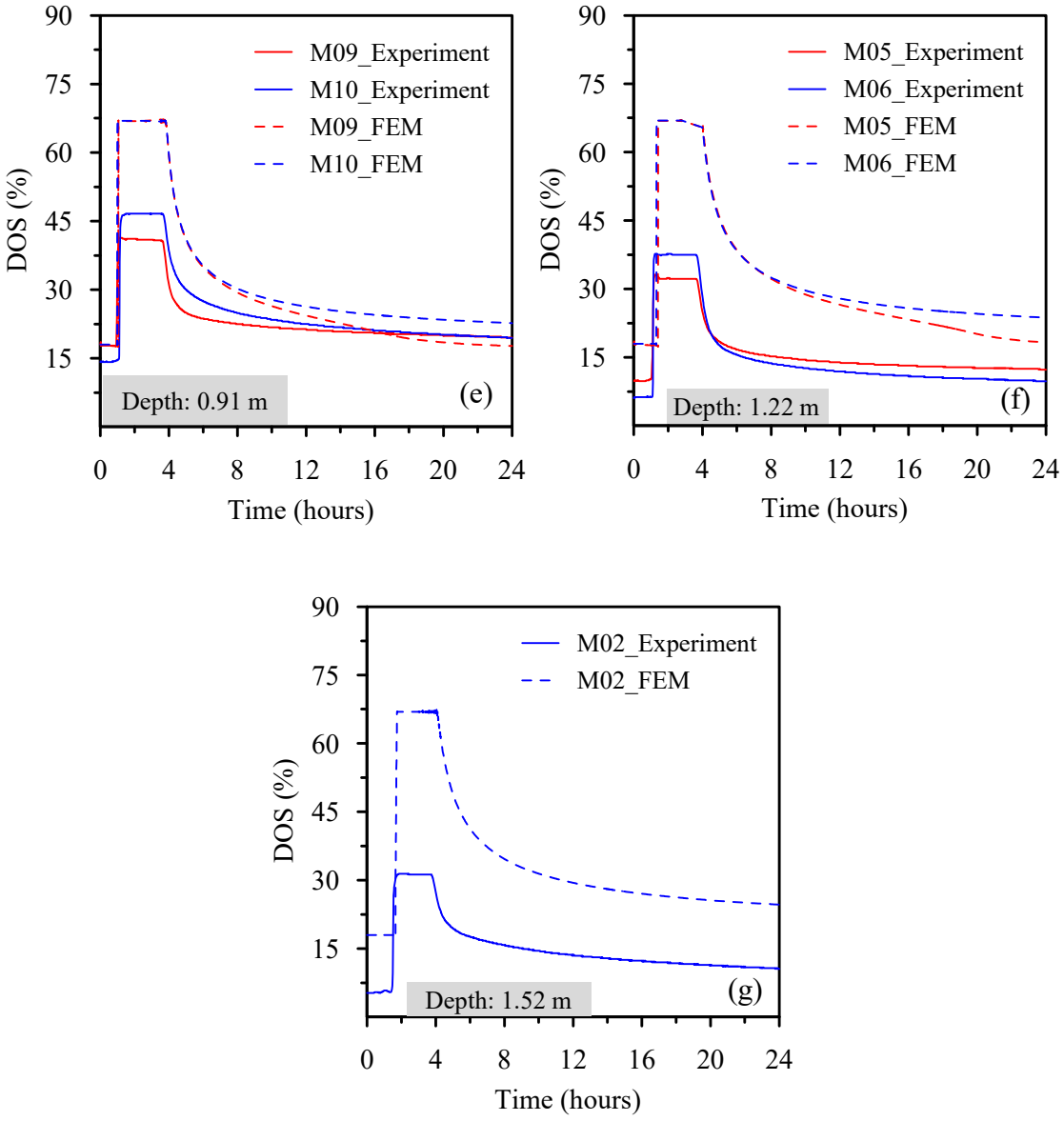

Figure 4.18. Experimental and FEM comparison of temporal variation of the degree of saturation at (a) 0.10 m, (b) 0.20 m, (c) 0.30 m, (d) 0.61 m, (e) 0.91 m, (f) 1.22 m (g) 1.52 m depths from ground level for low-intensity rainfall

Figure 4.19 shows the comparison of temporal variation of DOS at various depths for the medium-intensity rainfall application for the small-scale experiment and FEM. The maximum DOS for FEM for medium-intensity rainfall was 72%.

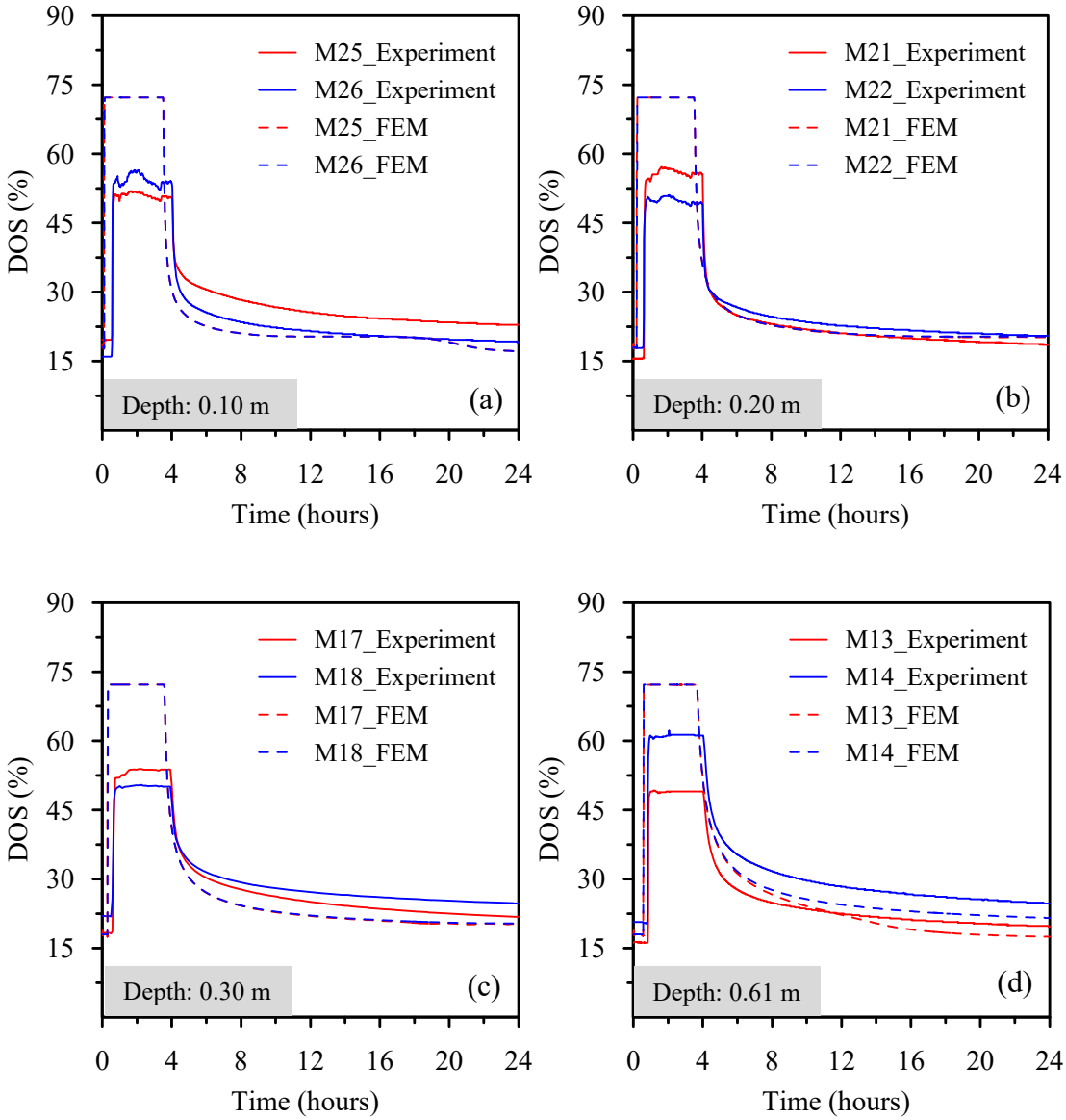
M25_Experiment
M26_Experiment
M25_FEM
M26_FEM
DOS (%)
Time (hours)
Depth: 0.10 m
(a)
M21_Experiment
M22_Experiment
M21_FEM
M22_FEM
Depth: 0.20 m
(b)
M17_Experiment
M18_Experiment
M17_FEM
M18_FEM
Depth: 0.30 m
(c)
M13_Experiment
M14_Experiment
M13_FEM
M14_FEM
Depth: 0.61 m
(d)

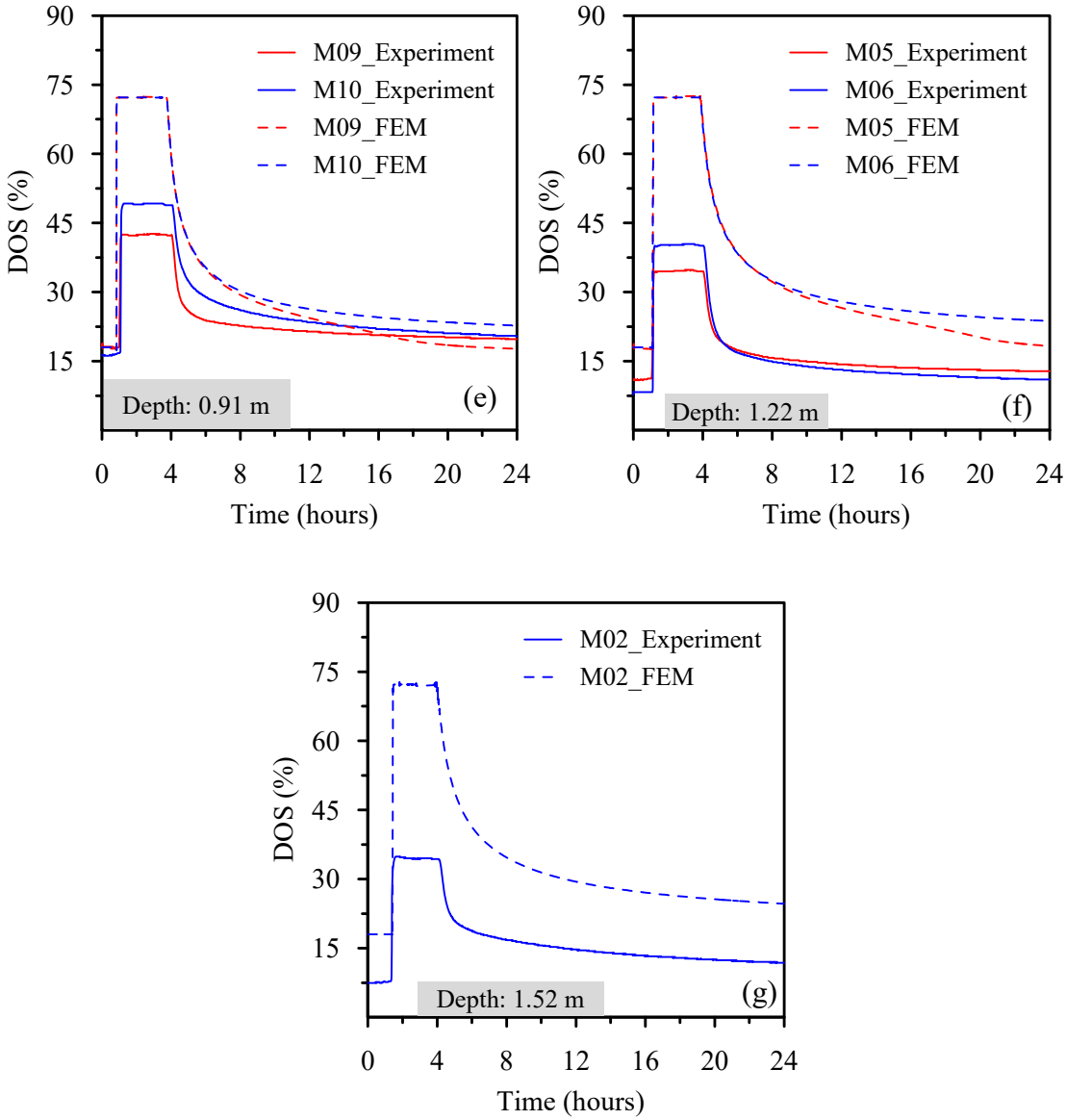

Figure 4.19. Experimental and FEM comparison of temporal variation of the degree of saturation at (a) 0.10 m, (b) 0.20 m, (c) 0.30 m, (d) 0.61 m, (e) 0.91 m, (f) 1.22 m (g) 1.52 m depths from ground level for medium-intensity rainfall

Figure 4.20 shows the comparison of temporal variation of DOS at various depths for the high-intensity rainfall application for the small-scale experiment and FEM. The maximum DOS for FEM for medium-intensity rainfall was 77%.

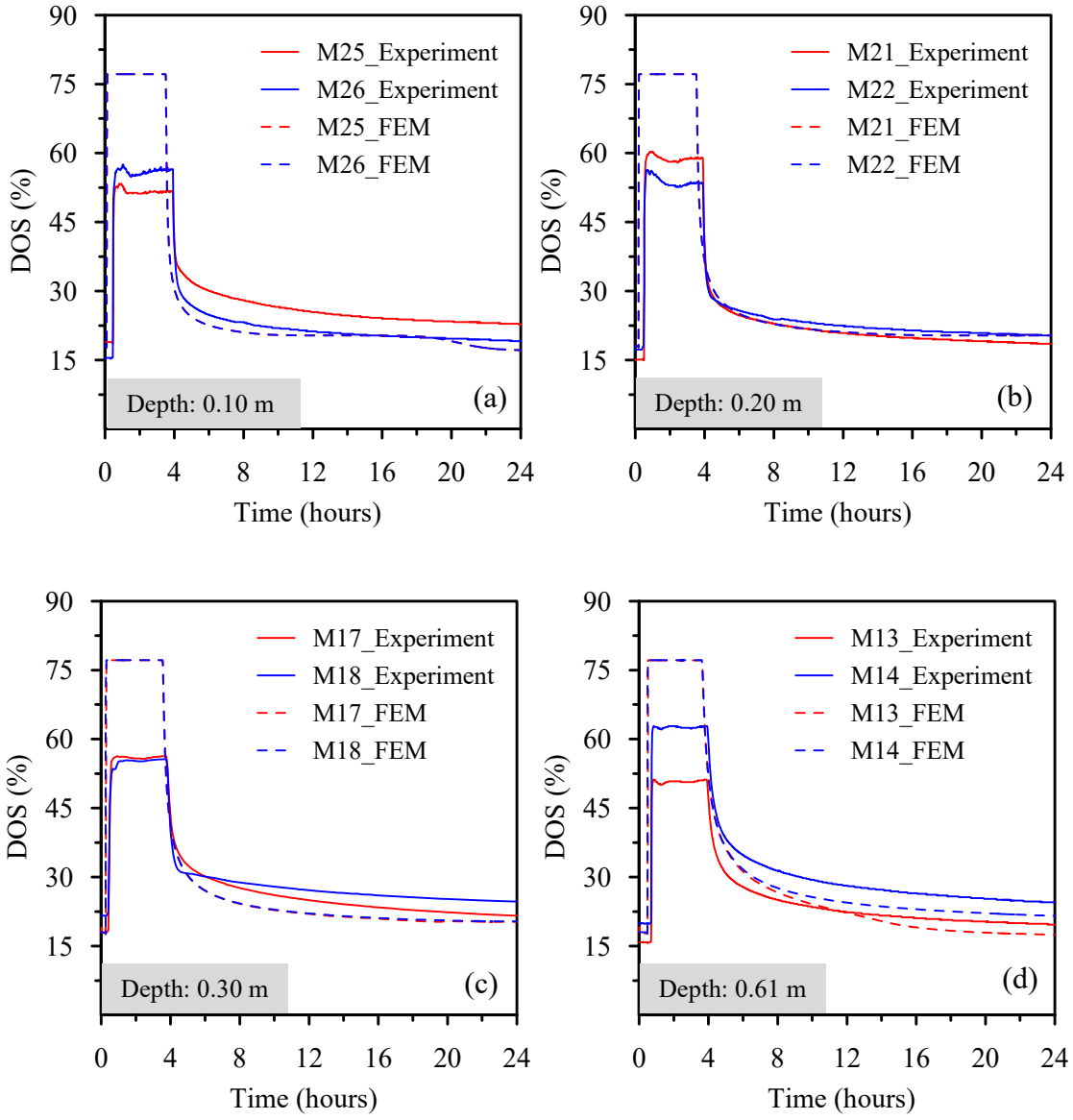
90
75
60
45
30
15
DOS (%)
0
4
8
12
16
20
24
Time (hours)
M25_Experiment
M26_Experiment
M25_FEM
M26_FEM
Depth: 0.10 m
(a)
M21_Experiment
M22_Experiment
M21_FEM
M22_FEM
Depth: 0.20 m
(b)
M17_Experiment
M18_Experiment
M17_FEM
M18_FEM
Depth: 0.30 m
(c)
M13_Experiment
M14_Experiment
M13_FEM
M14_FEM
Depth: 0.61 m
(d)

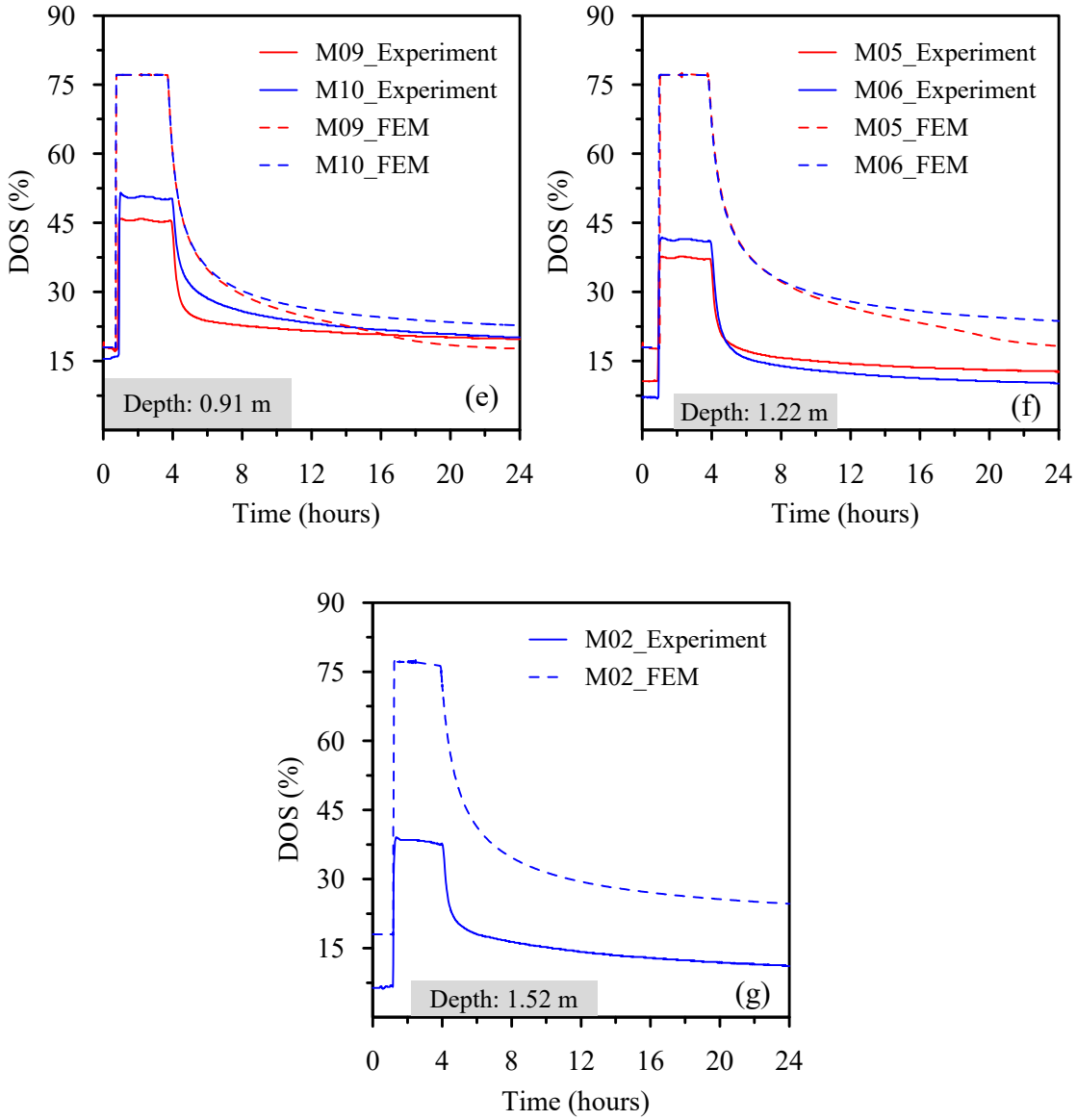

Figure 4.20. Experimental and FEM comparison of temporal variation of the degree of saturation at (a) 0.10 m, (b) 0.20 m, (c) 0.30 m, (d) 0.61 m, (e) 0.91 m, (f) 1.22 m (g) 1.52 m depths from ground level for high-intensity rainfall

The difference between the maximum DOS during rainfall from the low to medium to high-intensity rainfall for the experiment was 3%, while for FEM, this difference was 5%. Overall, the maximum DOS during rainfall for the low-, medium-, and high-intensity rainfall in FEM was higher than in the experiment. For the low-intensity rainfall, it can be

observed that at 0.1 m depth, the difference in the experiment and FEM maximum DOS is approximately 18%; at 0.20 m depth, the difference in maximum DOS is approximately 17%; at 0.30 m depth, the difference in maximum DOS is 15%, and at 0.61 m the difference in DOS is approximately 13%. Hence, a trend of reduction in the difference between the maximum DOS during the rainfall of the experiment and FEM is observed. This reduction of maximum DOS with depth up to 0.61 m is seen in medium-and high-intensity rainfall too. The maximum DOS differences below 0.61 m depth cannot be compared as the DOS in the experiment below 0.61 m depth were lower due to the initial mechanical pile load test, which may have caused dilation of the soil leading to a reduction in the DOS. The rising and falling limbs of the temporal DOS variation for experiment and FEM are observed to be close. This suggests that the wetting front moves at the same rate in FEM as compared to the experiment and also reaches the drilled shaft bottom at the same time.

Figures 4.21-4.23 show the comparison of the spatial variation of axial force for low-, medium, and high-intensity rainfall. To obtain the DOS profiles during rainfall for the low-, medium-, and high-intensity rainfall, maximum values of DOS from the corresponding DOS temporal variations were used. For the before rainfall case for FEM for the low-, medium-, and high-intensity rainfall, the DOS remains constant at 18% as that is the residual value input in PLAXIS 2D. For the during rainfall case for FEM for the low-, medium-, and high-intensity rainfall, the DOS remains constant at 67%, 72%, and 77%, respectively.

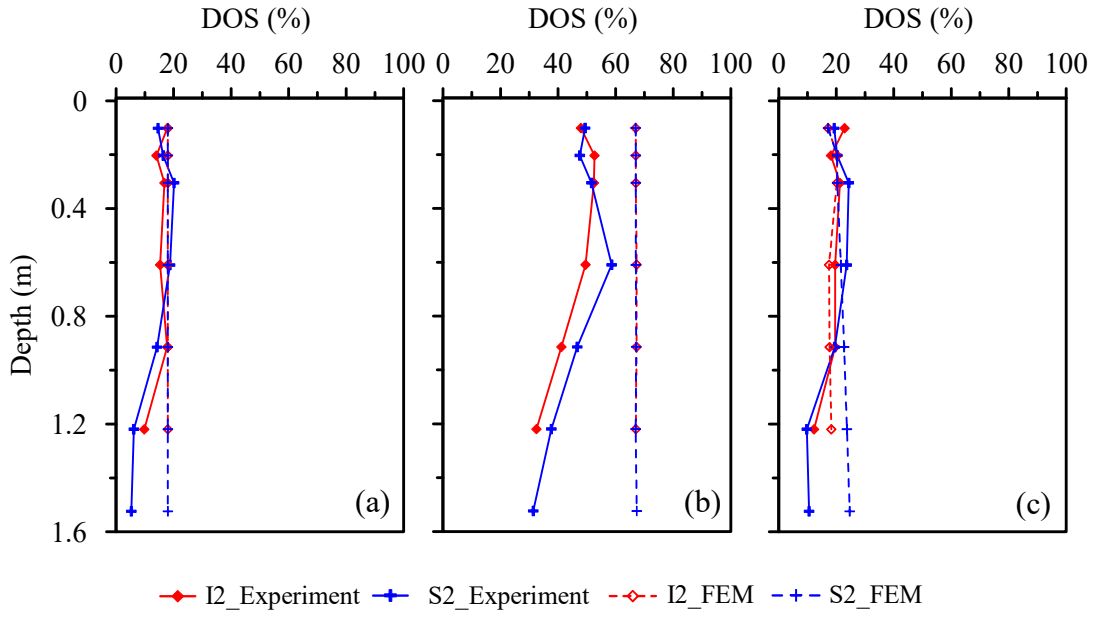

Figure 4.21. Experimental and FEM comparison of spatial variation of the degree of saturation (a) before, (b) during, and (c) 24 hours after low-intensity rainfall

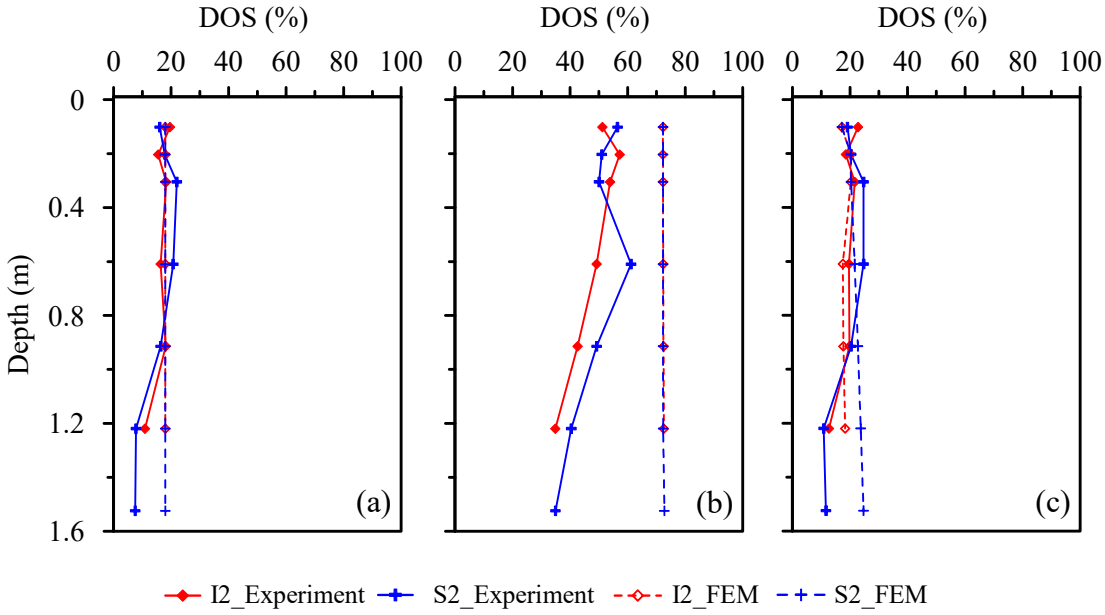

Figure 4.22. Experimental and FEM comparison of spatial variation of the degree of saturation (a) before, (b) during, and (c) 24 hours after medium-intensity rainfall

For the after-rainfall case for FEM, for the low-, medium-, and high-intensity rainfall, the DOS at the soil-pile interface, i.e., at I2, is lower than the DOS in soil, i.e., at S2 at depths below 0.3 m. Likewise, in the experiment, the DOS at the soil-pile interface is lower than DOS in soil between 0.2 m and 0.9 m depth. This drop in DOS at the soil-pile interface is also seen in the before and during cases of the experiment for the low-, medium-, and high-intensity rainfall. This drop in the DOS at the soil-pile interface suggests that the soil-pile interface has a low water-holding capacity and can influence the capacity of the drilled shaft.

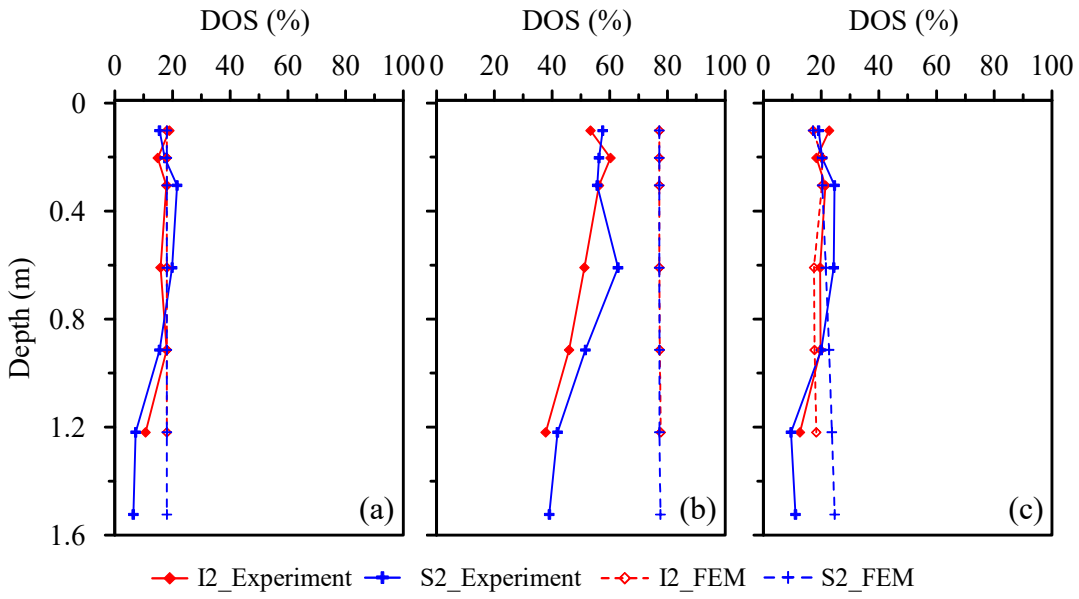

Figure 4.23. Experimental and FEM comparison of spatial variation of the degree of saturation (a) before, (b) during, and (c) 24 hours after high-intensity rainfall

Figures 4.24-4.26 show the comparison of temporal variation of pile and ground displacement for the experiment and FEM for the low-, medium, and high-intensity rainfall cases. The ground surface is observed to displace vertically upward during rainfall and gravity drainage. The ground surface at a radial distance of 0.50 m from the drilled shaft

center displaces vertically upward more than the ground surface at a distance of 0.25 m from the drilled shaft. During rainfall, the upward vertical displacement of the top of the drilled shaft is seen, which continues until 17 hours, followed by settlement at the end of gravity drainage. The above-mentioned observations are consistent with the experiment and FEM results for the low-, medium, and high-intensity rainfall cases.

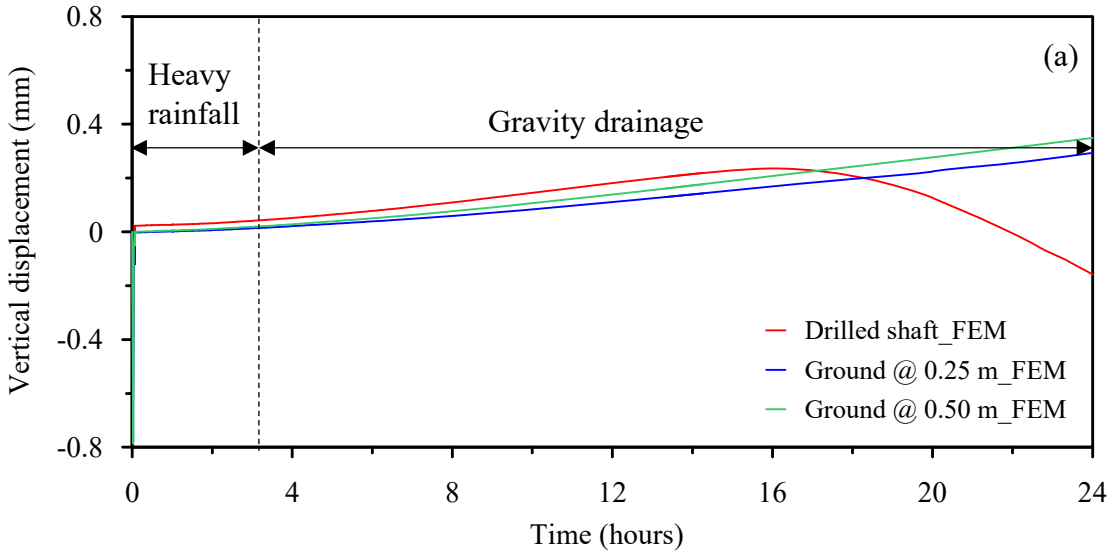

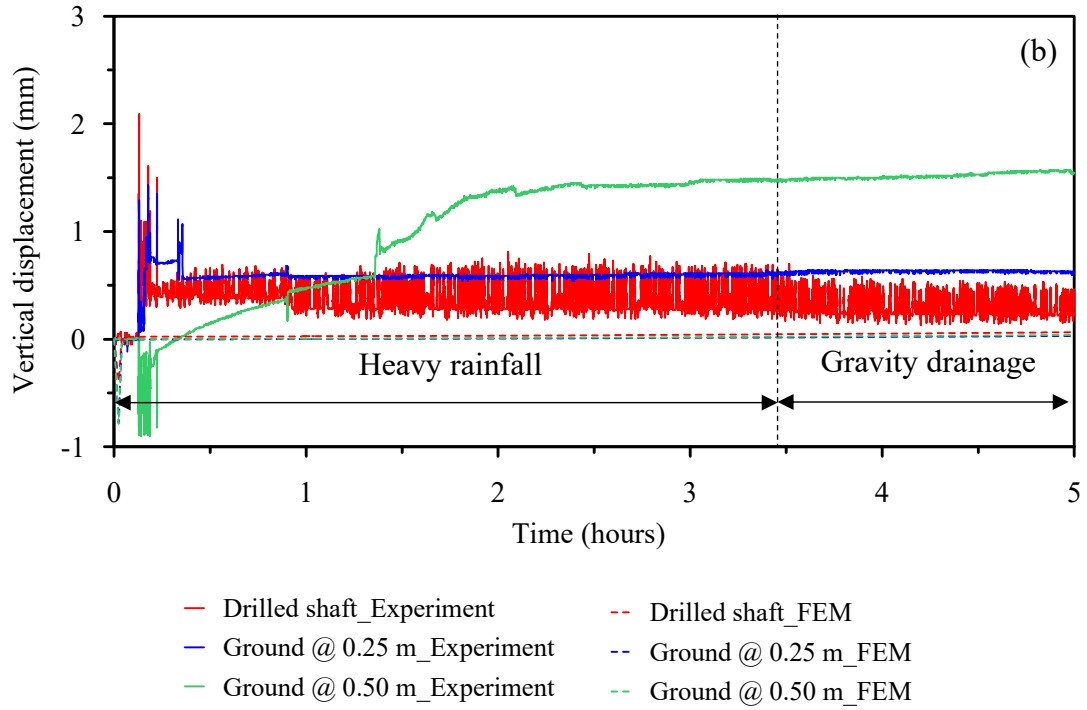

Figure 4.24. (a) FEM, and (b) Experimental and FEM comparison of temporal variation of vertical displacement for low-intensity rainfall

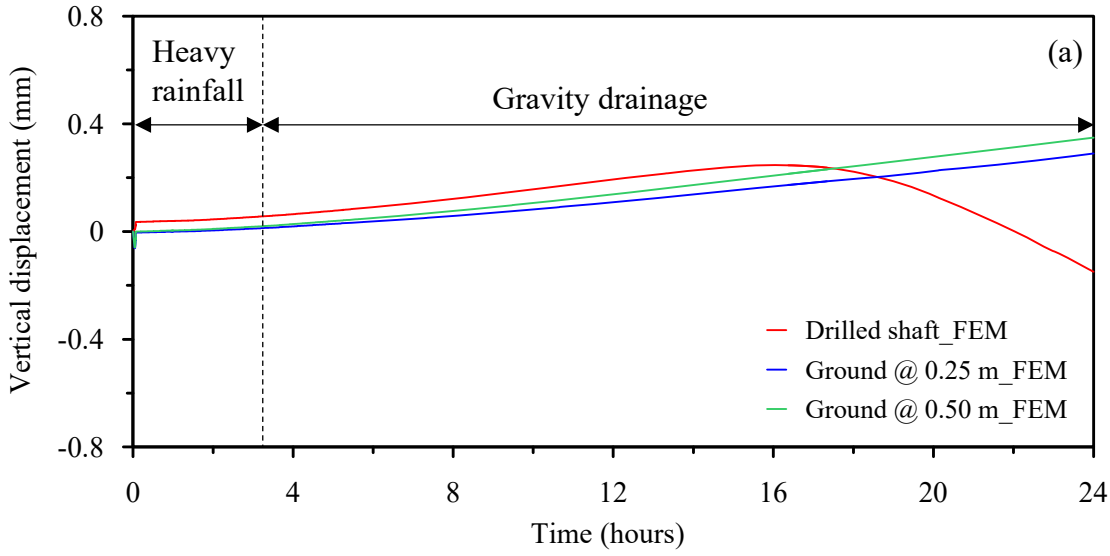

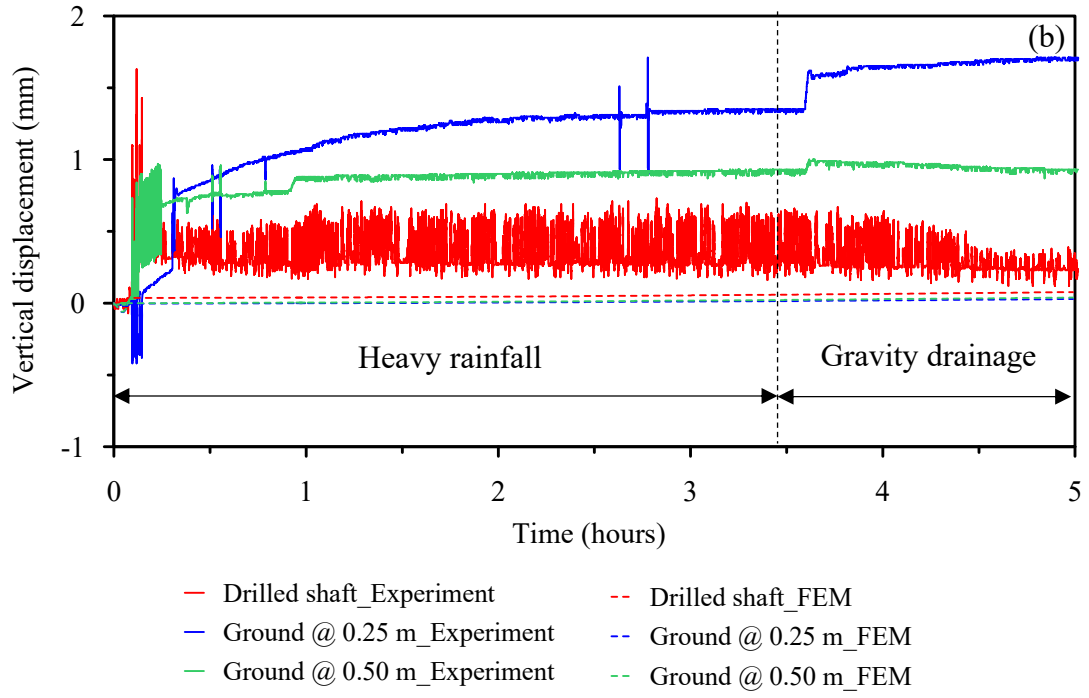

Figure 4.25. (a) FEM, and (b) Experimental and FEM comparison of temporal variation of vertical displacement for medium-intensity rainfall

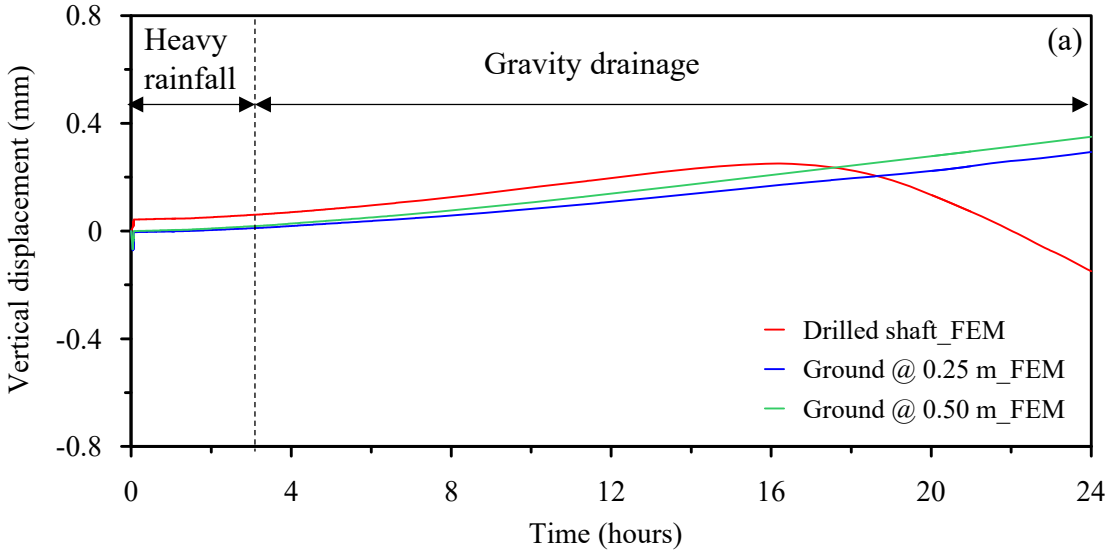

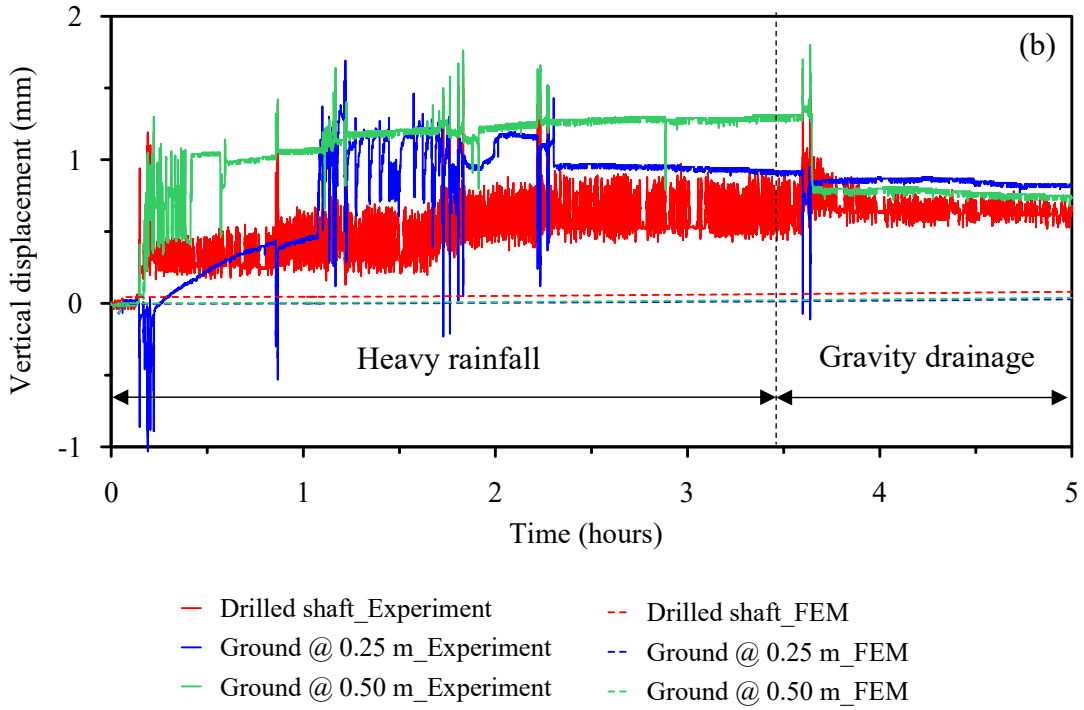

Figure 4.26. (a) FEM, and (b) Experimental and FEM comparison of temporal variation of vertical displacement for high-intensity rainfall

Figure 4.27 shows the axial force variation at various time intervals during rainfall and gravity drainage for FEM, and Figures 4.28-4.30 show the comparison of axial force variation at various time intervals during rainfall and gravity drainage for FEM and experiment. The axial force values for the experiment below 0.45 m depth were linearly extrapolated using the data points at 0.30 m and 0.45m depths shown by dashed lines in Figures 4.28-30. For the low-intensity rainfall in FEM, after 1.35 hours of rainfall, the axial force significantly decreases up to 0.45 m depth and increases below this depth up to the bottom of the drilled shaft. This behavior is consistent with the low-intensity rainfall in the experiment. At the end of rainfall in FEM, the axial force decreases up to 0.45 m depth and then increases below this depth up to the bottom of the drilled shaft. This behavior is

inconsistent with the low-intensity rainfall in the experiment. At 24 hours, i.e., at the end of gravity drainage in FEM, the axial force increases after the end of rainfall up to 0.45 m depth and decreases lower than the axial force at the end of rainfall below this depth up to the bottom of the drilled shaft. This behavior is consistent with the low-intensity rainfall in the experiment. However, the axial force at 24 hours becomes almost equal to the before rainfall case in FEM. This behavior is inconsistent with the low-intensity rainfall in the experiment, where the axial force is observed to be more after 24 hours than before rainfall. Hence, in FEM, up to 0.45 m depth, the axial force decreases significantly until the end of rainfall and then increases until the end of gravity drainage. In the experiment where the vertical strain measurements were measured up to 0.45 m depth, the behavior is the same as observed in FEM up to 0.45 m with the exception that in the experiment, the axial force increases at the end of rainfall. Based on the observations up to 0.45 m depth, the top of the drilled shaft displaces vertically upward during rainfall and settles during gravity drainage. This behavior is also confirmed in Figure 4.24 (a), where upward vertical displacement during rainfall followed by settlement of the top of the drilled shaft during gravity drainage is seen.

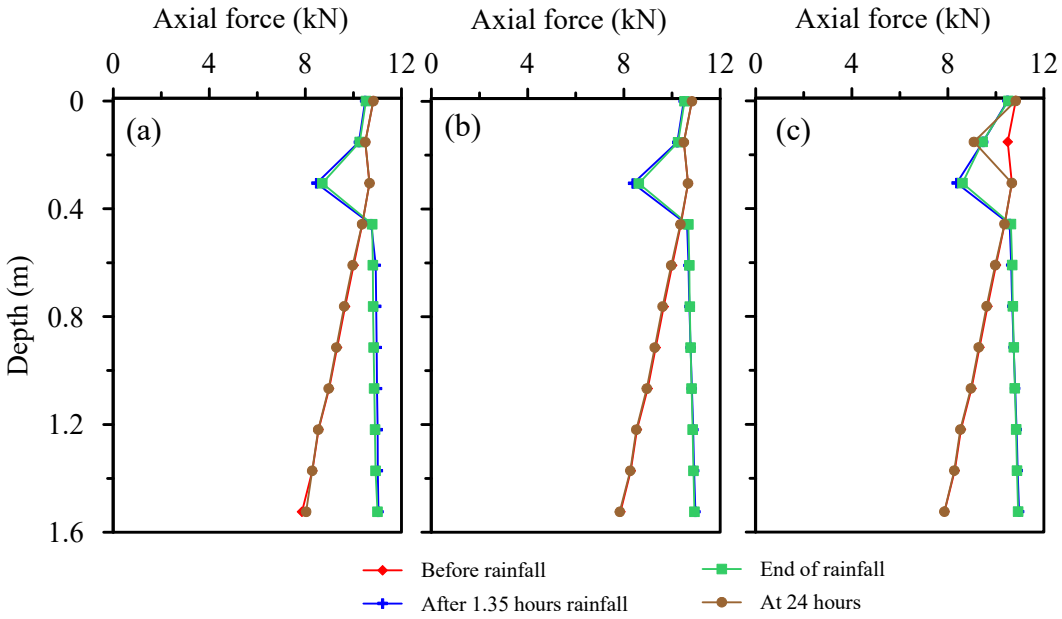

Figure 4.27. Spatial variation of axial force at various time intervals for (a) low-intensity, (b) medium-intensity, and (c) high-intensity rainfall in FEM

Also, for the low-intensity rainfall at 1.35 hours and the end of rainfall, the axial force increases below 0.45 m depth up to the bottom of the drilled shaft for both experiment and FEM. This means that the skin resistance is mobilized during rainfall, and the mechanical load is transferred to the bottom of the drilled shaft. This mobilization of skin resistance of the drilled shaft reduces the load-carrying capacity of the drilled shaft, and further transfer of the mechanical load to the bottom of the drilled shaft can lead to foundation failure if the end bearing capacity of the drilled shaft is completely utilized.

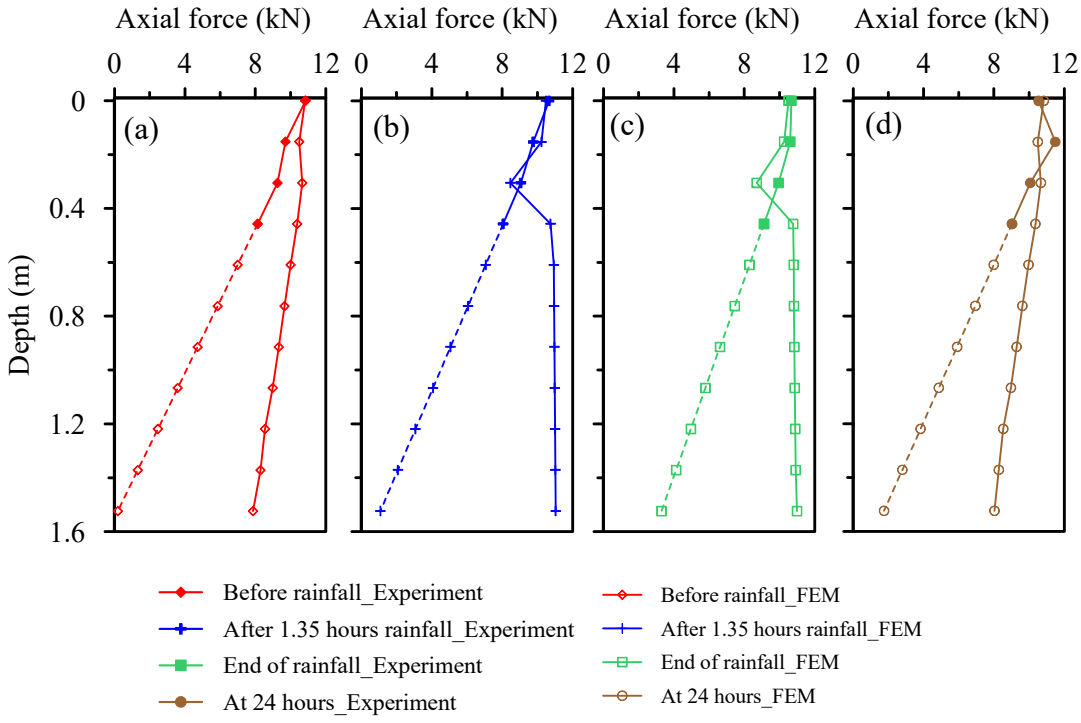

Figure 4.28. Experiment and FEM comparison of spatial variation of axial force at various time intervals for low-intensity rainfall

For the medium-intensity rainfall in FEM, after 1.35 hours of rainfall, the axial force significantly decreases up to 0.45 m depth and increases below this depth up to the bottom of the drilled shaft. This behavior is consistent with the medium-intensity rainfall in the experiment. At the end of rainfall in FEM, the axial force decreases up to 0.45 m depth and then increases below this depth up to the bottom of the drilled shaft. This behavior is inconsistent with the medium-intensity rainfall in the experiment, where the axial force is observed to decrease up to the bottom of the drilled shaft at the end of rainfall. At 24 hours, i.e., at the end of gravity drainage in FEM, the axial force increases after the end of rainfall up to 0.45 m depth and decreases lower than the axial force at the end of rainfall below this depth up to the bottom of the drilled shaft. This behavior is consistent

with the medium-intensity rainfall in the experiment. However, the axial force at 24 hours becomes almost equal to the before rainfall case in FEM. This behavior is inconsistent with the medium-intensity rainfall in the experiment, where the axial force after 24 hours is observed to be lower than before rainfall. Hence, in FEM, up to 0.45 m depth, the axial force decreases significantly until the end of rainfall and then increases until the end of gravity drainage. In the experiment where the vertical strain measurements were measured up to 0.45 m depth, the behavior was the same as observed in FEM up to 0.45 m. Based on the observations up to 0.45 m depth, the top of the drilled shaft displaces vertically upward during rainfall and settles during gravity drainage. This behavior is also confirmed in Figure 4.24 (b), where upward vertical displacement during rainfall followed by settlement of the top of the drilled shaft during gravity drainage is seen.

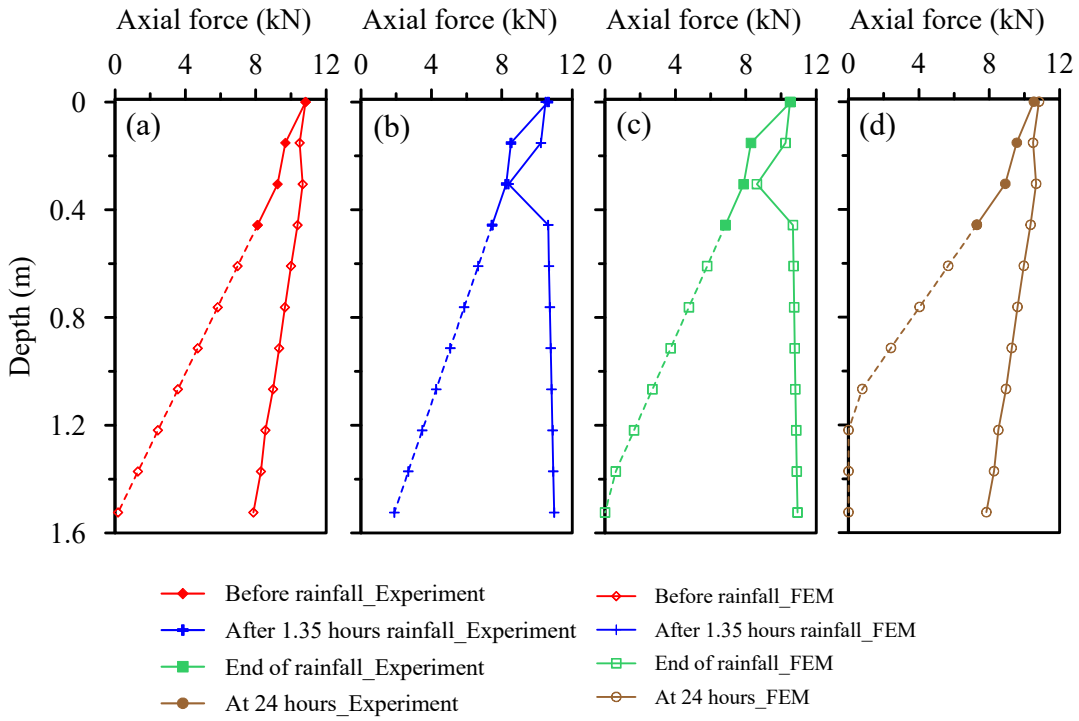

Figure 4.29. Experiment and FEM comparison of spatial variation of axial force at various time intervals for medium-intensity rainfall

For the high-intensity rainfall in FEM, after 1.35 hours of rainfall, the axial force significantly decreases up to 0.45 m depth and increases below this depth up to the bottom of the drilled shaft. This behavior is inconsistent with the high-intensity rainfall in the experiment, where the axial force decreases throughout the depth after 1.35 hours of rainfall. At the end of rainfall in FEM, the axial force decreases up to 0.45 m depth and then increases below this depth up to the bottom of the drilled shaft. This behavior is inconsistent with the high-intensity rainfall in the experiment, where the axial force is observed to decrease up to the bottom of the drilled shaft at the end of rainfall. At 24 hours, i.e., at the end of gravity drainage in FEM, the axial force increases after the end of rainfall up to 0.45 m depth and decreases lower than the axial force at the end of rainfall below this depth up to the bottom of the drilled shaft. This behavior is consistent with the high-intensity rainfall in the experiment. However, the axial force at 24 hours becomes almost equal to the before rainfall case in FEM. This behavior is inconsistent with the high-intensity rainfall in the experiment, where the axial force after 24 hours is observed to be lower than before rainfall. Hence, in FEM, up to 0.45 m depth, the axial force decreases significantly until the end of rainfall and then increases until the end of gravity drainage. In the experiment where the vertical strain measurements were measured up to 0.45 m depth, the behavior is the same as observed in FEM up to 0.45 m. Based on the observations up to 0.45 m depth, the top of the drilled shaft displaces vertically upward during rainfall and settles during gravity drainage. This behavior is also confirmed in Figure 4.24 (c),

where upward vertical displacement during rainfall followed by settlement of the top of the drilled shaft during gravity drainage is seen.

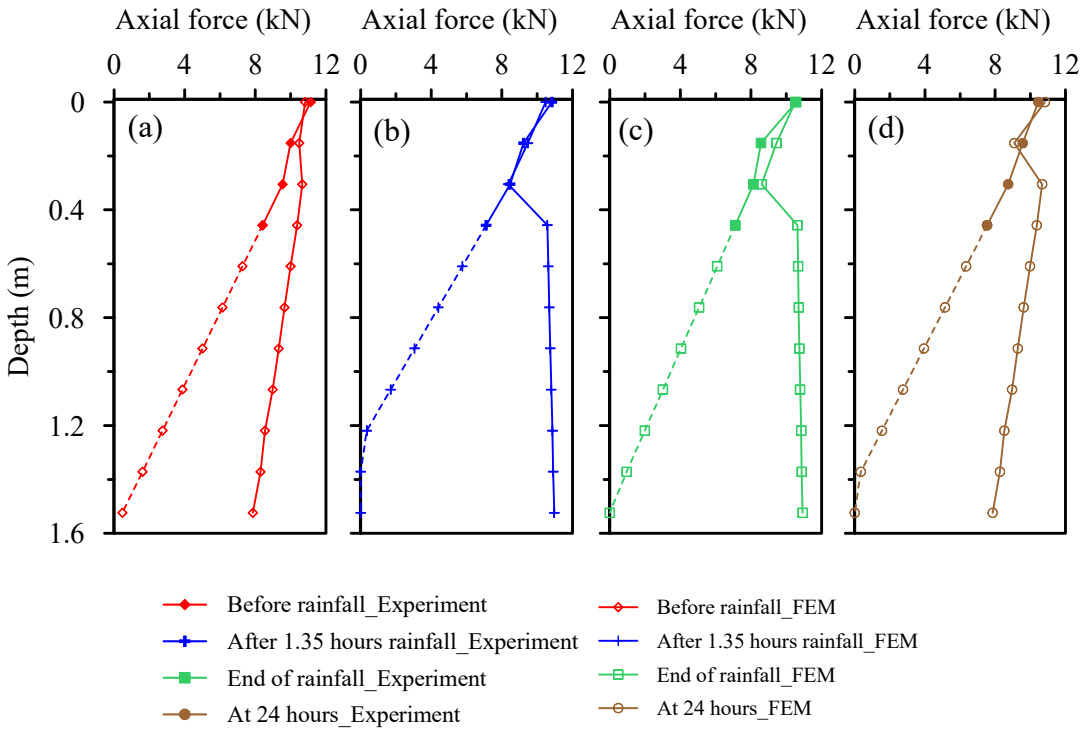

Figure 4.30. Experiment and FEM comparison of spatial variation of axial force at various time intervals for high-intensity rainfall

It is worth noting that in both experiment and FEM, the spatial variation of the axial force above 0.45 m depth is opposite below the 0.45 m depth for many cases for the low-, medium-, and high-intensity rainfall. The low-intensity rainfall caused the settlement of the drilled shaft, which caused a decrease in the total bearing capacity of the drilled shaft due to the mobilization of the skin resistance to the bottom of the drilled shaft. The medium-and high-intensity rainfall mostly caused the upward vertical displacement of the drilled shaft, which caused an increase in the total bearing capacity of the drilled shaft. However, it should be noted that the Test San used for this study had a relative compaction

of 96%, and infiltration of large volumes of water from medium- and high-intensity rainfall caused the sand to increase in volume causing the drilled shaft to displace vertically upward. A looser soil will cause the drilled shaft to respond differently to the low-, medium, and high-rainfall intensities.

4.5. CONCLUSION

This study attempts to validate the FEM model against a small-scale experiment where the small-scale drilled shaft was subjected to a constant mechanical load and different rainfall intensities. The following are the key observations:

1. In the experiment, inconsistencies in the DOS variation are due to old EC-5 moisture sensors, which may have poor calibration, possible disturbance to the moisture sensors during the initial multiple mechanical pile load tests, and placing the moisture sensors too close to the drilled shaft.
2. In the experiment and FEM, the DOS increased with the increase in rainfall intensity. The difference between the maximum DOS during rainfall from the low to medium to high-intensity rainfall for the experiment was 3%, while for FEM, this difference was 5%.
3. The wetting front moves at the same rate in FEM as compared to the experiment and also reaches the drilled shaft bottom at the same time.
4. The DOS is lower at the soil-pile interface compared to the soil in the experiment and FEM, which suggests that the soil-pile interface has a low water-holding capacity and can affect the capacity of the drilled shaft.

5. A trend of reduction in the difference between the DOS of the experiment and FEM is observed.
6. In the experiment and FEM, upward vertical displacement during rainfall and settlement during gravity drainage is observed for the top of the drilled shaft and ground surface. The upward vertical displacement of the ground surface increases with the intensity of rainfall and the radial distance away from the drilled shaft in both FEM and experiment.
7. The axial force in the drilled shaft decreases during rainfall as compressive strains are induced at the soil-pile interface due to the upward vertical displacement of the surrounding soil.
8. The axial force in the drilled shaft increases during gravity drainage as tensile strains are induced at the soil-pile interface due to the settlement of surrounding soil.
9. The low-intensity rainfall caused the settlement of the drilled shaft, which caused a decrease in the total bearing capacity of the drilled shaft due to the mobilization of the skin resistance to the bottom of the drilled shaft. The medium- and high-intensity rainfall mostly caused the upward vertical displacement of the drilled shaft, which caused an increase in the total bearing capacity of the drilled shaft.
10. In FEM, the drilled shaft behaves as an end-bearing shaft. However, in the experiment, the values of axial force below 0.45 m depth were extrapolated and may as well behave as an end-bearing shaft. The axial force variation

at various time intervals for the FEM matches with the experiment qualitatively in various aspects.

11. The compaction of soil plays a crucial role and will cause the drilled shaft to respond differently to the low-, medium, and high-rainfall intensities. Hence, more experimental tests with different relative compaction of soil should be conducted.

REFERENCES

ACI Committee 543. (2012). Design, Manufacture, and Installation of Concrete Piles.

ASTM D698. Standard Test Methods for Laboratory Compaction Characteristics of Soil Using Standard Effort.

Campanella, C., Cuccovillo, A., Campanella, C., Yurt, A. and Passaro, V. (2018). Fibre Bragg Grating Based Strain Sensors: Review of Technology and Applications. Sensors, 18(9), p.3115.

Carsel, R.F., Parrish, R.S. (1988). Developing joint probability distributions of soil water retention characteristics. Water Resources Research, 24(5), 755–769.

Coyle, H. M. and Castello, R. R. (1981). "New Design Correlations for Piles in Sand," Journal of the Geotechnical Engineering Division, American Society of Civil Engineers, Vol. 107, No. GT7, pp. 965–986.

Davisson, M. T. (1972). High capacity piles. Proceedings of Lecture Series on Innovations in Foundation Construction, American Society of Civil Engineers, ASCE, Illinois Section, Chicago, March 22, pp. 81 - 112.

Decagon Devices. (2001-2010). EC-20, EC-10, EC-5: User's Manual. Pullman, WA: Author.

Fempto Fibertec (2022). FEMTO FIBER TEC - FEMTO FIBER TEC. (n.d.). Retrieved May 12, 2022, from https://www.femtofibertec.de/en/home#home

Ferraro, P. and De Natale, G. (2002). On the possible use of optical fiber Bragg gratings as strain sensors for geodynamical monitoring. Optics and Lasers in Engineering, 37(2-3), pp.115-130.

Hill, K. and Meltz, G. (1997). Fiber Bragg grating technology fundamentals and overview. Journal of Lightwave Technology, 15(8), pp.1263-1276.

IPCC.(2013). Climate Change 2013: The Physical Science Basis. Cambridge University Press.

Kreuzer, M. (1970) Strain measurement with fiber Bragg grating sensors: Semantic scholar. Available at: https://www.semanticscholar.org/paper/Strain-Measurement-with-Fiber-Bragg-Grating-Sensors-Kreuzer/1b00007973bbc79670d6919b5d2688085266d048.

Meter Group (2022). https://www.metergroup.com/en/meter-environment/products/rt-1-soil-temperature-sensor

Micronoptics (2022). http://micronoptics.ru/uploads/library/documents/Datasheets/Micron%20Optics%20sm125.pdf

NewAge Industries. (2022). https://www.newageindustries.com/products/tubing-hose/nylon/nylotube-nylon-tubing/

NOAA (2022). U.S. Billion-Dollar Weather & Climate Disasters 1980-2022. https://www.ncei.noaa.gov/access/billions/events.pdf

NYDOT (2015). Geotechnical Control Procedure: Static Pile Load Test Manual. P: 30.

Omega (2022). https://www.omega.com/en-us/

Spraying Systems Co. (2022). https://www.spray.com/

Topp, G.C., Davis, J.L. and Annan, A.P. (1980) 'Electromagnetic determination of soil water content: Measurements in coaxial transmission lines,' Water Resources Research, 16(3), pp. 574–582. doi:10.1029/wr016i003p00574.

WMO (2021). https://public.wmo.int/en/media/press-release/weather-related-disasters-increase-over-past-50-years-causing-more-damage-fewer

CHAPTER 5. MULTI-HAZARD ANALYSIS OF DEEP FOUNDATION

5.1. ABSTRACT

This study evaluates the effect of single and multiple extreme hydroclimatic events, including heavy rainfall and heavy rainfall followed by an earthquake, on the structural response of drilled shaft designed for a hypothetical three-story building. Initially, a pushover analysis was conducted to validate the drilled shaft model in lateral pile analysis software, RSPile, against the model in fully-coupled Geotechnical-Hydrological finite element code PLAXIS 2D by subjecting the drilled shaft to pseudo-static load from an earthquake. A modified Mohr-Coulomb (MMC) model capable of updating the yield criterion and modulus with changes in matric suction and/or degree of saturation was used to represent the stress-strain behavior of the partially saturated soil in PLAXIS 2D. Then, the drilled shaft model in PLAXIS 2D was subjected to heavy rainfall and heavy rainfall followed by an earthquake, and the structural responses of the drilled shafts were evaluated. Results showed that when the drilled shaft was subjected to the dynamic load from heavy rainfall followed by dynamic load from the earthquake, the vertical settlement for the drilled shaft was very high (7.74 mm) compared to the case where the drilled shaft was subjected to dynamic load from the earthquake (0.01 mm). Hence, the combined effect of heavy rainfall and earthquake can cause more damage to the deep foundations.

5.2. INTRODUCTION

In recent years, climate change has become a growing concern as human activity contributes largely to greenhouse gas emissions, namely carbon dioxide and methane. Energy, industry, agriculture, and waste disposal have been the largest contributors to emissions, and their effects can be seen through the increase in temperature. However, the temperature change is not the only consequence. Droughts, water scarcity, severe fires, rising sea levels, flooding, melting polar ice, catastrophic storms, and declining biodiversity are some of the overarching repercussions. More specifically, climate change is affecting human health, the ability to grow food, housing, safely, and work (United Nations 2022). The impact of natural hazards on deep foundations can be critical and highly unpredictable when extreme hydrological and seismic events occur simultaneously or in sequence. Most major environmental disasters result from compound climate extremes (Zscheischler et al. 2018)

Natural events like heavy rainfall, drought, and earthquake can cause significant variations in the strength and deformation properties of the soil resulting in significant variations in the bearing capacity capacities of deep foundations, resulting in the failure of foundations that support critical infrastructure. Forecasts indicate that these natural events will become increasingly common in the future. Therefore, it is important to understand and quantify the impacts of such events on the behavior of deep foundations. Geotechnical systems are also drastically affected by climate change. In the US, the west is consistently in a period of drought, whereas the east is characterized by flooding. As the degree of saturation and water table changes, soil properties and how soil behaves under loading also

alters, which means geotechnical systems will vary considerably across the US. Other systems, such as dam and levee capacities as well as roadway embankment stability, are also affected. In another study, Vickneswaran et al. (2021) investigated the soil capacity to support buried concrete pipes in heavy rainfall-induced flooding at the ground surface as well as the reduction of soil shear strength due to infiltration and leakage from the pipe. PLAXIS 2D is a finite element software widely used for engineering projects, including groundwater seepage, consolidation, and dynamic analysis capabilities. Also, this software can be used to predict the development of the deformations and pore pressures that occur in partially saturated soils subjected to time-dependent changes in hydrological and earthquake loads using fully-coupled flow-deformation analysis. The study conducted a fully-coupled flow deformation analysis using the finite element software PLAXIS 2D and determined deflection, bending moment, and shear force in the pipe. However, this study conducts analysis and determines the same parameters for a deep foundation system.

In this study, the effect of single and multiple extreme hydroclimatic events was analyzed for deep foundations under mechanical and hydroclimatic loading conditions, where small changes can have a significant impact on the performance of the foundation. The pushover analysis was performed in RSPile and was calibrated based on the laterally loaded analysis in PLAXIS 2D. The structural responses of deep foundations were further investigated in PLAXIS 2D.

5.3. MATERIAL PROPERTIES AND LOADING CONDITIONS

The following sections list the properties of soil, full-scale drilled shaft, and hydrological and earthquake loading conditions, which were used as inputs in RSPile and PLAXIS 2D.

5.3.1. Soil properties

Tables 5.1 and 5.2 enlist the soil properties used as input in RSPile and PLAXIS 2D for the pushover analysis and the multi-hazard analysis. The pushover analysis included adjusting the value of the initial stiffness of the p-y curve (K_{py}) required as input in RSPile to calibrate the RSPile model against the PLAXIS 2D model, where the drilled shaft was subjected to a pseudo-static lateral load. The resulting value of K_{py} from the pushover analysis was 11770 kN/m^3. The multi-hazard analysis was conducted using PLAXIS 2D. A modified Mohr-Coulomb (MMC) model capable of updating the yield criterion and modulus with changes in matric suction and/or degree of saturation (Vickneswaran and Ravichandran 2022) was used to represent the stress-strain behavior of the partially saturated soil in PLAXIS 2D. The MMC model fitting parameters are shown in Table 5.2, which were calculated using the general and hydraulic properties. To define the saturation-suction behavior of soil, there are many Soil Water Characteristic Curves (SWCCs) and corresponding relative hydraulic conductivity functions available in the literature. In this study, the Mualem-van Genuchten model (Mualem 1976; van Genuchten 1980) and the van Genuchten model (van Genuchten 1980) were used for defining the relative hydraulic conductivity functions and the SWCC, which are available in PLAXIS 2D. The unsaturated

hydraulic conductivity (k_{unsat}) is calculated as a product of saturated hydraulic conductivity (k_{sat}) and relative hydraulic conductivity (k_r).

Table 5.1. Input soil properties in RSPile

General properties	Sand
Saturated unit weight (kN/m^3)	18.59
Effective angle of friction (°)	39.22
Initial stiffness of p-y curve, K_{py} (kN/m^3)	1170

Table 5.2. Input soil properties in PLAXIS 2D

General properties	Sand
Saturated unit weight (kN/m^3)	18.57
Unsaturated unit weight (kN/m^3)	14.49
Saturated Young's modulus (MN/m2)	35.65
Poisson's ratio	0.300
Effective angle of friction (°)	39.22
Hydraulic properties	**Sand**
Void ratio	0.88
Residual water content	0.045
Saturated water content	0.43
Model parameter, g_a (m^{-1})	14.50
Model parameter, g_n	2.68
Saturated hydraulic conductivity, k_{sat} (m/day)	21.78

MMC model properties	Sand
Alpha	2.00
Beta	1.00
S (%)	25.60

5.3.2. Drilled shaft properties

A concrete mix design of 1:2:2.5:0.45 was used (ACI 543R 2012) to obtain the 28-day compressive strength of 35 MPa. In practice, most of the structural elements are designed to behave within the elastic range. Hence, in this study, the drilled shaft was considered to behave in the linear elastic range. Therefore, the stress-strain behavior of the drilled shaft was represented by a linear elastic model and using a non-porous drainage type in PLAXIS 2D. Table 5.3 shows the input properties of the drilled shaft in RSPile and PLAXIS 2D.

Table 5.3. Input drilled shaft properties

Parameter	Value
Material type	Elastic
Unit weight (kN/m^3)	25.00
Modulus (GPa)	27.81
Poisson's ratio	0.15

5.3.3. Mechanical load

The dimensions of a single drilled shaft were designed for a hypothetical three-story building. The floor-to-floor height of the building was 3 m, and the dimensions of the

building in the plan view were 22 m (length) × and 11 m (breadth). The height of the building was 11.4 m. A total number of 6 drilled shafts were used in the design. The dimensions of the building and the location of the drilled shafts are shown in Figure 5.1. The axial load on the drilled shaft was the summation of the dead load and the live load of the building. The dead load was calculated as the sum of weights of components of the building like beams, columns, slabs, and walls as 11780.86 kN. A live load of 2 kN/m^2 is assumed to act on the slabs. Hence the total weight of the three-story building was calculated as 13858.62 kN. The mechanical load on a single drilled shaft was calculated by dividing the total weight by the number of drilled shafts as 2310 kN.

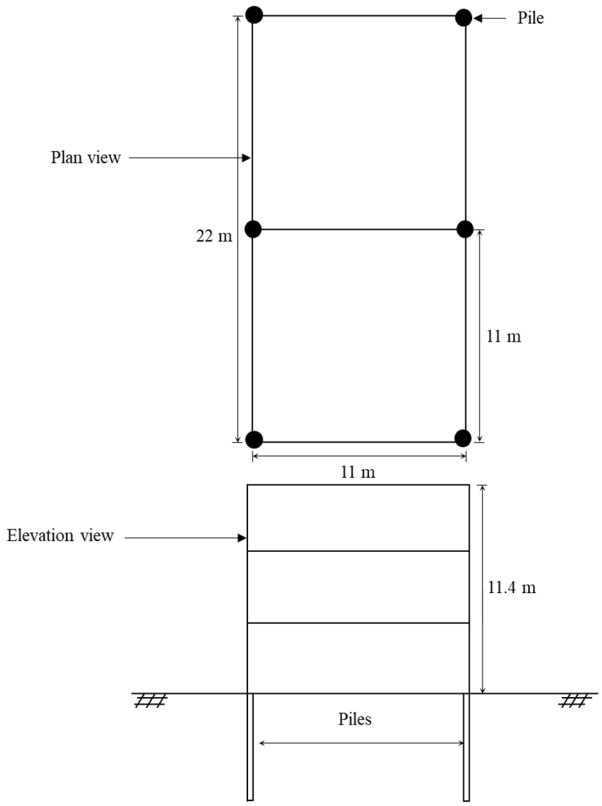

Figure 5.1. Plan and elevation view of the building

5.3.4. Earthquake load

The selected earthquake was the Northridge (1994), having a moment magnitude of 6.7, source-to-site distance of 38.3 km, and Peak Ground Acceleration (PGA) of 1.98 m/s^2. The earthquake load was applied at the bottom horizontal boundary of the finite element model in the form of acceleration-time history. For the RSPILE model calibration (pushover analysis) and the laterally loaded pile analysis in RSPile and PLAXIS 2D, a pseudo-static lateral load was applied on the top of the drilled shaft. The lateral load was calculated as 466.4 kN using Newton's second law as the product of the mass of the building and the PGA of 1.98 m/s^2.

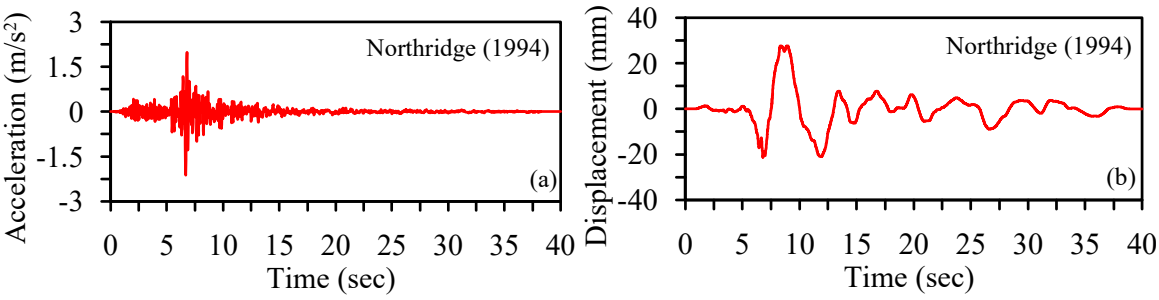

Figure 5.2. 1994 Northridge earthquake time history (a) acceleration and (b) displacement

5.3.5. Hydrological load

The hydrological load was applied as a time-history in PLAXIS 2D. The heavy rainfall data was obtained from an event on 26th August 2017 in Houston, TX, obtained from the National Climatic Data Center (NCDC). The heavy rainfall had a maximum intensity of 264 mm/day which was applied as a time-history with a constant value starting from day zero. Two types of analysis were conducted- (1) wetting front reaching halfway

along the length of the drilled shaft, having a duration of 12.5 days; and (2) wetting front reaching beyond the bottom of the drilled shaft, having a duration of 26 days.

5.4. PUSHOVER ANALYSIS

The design was carried out for a single full-scale drilled shaft subjected to an axial load of 2310 kN resulting from the mechanical load of the three-story building and a pseudo-static lateral load of 466.4 kN resulting from the Northridge (1994) earthquake. A pushover analysis was conducted in RSPile and PLAXIS 2D where the drilled shaft was (1) subjected to the pseudo-static lateral load from the Northridge (1994) earthquake and then (2) subjected to combined axial load from the mechanical load of the three-story building and pseudo-static load from the Northridge (1994) earthquake. RSPile is a software used to analyze axially loaded piles and laterally loaded piles. It can compute the pile's internal forces and displacements under various loads and soil displacements. The laterally loaded pile analysis (Reese et al. 1974) subjected to pseudo-static load from the Northridge (1994) earthquake was conducted in RSPile. In PLAXIS 2D, the full-scale drilled shaft was modeled using the "plate" element, which is a flexural structural member and a linear elastic material. The pseudo-static lateral load was then applied as a point load at the top of the drilled shaft. The two-dimensional plane strain formulation was used to model the soil-pile interaction. The simulation domain was spatially discretized using 15-Node triangular elements. The mesh was refined around the drilled shaft to accurately capture the stress and deformation variation. A mesh sensitivity study was performed to select the size and mesh of the simulation domain, which does not affect the computed results. For the vertical boundaries of the domain, the displacement was restrained in the

x- direction, and for the bottom horizontal boundary of the domain, displacement was restrained in both x and y- directions. The groundwater flow was closed for both the vertical boundaries and open for both the top and bottom horizontal boundaries of the domain. The groundwater level was set at the ground level; hence the soil domain degree of saturation was 100%. The soil properties were input as given in Table 5.1, and 5.2 were used as input in RSPile and PLAXIS 2D.

For the drilled shaft design, the first case was evaluated where the drilled shaft was subjected to the pseudo-static load from the earthquake. In this case, the pile head deflection obtained from RSPile was matched close to that obtained from PLAXS 2D by adjusting the initial stiffness of the p-y curve (K_{py}). The length of the drilled shaft was determined such that the drilled shaft achieves fixity subjected to lateral loading. The pushover analysis resulted in a 1.0 m diameter and 35 m long drilled shaft where the value of K_{py} was equal to 11770 kN/m^3 with corresponding pile head deflection in RSPile (60.26 mm) and PLAXIS 2D (67.61 mm) was close. The axially loaded analysis (Kulhawy et al. 1983; Kulhawy 1991; Coyle & Castello 1981; Reese and O'Neill 1988; Reese et al. 1974) in RSPile for the 1.0 m diameter and 35 m long drilled shaft resulted in the total axial bearing capacity was calculated as 23531 kN, corresponding to vertical settlement of 3.37 mm, where 87% of the total axial bearing capacity was provided by end bearing resistance and the rest by skin friction of the drilled shaft having a safety factor of 10.18. The lateral load governed the drilled shaft design. Additionally, the pushover analysis was also conducted for drilled shaft subjected to the combined axial load and pseudo-static load in RSPile and PLAXIS 2D. In PLAXIS 2D, the deadweight equal to the total ultimate

capacity of the drilled shaft representing the mechanical load (2310 kN) was modeled using the “plate” element available in PLAXIS 2D, which is a flexural structural member and as a linear elastic material on the top of the drilled shaft. Hence, the 1.0 m diameter and 35 m long drilled shaft were used for the combined axial load and pseudo-static load in the pushover analysis and later used in the multi-hazard analysis.

5.4.1. Drilled shaft subjected to pseudo-static load from the earthquake

Figure 5.3 shows the structural response of the drilled shaft subjected to pseudo-static loading from the earthquake. The pile head deflection in RSPile and PLAXIS 2D were 60.36 mm and 67.61 mm, respectively. The maximum shear force in RSPile (468.43 kN) was slightly higher than PLAXIS 2D (462.48 kN). The maximum bending moment in RSPile (1446.13 kN-m) was significantly higher than PLAXIS 2D (1022.67 kN-m). This case was used for the design of the drilled shaft.

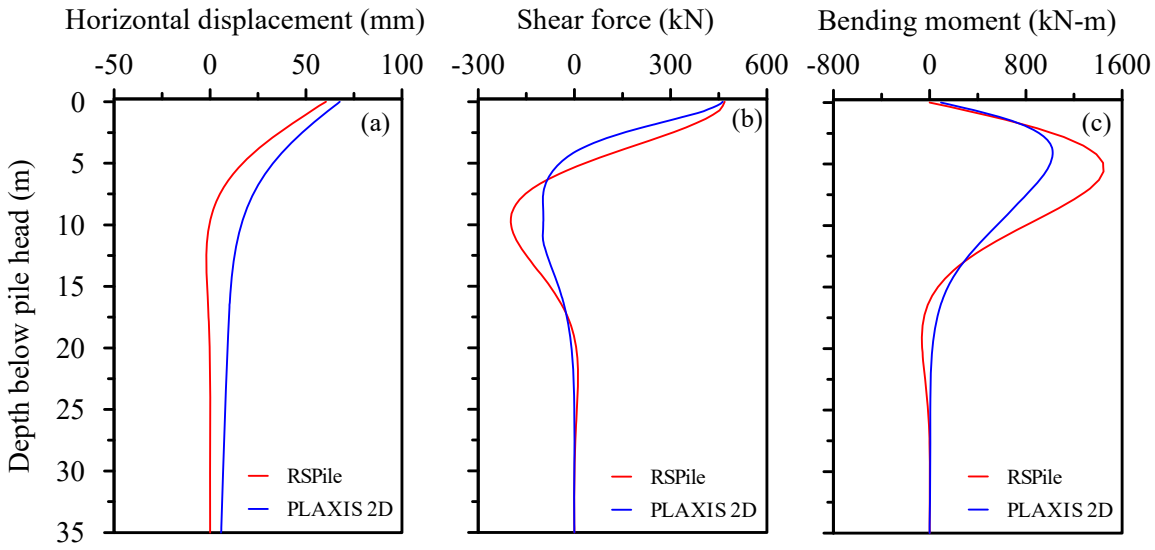

Figure 5.3. (a) Horizontal displacement, (b) shear force, and (c) bending moment variation in drilled shaft subected to pseudo-static lateral load from the earthquake

5.4.2. Drilled shaft subjected to combined axial and pseudo-static load from the earthquake

Figure 5.4 shows the structural response of the drilled shaft subjected to combined axial load from the three-story building and pseudo-static load from the earthquake. Vertical settlement of the drilled shaft was seen in both RSPile and PLAXIS 2D. The maximum vertical displacement in RSPile (3.37 mm) was very low compared to the maximum vertical displacement in PLAXIS 2D (75.6 mm). The pile head deflection in RSPile (60.35 mm) was slightly higher than PLAXIS 2D (47.89 mm). The axial force at the top of the drilled shaft in RSPile was equal to PLAXIS 2D (2304.3 kN). However, the axial force at the bottom of the drilled shaft in RSPile (719.36) was significantly higher than PLAXIS 2D (130.42 kN). The skin resistance was seen to increase with depth, where the maximum value In RSPile (1584.9 kN) was lower than PLAXIS 2D (2173.8 kN). The maximum shear force in RSPile (468.43 kN) was slightly higher than PLAXIS 2D (460.10 kN). The maximum bending moment in RSPile (1446.13 kN-m) was significantly higher than PLAXIS 2D (883.95 kN-m). The maximum pile head deflection for the combined loading was lower by 19.71 mm as compared to the pseudo-static lateral loading in PLAXIS 2D. The maximum shear force for the combined loading was lower by 2.38 kN as compared to pseudo-static lateral loading in PLAXIS 2D. Similarly, the maximum bending moment for combined loading was lower by 138.72 kN-m as compared to pseudo-static lateral loading in PLAXIS 2D. Overall, there were no considerable quantitative differences in the case where the drilled shaft was subjected to pseudo-static lateral load from the earthquake as compared to the combined loading.

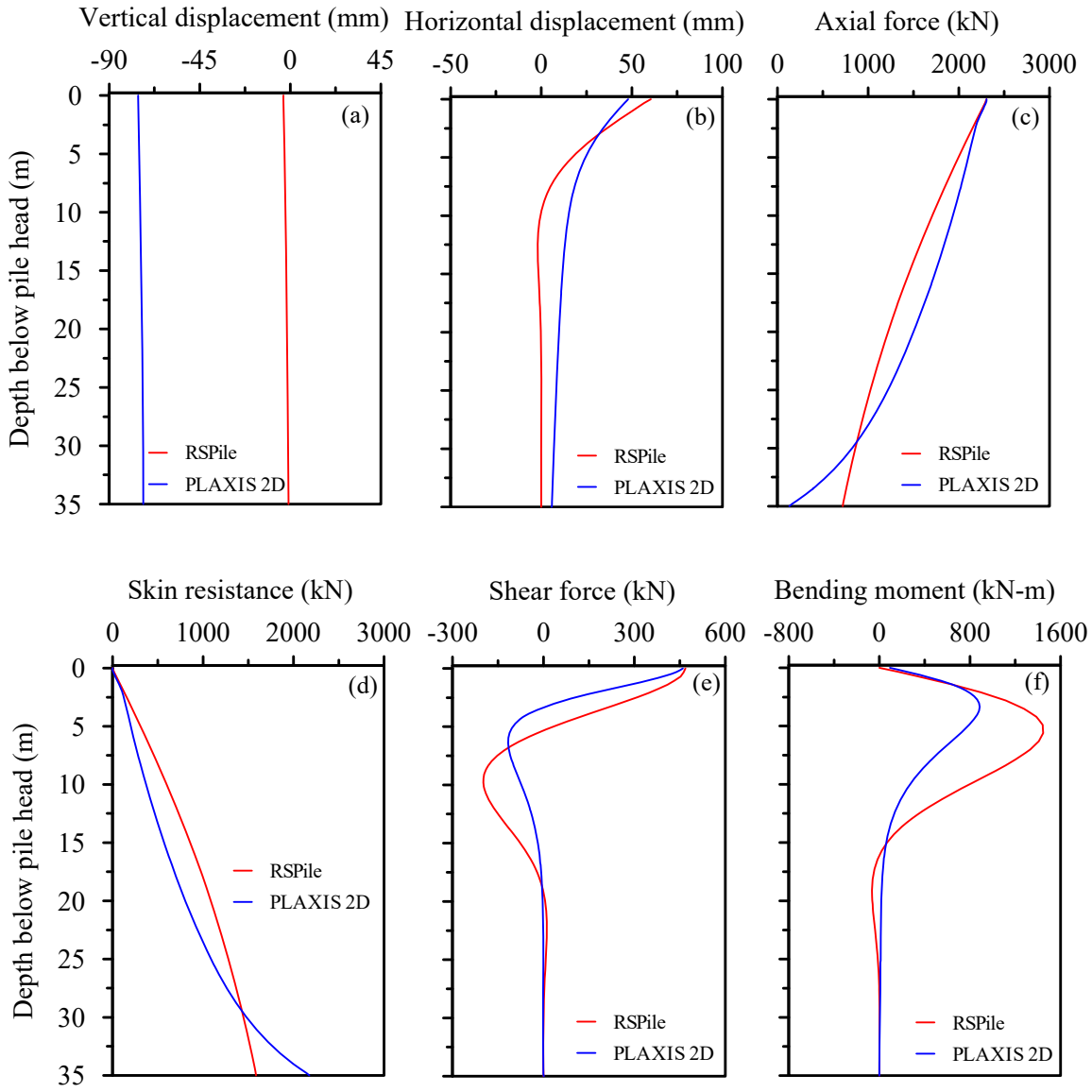

Figure 5.4. (a) Vertical displacement, (b) horizontal displacement, (c) Axial force, (d) skin resistance, (e) shear force, and (f) bending moment variation in drilled shaft subjected to combined axial and pseudo-static load from the earthquake

5.5. MULTI-HAZARD ANALYSIS

The multi-hazard analysis was conducted using the fully-coupled finite element code PLAXIS 2D, where the drilled shaft was subjected to (1) dynamic earthquake load, (2) dynamic hydrological load, (3) dynamic hydrological load when the wetting front reached halfway along length of the drilled shaft (@ 12.5 days) followed by dynamic earthquake load, and (4) dynamic hydrological load when wetting front reaches beyond the bottom of the drilled shaft (@ 26 days) followed by dynamic earthquake load. The full-scale drilled shaft and the deadweight equal to the total ultimate capacity of the drilled shaft representing the mechanical load were modeled using the "plate" element, which is a flexural structural member and defined as a linear elastic material. The dead weight represented the mechanical load (2310 kN) applied on the top of the drilled shaft. The soil deformation properties change with the flow of water (degree of saturation); hence it is crucial to couple the flow with the soil deformation. A modified Mohr-Coulomb (MMC) model capable of updating the yield criterion and modulus with changes in matric suction and/or degree of saturation (Vickneswaran and Ravichandran 2022) was used to represent the stress-strain behavior of the partially saturated soil in PLAXIS 2D. The flow of water, in general, in the three-phase media is represented by the well-known Richards equation (Dogan and Motz 2005), which is also used in PLAXIS 2D. To define the saturation-suction behavior of soil, there are many Soil Water Characteristic Curves (SWCCs) and corresponding relative hydraulic conductivity functions available in the literature. In this study, the Mualem-van Genuchten model (Mualem 1976; van Genuchten 1980) and the van Genuchten model (van Genuchten 1980) were used for defining the relative hydraulic

conductivity functions and the SWCC, which are available in PLAXIS 2D. The unsaturated hydraulic conductivity (k_{unsat}) is calculated as a product of saturated hydraulic conductivity (k_{sat}) and relative hydraulic conductivity (k_r). The two-dimensional plane strain formulation was used to model the soil-pile interaction. The simulation domain was spatially discretized using 15-Node triangular elements. The mesh was refined around the drilled shaft and ground surface to accurately capture the stress and deformation variation due to hydrological loading. A mesh sensitivity study was performed to select the size and mesh of the simulation domain, which does not affect the computed results. For the vertical boundaries of the domain, the displacement was restrained in the x- direction, and for the bottom horizontal boundary of the domain, displacement was restrained in both x and y-directions. The groundwater flow was closed for both the vertical boundaries and open for both the top and bottom horizontal boundaries of the domain. The earthquake boundaries used in PLAXIS 2D include viscous boundaries on the vertical sides and a prescribed displacement with the acceleration-time history along the bottom of the model. Figure 5.3. shows the simulation domain for the full-scale drilled shaft in the sand.

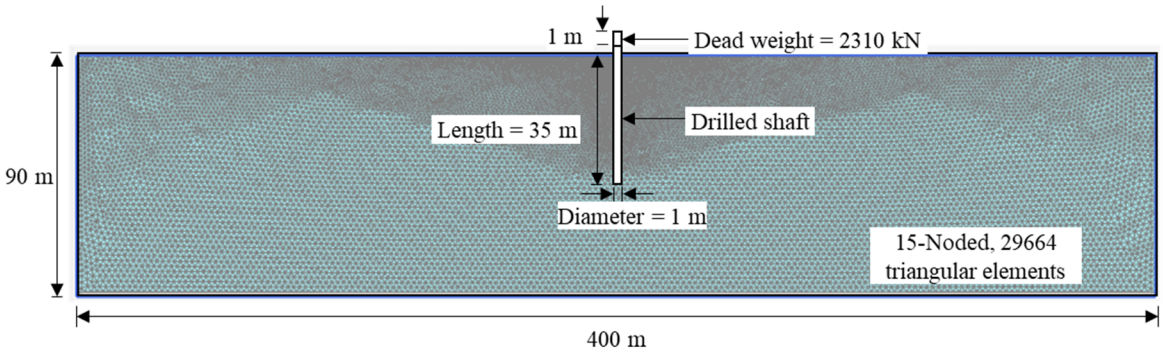

Figure 5.5. Simulation domain in PLAXIS 2D

5.5.1. Drilled shaft subjected to dynamic load from the earthquake

Figure 5.6 shows the structural response of the drilled shaft subjected to dynamic load from the earthquake. Negligible vertical settlement and horizontal displacements of the drilled shaft were seen. The axial force at the bottom of the drilled shaft was equal to 52.55 kN, which suggests that most of the bearing capacity is contributed by skin resistance. The maximum shear force was equal to 14.6 kN, and the maximum bending moment was 6.34 kN-m. Overall, the displacements, shear force, and bending moment induced in the drilled shaft when subjected to dynamic load from the earthquake were very low as compared to the pseudo-static and combined loading.

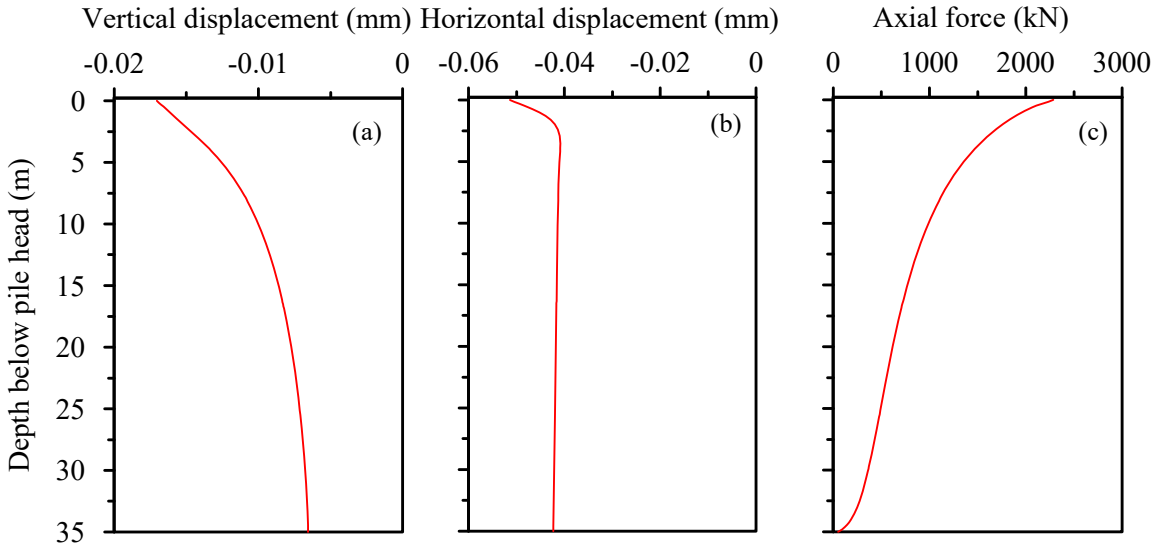

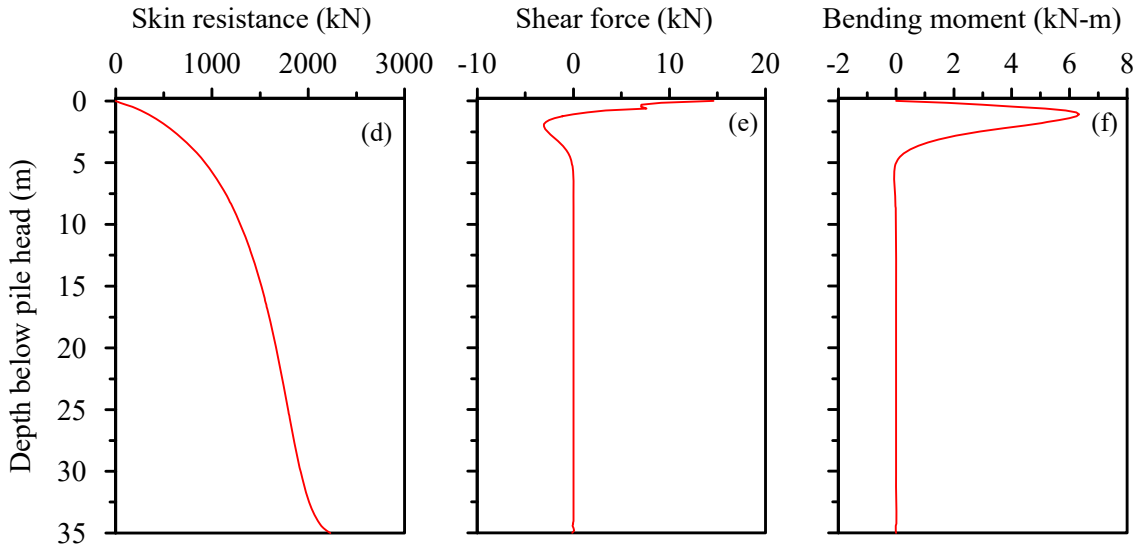

Figure 5.6. (a) Vertical displacement, (b) horizontal displacement, (c) Axial force, (d) skin resistance, (e) shear force, and (f) bending moment variation in drilled shaft subjected to dynamic load from the earthquake

5.5.2. Drilled shaft subjected to dynamic load from heavy rainfall

Figure 5.7 shows the structural response of the drilled shaft subjected to dynamic load from heavy rainfall. The maximum degree of saturation (DOS) within the wetting front was approximately 50%, and the minimum DOS below the wetting front was approximately 11%. Slight vertical upward vertical displacement and negligible horizontal displacements of the drilled shaft were seen. Upward vertical displacement occurs due to an increase in the volume of the soil when water enters the soil matrix from heavy rainfall. The upward vertical displacement of the drilled shaft when the wetting front reaches halfway along the length of the drilled shaft (1.60 mm) was more than the upward vertical displacement when the wetting front reaches below the bottom of the drilled shaft (1.5 mm). Hence, the upward vertical displacement was maximum at the start of heavy rainfall and then resided as the wetting front traveled down. The axial force at the bottom of the

drilled shaft was equal to 52.55 kN, which suggests that most of the bearing capacity is contributed by skin resistance. There were negligible differences in the axial force and skin resistance when the wetting front reached halfway as compared to the wetting front reaching below the drilled shaft.

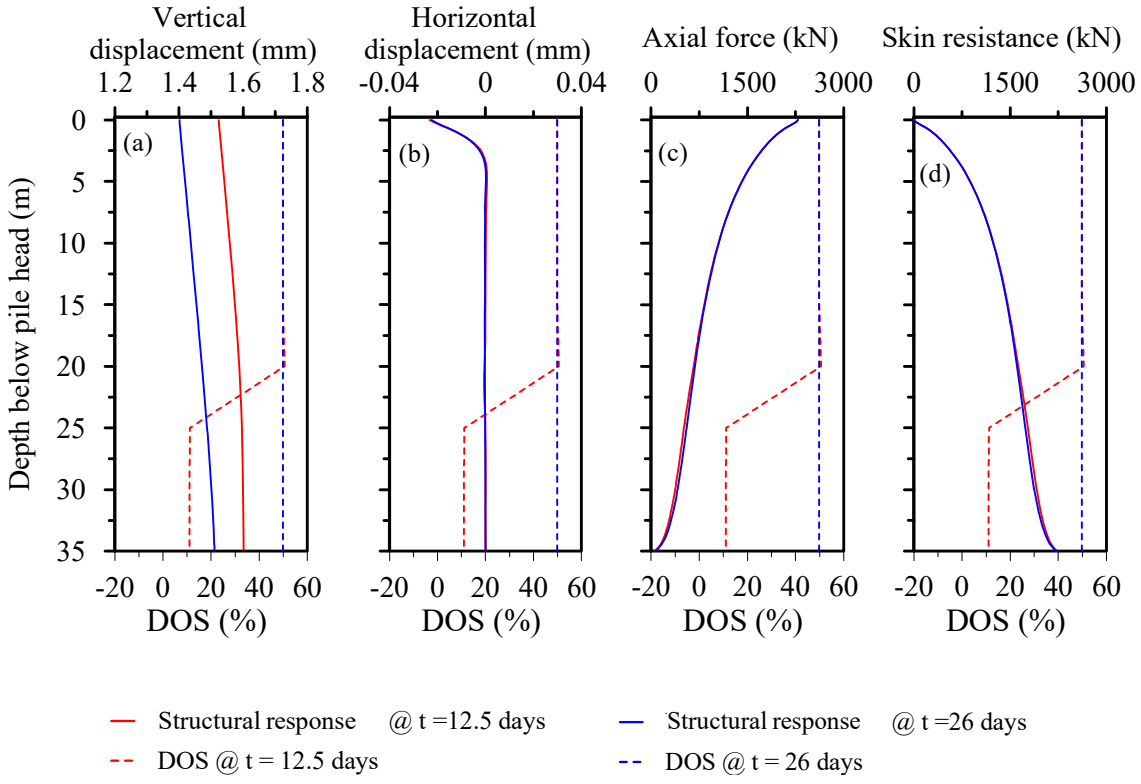

Figure 5.7. (a) Vertical displacement, (b) horizontal displacement, (c) Axial force, (d) skin resistance variation in drilled shaft subjected to dynamic load from heavy rainfall

5.5.3. Drilled shaft subjected to dynamic load from heavy rainfall and earthquake

Figure 5.8 shows the structural response of the drilled shaft subjected to dynamic load from heavy rainfall followed by dynamic load from the earthquake. The results were obtained at the end of the earthquake. Significant vertical settlement and negligible horizontal displacements of the drilled shaft were seen. The vertical settlement for drilled shaft subjected to dynamic load from rainfall followed by the earthquake (7.74 mm) is very high compared to the case where the drilled shaft was subjected to dynamic load from the earthquake (0.01 mm). Hence, the combined effect of heavy rainfall and earthquake can cause more damage to the deep foundations. The maximum shear force when the wetting front reaches halfway was slightly higher (8.18 kN) than the case when the wetting front reaches beyond the bottom of the drilled shaft (7.61 kN). Similarly, the maximum bending moment when the wetting front reaches halfway was slightly higher (8.41 kN-m) than the case when the wetting front reaches beyond the bottom of the drilled shaft (8.22 kN-m). Therefore, the case when the wetting front reaches halfway was slightly worse than when the wetting front reaches beyond the bottom of the drilled shaft.

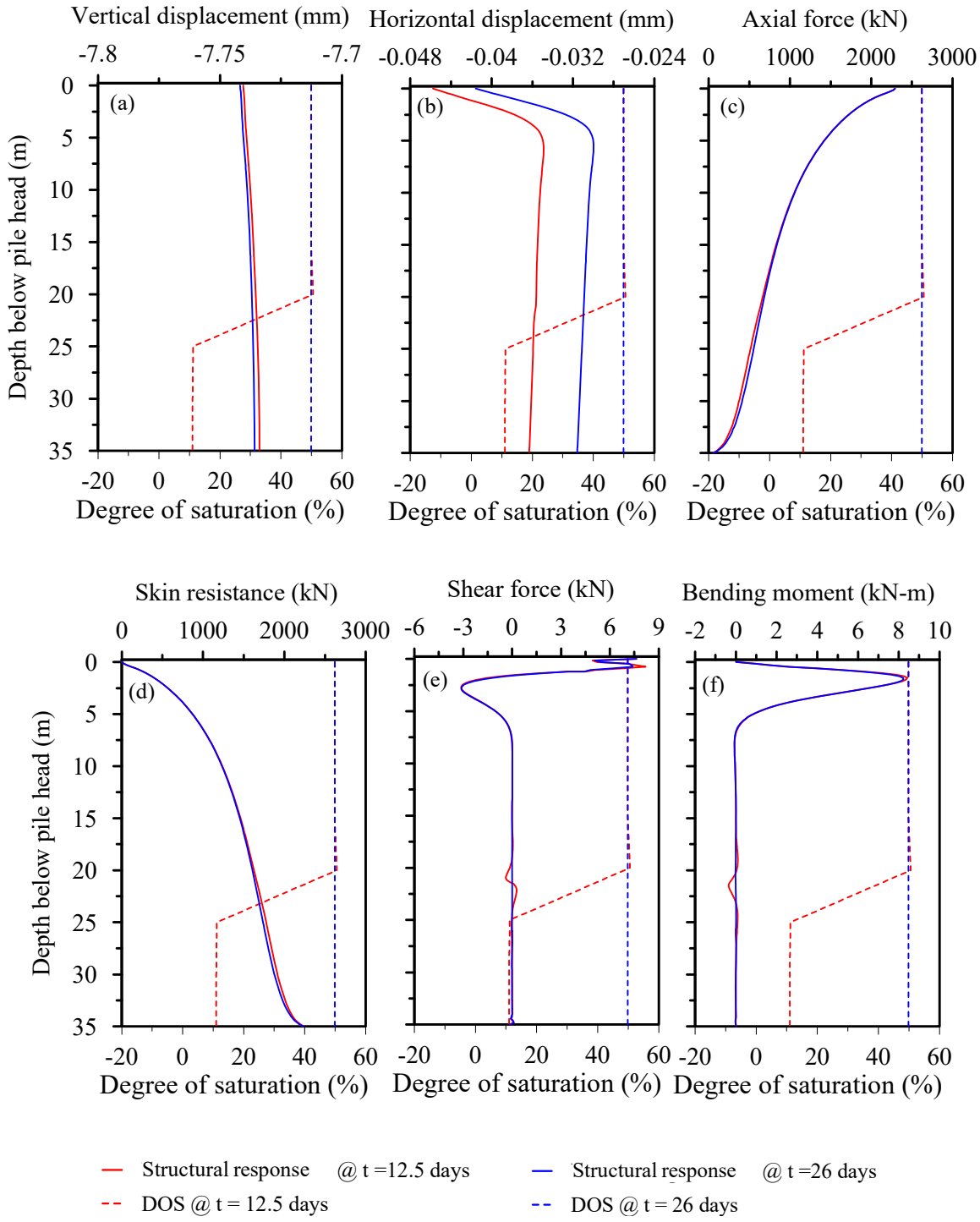

Figure 5.8. (a) Vertical displacement, (b) horizontal displacement, (c) Axial force, (d) skin resistance, (e) shear force, and (f) bending moment variation in drilled shaft subected to dynamic load from heavy rainfall and earthquake

5.6. CONCLUSION

This study evaluates the effect of multi-hazard events, including heavy rainfall followed by an earthquake, on the structural responses of a drilled shaft designed for a three-story building. Following were the key observations.

1. The displacements, shear forces, and bending moments induced in the drilled shaft when subjected to dynamic loading from the earthquake were very low as compared to the pseudo-static loading from the earthquake and also combined axial loading from the three-story building and pseudo-static loading from the earthquake.
2. When the drilled shaft was subjected to the dynamic load from heavy rainfall, upward vertical displacement occurred due to an increase in the volume of the soil when water entered the soil matrix from the heavy rainfall. The upward vertical displacement was maximum at the start of heavy rainfall and then resided as the wetting front traveled down.
3. When the drilled shaft was subjected to the dynamic load from heavy rainfall followed by dynamic load from the earthquake, the vertical settlement for the drilled shaft was very high (7.74 mm) compared to the case where the drilled shaft was subjected to dynamic load from the earthquake (0.01 mm). Hence, the combined effect of heavy rainfall and earthquake can cause more damage to the deep foundations.
4. There were no considerable differences observed in the structural response of the drilled shaft when the wetting front reaches halfway along the length of the drilled

shaft as compared to when the wetting front reaches beyond the bottom of the drilled shaft.

5. The shear strength of soils decreases with an increase in the degree of saturation/loss of matric suction (Fredlund et al. 1978). In this study, the drilled shaft in the sand was evaluated, which did not saturate completely. Hence, other types of soils should also be evaluated to gain a better understanding of the multi-hazard effects on the deep foundation.

REFERENCES

Aviles Engineering Corporation. (2010). Geotechnical Investigation, City of Houston, Surface Water Transmission Program, Houston, Texas (p. 65). Houston, Texas: Aviles Engineering Corporation.

Bentley. (2021). PLAXIS 2D- Reference Manual.

Carsel, R.F., Parrish, R.S. (1988). Developing joint probability distributions of soil water retention characteristics. Water Resources Research, 24(5), 755–769.

Coyle, H. M. and Castello, R. R. 1981. New design correlations for piles in sand. J. Geotech. Engrg. Div., ASCE, 107(GT7), 965-986

Documentation and Theory Overview. Rocscience. (2022). https://www.rocscience.com/help/rspile/overview

Dogan, A., and Motz, L. H. (2005). "Saturated-unsaturated 3D (SU3D) groundwater model, I: Development." J. Hydrologic Eng. 10(6), 492–504.

Fredlund, D.G., Morgenstern, N.R., Widger, R.A. (1978). "The shear strength of unsaturated soils." Can. Geotech. J, 15 (3), 313–321.

Kulhawy, F. H., Trautmann, C. H., Beech, J. F., O'Rourke, T. D., McGuire, W., Wood, W.A., and Capano, C. (1983). "Transmission line structure foundations for uplift-compression loading." Electric Power Research Institute, Palo Alto, Calif.

Kulhawy, F. H. 1991. "Drilled shaft foundations, Foundation engineering handbook," 2nd Ed., Chap. 14, H.-Y. Fang ed., Van Nostrand Reinhold, New York.

Reese, L. C., and O'Neill, M. W. (1988). "Drilled shafts: Construction and design." FHWA, Publication No. HI-88-042.

Reese, L.C., W.R. Cox & F.D. Koop. (1974). Field testing and analysis of laterally loaded piles in sand. Proceedings of the VI Annual Offshore Technology Conference, Houston, Texas, 2(OTC 2080): 473-485.

United Nations. (2022). What is Climate Change? United Nations. https://www.un.org/en/climatechange/science/key-findings#physical-science

Vickneswaran, T., Jella, V. S., Ravichandran, N., & Piratla, K. R. (2021). Fully Coupled Flow Deformation Analysis of Buried Concrete Pipe Using Finite Element Software Plaxis 2D. *Geo-Extreme 2021*. https://doi.org/10.1061/9780784483695.021

Vickneswaran, T., and Ravichandran, N. (2023). "Performance of Geotechnical Systems Under Extreme Hydroclimatic Events Using a New User-defined Soil Model in Plaxis." Journal of GeoEngineering, Vol. 18 Issue 1, p21-31. 11p

Zscheischler, J., Westra, S., van den Hurk, B. J. J. M., Seneviratne, S. I., Ward, P. J., Pitman, A., AghaKouchak, A., Bresch, D. N., Leonard, M., Wahl, T., & Zhang, X. (2018). Future climate risk from compound events. Nature Climate Change, 8(6), 469–477. https://doi.org/10.1038/s41558-018-0156-3

CHAPTER 6. COMPARISON OF STRUCTURAL RESPONSE OF BRIDGE DRILLED SHAFT PREDICTED FROM DIFFERENT METHODS SUBJECTED TO LIQUEFACTION-INDUCED LATERAL SPREADING

6.1. ABSTRACT

There are several methods used to design drilled shafts subjected to liquefaction-induced lateral spread, but their accuracy and applicability are not well understood. In this study, the structural performance of drilled shaft at an End bent of a proposed bridge located at the U.S. Highway 76 over Lynches River, Florence/Lee County, South Carolina, was predicted using three different methods considering during- and after-liquefaction scenarios, and the results were compared. These methods include (a) simplified analytical method, (b) rigorous analytical method, and (c) coupled finite element method. The simplified analytical method included using site-specific pseudo-static loading, while the rigorous analytical method included using site-specific dynamic loading considering multiple earthquake scenarios for comparison purposes. The coupled finite element simulations were conducted considering multiple earthquake scenarios using RS2 software capable of modeling soil-pile interaction. The soil properties and the other input parameters were obtained from the initial geotechnical design report. Results showed that the predicted drilled shaft structural response from the three methods was highest for the during-liquefaction scenario. The structural response estimated using the finite element method provided more realistic results than the analytical methods.

6.2. INTRODUCTION

Liquefaction occurs when a loose saturated granular soil deposit is subjected to cyclic loading from an earthquake, resulting in the buildup of excess pore water pressures and causing limited or complete soil shear strength loss. After the dissipation of pore water pressures, some shear strength is recovered to a residual value. Lateral spreading occurs due to the liquefaction of such a soil deposit located below a non-liquefiable deposit on a gentle slope which results in finite lateral movement of the non-liquefiable deposit, causing slope movement and instability. Hence, the shear strength of the liquefiable soil deposit during- and after-liquefaction conditions needs to be considered for designing bridge foundations subjected to liquefaction-induced lateral spreading.

In the case of bridge foundations, particularly at End-bents, where the deep foundation is already subjected to lateral load from the embankment and the horizontal load from the vehicles on the deck, the liquefaction-induced lateral spreading imposes an additional lateral load on the deep foundation, which can exceed its lateral capacity causing damage to the deep foundation and the bridge if not accounted in the design stage. The liquefaction-induced lateral spreading caused by the 2010 El Mayor-Cucapah earthquake of magnitude 7.2 damaged a pair of parallel bridges in northern Baja California, Mexico (Turner et al. 2016). It resulted in the collapse of the railroad bridge, and flexural cracking was observed in the highway bridge columns. The 1995 Hyogoken-Nambo earthquake caused severe damage to many structures, including the bridge foundations located along

the coastal line, due to liquefaction-induced lateral spreading (Hamada et al. 1996).

The existing analytical methods used to evaluate the structural response of bridge foundations caused by liquefaction-induced lateral spreading are based on simplified or rigorous analytical methods. The simplified analytical methods include (a) the Displacement Based Method (SCDOT GDM 2022, Section 14.8.6.1 and CALTRANS 2017) based on the Simplified Rigid Block Newmark Analysis, which requires inputting various parameters into empirically calibrated equations that estimate the free-field slope displacement (Jibson et al. 2013) and imposing the estimated displacements on the foundation to estimate the foundation structural response, and (b) the Force Based Method which includes imposing limit pressures which are calculated as 30% of total overburden pressure (SCDOT GDM 2022, Section 14.8.6.2) and then imposed on the foundation to estimate the foundation structural response. However, the Force-Based Method is considered over-conservative as it provides less insight than the Displacement-Based Method (Ashford et al. 2011) and a relatively more restrictive approach because it assumes that soil displacements are large enough to fully mobilize the lateral earth pressures from the spreading crust and liquefiable layer against the deep foundations (SCDOT GDM 2022, Section 14.8.6). The simplified analytical method selected for this study is the Displacement Based Method which uses an empirical equation that is also available as a chart called the Simplified Newmark chart (Anderson et al. 2008). This empirical equation is a result of Newmark sliding block analyses conducted on a set of strong ground motion records (Hynes and Franklin 1984) and regression analysis for the Central and Eastern United States (CEUS) region and soil site conditions. Amiri (2008) followed a similar

methodology to the simplified analytical method used in this study and used the charts developed by Martin and Qiu (1994) to estimate design displacement demands on foundations for the Missouri Bridge, MO, and Washington Bridge, WA. The design displacement demands were reported as 508 mm and 330 mm, respectively, for a 2475-year return period. Yang et al. (2020) proposed a simplified method based on Newmark sliding block analysis to predict lateral spreading displacements. This method underpredicted the real site-specific recorded displacements for five case histories, and a safety factor was recommended.

The existing simplified analytical method has several limitations: (a) the use of pseudo-static seismic load for the slope stability analysis, but dynamic load needs to be used for accuracy, and (b) the limit state analysis cannot consider the soil-structure interaction, which is important for accurately predicting the additional force on the foundation due to lateral spreading. To overcome the first limitation and for accuracy, the rigorous analytical method is used in this study which is based on the Rigorous Rigid Block Newmark Analysis, where the cumulative slope displacements are calculated by double integrating the parts of the acceleration-time history of input ground motions that lie above the critical acceleration (Jibson et al. 2013; Rocscience 2022). However, the design manuals do not describe the procedure for estimating the free-field slope displacement and imposing the estimated displacements on the foundation for the rigorous analytical method. Hence, a similar procedure as described for the simplified analytical method was used for the rigorous analytical method to estimate the foundation structural responses. The finite element method is capable of modeling dynamic loading as well as soil-pile interaction,

which facilitates overcoming both limitations.

The objective of this study is to quantify the structural response of the bridge drilled shaft foundation caused by liquefaction-induced lateral spreading before-liquefaction (BL), during-liquefaction (DL), and after-liquefaction (AL) using the simplified analytical method, rigorous analytical method, and finite element method and comparing them. The DL and AL scenarios were simulated by assigning the corresponding residual shear strength properties to the liquefiable layer.

6.3. CASE STUDY

6.3.1. Site location

Figure 6.1 (a) shows the location of the new bridge currently under construction (Figure 1 (c)) that will replace the existing old bridge (Figure 6.1 (b)) at U.S. Highway 76 over Lynches River in Florence/Lee County, South Carolina. Figure 1 (d) shows the elevation view of the new bridge with the soil profile and location of the End bent-1 considered in this study. The groundwater table varies from 7.13 to 11.2 m measured from the top of the Fill due to seasonal and climatic variations, and it was assumed to be at 9.12 m depth (GeoStellar Engineering, LLC 2019). At the End bent-1, the fill (SM-SC) thickness is approximately 5.5 m, and the Duplin upper formation (CL) extends to approximately 2.0 m below the Fill. The medium-dense saturated alluvial soil deposits SP1 and SP2 (SP) extend 3.8 m below the Duplin upper formation. According to the seismic hazard evaluation discussed in the subsequent section, the SP2 deposit was evaluated as susceptible to limited to complete liquefaction.

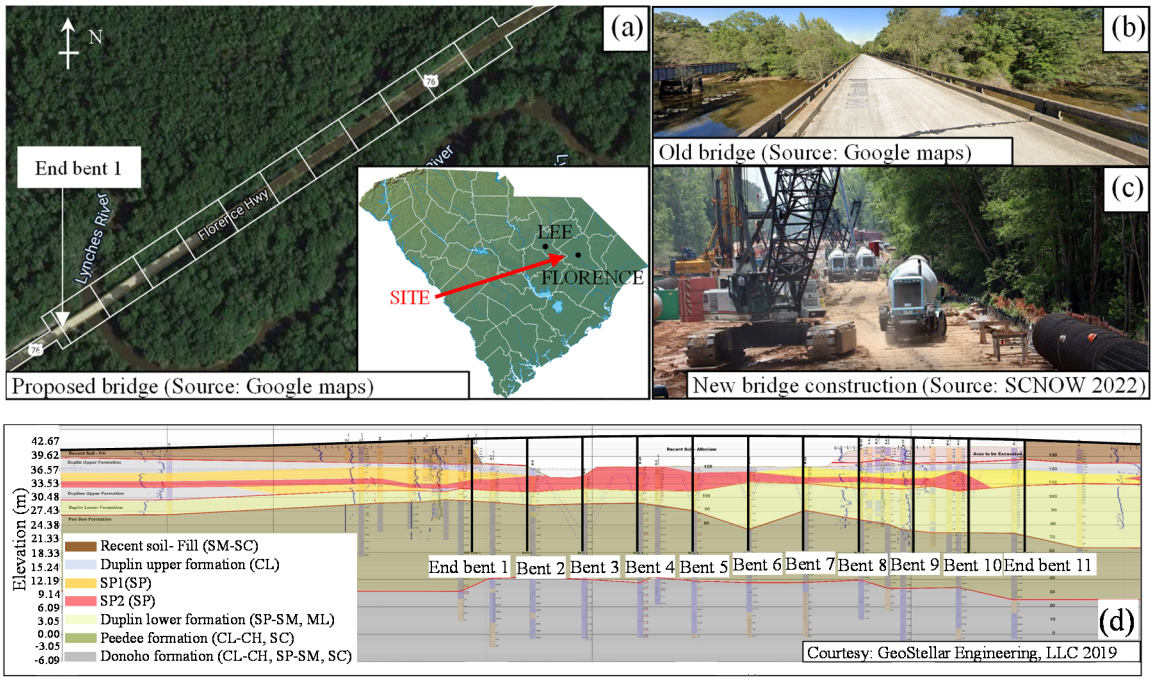

Figure 6.1. (a) Proposed location of the new bridge, (b) old bridge, (c) new bridge under construction, and (d) soil profile and the new bridge elevation

6.3.2. Soil properties

Table 6.1 shows the soil properties adopted for the seismic slope stability analysis using SLIDE2 (v9.0), pushover analysis using RSPile (v3.0), and finite element analysis using RS2 (v11.0). The site-specific soil properties for BL, DL, and AL scenarios, which include cohesion (c), friction angle (ϕ), and unit weight (γ), were estimated from the SPT and CPT data, and the undrained shear strength (c_u) were obtained from the laboratory triaxial tests (GeoStellar Engineering, LLC 2019). The shear wave velocity (V_s) and Poisson's ratio were estimated from the downhole shear wave velocity test data (GeoStellar Engineering, LLC 2019). Based on the elastic theory, Young's moduli (E) were then estimated using V_s. The relative densities (D_r) were calculated from the SPT data (Skempton 1986). The residual shear strength parameters for DL and AL scenarios were

calculated only for the SP2 deposit as it was found to be susceptible to limited to complete liquefaction based on the seismic hazard evaluation (SCDOT GDM 2022, Section 13.6-13.10). For the AL scenario, these parameters were obtained from soil shear strength loss (SSL) seismic hazard evaluation. For the DL scenario, these parameters were calculated using the residual strength-relative density relationship chart (Hargy 2011), which is based on modified triaxial tests. This chart was developed based on dynamic laboratory tests, including the centrifuge slip ring test, centrifuge drive motor test, ring shear test, and modified triaxial test. The p-y curves for sand (Reese et al. 1974), soft clay (Matlock 1970), and stiff clay without free water (Welch and Reese 1972) available in RSPile were used for the pushover analysis.

Table 6.1. Input soil properties for SLIDE2, RSPile, and RS2

	Fill	**Duplin Upper**	**SP1**	**SP2**			**Duplin lower**	**Peedee**	**Donoho**
				BL	**DL**	**AL**			
ϕ (°)	33	5	34	32	0	0	10	5	5
c (kPa)	8.62	38.30	2.39	2.38	1.67	9.09	35.91	167.58	191.52
γ (kN/m^3)	18.85	18.06	15.71	15.71	15.71	15.71	15.71	19.63	19.63
D_r (%)	51.64	22.36	41.82	28.86	28.86	28.86	22.36	64.82	65.82
E (MPa)	266	266	129	129	129	129	382	1150	398
c_u (kPa)	-	23.94	-	-	-	-	-	112.52	167.58
ε_{50}	-	0.02	-	-	-	-	-	0.005	0.005
k_{py} (MN/m^3)	25.02	-	5.56	2.78	2.78	2.78	5.56	-	-

ε_{50}- strain corresponding to one-half of the maximum principal stress difference; k_{py}- initial stiffness of the p-y curve.

6.3.3. Initial drilled shaft geometry and properties

A drilled shaft with a diameter of 1.37 m was used, and its length was determined from minimum penetration analysis, as discussed in the subsequent section. The compressive strength of 35.85 MPa for the concrete and yield strength of 455 MPa for the rebar was used in this study. Sixteen US#11 rebars (8 bundles of 2) with a concrete cover of 140 mm were used for the drilled shaft. The dimensions of the drilled shaft and concrete and rebar properties at End bent-1 were used in RSPile and RS2 and were obtained from the geotechnical report (GeoStellar Engineering, LLC 2019).

6.4. METHOD 1: STRUCTURAL RESPONSE OF DRILLED SHAFT USING SIMPLIFIED ANALYTICAL METHOD

Initially, the design displacement demand induced by liquefaction-induced lateral spreading on the drilled shaft foundation at End bent-1 was determined per the procedure outlined in CALTRANS (2017) and SCDOT GDM (2022) for the DL and AL scenarios. This procedure involved: (1) Soil SSL seismic hazard evaluation; (2) Generation of the displacement response of the sliding mass curve; (3) Generation of foundation resisting force vs. soil displacement curve; (4) Determination of design displacement demand.

The site-specific design earthquake parameters for the SEE event with peak ground acceleration (PGA) of 0.279 g, moment magnitude (M_w) of 7.37, and epicentral distance

(R) of 38.3 km were obtained from a computer program called Scenario_PC (Chapman 2006) for seismic hazard analysis in South Carolina. The site was classified as class D. Then, a minimum penetration analysis was conducted by imposing the design displacement demand on the drilled shaft to determine the minimum length of the drilled shaft, which can attain fixity. Finally, the structural response of the drilled shaft foundation at End bent-1 corresponding to the design displacement demands was determined for the DL and AL scenarios.

6.4.1. Simplified Analytical Method for Determination of the Design Displacement Demand

The determination of design displacement demand on the drilled shaft at End bent-1 induced by liquefaction-induced lateral spreading was conducted for the DL and AL scenarios using the simplified analytical method as follows:

6.4.1.1. Step 1: Soil SSL seismic hazard evaluation to determine AL residual shear strength:

The soil SSL seismic hazard evaluation started with the soil SSL susceptibility screening process, followed by soil SSL triggering analysis, and concluded with determining AL residual shear strength as per SCDOT GDM (2022), Section 13.6-13.10 (GeoStellar Engineering, LLC 2019). The evaluation was conducted using in-situ characterization data, the geological age of soil deposits, and seismic response analysis results (GeoStellar Engineering, LLC 2019). Based on the screening process, the

equivalent clean sand SPT corrected blow count ($N^*_{1,60,cs}$) values for the saturated deposits were estimated-Duplin upper (9.1), SP1 (12.1), SP2 (7.6), Duplin lower (9.8), Peedee and Donoho (26-46) which were lower than 30 blows/ft (SCDOT GDM 2022, Section 13.6.1) revealed that deposits above Peedee are susceptible to SSL (GeoStellar Engineering, LLC 2019). The susceptibility of sand-like soils has been found to be a function of geologic age which is estimated by liquefaction age correction factor (K_{DR}) and calculated as per SCDOT GDM (2022) Section 13.9.5.2, Eq 13.30. The K_{DR} value was equal to 1-1.2 for the SP2 deposit and above. The Duplin lower, Peedee, and Donoho formations had K_{DR} values equal to 4.6, 3.0, and 3.0, respectively. A higher K_{DR} value suggests more resistance to liquefaction. The Duplin upper formation is composed of clay-like soils and is not susceptible to SSL due to cyclic liquefaction. Based on the triggering analysis, the ratio of magnitude-weighted and equivalent-seismically induced Cyclic Stress Ratio to corrected, magnitude-weighted, and normalized Cyclic Resistance Ratio (CSR^*_{eq}/CRR^*_{eq}) and SSL resistance factor (φ_{SL}) values was estimated (SCDOT GDM 2022, Section 13.3.2). The following -(CSR^*_{eq}/CRR^*_{eq})<(φ_{SL}) values were obtained- Duplin upper (No SSL), SP1 (0.18<0.7), SP2 (0.72<0.85 to 1.0>0.85), Duplin lower (0.15 to 0.31<0.7), Peedee and Donoho (0 to 0.25<0.85) which showed that limited to full liquefaction can occur in SP2. Also, the excess pore pressure ratio (R_u) values were calculated- Duplin upper (No SSL), SP1 (0.19<1.0), SP2 (0.4<1.0 to 1.0), Duplin lower (0.19<1.0), Peedee and Donoho (No SSL) which supports this inference (SCDOT GDM 2022, Section 13.7; GeoStellar Engineering, LLC 2019). Hence, the SP2 deposit was selected to be susceptible to liquefaction for the lateral spreading analysis. Finally, the AL residual shear strength of

SP2 was estimated (SCDOT GDM 2022, Section 13.10.2).

6.4.1.2. Step 2: Generation of the displacement response curve of sliding mass (Curve 3) based on Simplified Rigid Block Newmark Analysis

Curve 3 was obtained by conducting seismic slope stability analysis in SLIDE2 using Spencer's method. A uniform live traffic surcharge load of 6 kPa as per SCDOT GDM (2022), Section 8.7, Table 8.8. and a pseudo-static seismic load from the SEE event (PGA= 0.279 g) was applied. First, a free field condition was modeled, which provided the depth of the critical failure surface. Figure 6.2 shows the Factor of Safety (FS) variation in the slope obtained from SLIDE2 for the seismic slope stability analysis conducted for the AL free-field condition and subjected to a pseudo-static load of the SEE event (PGA = 0.279 g). The minimum FS was obtained as 0.6. The corresponding failure surface was selected at a radius of 31.53 m. The failure surface depth from Ground Level (GL) was 11.36 m in the middle of the liquefied soil deposit (SP2). The maximum driving force (D) and resisting force (C) were 1472.2 kN and 901.02 kN, respectively, giving the D/C ratio equal to 1.63 and the C/D ratio or FS equal to 0.6. The yield coefficient (k_y) was obtained at the exact same location, which was equal to 0.097 g. Then, the corresponding free-field soil displacement was calculated using the SCDOT GDM (2022), Equation 13-72 which is based on the Simplified Newmark chart (Anderson et al. 2008). This equation is a result of direct Newmark sliding block analyses conducted on a set of strong ground motion records (Hynes and Franklin 1984) and regression analysis for the Central and Eastern United States (CEUS) region and soil site conditions. The calculated soil displacements were

doubled to obtain soil displacements at an 84% confidence level (Kavazanjian et al. 2011).

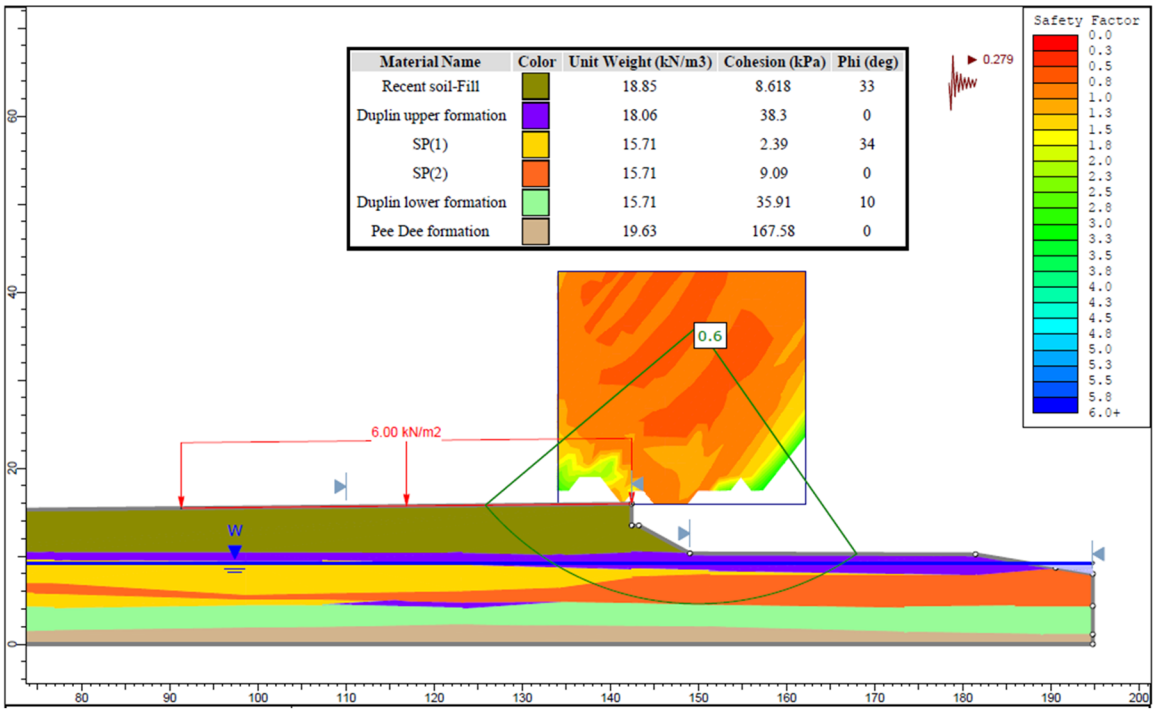

Figure 6.2. Seismic slope stability analysis for AL scenario and free field conditions using the simplified analytical method

Figure 6.3 shows the FS variation in the slope obtained from SLIDE2 for the seismic slope stability analysis conducted for DL free-field condition and subjected to a pseudo-static load of the SEE event (PGA=0.279 g) obtained from SLIDE2. The minimum FS was obtained as 0.35. The corresponding failure surface was selected at a radius of 73.68 m. The failure surface depth from GL was 8.34 m at the top of the SP1 soil deposit. The maximum driving force (D) and resisting force (C) were 1726.57 kN and 597.97 kN, respectively, giving the D/C ratio equal to 2.88 and the C/D ratio or FS equal to 0.35. The yield coefficient (k_y) was obtained at the exact same location, which was equal to 0.047

g. Then, the corresponding free-field soil displacement was calculated using the SCDOT GDM (2022), Equation 13-72.

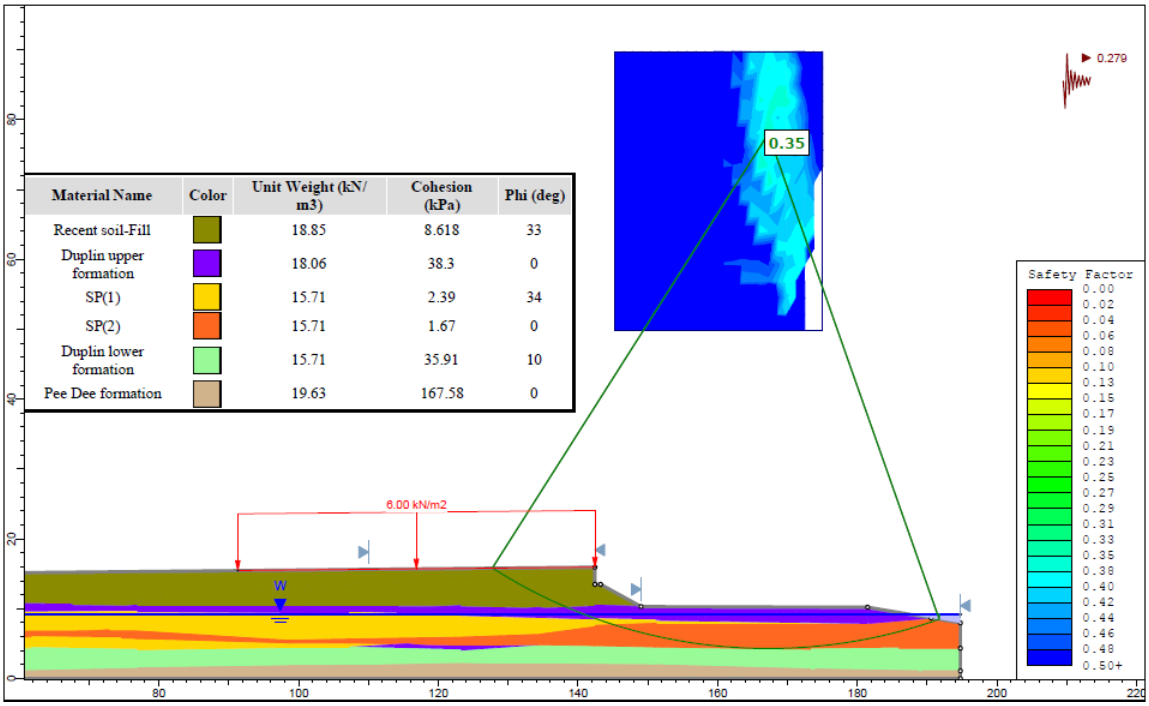

Figure 6.3. Seismic slope stability analysis for DL scenario and free field conditions using the simplified analytical method

Then, a model considering the foundation restraining action was created to obtain the maximum resisting force, which corresponds to FS=1 and zero displacements (k_y = PGA= 0.279 g) for the AL and DL scenarios. Figure 6.4 shows the FS variation in the slope for the seismic slope stability analysis conducted for the AL scenario using a restraining element and subjected to a pseudo-static load of the SEE event (PGA = 0.279 g). The maximum resisting force equal to 650 kN/m was obtained for achieving the FS equal to 1.0.

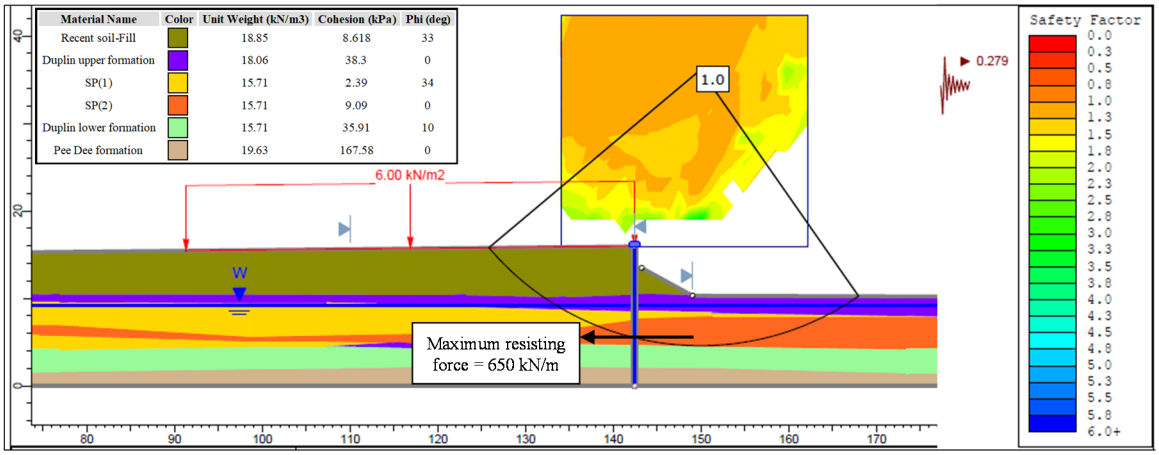

Figure 6.4. Seismic slope stability analysis for AL scenario with restraining element (FS=1) using the simplified analytical method

Figure 6.5 shows the FS variation in the slope for the seismic slope stability analysis conducted for the DL scenario using a restraining element and subjected to a pseudo-static load of the SEE event (PGA = 0.279 g) obtained from SLIDE2. The maximum resisting force equal to 1150 kN/m was obtained for achieving the FS equal to 1.0.

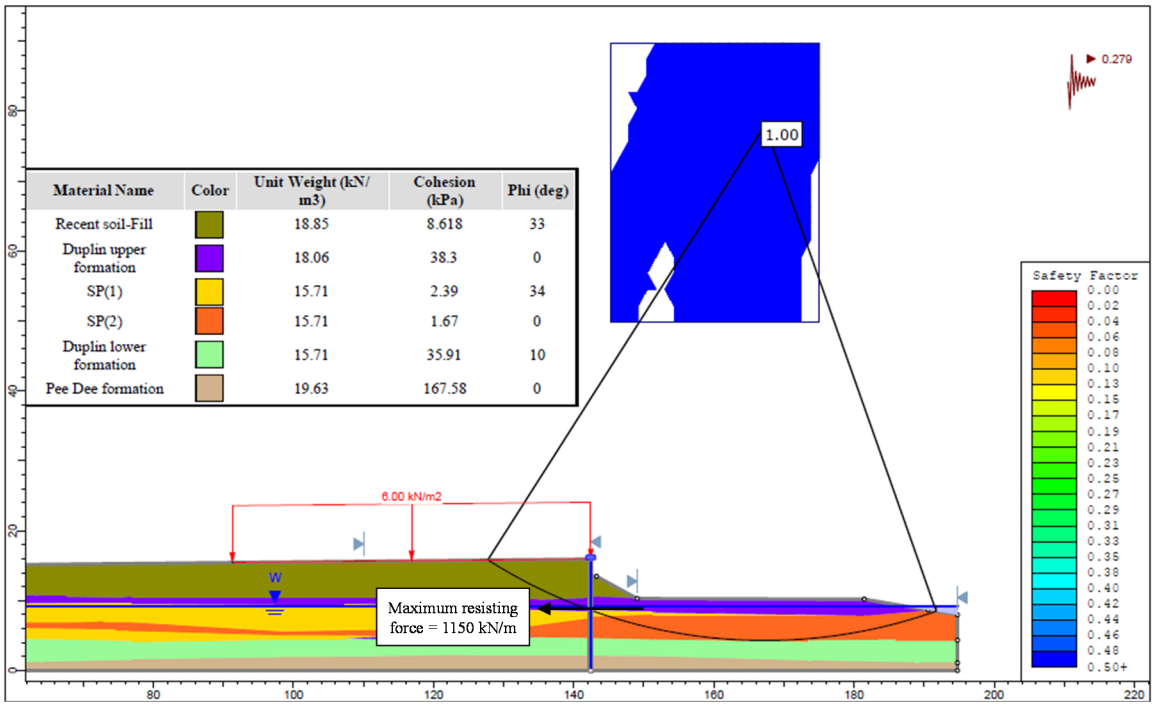

Figure 6.5. Seismic slope stability analysis for DL scenario with restraining element (FS=1) using the simplified analytical method

Apart from the yield coefficient, k_y values for the free-field or zero resisting force (critical FS), and maximum resisting force (FS=1), eight more cases were evaluated by varying the restraining force from the maximum value to the minimum value and the corresponding k_y values for the eight cases were obtained. Then, the soil displacements were calculated as per SCDOT GDM (2022), Equation 13-72, using the obtained k_y values, the restraining forces (kN/m) were multiplied by the effective width of the embankment (W_e=W+(m/2)*H=21.33 m; W=15.85 is the top width, m=2H:1V is the slope, and H=5.48 m is the height of embankment) and Curve 3 was plotted for the AL and DL scenarios as shown in Figure 6.6. For the AL scenario, the maximum resisting force after multiplying by the effective embankment width was equal to 13868.4 kN at zero displacement, and the

maximum soil displacement was 211.053 mm for zero resisting force, which can be noted in Curve 3 in Figure 6.6 (a). For the DL scenario, the maximum resisting force after multiplying by the effective embankment width was equal to 24536.4 kN at zero displacement, and the maximum soil displacement was 875 mm for zero resisting force, as seen in Figure 6.6 (b).

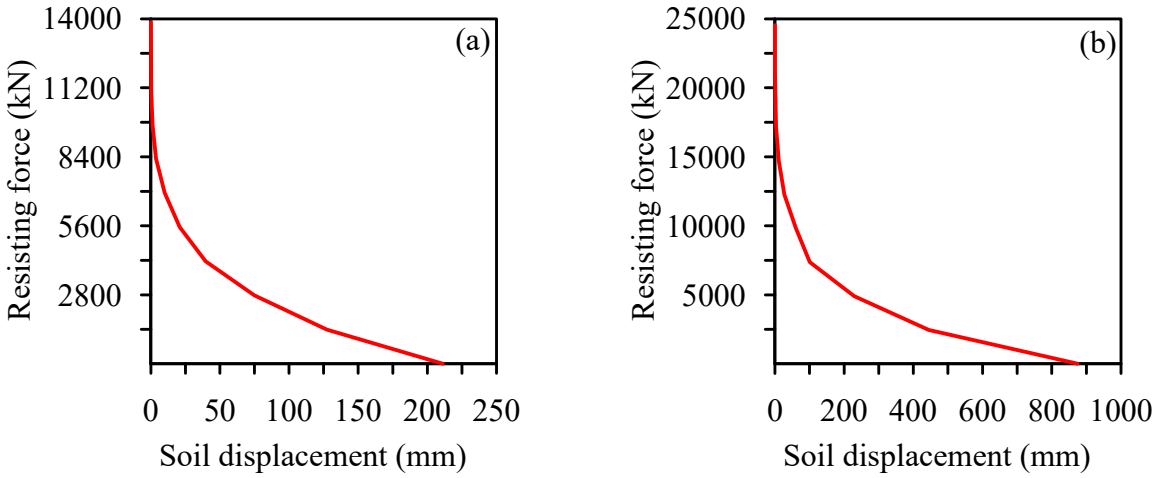

Figure 6.6. Displacement response of sliding mass (Curve 3) for (a) AL and (b) DL scenarios using the simplified analytical method

6.4.1.3. Step 3: Generation of foundation resisting force vs. soil displacement curves (Curve 1 and Curve 2)

Curve 1 and Curve 2 were generated by conducting pushover analysis for a single equivalent pile representing the pile group in RSPile. The p-y curves for sand (Reese et al. 1974), soft clay (Matlock 1970), and stiff clay without free water (Welch and Reese 1972) available in RSPile were used for the pushover analysis. First, the p-multiplier profile was defined to account for the reduction in group efficiency of the drilled shaft bent at End bent-1 for the AL and DL scenarios. The p-multiplier values of 0.36 up to the bottom of

the Fill and 0.9 below the Fill were used in this study as obtained from the geotechnical report (GeoStellar Engineering, LLC 2019).

A constant axial load of 1112 kN was obtained from structural design (GeoStellar Engineering, LLC 2019), and a series of increasing soil displacement profiles were imposed on the foundation to obtain the shear force at the critical failure surface depth corresponding to each increment of a soil profile. For the AL scenario, a series of increasing soil displacement profiles were imposed on the drilled shaft at End bent-1, ranging from maximum values of 50 mm, 100 mm, 150 mm, 200 mm, 250 mm, and 300 mm. The failure surface depth from GL, as obtained from the seismic slope stability analysis, was 11.36 m, i.e., 7.22 m from the top of the drilled shaft, which was at the middle of the liquefied soil deposit (SP2). Hence, the maximum soil displacement ranging from 50 mm to 300 mm was applied up to the top of the SP2 soil deposit and linearly varied to zero up to the bottom of the SP2 deposit. Then, from the output of RSPILE, the shear forces at the failure surface location were obtained for each soil displacement, and Curve 1 was plotted, as shown in Figure 6.7 (a). Then, Curve 2, shown in Figure 6.7 (b), was generated by calculating the running average of the resisting forces to correct Curve 1 (CALTRANS 2017; SCDOT GDM 2022).

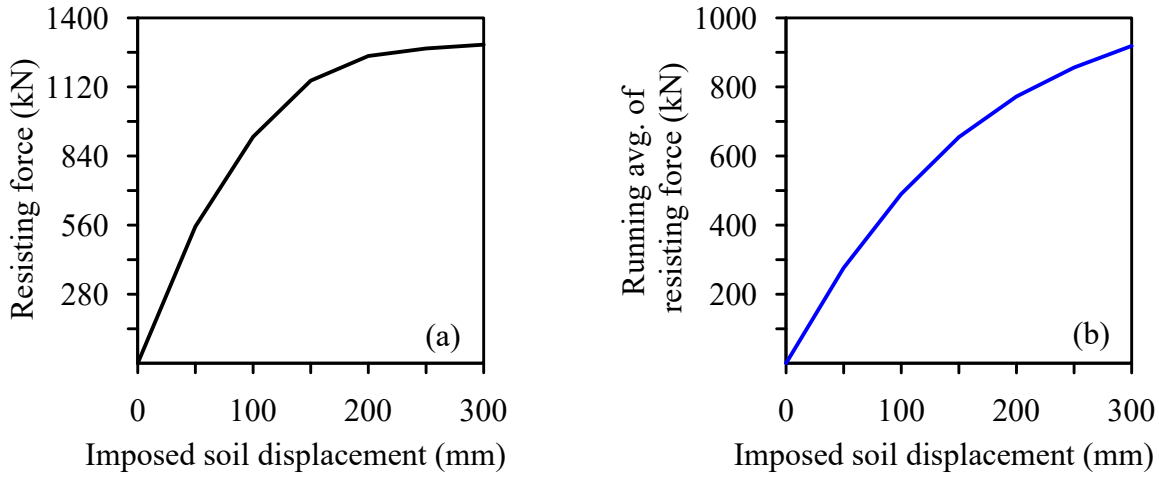

Figure 6.7. (a) Foundation resisting force vs. soil displacement (Curve 1) and (b) Running average of the foundation resisting force vs. soil displacement (Curve 2) for the AL scenario using the simplified analytical method

For the DL scenario, the same drilled shaft properties and p-y curves as used for the AL scenario were used for the DL scenario. The failure surface depth from GL, as obtained from the seismic slope stability analysis, was 8.34 m, i.e., 3.05 m from the top of the drilled shaft, which was at the top of the SP1 soil deposit. Hence, the maximum soil displacements ranging from 160 mm, 320 mm, 450 mm, 640 mm, 800 mm, and 1000 mm were applied up to the top of the SP1 soil deposit and linearly varied to zero up to the bottom of the SP1 deposit. The shear forces at the failure surface for the DL scenario were obtained for each soil displacement, and Curve 1 was plotted, as shown in Figure 6.8 (a). Then, Curve 2, shown in Figure 6.8 (b), was generated by calculating the running average of the resisting forces to correct Curve 1 (CALTRANS 2017; SCDOT GDM 2022

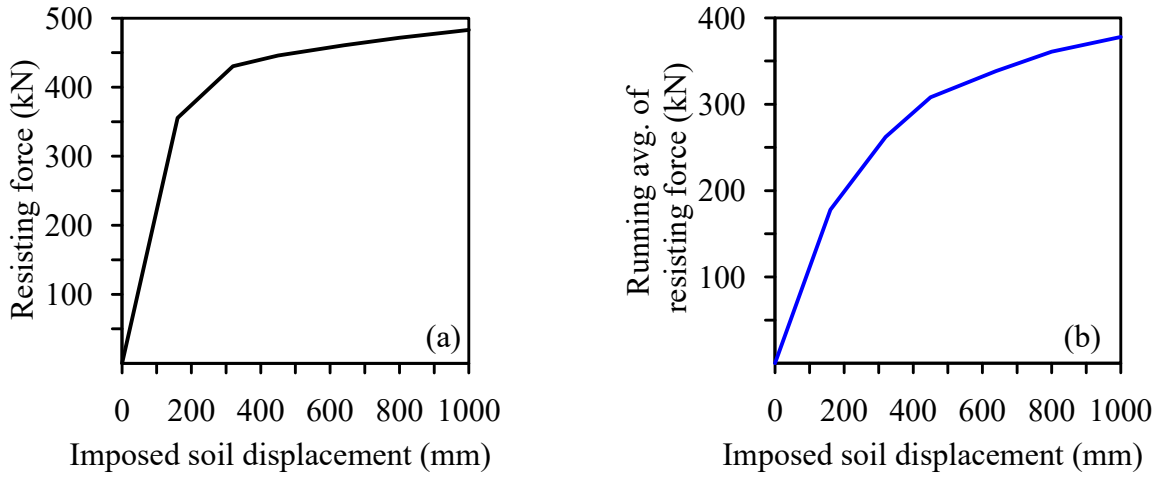

Figure 6.8. (a) Foundation resisting force vs. soil displacement (Curve 1) and (b) Running average of the foundation resisting force vs. soil displacement (Curve 2) for the DL scenario using the simplified analytical method

6.4.1.4. Step 4: Determination of design displacement demand

The design displacement demand was obtained from the intersection point of Curves 2 and 3 for the AL and Dl scenarios. Figure 6.9 shows the interaction curves with design displacement demands equal to 170 mm and 800 mm for the DL and AL scenarios.

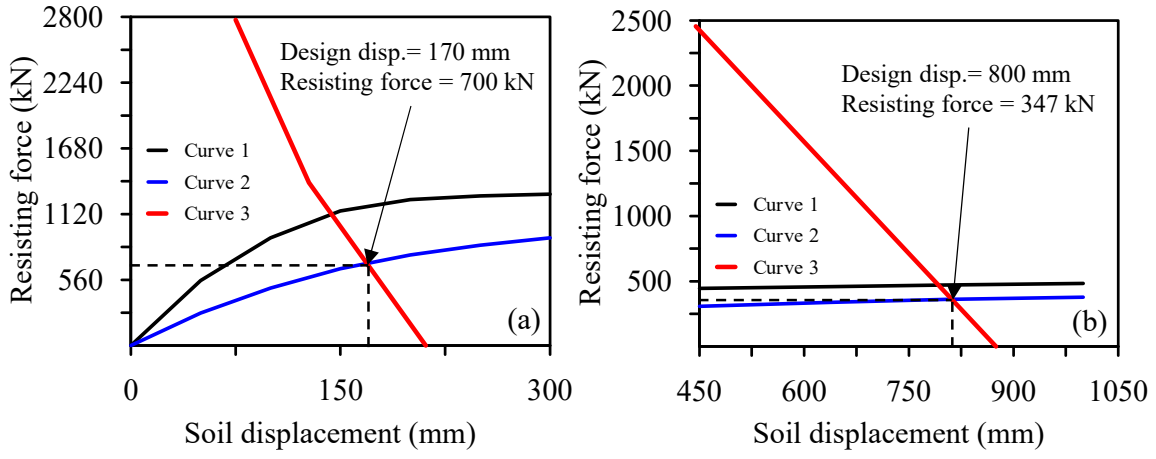

Figure 6.9. Interaction curves for (a) AL and (b) DL scenarios using the simplified analytical method

6.4.2. Minimum Penetration Analysis

The minimum penetration analysis was conducted to determine the minimum length of the drilled shaft, which can attain fixity. A constant axial load of 1112 kN and the soil displacement profile equal to the design displacement demand calculated in Step 4 were imposed on the foundation mm for drilled shaft lengths ranging from 32.5 m, 27 m, 21.5 m, and 13 m. Figure 6.10 (a) shows the imposed design displacement demand on the drilled shaft at the End bent-1 in RSPILE for the AL and DL scenarios. Figures 6.10 (b) and (c) show the lateral pile head deflection for various penetration depths of the drilled shaft for the AL and DL scenarios.

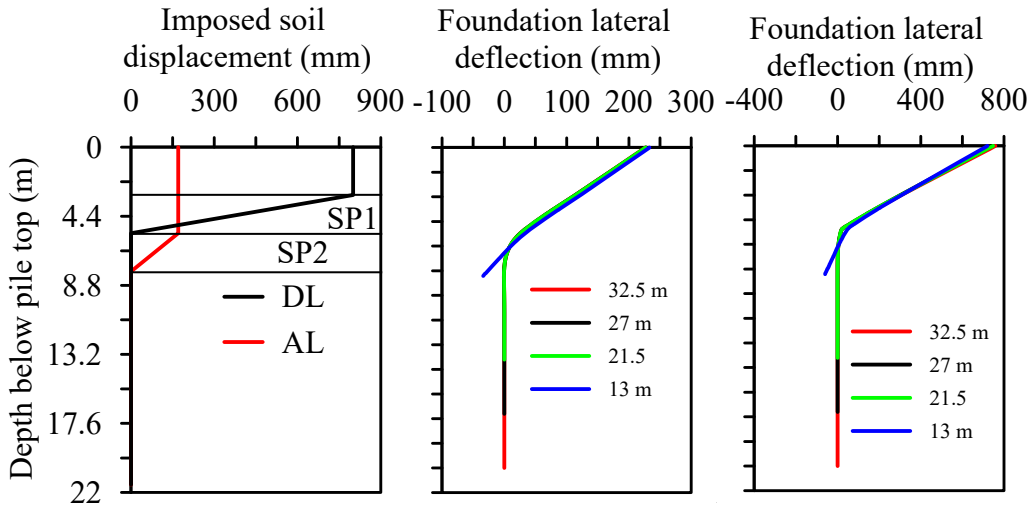

Figure 6.10. (a) Imposed soil displacement profiles for AL and DL scenarios; Foundation lateral displacement profiles resulting from minimum penetration analysis for (b) AL and (c) DL scenarios using the simplified analytical method

It can be seen that the drilled shaft length of 13 m does not provide fixity, and hence the drilled shaft length of 21.5 m was selected for the design. The pile head deflection was 227 mm for the AL scenario and 747 mm for the DL scenario for the 21.5 m length drilled

shaft. Hence, the minimum penetration analysis resulted in a 21.5 m length drilled shaft for the DL and AL scenarios and was used to determine the other drilled shaft foundation structural responses in the final step.

6.4.3. Analysis and Discussion

Finally, the design displacement demands were imposed on the 21.5 m long drilled shaft as soil displacement profiles for DL and AL scenarios to obtain the drilled shaft foundation structural response. Figure 6.11 shows the lateral deflection, shear force, and bending moment profiles for the AL and DL scenarios. The maximum lateral deflection for the DL scenario (747 mm) was significantly higher than the AL scenario (227 mm). The maximum shear force for the AL scenario (1216.4 kN) was approximately at the middle of the liquefiable deposit, SP2, and was slightly lower than the DL scenario (1306.5 kN), which was approximately at the middle of the SP1 deposit. Similarly, the maximum bending moment for the AL scenario (4169.6 kN-m) was slightly lower than the DL scenario (4273.3 kN-m) near the bottom of the SP2 deposit. Hence, the drilled shaft foundation structural response was highest for the DL scenario.

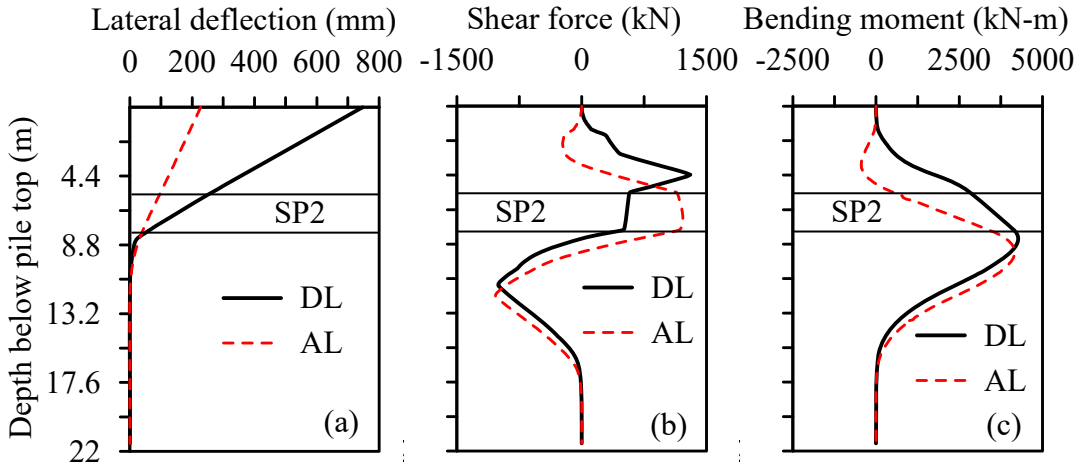

Figure 6.11. (a) Lateral deflection, (b) shear force, and (c) bending moment profiles for AL and DL scenarios using the simplified analytical method

6.5. METHOD 2: STRUCTURAL RESPONSE OF DRILLED SHAFT USING RIGOROUS ANALYTICAL METHOD

The simplified analytical method is based on the Simplified Rigid Block Newmark Analysis, where an empirical regression relationship (Anderson et al. 2008) is used to predict displacement based on pseudo-static seismic load. An alternative method to the simplified analytical method called the rigorous analytical method, which uses dynamic loading to predict displacement, is used in this study for comparison. This method is based on the Rigorous Rigid Block Newmark Analysis, where the cumulative displacements are calculated by double integrating the parts of the acceleration-time history of input ground motions that lie above the critical acceleration. The structural response of the drilled shaft foundation at End bent-1 was determined similarly to the simplified analytical method, except that the generation of the sliding mass displacement response curve (Curve 3) was based on Rigorous Rigid Block Newmark Analysis using site-specific ground motions.

6.5.1. Rigorous Analytical Method for Determination of the Design Displacement Demand

The design displacement demand on the drilled shaft at End bent -1 induced by liquefaction-induced lateral spreading for the rigorous analytical method was determined similar to the simplified analytical method for the DL and AL scenarios with the following alterations:

6.5.1.1. Selection of input ground motions:

Three site-specific ground motions were used for the Rigorous Rigid Block Newmark Analysis in SLIDE2 (Jibson et al. 2013; Rocscience 2022). The uniform hazard spectrum (UHS) and deaggregation parameters for the site were obtained from Scenario_PC. The suite of ground motions for the site was obtained from the NUREG/CR-6728 database (Mcquire et al. 2001). The ground motions were filtered out based on magnitude (M_w), source-to-site distance (R), and the shape of the response spectrum. Table 6.2 shows the M_w, R, PGA, and Arias Intensity (AI) for selected earthquakes.

Table 6.2. Selected time histories from the database

Record ID	Earthquake	Station	M_w	R (km)	PGA(g)	AI (g)
LV5000	Northridge (1994)	Leona Valley#5-Ritter#	6.7	38.3	0.317	0.86
WND233	San Fernando (1971)	Whittier Narrows Dam	6.6	45.1	0.263	1.15
L-BPL160	Mammoth Lakes (1980)	Bishop-Paradise Lodge	6.0	43.7	0.324	0.85

The suite of seed (real/actual earthquake recordings) time histories was spectrally matched to the UHS using the time-domain spectral matching algorithm in RSPMatch09 (Al-Atik and Abrahamson 2010). The modified acceleration time histories were used as input ground motions in SLIDE2 to determine the drilled shaft foundation structural response. Figure 6.12 shows the input acceleration-time history and baseline corrected displacement-time history for the San Fernando (1971) earthquake.

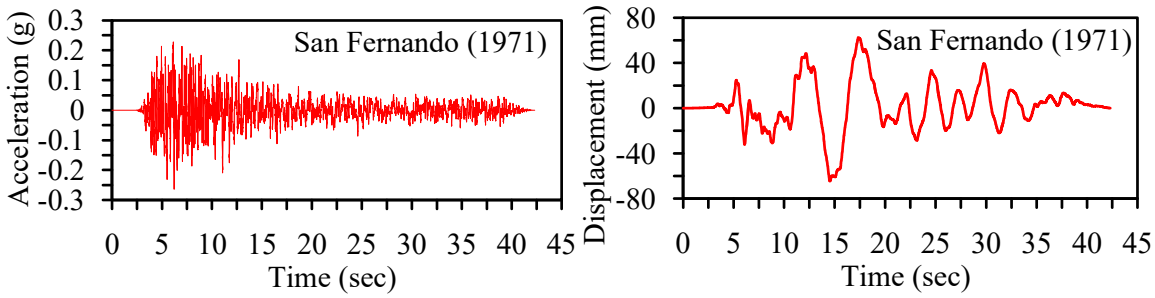

Figure 6.12. San Fernando (1971) earthquake (a) acceleration and (b) displacement time history

6.5.1.2. Generation of the sliding mass displacement response curve (Curve 3) based on Rigorous Rigid Block Newmark Analysis

Curve 3 was obtained by conducting Rigorous Rigid Block Newmark Analysis in SLIDE2 (Jibson et al. 2013; Rocscience 2022) using Spencer's method. A uniform live traffic surcharge load of 6 kPa as per SCDOT GDM (2022), Section 8.7, Table 8.8 was applied. First, the Rigorous Rigid Block Newmark Analysis was conducted for the AL scenario to obtain the displacement corresponding to the free field conditions and subjected to the input earthquake acceleration-time history. The soil displacement was obtained at the critical failure surface location (FS= 0.6), having a radius of 31.53 m. The failure

surface depth from Ground Level (GL) was 11.36 m in the middle of the liquefied soil deposit (SP2). The analysis was repeated for the DL scenario where the soil displacements were obtained at the critical failure surface location (FS= 0.35) having a radius of 73.68 m. The failure surface depth from GL was 8.34 m at the top of the SP1 soil deposit. The analysis was conducted to obtain the free-field soil displacements corresponding to the three earthquakes (Northridge (1994), San Fernando (1971), and Mammoth Lakes (1980)) for the AL and DL scenarios.

Then, models considering the foundation restraining action were created to produce 10 cases ranging from maximum restraining force corresponding to zero displacement (FS=1) to zero restraining force corresponding to maximum displacement or free-field condition (critical FS) for the three earthquakes for the AL and DL scenarios. The restraining force was varied between maximum and zero restraining force (8 cases) and the corresponding soil displacements. The computed soil displacements were then doubled to obtain soil displacements at 84% confidence level (Kavazanjian et al. 2011), and the restraining forces (kN/m) were multiplied by the effective width of the embankment (W_e=W+(m/2)*H=21.33 m; W=15.85 is the top width, m=2H:1V is the slope, and H=5.48 m is the height of embankment). For the AL scenario, the maximum restraining force after multiplying by the effective embankment width was 13868.4 kN at zero displacement, and the maximum soil displacements corresponding to zero restraining force were 30.88 mm for the Northridge (1994) earthquake, 40.84 mm for the San Fernando (1971) earthquake, and 34.38 mm for the Mammoth Lakes (1980) earthquake. For the DL scenario, the maximum restraining force after multiplying by the effective embankment width was

24536.4 kN at zero displacement, and the maximum soil displacements corresponding to zero restraining force were 183.3 mm for the Northridge (1994) earthquake, 226.42 mm for the San Fernando (1971) earthquake, and 149.62 mm for the Mammoth Lakes (1980) earthquake. The design displacement demand was obtained from the intersection of Curve 2 (same as obtained from the simplified analytical method) and Curve 3 for the AL and DL scenarios for the three earthquakes. Figure 6.13 shows the interaction curves with design displacement demands for the Northridge (1994), San Fernando (1971), and Mammoth Lakes (1980) earthquakes.

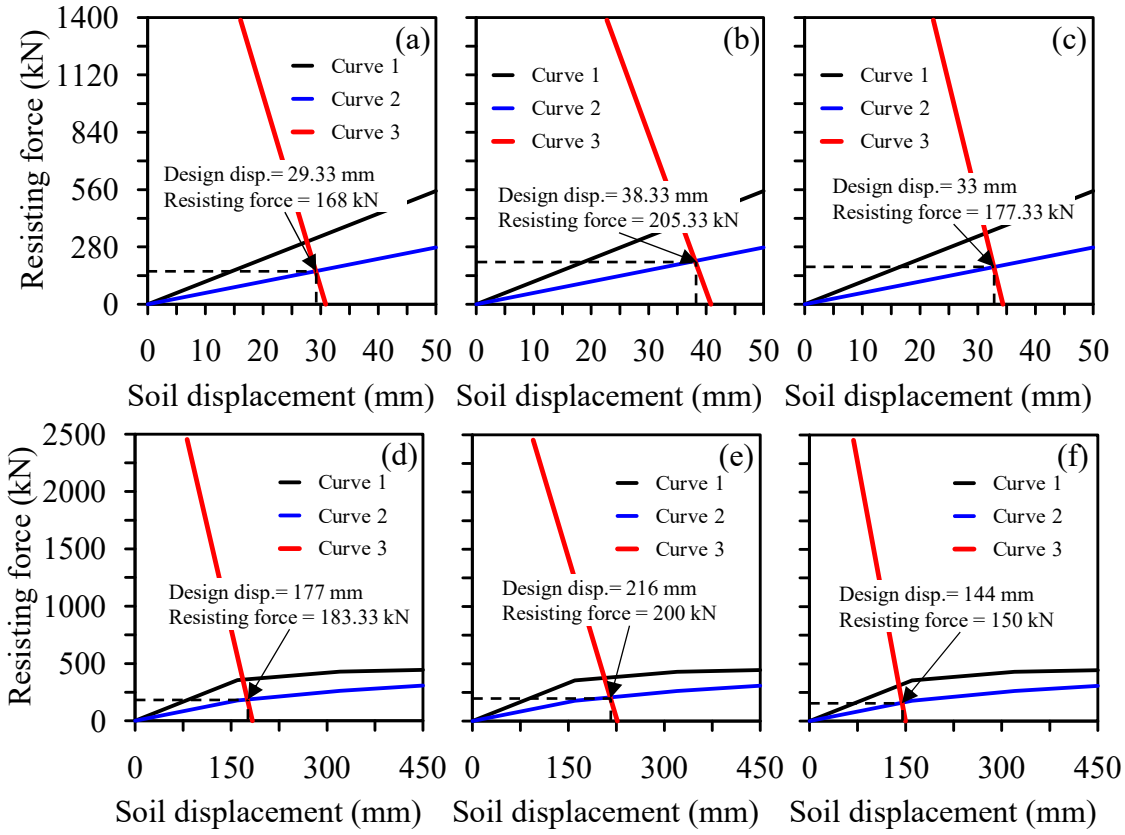

Figure 6.13. Interaction curves for (a) Northridge (1994), (b) San Fernando (1971), and (c) Mammoth Lakes (1980) earthquakes for AL scenario and (d) Northridge (1994), (e) San Fernando (1971), and (f) Mammoth Lakes (1980) earthquakes for DL scenario using the rigorous analytical method

6.5.2. Analysis and Discussion

The drilled shaft length of 21.5 m, which resulted from the minimum penetration analysis conducted in the simplified analytical method, was used to determine the drilled shaft foundation structural response using RSPILE for the DL and AL scenarios for the three earthquakes. The design displacement demands for the three earthquakes, as shown in Figure 6.13, were imposed on the 21.5 m long drilled shaft as soil displacement profiles to obtain the drilled shaft foundation structural response for the DL and AL scenarios. Figure 6.14 shows the lateral deflection, shear force, and bending moment profiles for AL and DL scenarios for the three earthquakes. It can be observed that the lateral deflection, shear force, and bending moment profiles have the least magnitude for the AL scenario and the maximum for the DL scenario. Also, for the DL scenario, there is a significant difference observed between the structural responses for the three earthquakes. The maximum lateral deflection, shear force, and bending moment values are observed for the San Fernando (1971) earthquake, followed by the Northridge (1994) earthquake, and the least for the Mammoth Lakes (1980) earthquake for the DL scenario. It is worth noting that this can be attributed to the decreasing Arias Intensity values from the San Fernando (1971) earthquake (1.15g) to the Northridge (1994) earthquake (0.86g) and then the Mammoth Lakes (1980) earthquake (0.85g). The Arias Intensity correlates well with several commonly used demand measures of structural performance, liquefaction, and seismic slope stability (Travasarou et al. 2003). The maximum lateral deflection, shear force, and bending moment values were observed for the San Fernando (1971) earthquake for the DL scenario equal to 200.28 mm, 978.05 kN, and 3374.04 kN-m, respectively. For the AL

scenario, a smaller difference is observed between the structural responses for the three earthquakes compared to the DL scenario. The maximum lateral deflection, shear force, and bending moment values are observed for the San Fernando (1971) earthquake, followed by the Mammoth Lakes (1980) earthquake, and the least for the Northridge (1994) earthquake. However, the difference between the structural responses for the Northridge (1994) earthquake and the Mammoth Lakes (1980) earthquake is negligible.

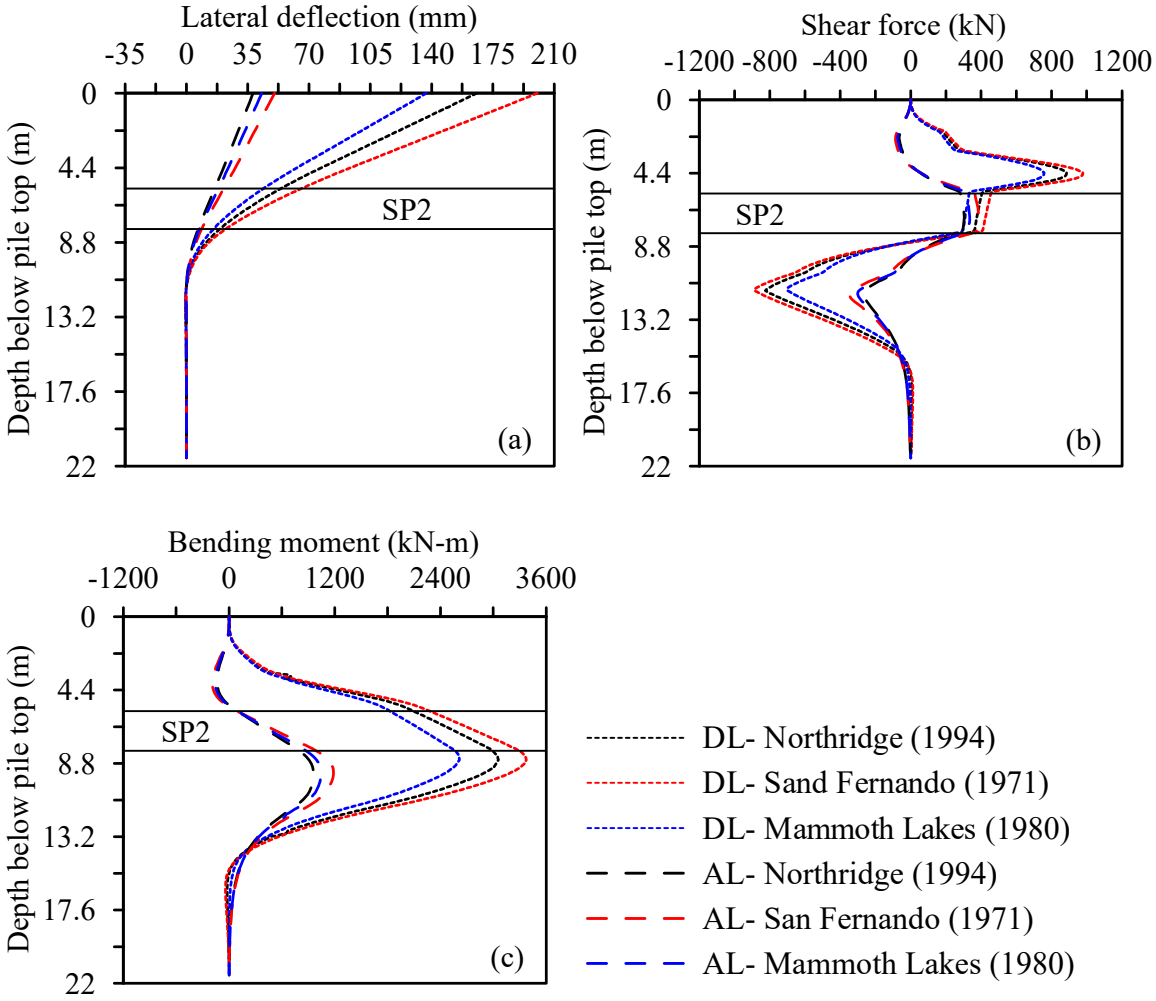

Figure 6.14. (a) Lateral pile head deflection, (b) shear force, and (c) bending moment profiles for AL and DL scenarios using the rigorous analytical method

6.6. METHOD 3: STRUCTURAL RESPONSE OF DRILLED SHAFT USING COUPLED FINITE ELEMENT METHOD

6.6.1 Finite Element Model

The SLIDE2 models were imported into RS2 for conducting finite element analyses. The simulation domain was spatially discretized with 39855 6-noded triangular plane-strain elements. The available bedrock depth in the geotechnical report (GeoStellar Engineering, LLC 2019) was used for the simulation domain. A model size sensitivity study and a mesh sensitivity study were conducted by varying simulation domain size and the number of elements in the simulation domain to obtain a suitable size and mesh, ensuring that any change in the domain and mesh size does not affect the predicted results. For deformation, the vertical boundaries of the simulation domain were restrained in the horizontal direction and allowed to move freely in the vertical direction. The bottom was fixed in both horizontal and vertical directions. The top boundary was assigned to be traction-free. The acceleration-time histories considered in this study were baseline corrected using the cubic baseline correction technique and applied at the base of the simulation domain.

A 1.37 m diameter and 21.5 m long drilled shaft embedded in soil was represented by a linear elastic beam element. The End bent-1 for retaining backfill was modeled as linear elastic material with concrete properties the same as drilled shaft. The non-linear elastoplastic stress-strain behavior of the soil was modeled using the widely used Mohr-Coulomb (MC) constitutive model. The MC model parameters include unit weight, peak,

residual friction angle, and cohesion. The values are tabulated in Table 6.1. The analysis was conducted in three phases: (1) Initial phase (Imported SLIDE2 model), where initial stresses were generated due to gravity; (2) Excavation and construction phase, where the slope was excavated, and the liner element and End bent-1 section was activated; and (3) Dynamic phase where the input earthquake acceleration-time histories were assigned at the bottom boundary. The three modified site-specific acceleration-time histories were used as input ground motions in RS2 to determine the drilled shaft foundation structural response. Figure 6.15 shows the simulation domain for the dynamic phase.

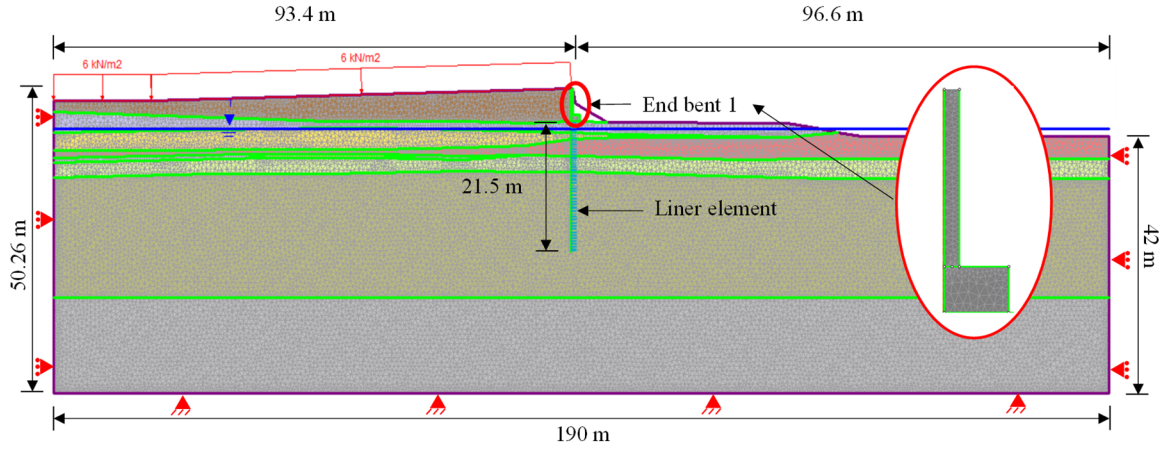

Figure 6.15. Simulation domain for the dynamic phase in RS2

6.6.2. Analysis and Discussion

Figure 6.16 shows the lateral pile deflection, shear force, and bending moment profiles for the three earthquakes for BL, DL, and AL scenarios. It can be observed that the lateral deflection, shear force, and bending moment profiles have the least magnitude for the BL scenario, followed by the AL scenario and the maximum for the DL scenario.

Also, the maximum lateral deflection, shear force, and bending moment values are observed for the San Fernando (1971) earthquake, followed by the Northridge (1994) earthquake, and the least for the Mammoth Lakes (1980) earthquake for the DL scenario. This can be attributed to the decreasing Arias Intensity values from the San Fernando (1971) earthquake (1.15g) to the Northridge (1994) earthquake (0.86g) and then the Mammoth Lakes (1980) earthquake (0.85g). The Arias Intensity correlates well with several commonly used demand measures of structural performance, liquefaction, and seismic slope stability (Travasarou et al. 2003). Overall, the maximum lateral deflection, shear force, and bending moment values were observed for the San Fernando (1971) earthquake for the DL scenario equal to 125.59 mm, 1121.7 kN, and 4503 kN-m, respectively. For the AL scenario, the maximum lateral deflection, shear force, and bending moment were induced by the Northridge (1994) earthquake. However, the difference between the bending moment and shear force profiles for the Northridge (1994) earthquake and the San Fernando (1971) earthquake was negligible.

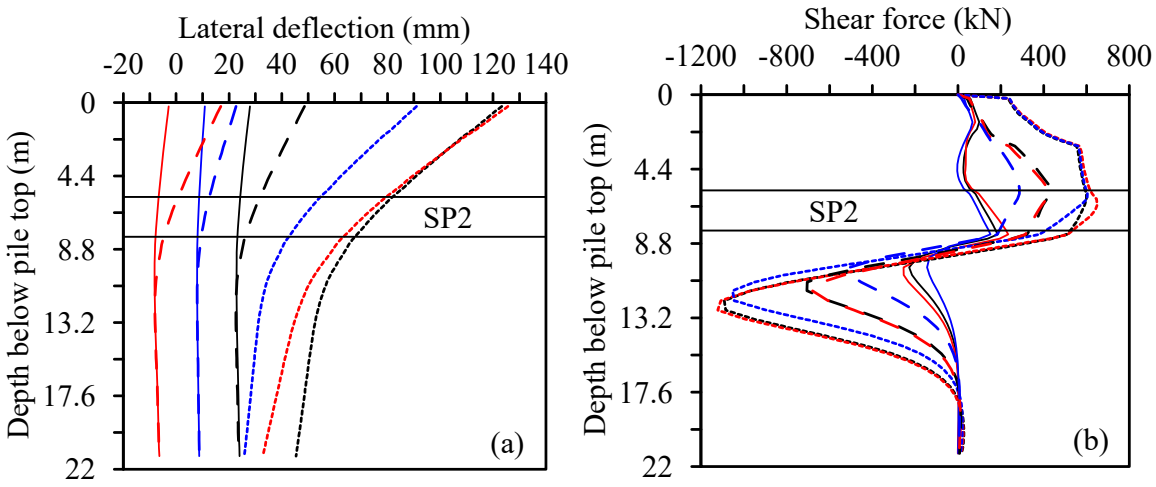

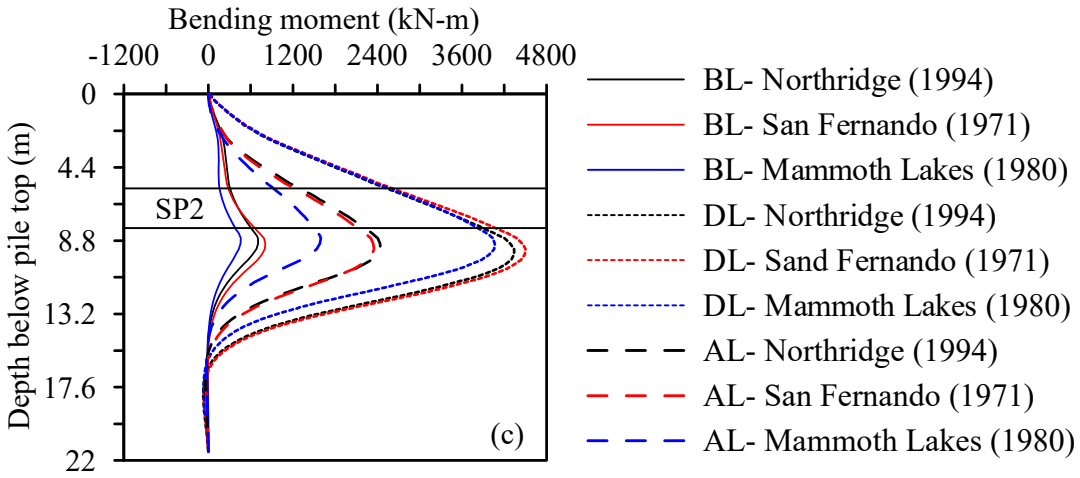

Figure 6.16. (a) Lateral pile deflection, (b) shear force, and (c) bending moment profiles for BL, DL, and AL scenarios using the finite element method

6.7. COMPARISON OF PREDICTED RESPONSES USING THE THREE METHODS AND DISCUSSION

Figure 6.17 shows the lateral pile deflection, shear force, and bending moment profiles obtained using analytical and finite element methods for the DL and AL scenarios. It can be observed from Figure 6.17 (a), (b), and (c) that the maximum lateral deflection values for the AL and DL scenarios for the three earthquakes determined using the rigorous analytical method and finite element method are close while those determined using the simplified analytical method are significantly higher. For instance, the maximum lateral head defection for the DL scenario for the San Fernando (1971) earthquake determined using the rigorous analytical method (200.28 mm) was close to the value determined using the finite element method (125.59 mm). However, the lateral deflection value determined using the simplified analytical method for the same case was equal to 746.94 mm. The maximum lateral deflection values for the DL scenario for all three earthquakes are observed to be maximum for the simplified analytical method, followed by the rigorous analytical method, and the least for the finite element method. The maximum bending

moment values lie near the bottom of the SP2 deposit, where the maximum values for simplified analytical and finite element methods are close, while the maximum values for the rigorous analytical method are significantly lower for the three earthquakes for the DL and AL scenarios.

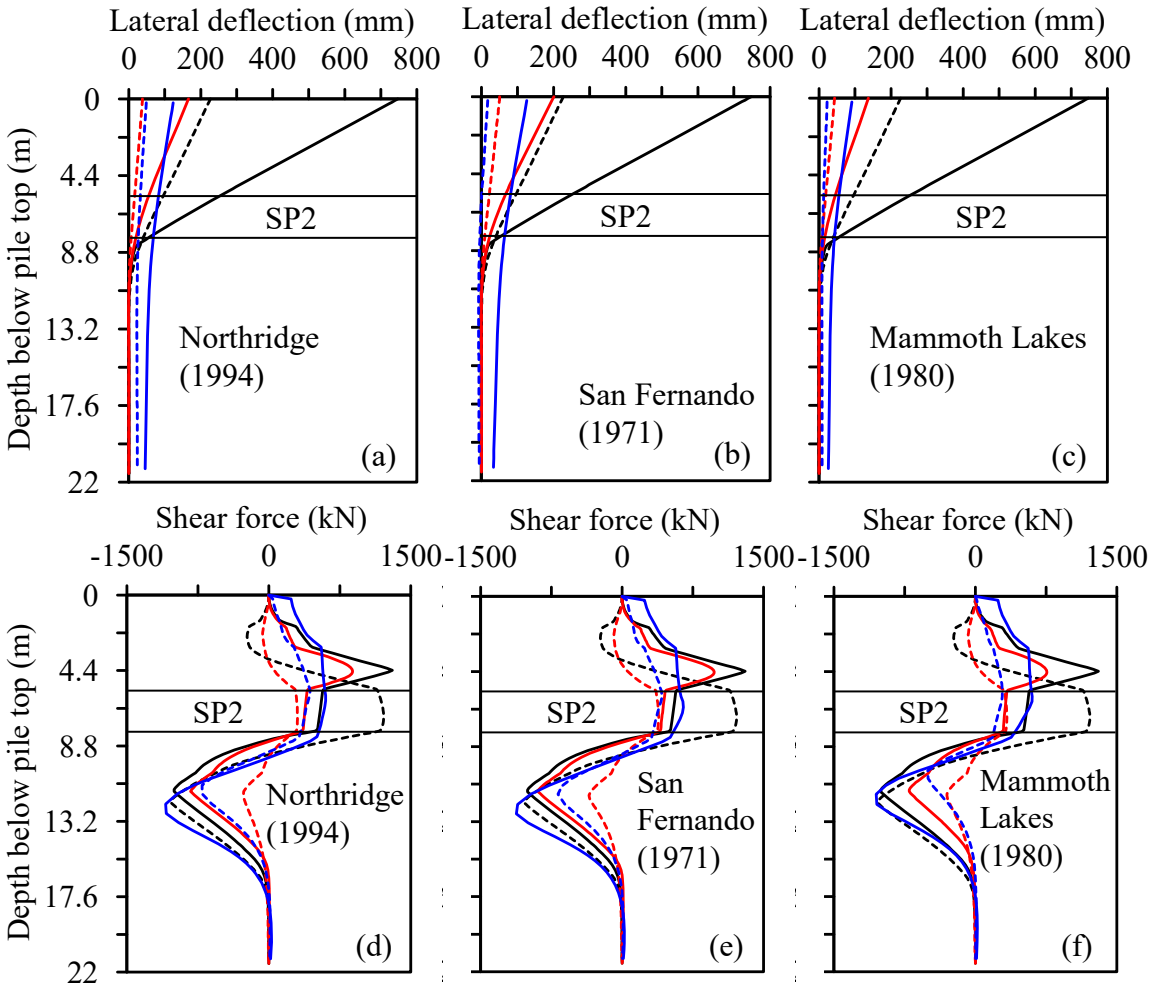

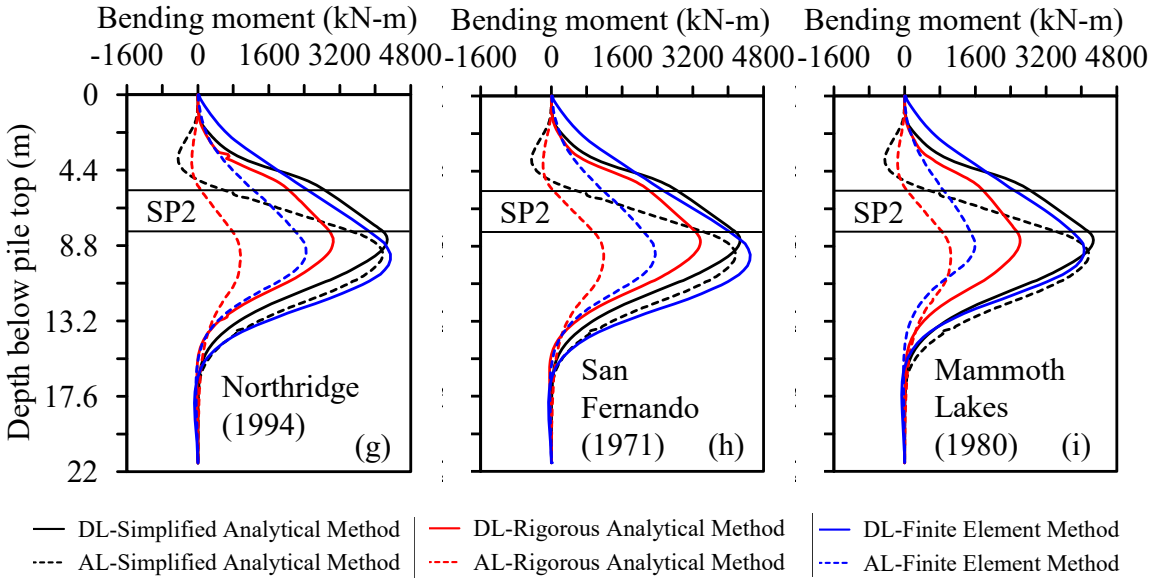

Figure 6.17. Comparison of methods showing lateral pile deflection profiles for (a) Northridge (1994), (b) San Fernando (1971), and (c) Mammoth Lakes (1980) earthquakes, shear force profiles for (d) Northridge (1994), (e) San Fernando (1971), and (f) Mammoth Lakes (1980) earthquakes, and bending moment profiles for (g) Northridge (1994), (h) San Fernando (1971), and (i) Mammoth Lakes (1980) earthquakes for the AL and DL scenarios

Table 6.3 shows the comparison of maximum values of lateral pile deflection, shear force, and bending moment for the AL and DL scenarios using the analytical and finite element methods.

Table 6.3. Comparison of maximum structural responses for the DL and AL scenarios

Parameter	Simplified analytical method		Rigorous analytical method		Finite element method	
	AL	DL	AL	DL	AL	DL
Lateral deflection (mm)	227.00	746.94	50.29	200.28	48.55	125.59
Shear force (kN)	1216.40	1306.50	387.46	978.05	705.01	1121.7
Bending moment (kN-m)	4169.60	4273.3	1185.09	3374.04	2441.2	4503.05

6.8. Comparison of Predicted and Field-Measured Lateral Spread Displacements from Case Studies and Discussion

Yang et al. (2020) compared the liquefaction-induced lateral spread displacements obtained from the Simplified Newmark Analysis and Rigorous Newmark Analysis with five case histories and concluded that the Simplified Newmark Analysis overpredicted the displacements for some cases while underpredicted displacements for other cases. Table 6.4 shows the comparison of predicted and field-measured lateral spread from case studies and this study. The predicted lateral spread displacements in this study were obtained using the seismic slope stability analysis in SLIDE2 for the free-field condition as discussed in Methods 1 and 2 for the AL scenario. The predicted lateral spread displacements for Method 2 were taken as averages of the lateral spread displacements resulting from the Northridge (1994), San Fernando (1971), and Mammoth Lakes (1980) earthquakes. The lateral spread displacement predicted in this study for the South Carolina site using the simplified analytical method showed close agreement with the field-measured values from the case studies in California.

Table 6.4. Comparison of predicted and field-measured lateral spread displacements from case studies

Case study	Predicted lateral spread (mm)		Field-measured lateral spread (mm)
	Simplified analytical method	Rigorous analytical method	
Florence/Lee County, South Carolina (This study)	211	35.36	-
Moss landing site, California*	170	670	280

Northridge site, California*	150	160	150
Wildlife site, California*	20	90	180

* Yang et al. (2020)

Kavazanjian et al. (2011) concluded that the Newmark sliding block analysis is conservative because it is assumed that liquefaction occurs immediately at the start of the earthquake (National Academies of Sciences, Engineering, and Medicine 2021). In this study, the analytical methods resulted in higher soil displacements and, consequently, higher lateral pile deflections than those obtained from the finite element method. However, the accuracy of the analytical methods could not be assessed. Hence the accuracy of the analytical methods needs to be validated by comparison studies between the results of analytical methods used in this study with more documented case histories of liquefaction-induced lateral spreading and centrifuge experiments is needed (National Academies of Sciences, Engineering, and Medicine 2021).

6.9. CONCLUSION

The drilled shaft foundation structural responses before, during, and after liquefaction-induced lateral spreading were predicted at an end-bent of a new bridge in SC using three different methods, and the results were compared. The results obtained from the simplified analytical and rigorous analytical methods show that the structural responses were observed to be higher for the DL scenario than for the AL scenario. The results obtained from the finite element method show that the structural responses have the lowest magnitude for the BL scenario, followed by the AL scenario, and the maximum for the DL

scenario. Hence, the DL proved to be the worst-case scenario. The decreasing lateral deflection, shear force, and bending moment values for the three earthquakes for the DL scenario determined using the rigorous analytical and finite element methods may be attributed to the decreasing Arias Intensity of these earthquakes. The maximum lateral deflection values for the AL and DL scenarios for the three earthquakes determined using the rigorous analytical method and finite element method were close, while those determined using the simplified analytical method were significantly higher. The structural response estimated using the finite element method provided more realistic results than the analytical methods. The accuracy of the analytical methods could not be assessed, and their accuracy needs to be validated by comparison studies between the results of analytical methods with more documented case histories of liquefaction-induced lateral spreading and centrifuge experiments.

REFERENCES

Al Atik, L., and Abrahamson, N. A. (2010). "An improved method for non-stationary spectral matching," Earthquake Spectra, 26(3), pp.601-617.

Amiri, S. (2008). The Earthquake Response of Bridge Pile Foundations to Liquefaction Induced Lateral Spread Displacement Demands. Ph.D. University of Southern California.

Anderson, D. G., Martin, G. R., Lam, I. and Wang, J. N., (2008). "Seismic Analysis and Design of Retaining Walls, Buried Structures, Slopes and Embankments", NCHRP Report 611, Volumes 1 and 2, Transportation Research Board.

Ashford, S., Boulanger, R. and Brandenberg, S. (2011). Recommended Design Practice for Pile Foundations in Laterally Spreading Ground. PEER Report 2011-04, Pacific Earthquake Engineering Research Center. https://peer.berkeley.edu/publications/2011-04

SCNOW (2022). <https://scnow.com/news/local/cartersville-bridge-replacement-heading-toward-november-completion/article_06e3c10c-d06b-11ec-a07a-9b96a05bb0e8.html>

Chapman, M. C. (2006). User's Guide to SCENARIO_PC and SCDOTSHAKE, Report to the South Carolina Department of Transportation, Columbia, SC.

GeoStellar Engineering, LLC. (2019). US 76 Bridge Replacement Over Lynches River Florence/Lee Counties, South Carolina.

Hamada, M., Isoyama, R. And Wakamatsu, K. (1996). Liquefaction-Induced Ground Displacement and its Related Damage to Lifeline Facilities. Soils And Foundations, 36(Special), Pp.81-97.

Hargy, J. (2011). Measuring residual strength of liquefied soil with the ring shear device, Master's Theses, and Capstones. 828. https://scholars.unh.edu/thesis/828.

Hynes, M. E. and Franklin, A. G., (1984), "Rationalizing the Seismic Coefficient Method," Miscellaneous Paper GL-84-13, U.S. Army Waterways Experiment Station, Vicksburg, MS, July.

Jibson, R.W., Rathje, E.M., Jibson, M.W., and Lee, Y.W. (2013). SLAMMER – *Seismic LandSlide2 Movement Modeled using Eatherquake Records* (ver.1.1, November 2014): U.S. Geological Survey Techniques and Methods, book 12, chap. B1, unpaged.

Kavazanjian, E., Jr., J.-N.J. Wang, G.R. Martin, A. Shamsabadi, I. Lam, S.E. Dickenson, C.J. Hung. (2011). LRFD Seismic Analysis and Design of Transportation Geotechnical Features and Structural Foundations Reference Manual. NHI Course No. 130094 Reference Manual. Geotechnical Engineering Circular No. 3. Washington, DC: National Highway Institute, U.S. Department of Transportation, Federal Highway Administration. https://www.fhwa.dot.gov/engineering/geotech/pubs/nhi11032/nhi11032.pdf.

Martin, G.R., and Qiu, P.(1994). "Effects of Liquefaction on Vulnerability Assessment," NCEER Highway Project on Seismic Vulnerability of New and Existing Highway Construction. One Year Research. Technical Research Paper.

Matlock, H. (1970). Correlations for design of laterally loaded piles in soft clay. Proceedings of the II Annual Offshore Technology Conference, Houston, Texas, (OTC 1204): 577-594.

Mcquire, R., Silva, W. and Constantino, C. (2001). Technical Basis for Revision of Regulatory Guidance on Design Ground Motions: Hazard and Risk-Consistent Ground Motion Spectra Guidelines. NUREG/CR-6728. US Nuclear Regulatory Commission.

Memo to Designers, Caltrans. (2017). Lateral Spreading Analysis for New and Existing Bridges.

National Academies of Sciences, Engineering, and Medicine. (2021). State of the Art and Practice in the Assessment of Earthquake-Induced Soil Liquefaction and Its Consequences. Washington, DC: The National Academies Press. https://doi.org/10.17226/23474.

Reese, L.C., W.R. Cox and F.D. Koop. (1974). Field testing and analysis of laterally loaded piles in sand. Proceedings of the VI Annual Offshore Technology Conference, Houston, Texas.

Rocscience Inc. (2022). Rocscience software suite. <https://www.rocscience.com/>

South Carolina Department of Transportation (SCDOT). (2022). Geotechnical Design Manual.

Skempton, A. (1986). Standard penetration test procedures and the effects in sands of overburden pressure, relative density, particle size, ageing and overconsolidation. Geotechnique, 36(3).

Travasarou, T., Bray, J. and Abrahamson, N. (2003). Empirical attenuation relationship for Arias Intensity. Earthquake Engineering & Structural Dynamics, 32(7), pp.1133-1155.

Turner, B., Brandenberg, S. and Stewart, J. (2016). Case Study of Parallel Bridges Affected by Liquefaction and Lateral Spreading, Jour. Geotech. and Geoenviron. Eng, 142(7).

Welch, R.C. and L.C. Reese. (1972). Laterally loaded behavior of drilled shafts. Research Report 35-65-89. Center for Highway Research. University of Texas, Austin.

Yang, Y., Chen, J., Zhang, Z. and Ma, J. (2020). Evaluating Lateral Spreading Using Newmark Method Based on Liquefaction Triggering. Advances in Civil Engineering, 2020, pp.1-17.

CHAPTER 7 SUMMARY AND CONCLUSIONS

This dissertation commenced with analyzing the effect of extreme hydroclimatic events, including heavy rainfall and prolonged drought, on the deformation and bearing capacity behavior of deep foundations. Initially, the analytical design of a full-scale drilled shaft and a proportionate small-scale drilled shaft in sand and silty sand was done. Then, the temporal variation of the end bearing capacity, skin resistance, and vertical settlement of the drilled shafts due to hydrological load was carried out using the fully- coupled Geotechnical- Hydrological finite element code PLAXIS 2D. A modified Mohr-Coulomb (MMC) model capable of updating the yield criterion and modulus with changes in matric suction and/or degree of saturation was used to represent the stress-strain behavior of the partially saturated soil in PLAXIS 2D as soil deformation properties change with the flow of water. Overall, the effects on the deformation and bearing capacity were very small. The settlement of the sand caused the drilled shaft to settle during rainfall which was attributed to the hydrodynamic load induced by the heavy rainfall on the ground, low density and decreasing porewater pressure. This settlement caused a decrease in skin resistance/increase in the end-bearing resistance of the drilled shaft. Upward vertical displacement of the sand and drilled shaft during drought was observed, which was attributed to the rebound of elastic settlement as the DOS decreases, the hydrodynamic loading on the ground is reduced and PWP increases. The upward vertical displacement caused an increase in skin resistance/decrease in the end-bearing resistance of the drilled shaft. The silty sand under study was relatively dense compared to the sand, and the increase in the degree of saturation in silty sand during rainfall was higher than the sand.

Hence, upward vertical displacement of the silty sand caused the upward displacement of the drilled shaft during heavy rainfall, which was attributed to an increase in the soil volume as the rainwater enters the soil matrix and increasing porewater pressure. However, the upward vertical displacement was only at shallow depths, and settlement was observed at deeper depths. Then during drought, settlement of the drilled shaft was observed, which was attributed to a decrease in soil volume as the degree of saturation drops to a residual value and decreasing porewater pressure. It was noted that the loss of skin resistance caused by loss of normal stress at the soil-pile interface due to shrinkage of soil during drought is not captured in numerical modeling, and hence, an experimental investigation was crucial for observing realistic behavior.

An experimental investigation was carried out for the small-scale precast drilled shaft subjected to rainfall with three different intensities- low, medium, and high. The materials and methods adopted for the construction of the experimental setup were discussed, which included the design and construction of the precast drilled shaft, soil box, and the instrumentation and calibration of sensors and loading setups. The results obtained from the experimental investigation were used to validate the finite element model in PLAXIS 2D. It was observed that the wetting front moves at the same rate in FEM as compared to the experiment and also reaches the drilled shaft bottom at the same time. The low-intensity rainfall caused the settlement of the drilled shaft, which caused a decrease in the total bearing capacity of the drilled shaft due to the mobilization of the skin resistance to the bottom of the drilled shaft. The medium- and high-intensity rainfall mostly caused the vertically upward displacement of the drilled shaft at shallow depths, which caused an

increase in the total bearing capacity of the drilled shaft. The axial force variation at various time intervals for the FEM matched with the experiment qualitatively in various aspects. The compaction of soil plays a crucial role and will cause the drilled shaft to respond differently to the low-, medium, and high-rainfall intensities. Hence, more experimental tests with different relative compaction of soil should be conducted in the future.

Further, the study was extended to analyze the combined effect of hydrological and earthquake loads and the individual effect of seismic load on the foundation structural response for a full-scale drilled shaft in Test Sand using the MMC model in the fully-coupled finite element code PLAXIS 2D. When the drilled shaft was subjected to the dynamic load from heavy rainfall, upward vertical displacement occurred due to an increase in the volume of the soil when water entered the soil matrix from the heavy rainfall. The upward vertical displacement was maximum at the start of heavy rainfall and then resided as the wetting front traveled down. When the drilled shaft was subjected to the dynamic load from heavy rainfall followed by dynamic load from the earthquake, the vertical settlement for the drilled shaft was very high compared to the case where the drilled shaft was subjected to dynamic load from the earthquake. Hence, the combined effect of heavy rainfall and earthquake can cause more damage to the deep foundations.

Finally, a case study was adopted to predict the structural response of a deep foundation at the end bent of a proposed bridge subjected to liquefaction-induced lateral spreading caused by an extreme seismic event. The structural responses of the bridge foundation before, during, and after liquefaction-induced lateral spreading were predicted using the simplified analytical method, rigorous analytical method, and the coupled finite

element method using the 2D finite element program RS2 considering before-liquefaction (BL), during-liquefaction (DL), and after-liquefaction (AL) scenarios, and the results were compared. The results obtained from the simplified analytical and rigorous analytical methods show that the structural responses were observed to be higher for the DL scenario than for the AL scenario. The results obtained from the finite element method show that the structural responses have the lowest magnitude for the BL scenario, followed by the AL scenario, and the maximum for the DL scenario. Hence, the DL proved to be the worst-case scenario. The accuracy of the analytical methods could not be assessed, and their accuracy needs to be validated by comparison studies between the results of analytical methods with more documented case histories of liquefaction-induced lateral spreading and centrifuge experiments.